# Kinetic studies of gas-liquid reactions in capillary microreactors

*by*

**Chara Psyrraki**

Department of Chemical Engineering

University College London

February 2015

A thesis submitted for the degree of Doctor of Philosophy

Declaration of Authorship

I, Chara Psyrraki, declare that this thesis titled 'Kinetics of gas-liquid reactions in capillary microreactors' and the work presented in it are my own and have been generated by me as the result of my own original research. Where information has been derived from other sources, I can confirm that this has been clearly indicated in the thesis.

To my dad.

## Abstract

The main aim of this study was to develop a rate expression for the first stage reaction for the production of methyl methyl acrylate (methyl ester of methacrylic acid or MMA) using Lucite International Alpha Process. MMA is an acrylic glass material which main features such as transparency, high hardness, resistance to fracture and chemical stability makes it suitable for a wide range of industrial applications. The first stage of the Alpha process is the synthesis of methyl propionate (MeP) from ethylene, carbon monoxide and methanol over homogenous Pd catalyst with selectivity higher than 99.9%. It is a gas-liquid catalytic reaction that takes place at high temperature and pressure conditions. For the kinetic study of this system, experimental studies were performed under a range of inlet conditions (temperature, catalyst, gas and liquid inlet compositions) using capillary microreactors. Moreover, a kinetic model for this system was developed and its validity was verified by comparison with experimental results. Furthermore, a reactor model was developed to simulate the reaction process and was further used for parametric estimation of the kinetic model. For the validation of the reactor model, experiments with a model system, a reaction with well-studied kinetics were performed and the model predictions were compared with the experimentally obtained results. For the complete characterisation of the gas-liquid system, hydrodynamic study of the system was conducted to identify the flow pattern, the void fraction and the mass transfer characteristics of the system. Furthermore, hydrodynamic studies on other gas-liquid systems were performed to investigate the effect of parameters such as the gas-to-liquid ratio, the channel diameter and the fluid properties on the hydrodynamic characteristics of the systems. Comparison with previous hydrodynamic models was conducted and a new correlation for the prediction of void fraction in gas-liquid systems under similar conditions was suggested.

## Acknowledgements

This dissertation would not have been possible without the help of so many people in so many ways.

First, I would like to express my deepest gratitude to my supervisor, Professor Asterios Gavriilidis, for his full support, guidance and mentorship throughout my study. I feel truly honoured of being one of his students. Furthermore, I wish to express my sincere thanks to Lucite International and specifically to Dr. Morris, Dr. Gobby, Dr. Tindale, Dr. Turner and Dr. Waugh for the financial support, the insightful comments and the catalyst they provided to carry out the experiments. Special thanks should be given to Dr. Galvanin for his collaboration and help in my starting steps in the field of kinetic modelling.

I also want to thank all my friends at UCL and especially Noor, Mithila, Rema, Shade, Eria, Dave, Erik, Savio and Miguel for the time we spent together in the office and the labs, our special tea and coffee breaks, the Fridays at ULU and all the laughs. I will miss all of these a lot! I am also very grateful to some very special friends of mine, Andrea, Ioli, Niki, Aggelakos, Aggelica and Myrto who shared this journey with me with inestimable support.

Above all I wish to thank my parents and my brothers for their faith in me, their unconditional love, their endless support and understanding throughout all these years. None of this would be possible without them and to them I am eternally grateful.

Last but certainly not least, I would like to thank Aristotle for his constant love, support, motivation, encouragement and patience at all times. He was always cheering me up and stood by me through the good and bad times.

# Contents

# List of Figures

# List of Tables

# Nomenclature

| Symbol | Name | Unit |
|---|---|---|
| A | Interfacial area or<br>Numerical prefactor | $cm^2$ |
| C | Concentration | mol/ml |
| $C_p$ | Specific heat | kg/s |
| D | Diffusion coefficient or | $cm^2/s$ |
| | Dispersion coefficient or | $cm^2/s$ |
| | Diameter | cm |
| d | density | kg/ml |
| F | Molar Flowrate | mol/min |
| H | Solubility or<br>Fisher information matrix | mol/(ml·atm) |
| h | Heat transfer coefficient | $W/m^2K$ |
| He | Henry's constant | - |
| ID | Inner diameter | cm |
| j | Superficial velocity | cm/min |
| k | Reaction rate constant or | $s^{-1}$ |
| | Thermal conductivity | W/m·K |
| K | Equilibrium constant | - |
| $k_\ell$ | Mass transfer coefficient | |
| L | Length | cm |
| m | Mass | kg |
| N | Moles or | mol |
| | Number of data | - |

| | | |
|---|---|---|
| n | Viscosity | Pa·s |
| OD | Outer diameter | cm |
| P | Pressure | bar |
| p | Perimeter | cm |
| Q | Sensitivity matrix | |
| R | Gas constant | ml·atm/K·mol |
| r | Reation rate | |
| s | Standard deviation | |
| T | Temperature | $^{o}$C or K |
| t | Time | min |
| TOF | Turn over frequency | mol/mol·min |
| V | Volume | ml |
| X | conversion | - |
| x | Liquid fraction or | - |
| | Distance | cm |
| y | Gas fraction | - |
| Z | Compressibility factor | |

Greek Symbols

| | | |
|---|---|---|
| α | Interfacial area | cm$^2$ |
| β | Carbonate-to-bicarbonate ratio or | - |
| | Volumetric quality | - |
| γ | Surface tension or | N/m |
| | Activity coefficient | - |
| δ | Film thickness | μm |
| ε | Void fraction | - |

| | | |
|---|---|---|
| θ | Dimensionless time or Model parameters | - |
| μ | Viscosity | Pa·s |
| π | Pi number | - |
| ρ | Density | kg/ml |
| τ | Residence time | min |
| υ | Volumetric Flowrate | ml/min |
| φ | Fugacity coefficient | - |

Dimensional Numbers

| | |
|---|---|
| D/uL | Vessel dispersion number |
| Ha | Hatta number |
| Nu | Nusselt number |
| Pe | Peclet number |

Subscripts

| | |
|---|---|
| 0 | Initial |
| c | Cross sectional or Critical |
| cal | Calculated |
| D | Diameter |
| exp | Experimental |
| f | Final |
| g | Gas |
| ℓ | Liquid |
| ov | Overall |
| s | saturated |
| v | vapour |

# CHAPTER 1. Introduction & Background

## 1.1 Scope of Thesis

The scope of the thesis is to study the kinetics of the first stage reaction for the production of methyl methacrylate (MMA) using Lucite International Alpha Process. The first stage of the Alpha process is the synthesis of methyl propionate (MeP) from ethylene, carbon monoxide and methanol over homogenous Pd catalyst with selectivity higher than 99.9%. It is a gas-liquid catalytic reaction that takes place at high temperature and pressure conditions. The kinetic study will involve understanding of the effect of reactant's and catalyst concentrations as well as of temperature on reaction rate. The main aim of this study is a rate expression for the methoxycarbonylation of ethylene that is valid over a range of experimental conditions.

In order to develop fundamental process knowledge accurate kinetic data are essential. For this purpose, a capillary microreactor will be utilised for this study as due to the advantages of microreactor technology it is believed that it will produce accurate kinetic data. Moreover, mathematical models will be developed to simulate the reaction process and used further for parameter estimation. Aim of this project is to address all the phenomena included in this process such as hydrodynamic aspects and vapour-liquid equilibrium.

Finally, this study will act also as a validation of the integrated microreactor technology that will be developed for kinetic studies, so in the future kinetic evaluation of other reactions of this nature will be able to be performed in this system with confidence.

## 1.2 Methyl Methacrylate: Applications and Production Processes

### 1.2.1 Background Information on Methyl Methacrylate

Methyl methacrylate (MMA) is a very important and industrially interesting monomer with excellent transparency, strength and outdoor durability. It is an essential for the production of acrylic-based products with wide range of applications from resins, coatings, adhesives to work surfaces and automotive lights to signage, baths, and to dental prostheses and other medical diagnostics equipment (Figure 1.1). Moreover it is a very environmental friendly chemical due to its unique and cost effective recycling capability.

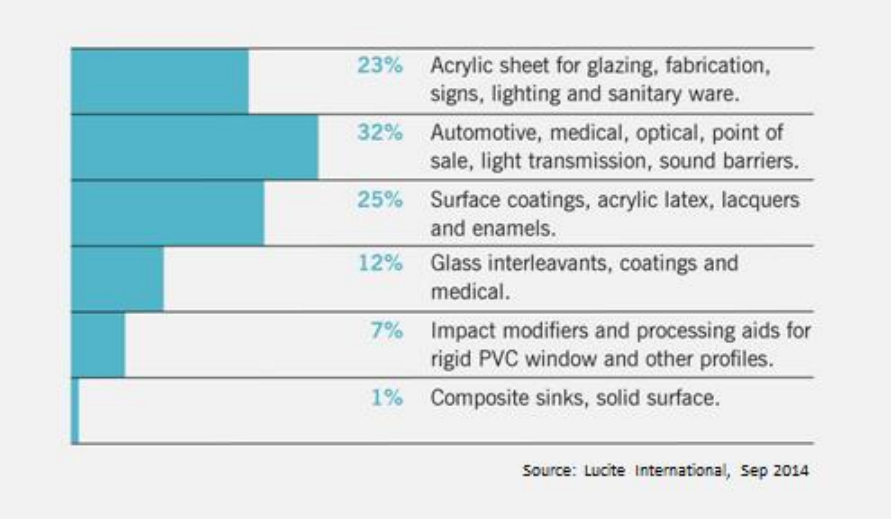


**Figure 1.1** *Methyl methacrylate downstream uses in a mature market.*

Another very exciting feature of the MMA market is the increasing level of global growth. MMA demand has grown year-on-year over decades (Figure 1.2) at a rate that is well above the global GDP and is currently approximately 3 million tes/annum.

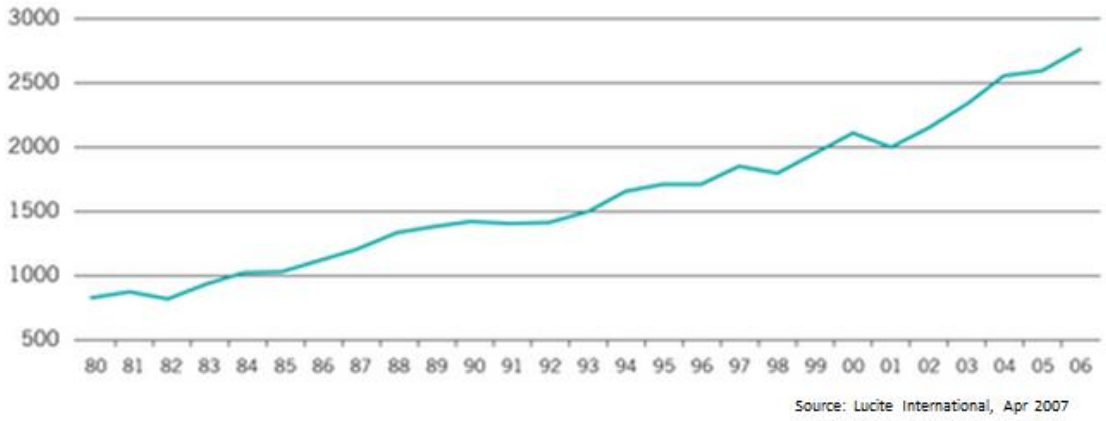


**Figure 1.2** *Global consumption of methyl methacrylate during 1980-2006.*

### 1.2.2 MMA Production Processes

Over the years several routes were investigated for MMA production with feedstock ranging from hydrogen cyanide, isobutylene, tert-butanol, isobutene and ethylene.

The first process to produce methacrylic resin was introduced by Rohm & Haas in 1933. Then, ICI developed and commercialised the ACH process (Figure 1.3) in 1937. It starts form acetone and acetone cyanide and proceeds via dehydration, hydrolysis and esterification. The ACH process was actually the only industrial method for the production of MMA until 1982 and still is the predominant one in Europe and the U.S. accounting for roughly 80% of world's total MMA capacity.

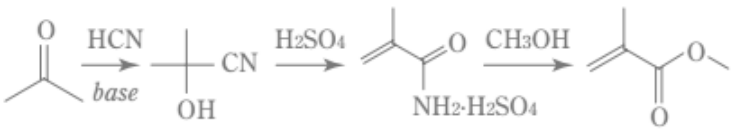


**Figure 1.3** *ACH process.*

However, it is a very high energy and capital demanding process due to the intensive acid recovery and regeneration. Furthermore, there are also environmental concerns related to this process due to the cyanide handling and the great acid waste it produces.

An improvement of the ACH process was suggested by Mitsubishi Gas Chemicals in 1997 that solved the cyanide problem and waste problem. However, this process involves a large number of reaction steps and consequently an even larger number of energy demand due to the separation and purification required in each step.

In 1984 Asahi Chemical developed a different route to produce MMA, through methacylonitrile using isobutylene as raw material (Figure 1.4).

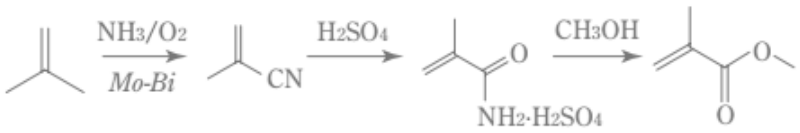


**Figure 1.4** *MAN Process.*

However, this process presents disadvantages such as large waste due to the production of ammonium bisulfate and use of ammonium that make the process unattractive.

Asahi Chemical developed then the direct oxidative esterification process, a process that does not produce ammonium bisulfate as a by-product. It is a two-stage gas-phase oxidation followed by esterification (i-C4 route). In this case the raw material is isobutylene or tert-butanol (Figure 1.5).

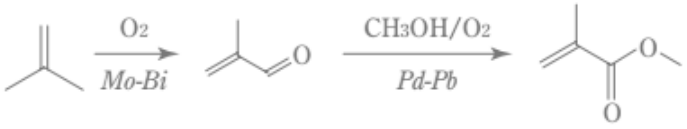


**Figure 1.5** *Direct Oxidative Esterification Process.*

The main disadvantage of this process appears to be the large amount of energy needed for separation of by-products.

This process was first studied by Rohm & Haas and after that by Asahi Chemical, Sumitomo Chemical and Mitsubishi Rauon. It is the only method that does not use unsaturated hydrocarbons as the raw material and produces methacrylic acid one step (Figure 1.6).

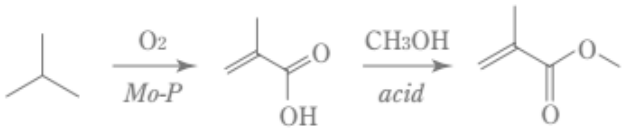


**Figure 1.6** *Isobutane process.*

However, low catalyst's selectivity (~70%) makes this process still not possible commercially.

This process was developed and was commercialised by BASF in 1989 using ethylene as a raw material using a homogeneous rhodium catalyst. It involves the hydroformulation of ethylene to propionaldehyde, condensation with formaldehyde to methacrolein, followed by oxidation and esterification. The main drawback of this process is having to go through methacrolein as an intermediate because of the high cost of methacrolein oxidation.

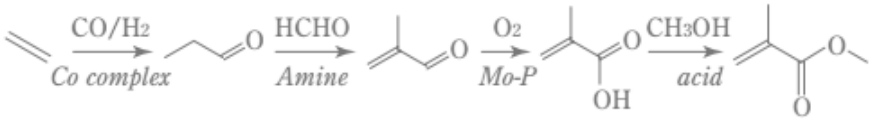


**Figure 1.7** *BASF process.*

Lucite International has invented a new two-stage process for the manufacture of methyl propionate via carbonylation and esterification of ethylene to methyl propionate which is then reacted with formaldehyde under almost anhydrous conditions to form methyl methacrylate (Figure 1.8) [1].

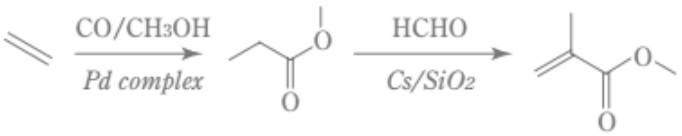


**Figure 1.8** *Alpha Process.*

This technology was first demonstrated commercially in 2008 with a 100 kte/annum plant in Singapore and currently is the only existing technology

that can compete the ACH process economically and in terms of production. Unlike traditional MMA processes there are no polymer/solids blockage, corrosion or machine issues or vulnerabilities and can cut the cost of making MMA by 40%.

## 1.3 Microreactors

Advances in microfabrication techniques have allowed the rapid evolution of microtechnology, widening the chemical engineering toolbox with devices with feature sizes in the submillimeter range [2,3]. Nowadays, most process equipment available in large scale has also been redesigned and studied in the microscale, from micro-mixers and microreactors to microseparators and microdistillation columns.

Microreactors have attracted increasing interest the last two decades due to their unique features that create the potential for high performance chemicals and information processing. These include high mass and heat transfer rates due to the high surface-to volume ratio they provide, allowing the kinetic study of traditionally mass transfer limited, highly exothermic reactions but also high temperature and pressure processes with great accuracy and safety. Furthermore, due to their significantly smaller volume compared to conventional reactors, they provide a more controlled and hence safer environment for the study of reactions containing poisonous and hazardous components. Moreover, their small volume results also to more economical processes as smaller chemical amounts are required, crucial when handling very expensive or difficult to produce chemicals. Due to their significant advantages, microreactors have been widely used the last decade for chemical kinetic studies, chemical synthesis, process development and new chemistry discovery in general by widening the window of operating conditions and increasing the rate of information generation.

## 1.4 Outline of Thesis

The thesis consists of seven chapters. In Chapter 2 literature relevant to the thesis is reviewed. Topics include operational regimes in gas-liquid reactions, benefits and kinetic studies in microreactors, hydrodynamic studies of gas-liquid systems in microchannels (flow pattern, mass transfer, void fraction, dispersion, etc.), homogenous catalysis and methoxycarbonylation of ethylene. Chapter 3 focuses on the development of a mathematical model to simulate the capillary reactor used in the study. The reactor model will be a powerful tool in the kinetic study of the methoxycarbonylation of ethylene. Validation of the reactor model was conducted with experiments with a model reaction, a system with well-studied kinetics. In Chapter 4 hydrodynamic studies of gas-liquid systems in microcapillaries are presented and the effects of gas-to-liquid ratio, fluid properties and channel size on the dispersion and the void fraction of the system are studied. Comparison of void fraction results with previous hydrodynamic models is shown and a new void fraction correlation is suggested. Chapter 5 reviews the set-up design, the analysis methodology and the catalyst preparation methodology for the study of methoxycarbonylation of ethylene. Moreover, the hydrodynamic characteristics of the system are investigated based on residence time distribution experiments performed under reaction conditions. Also, considerations on the vapour-liquid equilibrium of the system are presented. Chapter 6 focuses on the kinetic study of the methoxycarbonylation of ethylene and the effect of reactants' concentrations and temperature on the reaction rate is studied. Furthermore, a kinetic model that can fit all the experimental data of the system is suggested and parameter estimation is performed. Finally, in Chapter 7 the conclusions of the thesis are summarised and recommendations for future work are given.

# CHAPTER 2. Literature Review

## 2.1 Kinetic Studies of Gas-Liquid Reaction Systems

Gas-liquid reactions are a substantial sector of chemical reaction engineering and occur in many fields of experimental science. The kinetics of a chemical reaction can be described by the rate expression of the reaction that can explain adequately what parameters (i.e. concentrations of reactants, temperature) affect the rate of that reaction and in which extent each of these parameters affect the rate of the reaction. Knowledge of the kinetics of a reaction can result to a number of benefits. Firstly, it allows the optimisation of the reaction conditions which could lead to the decrease of the required feedstock and the energy needs of that reaction. In addition, information on the kinetics of a reaction system is essential when designing a reactor for that reaction system. Optimal reactor design can result to the decrease of the capital cost of a process. Hence, studying the kinetics of a reaction system has the potential to significantly increase the profitability of the specific process.

There are three main components that are essential for the kinetic study of any reaction system (Figure 2.1). A first very important tool for a kinetic study is a reactor model, a mathematical model that can describe the phenomena taking place in the reactor. Next, a kinetic model for the system is needed to describe the mechanism of the reaction and depict the effect of various parameters on the reaction rate.

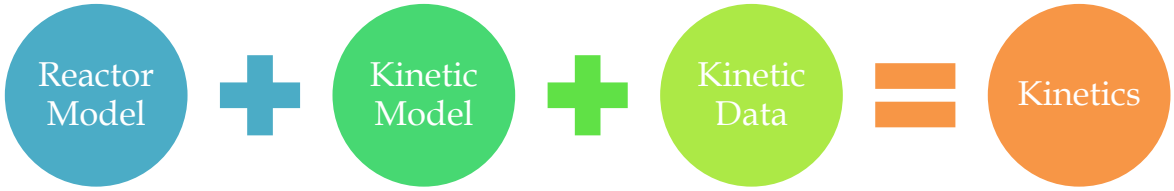


**Figure 2.1** *Essential tools for kinetics determination of a reaction system*

Finally, kinetic data of the reaction are required; data that will depict experimentally the effect of various parameters. The kinetic results are then compared with the proposed kinetic model in order to find the rate expression that fits satisfactorily all the experimental results. This comparison between the experimental data can be done by means of a reactor model.

Two are the most common methods for the analysis of kinetic data for the determination of the rate equation of a reaction; the initial rates method and the integral method. The initial rates method involves measurement of the reaction rates at very short times before any significant changes in concentration occur. This is particularly challenging in some cases, for example when studying reactions with long induction time; parallel reactions occurring at different rates. However, it is a simple method and its most important advantage is that the reaction order found is the true order without the influence from product inhibition or autocatalytic phenomena. Another very popular method is the integral method which is an easy method to use when testing particular mechanisms or simple rate expression. In this method, a particular rate equation is evaluated by integrating it and comparing the predicted curve (concentration, reaction rate, time) to the experimental observations.

### 2.1.1 Mass Transfer Models in Gas-Liquid Systems

In multiphase reactions in order to ensure that the collected data are intrinsic kinetic data and hence the reaction does not suffer from mass transfer limitations, hydrodynamic study of the system is essential. A chemical reaction can be either under mass transfer or kinetic control, depending on the relative values of the corresponding mass transfer rate and reaction rate of the reaction. For the kinetic study of a reaction system it is generally preferable the reaction to be under kinetic control, without any mass transfer resistances. It is also possible to study the kinetics of a reaction that is mass

transfer limited but then the corresponding model will be more complicated [4], as it should also take into account the mass transfer gradients into account.

Consequently, the first step of a kinetic study, is to ensure that the there are no mass transfer limitations. Several hydrodynamic models are available in the literature [5,6] to describe the mass transfer in the gas-liquid interface. The three most common mass transfer models are the film model, the Higbie and the Danckwerts penetration model.

The film model is the simplest and the oldest one and it assumes that near to any fluid interface there is a stagnant film of thickness $\delta$ through which the transport process takes place by simple molecular conduction, while the conditions outside this film, in the bulk of the phase are assumed to be constant. The mass transfer coefficient for physical absorption, $k_\ell^o$ is expressed by (2.1),

$$k_\ell^o = \frac{D_\ell}{\delta} \qquad \textbf{(2.1)}$$

where $D_l$ is the molecular diffusivity of the absorbing component in the liquid. The film model theory does not give any valuable information for the process. Usually it is used as a first reasonable guess or in problems that have already a lot of mathematical difficulties and they can be solved only using this model.

The Higbie's penetration model is based in the hypothesis that the gas-liquid interface is made up of a variety of small liquid elements, which are continuously brought up to the surface from the bulk of the liquid and vice versa by the motion of the liquid phase itself. Each element of liquid, as long as it stays on the surface, may be considered to be stagnant, and the concentration of the dissolved gas in the element may be considered to be everywhere equal to the bulk-liquid concentration when the element is brought to the surface. Therefore, mass transfer takes place by unsteady molecular diffusion in the various elements of the liquid surface.

Furthermore, another assumption of this model is that all the surface elements stay at the surface for the same amount of time $t^* = d / u_b$, where d is the length of the bubble and $u_b$ its velocity. The mass transfer coefficient for physical absorption, $k_l^0$ is expressed by (2.2),

$$k_\ell^o = 2\sqrt{\frac{D_\ell}{\pi t^*}} \tag{2.2}$$

The difference between Higbie's and Danckwerts' model is that the latter assumes that the probability for a surface element to disappear from the surface in a given time interval is independent of its age. In this case, the rate of disappearance of surface elements is simply proportional to the number of elements of that age which are present. The mass transfer coefficient for physical absorption, $k_\ell^o$ is expressed in this case by (2.3),

$$k_\ell^o = 2\sqrt{\frac{D_\ell}{t_D}} \tag{2.3}$$

where $t_D$ is an equivalent diffusion time and may be regarded as an average life of surface elements [5].

### 2.1.2 Operational Regimes in Gas-Liquid Reactions

In multiphase reaction systems mass transfer is a crucial phenomenon, leading the two phases to come into contact and afterwards to react. When considering a reaction between a gas (A) and a liquid (B) is considered, where the gas is soluble in the liquid while the liquid cannot enter the gas, the overall rate expression for this reaction should consists of both the mass transfer resistances and the resistance of the chemical reaction. Also, in this system, using the two film theory, there are two mass transfer resistances, in the gas film and in the liquid film [7]. Consequently, there are four main regimes, from instantaneous to very slow reaction. There are also some intermediate regimes, but here only the main regimes will be described [8].

For an instantaneous reaction, the mass transfer in the gas film is the rate controlling step and when the gas reaches the gas-liquid interface reacts instantaneously as it is shown in Figure 2.2.

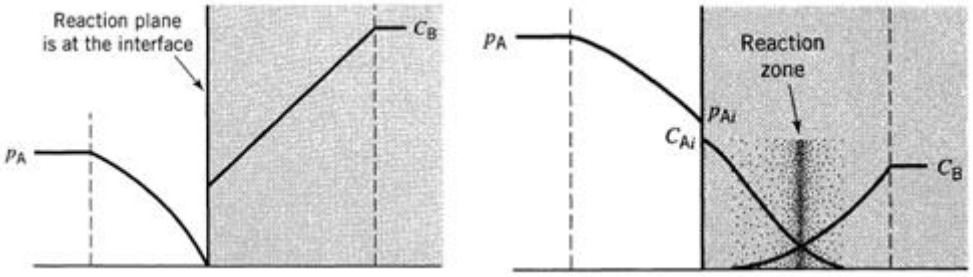


**Figure 2.2** *Concentrations of reactants for an instantaneous (on the left) and for a fast (on the right) reaction [8].*

For a fast reaction the diffusion of the gas into the gas and the liquid film is slow, but when the gas comes in contact with the gas-liquid interface does not react instantly. However reaction is fast enough and the gas reacts completely within the liquid film, as it is shown in Figure 2.2.

In Figure 2.3 (on the left) the case of a slow reaction appears where the reaction takes place in the main body of the liquid, while the two films still provide a resistance to the gas to transfer into the liquid bulk.

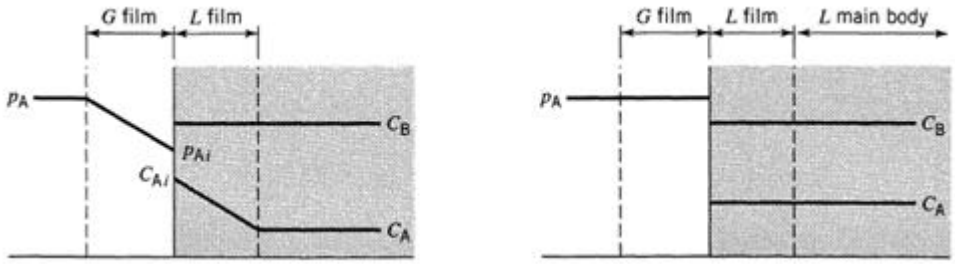


**Figure 2.3** *Concentrations of reactants for a slow (on the left) and for a very slow (on the right) reaction [8].*

For a very slow reaction, the mass transfer limitations are negligible and therefore the concentrations of the gas and the liquid are uniform in the liquid. The reaction takes place in the bulk of the liquid as it is shown in Figure 2.3 (on the right) and is the rate controlling step. Consequently, the overall rate expression of the reaction is determined by the kinetics alone.

The criterion to identify in which regime a reaction system operates is by calculating Hatta number.

### 2.1.3 Hatta Number Criterion

For a pseudo-first order reaction $\left(A_g + B_\ell \rightarrow C\right)$, assuming that the gas film resistance is negligible, the definition of the dimensionless Hatta number is expressed by (2.4),

$$Ha = \frac{\sqrt{k_r \cdot D_{A\ell}}}{k_\ell} \quad \textbf{(2.4)}$$

where $k_r (= s^{-1})$ is the reaction rate constant of the reaction, $D_{Al} (= m^2/s)$ is the reactant A diffusivity into the liquid and $k_l (= m/s)$ the mass transfer coefficient of A in the liquid phase.

The strict definition of Hatta criterion is that if Ha<<0.03 the reaction takes place into the bulk of the liquid [6,8-10] as it is shown in Figure 2.3 (on the right) where there are no mass transfer limitations (no concentration gradients of the gas into the liquid). However, many researchers have also studied the kinetics of reactions, assuming negligible mass transfer limitations, for Ha<<0.3 [11-13]. Concluding, although the strict criterion for the kinetic control of a reaction is when Ha<<0.03, at Ha up to 0.3 the reaction rate is not limited by mass transfer processes. Above this value Ha>0.3, mass transfer begins to influence the reaction rate as it is shown in Figure 2.2 (on the left) and surface area is the controlling rate factor.

## 2.2 Kinetic Studies in Capillary Reactors

### 2.2.1 What is a Capillary Microreactor?

When the technology that was needed to produce structures at micro-scales was developed, new designs of fluid flow systems on the micro-scale were opened up. Nowadays, microreactors with very small, down to few tens of microns, channel internal diameters can be produced by a variety of

manufacturing techniques, allowing the use of them. Capillary microreactors are the simplest kind of microreactors as they are just capillaries whose internal diameter ranges from some tens of microns to hundreds of microns.

Microreactors have been used in the past by many researchers for the study of not only single phase reactions [14,15] but also liquid-liquid [16-18], gas-liquid [11,19-32] (Table 2-1) and gas-liquid solid reactions [33-38] catalytic or non-catalytic. Many reviews are available in the literature for the potential and the challenges of microreactors [39-41].

**Table 2-1** Studies of gas-liquid reactions in microreactors in the literature.

| Author | Reaction/ Conditions | Reactor Design |
|---|---|---|
| Jähnisch [21] (2000) | Fluorination of toluene/ T=-15- -42°C | Falling film microreactor 0.1mm x 0.3mm cross section, Micro bubble columns 0.5mm x 0.5mm, 0.3mm x 0.1mm |
| Chambers [20] (2001) | Fluorination of 1,3-dicarbonyl substrates/ T=0-20°C | Nickel microchannel 0.5mm wide x 0.5mm deep L=10cm |
| Natividad [23] (2004) | Hydrogenation of 2-butyne-1,4-diol/ Pd-Al, P=1-3bar, T=25-55 °C | Capillary monolith ID=1mm and 2mm L=15cm and 34cm |
| Basheer [42] (2004) | Oxidation of glucose/ Gold(0), T=20°C | Glass capillary 5cm x 0.4mm |
| Önal [22] (2005) | Hydrogenation of α,β-unsaturated aldehydes/ Ru(II)-TPPTS, P=10-20bar, T=60°C | PTFE capillary ID=0.5, 0.75, 1.00 mm L=3, 6, 12m |
| Ducry [31] (2005) | Nitration of phenol/ T=5-60°C | Glass microchannel 10x0.5mm width |
| Enache [30] (2005) | Resorcinol hydrogenation/ Rh/γ-Al2O3 T=100°C, P=6-10bar | Capillary ID=3.86mm, L=50cm |
| Tsoligkas [24] (2007) | Hydrogenation of 2-butyne-1n4-diol/ Pd-Al, T=24-50°C | Ceramic capillary ID=1.69mm, L=30cm |
| Enache [43] (2007) | Resorcinol hydrogenation/ Rh-$Al_2O_3$, Pd-C T=100°C, P=10bar | HEx reactor 1-2mm width |

**Table 2-1** (continued)

| Author | Reaction/ Conditions | Reactor Design |
|---|---|---|
| Miller [28] (2007) | $^{11}CO$ carbonylative cross-coupling reactions/ Pd-complex, T=75°C | Teflon capillary ID=1mm, L=45cm |
| Murphy [44] (2007) | Aminocarbonylations of 3-iodoanisole, morpholine, 4-bromobenzonitrile/ Pd, T=98-160°C P=4.5-14.8bar | Silicon-Pyrex V=0.078-0.4ml |
| Wang [45] (2009) | Oxidation of alcohols/ Au-Pd, T=50-70°C | Capillary reactor ID=0.25mm, L=50cm |
| Rebrov [38] (2009) | Hydrogenation of 2-Methyl-3-butyne-2-ol/ Pd-$TiO_2$,$Pd_{25}Zn_{75}$/$TiO_2$ T=55-64 °C | Fused silica capillary ID=0.25mm, L=10m |
| De Mas [46] (2009) | Direct fluorination of toluene T=20°C | Silicon-Pyrex $D_h$=0.215mm L=20mm |
| Tsoligkas [25] (2009) | Hydrogenation of 4-nitrobenzoic acid/ Pd-Al, T=25°C | Alumina ceramic capillary ID=1.69mm, L=30cm |
| Ng [26] (2010) | Direct formation of hydrogen peroxide/ Pd complex, T=25°C | Glass capillary ID=0.5mm-2mm |
| Jetvic [27] (2010) | Cyclohexane oxidation with oxygen/ Cobalt naphthanate T=160°C, P=15.2bar | Stainless steel capillary ID=2.16mm, L=15m |
| Fischer [11] (2010) | Oxidation of cyclohexane with air/ P= 20-80bar, T=180-260°C | Stainless steel capillary ID=0.5, 0.75, 1.00, 2.15 mm L=0.6-8.3 m |
| Protasova [29] (2011) | Hydrogenation of citral (3,7-dimethyl-2,6-octadienal)/ Au-$TiO_2$, Pt-Sn-$TiO_2$ T=65-75 °C | Silica capillary ID=0.25mm, L=10m |
| Keybl [47] (2011) | Hydroformulation of 1-octene/$HRhCO(PPh_3)_3$, T=85-105°C P=25bar | Silicon-Pyrex 0.4 x 0.4mm cross section |

**Table 2-1** (continued)

| Author | Reaction/ Conditions | Reactor Design |
|---|---|---|
| Tidona [48] (2013) | $CO_2$ hydrogenation, Reverse water-gas shift, CO hydrogenation/ Pt-$CeO_2$, T=450-600$^oC$ P=200-1000bar | Stainless steel capillary ID=1mm |
| Al-Rawashdeh [49] (2013) | Hydrogenation of phenylacetylene/ [Rh(NBD)(PPh3)2]BF4] (NBD = norbornadiene) T=70$^oC$, P=10bar | Barrier-based microreactor 1.23mm width x 1.23mm depth L=2m |
| Liu [50] (2013) | Oxidation of alcohols, Conversion of aldehydes, amines to amides/ Ru-$Al_2O_3$, T=80-130$^oC$ | Silicon-Pyrex channel 27 × 8 × 0.6$mm^3$ |
| Paunovic [51] (2014) | Direct synthesis of hydrogen peroxide/ Au-Pd, T=30-42$^oC$ P=15-30bar | Capillary ID=0.32mm, L=1m |
| Truter [52] (2015) | Epoxidation of propene with hydrogen peroxide/ Si-Ti, P=6bar, T=40$^oC$ | PEEk capillary ID=0.9mm, L=350-595cm |

### 2.2.2 Advantages of Microreactors

Initially, researchers started using capillary reactors with internal diameters less than 1mm to study single phase reactions between two parallel fluid streams where diffusion between them was taking place [14,15]. They observed that one of the benefits of using channels with small diameters is that the diffusion pathway is much smaller fact that enhances largely the mass transfer rate [11,17-30,53]. It is well known that in a channel with diameter on the sub-millimetre scale, the fluid flow is mainly laminar (due to the small Reynolds numbers) and the main controlling factor in mass transfer is diffusion. Furthermore, to assess the efficiency of mixing between two fluids Fourier number, Fo, can be calculated, which relates the residence time in the mixing chamber or reactor to the binary diffusion coefficient and a characteristic length scale,

$$Fo = \frac{D \cdot t}{d^2} \quad \textbf{(2.5)}$$

where D is the fluid diffusivity ($m^2s^{-1}$), t is the contact time (s) and d is path length for diffusion (m), which concerning a reaction inside a capillary is its internal diameter. Good mixing is achieved for Fo > 0.1 and complete mixing for Fo > 1. Hence by decreasing the diffusion path length (e.g. by decreasing the internal diameter of the capillary) to the micro-scale, complete mixing can be achieved over time scales of few seconds, as the diffusivity of the most liquids ranges between $10^{-9}$ $m^2s^{-1}$ to $10^{-8}$ $m^2s^{-1}$. Consequently, the excellent mixing between two fluids is one of the first advantages researchers observed in capillary microreactors.

Rapid development of microreactors for gas-liquid applications was observed due to their benefits compared to conventional multiphase reactors. Hessel et al. [21] studied the direct fluorination of toluene in microreactors using bubbly or slug flow and observed that due to the high interfacial surface area provided, the mass and the heat transfer were significantly enhanced leading to an increase in conversion and selectivity in microreactors compared to the laboratory benchmark. Gas-liquid interfacial mass transfer is enhanced in microreactors due to the thinness of the liquid film, leading to increased reaction rates for mass transfer limited reaction [16,17,21,22,25,30]. In addition, enhanced mass transfer rates under slug flow in microreactors was also attributed to the internal convective circulations taking place inside the plugs due to the shear forces at the walls opposite to the flow direction. Further increase in the average flow velocity was found to increase the intensity of these internal circulations [54]. This enhancement of mass transfer in microreactors leads to reaction performance better than that provided by conventional multiphase reactors especially for mass transfer limited reactions.

Due to the large interfacial area that microreactors provide, heat transfer is also significantly enhanced. This feature allows reactions that in

conventional reactors are taking place in mild conditions due to safety reasons, to be performed in microreactors under much harsher conditions [55]. For example, many researchers studied the direct fluorination of aromatics in microreactors [19-21,56]. Those reactions are highly exothermic and in conventional rectors (e.g. batch reactors) the safety issues regarding the temperature control are very important especially on a large scale leading to mild operating conditions. However, in microreactors where heat transfer is largely enhanced, these reactions can take place isothermally even under severe conditions leading to increased yields. This feature of microreactors results also to less substrate degradation as well as increased reaction selectivity.

The nitration of aromatics is another example illustrating how suitable capillary reactors are for the study of highly exothermic reactions. Dummann et al. [18] studied this liquid-liquid reaction isothermally into PTFE capillaries with inner diameters 0.5 to 1mm. They reported that due to the high specific area, the heat transfer was efficient enough to remove the released heat by the exothermic reaction, allowing an isothermal operation. Another benefit of capillary microreactors that they observed is the formation of a stable two-phase plug flow pattern for the immiscible liquids, which results to a uniform and well defined interfacial area and consequently better control of the reaction.

Another noteworthy example of processes that have been benefited by the development of microreactors is those that require extreme temperature and pressure conditions such as the hydrogen peroxide. The direct catalytic formation of hydrogen peroxide from hydrogen and oxygen requires extreme and dangerous operating conditions such as high pressures. However, the last years many researchers have demonstrated the possible use of microreactors for the production of hydrogen peroxide [51,57-59].

Apart from reactions at extreme temperature and pressure conditions, other reactions facilitated in microreactors are those with explosive, toxic or

hazardous chemicals involved. This is because microreactors offer enhanced safety compared to conventional reactors due to their small volumes. Typical example is Maurya et al. [60] who used microcapillaries for multiple reactions and separations of hazardous ethyl diazoacetate, one of the most common diazocompounds and very industrially interesting compound in fine chemicals and pharmaceutical production.

Moreover, another benefit of microreactors is the small reagents volumes that require due to their small volumes. This feature is essential when the reagents are very expensive or minimal amounts are available, often in fine chemicals and pharmaceutical industries.

Another significant benefit of microreactors that was early recognised [61-64] is the ease of transforming this microfluidic technology into an industrial tool by numbering up (use of parallel reactors) instead of scaling up (increase the characteristic dimensions of reactors) [53,65]. That's because the channel design that was used for the laboratory scale is the same as in the industrial scale. The only thing that differs is the number of channels that are needed to be used in parallel. In other words, scale up of microchannels is achieved by simple replication and not by increasing the size of the process unit [17]. Consequently, the development costs associated with the scale-up methodology followed for conventional systems are dramatically decreased. However, it should be noted that scaling out still involves challenges in inlet flow distribution [66] and reaction monitoring methods.

In conclusion, the miniaturisation of chemical reactors has lots of advantages, such as efficient mass and heat transfer, ability to operate at high pressures, safety advantages of small volume usage and ease of scale out. These advantages can largely be exploited from both academia by producing essential chemical information [67] but also by industry by achieving increased reaction rates and selectivity in a safer manner.

## 2.3 Hydrodynamic Studies of Gas-Liquid Systems

Gas-liquid two phase flow in small channels has been studied extensively the last decade [68-92]. This is due to the essential information it provides for many applications, such as the design and the optimisations of heat exchangers, multiphase reactors and other microstructured process units. The hydrodynamic study of a multiphase system provides information about the flow behaviour, the flow characteristics, the mixing quality and the mass transfer characteristics of the system and is essential for the complete understanding of any gas-liquid process. The hydrodynamics of multiphase systems in microchannels present differences compared to larger systems mainly due to the increased importance of surface over volume forces and hence flow behaviour predictions that exist for larger systems cannot be applied in smaller channels.

In Table 2-2 the studies available in the literature on two phase-flow systems in micro and mini-channels are listed.

**Table 2-2** Studies of two-phase flow in micro and mini-channels in the literature.

| **Author** | **Experimental Conditions** | **Findings** |
|---|---|---|
| Barajas et al. [73] (1999) | Pyrex, polyethylene, polyurethane, FEP<br>ID=1-9mm (C)<br>Air/Water | ▪ For partial- wetting surfaces ($\theta<90^o$) contact angle has little effect on transition boundaries, while for non-wetting surfaces ($\theta>90^o$) they changed significantly |
| Fukano et al. [74] (1999) | ID=1.6mm (C)<br>Air/Water | ▪ Flow direction does not affect significantly flow patterns |
| Coleman et al. [75] (1999) | Pyrex,<br>$D_h$=1.3-5.5mm (C), (R)<br>Air/Water | ▪ Channel diameter and surface tension affects the flow pattern and their transitions |
| Triplett et al. [69,76] (1999) | Pyrex,<br>ID=1.1, 1.45mm (C)<br>$D_h$=1.09, 1.49mm (T)<br>Air/Water | ▪ Channel geometry has little effect on flow patterns transitions<br>▪ Homogenous model predicts well pressure drop data except annular flow |
| Zhao et al. [77] (2001) | PMMA,<br>$D_h$=0.866-2.886mm (T)<br>Air/Water | ▪ Channel diameter affects flow transitions<br>▪ Sharp corners affect flow patterns |

**Table 2-2** (continued)

| Author | Experimental conditions | Findings |
|---|---|---|
| Serizawa et al. [71] (2002) | Silica quartz, ID=20-100μm (C) Air/Water, Steam | ▪ Two phase flow patterns are sensitive to surface wettability and contamination |
| Kawahara et al. [78] (2002) | Fused silica, ID=100μm (C) Nitrogen/Water | ▪ Time-averaged void fraction based on images analysis<br>▪ Pressure drop data were well correlated by Lockhart-Martinelli's separated flow model. |
| Chen et al. [79] (2002) | Glass, ID=1, 1.5mm (C) | ▪ Modified drift flux model was suggested for void fraction and bubble velocity |
| Chung et al. [72] (2004) | Fused silica, ID=50-530μm (C) Nitrogen/Water | ▪ Channel diameter affects flow pattern transition lines<br>▪ Void fraction deviated from Armand-type correlation<br>▪ Slug flow model was proposed for the prediction of pressure drop |
| Chung et al. [80] (2005) | Fused silica, ID=100μm (C) $D_h$=96μm (R) Nitrogen/Water | ▪ Deviated from Armand correlation<br>▪ Lockhart-Martinelli's separated flow model estimated well pressure drop |
| Ide et al. [84] (2007) | ID=1-4.9mm (C) $D_h$=1-1.98mm (R) Air/Water | ▪ Effects of tube diameters and aspect ratios on flow parameters were studied<br>▪ Flow frictional multiplier becomes very large compared to Chisholm's prediction.<br>▪ Correlations of holdup and pressure drop were proposed |
| Lee et al. [85] (2008) | Glass, Teflon, Polyurethane, ID=1.46-2mm (C) Air/Water, Methanol | ▪ Wet and dry flow patterns were identified |
| Warnier et al. [86] (2008) | Glass, D=100x50μm (R) Nitrogen/Water | ▪ Mass balance-based model was suggested for the prediction of void fraction and flow characteristics |
| Yue et al. [87] (2009) | PMMA, $D_h$=200-667μm (R) $CO_2$/Water | ▪ Flow map was suggested plotted with Weber numbers<br>▪ Separated flow model was used for the pressure drop estimation under churn, slug-annular and annular flow<br>▪ Empirical correlation was proposed to describe mass transfer data under short film contact film condition |

**Table 2-2** (continued)

| Author | Experimental conditions | Findings |
|---|---|---|
| Saisorn et al. [88] (2009) | Fused Silica, ID=150μm (C) Air/Water | ▪ Pressure drop correlation was developed based on separated flow model with a modified two phase frictional multiplier |
| Kawahara et al. [89] (2009) | Fused Silica, ID=250μm (C) Nitrogen/Water, Aqueous ethylene solutions | ▪ Two phase friction multiplier was lower for the flows with contraction<br>▪ Armand-type correlation could predict well the void fraction data<br>▪ A two-fluid model correlation was also suggested for the void fraction estimation with modified interfacial friction force |
| Sur et al. [90] (2012) | Fused Silica, $D_h$=100-324μm (R) Air/Water | ▪ Flow pattern-based models provided the best prediction of two-phase pressure drop data |
| Wang et al. [91] (2014) | Glass, Polydimethylsiloxane, $D_h$=66.7-133.3μm (R) Air/Water | ▪ Mass transfer performance in microchannels with different surface properties was studied and mass transfer correlations were suggested with a factor of wall wettability included |

C: circular, R: rectangular, T: triangular cross section of channel

### 2.3.1 Flow Patterns in Microcapillaries

When studying the hydrodynamics of a multiphase system, one of the most important issues is the flow pattern that describes the spatial distribution of the two phase flow in the channel. The importance of characterising the flow pattern of a system lies mainly on the fact that depending on the flow pattern the system presents different mass and heat transfer characteristics a different pressure drop. Flow patterns of gas-liquid systems in microchannels differ significantly to those in larger channels. This is mainly due to the increased relative importance of surface forces over volume forces. In addition, due to the small Reynolds numbers achieved in microchannels, laminar flow is established, where viscous forces dominate over inertial ones [93].

There are extensive studies on the characterisation of gas-liquid flows in microchannels [69,78,81,82,93-97]. The flow pattern depends on several

factors such as the gas and the liquid flowrates, the channel size and geometry, the channel wettability by the certain fluid and the fluid properties (e.g viscosity, density, surface tension)[93].

Typically, as the gas flowrate increases while keeping the liquid flowrate constant the observed flow patterns range from bubbly to slug (also called segmented or Taylor flow), churn, slug-annular and annular flow (Figure 2.4-Figure 2.5).

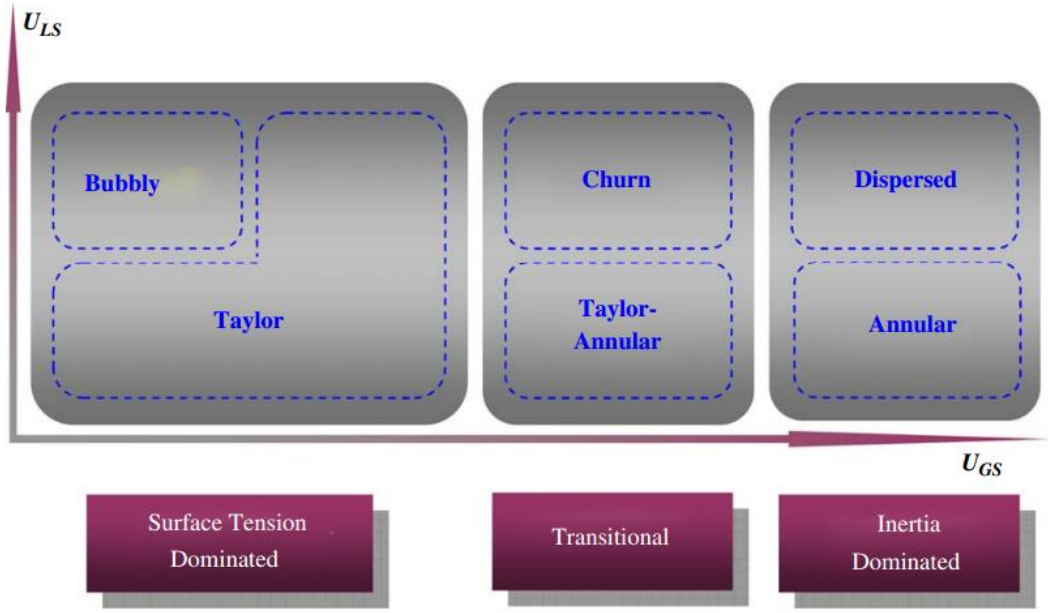


**Figure 2.4** *General classification of flow patterns [93].*

Bubbly flow is often observed when the superficial velocity of the gas phase is smaller than that of the liquid phase. The gas phase is dispersed as small bubbles, and the diameter of each bubble is much smaller than the diameter of the channel (Figure 2.5). When the gas and liquid phase velocities are similar to each other, the volume equivalent diameter of gas bubble becomes greater than the channel diameter, and liquid slugs are separated by the bubbles. This mode of flow is called slug flow, Taylor flow or segmented flow. At a high gas velocity, three different flow regimes may appear. In churn flow, each gas slug is followed by many small gas bubbles. In annular flow, the liquid forms a thin film on the inner wall. The gas phase flows through the central part of the microchannel. Slug-annular flow is sometimes

called Taylor-annular flow, and is similar to the annular flow, except that a wave with large amplitude travels on the liquid surface.

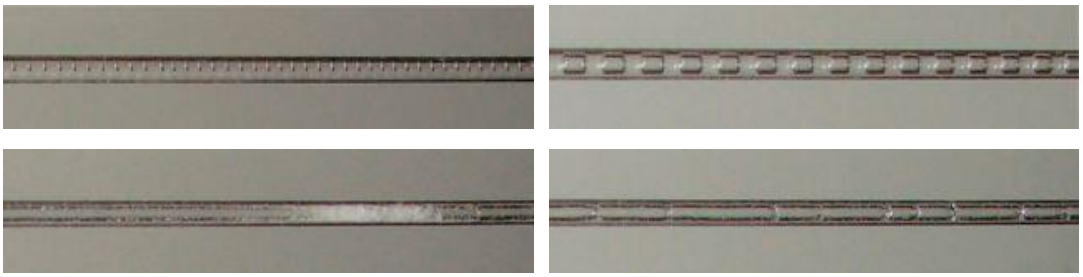

**Figure 2.5** *Photographs of gas-liquid flow patterns in a 1mm glass capillary (from top left clockwise bubbly, slug and slug-annular, churn flow)[98].*

### 2.3.2 Mass Transfer Studies of Gas-Liquid Reaction Systems in Capillary Microreactors

An important advantage of microreactors compared to conventional process equipment is the enhanced mass transfer rates they present principally due to the increased interfacial areas they provide [99]. Evaluation of the mass transfer characteristics is essential for the design of gas-liquid contactors as depending on the relative rates of diffusion and reaction, the system may fall into different reaction regimes. It has been reported that the mass transfer characteristics of a reaction are largely influenced by the flow pattern [25] of the system. Several authors [99-104] have studied the mass transfer characteristics of multiphase systems in microreactors and have proposed various correlations for the mass transfer coefficient mainly in slug flow regime.

One of the oldest mass transfer studies in circular capillaries is of Bercic and Pintar [102] who studied the absorption of methane in water using capillaries of 1.5, 2.5 and 3.1mm diameter. They found that the mass transfer coefficient is dependent on both gas and liquid superficial velocities and the length of the unit cell length and proposed the following empirical correlation for estimation of $k_\ell \alpha$ for Taylor flow in capillaries,

$$k_\ell \alpha = 0.111 \frac{\left(j_g + j_\ell\right)^{1.19}}{\left(\left(1-\varepsilon_g\right) L_{UC}\right)^{0.57}} \quad \textbf{(2.6)}$$

where $j_g$ $j_\ell$ are the gas and the liquid superficial velocities, $\varepsilon_g$ is the gas hold-up, and $L_{UC}$ is the unit cell length (length of one gas bubble and one liquid slug). It is noteworthy that (2.6) does not show any dependence on the capillary diameter. A possible reason for this is that Bercic and Pintar used in their study relatively large unit cell lengths, where the liquid film reaches saturation quickly and is not effective [101,103].

In contrast to the Bercic and Pintar approach, several authors [99-101,103-105] considered that both the two hemispherical caps and the film side of the bubble contribute to the mass transfer. van Baten and Krishna [105] used computational fluid dynamics (CFD) simulations of mass transfer in circular capillaries (1.5, 2, 3mm diameters) under Taylor flow. They showed that for large diameters (2, 3mm) the deviation from the prediction of (2.6) is remarkable and they developed a more fundamental model to describe the mass transfer from Taylor bubbles for short (Fo<0.1) and long (Fo>1) contact times.

In another study Vandu et al, [101] studied the mass transfer characteristics in an air-water system for short contact times (Fo<0.1) between the liquid film and the gas bubbles under Taylor using square and circular capillaries of 1, 2 and 3mm diameter and they suggested the following correlation (2.7),

$$k_\ell \alpha = 4.5 \sqrt{\frac{D \cdot j_g}{\cdot L_{UC}}} \frac{1}{d} \quad \textbf{(2.7)}$$

where, D is the liquid phase diffusivity, $L_{UC}$ is the unit cell length and d is the capillary inner diameter.

For long contact times (Fo>1) between the liquid film and the gas bubbles, the liquid film approaches saturation and therefore its contribution to the

overall mass transfer rate becomes gradually negligible. A criterion to identify whether the film contribution to the mass transfer is active or not was developed by Pohorecki [106].

$$\frac{L\,D}{u\,\delta^2} \ll 1 \qquad \textbf{(2.8)}$$

where L is the bubble length, D is the diffusivity, u is the bubble velocity and $\delta$ is film thickness.

The corresponding correlation of mass transfer coefficient for long contact times (Fo>1) was proposed by van Baten and Krishna [105] in (2.9).

$$k_\ell \alpha = k_{\ell,cap}\alpha_{cap} + k_{\ell,film}\alpha_{film} = 2\frac{\sqrt{2}}{\pi}\sqrt{\frac{Du_B}{d}}\frac{4}{L_{UC}} + 3.41\frac{D}{\delta_{film}}\frac{4\varepsilon_g}{d} \qquad \textbf{(2.9)}$$

In a more recent study, Yue et al. [99] studied $CO_2$ absorption into water, a sodium carbonate/bicarbonate buffer solution and a sodium hydroxide solution, in a horizontal rectangular microchannel with a hydraulic diameter of 667μm. They proposed correlations for the mass transfer coefficient under slug flow (2.10) and under slug-annular and churn flow (2.11).

$$Sh_\ell \cdot \alpha \cdot d = 0.084\,\mathrm{Re}_g^{0.213}\,\mathrm{Re}_\ell^{0.937}\,Sc_\ell^{0.5} \qquad \textbf{(2.10)}$$

$$Sh_\ell \cdot \alpha \cdot d = 0.058\,\mathrm{Re}_g^{0.344}\,\mathrm{Re}_\ell^{0.912}\,Sc_\ell^{0.5} \qquad \textbf{(2.11)}$$

where, $Sh_\ell$ is the liquid Sherwood number, $\mathrm{Re}_g$ and $\mathrm{Re}_\ell$ are the gas and the liquid Reynolds number and $Sc_\ell$ is the liquid Schmidt number. Yue et al. [99] concluded that at a fixed superficial liquid velocity, both liquid side volumetric mass transfer coefficient and interfacial area are increased by an increase of the superficial gas velocity, while at a fixed superficial gas velocity when increasing the superficial velocity only the liquid side volumetric mass transfer coefficient is increased. This is because in the former case, the bubble length increases resulting to an increase of the gas-liquid interfacial area, while in the latter case it is the liquid film around the

gas bubbles that becomes thicker in which case the interfacial area remains approximately the same.

Sobieszuk et al. [107] studied $CO_2$ absorption into a $K_2CO_3/KHCO_3$ aqueous buffer solution containing hypochlorite catalyst in a circular capillary of 0.4mm diameter and measured the mass transfer characteristics of that system. They also compared their measured mass transfer coefficients with the corresponding literature correlations (2.6), (2.7) and (2.11). They concluded that the correlation from Yue et al. (2.11) is very close to their results, while the correlations of Bercic and Pintar (2.6) and of Vandu (2.7) overestimated their results.

### 2.3.3 Void Fraction in Gas-Liquid Systems

Void fraction of a multiphase system in a microchannel is the fraction of volume the gas occupies to the total volume of the channel as shown in (2.12),

$$\varepsilon_g = \frac{V_g}{V_{total}} = 1 - \frac{\tau_\ell . \upsilon_\ell}{V_{total}} \qquad \textbf{(2.12)}$$

where $\tau_\ell$ is the liquid mean residence time [s], $V_{total}$ is the volume of the reactor [$m^3$] and $\upsilon_\ell$ is the volumetric flow rate of liquid [$m^3/s$].

When studying a multiphase reaction in a microchannel, knowledge of the void fraction of the system is essential for the determination of the reaction volume, the pressure drop along a channel and the mass and heat transfer characteristics which is crucial for the design of microstructured process devices for gas-liquid or gas-liquid solid systems such as multiphase reactors.

There are several models available in the literature for the calculation of void fraction of as gas-liquid system in microchannels. These models are summarised in Table 2-3 together with the experimental conditions for which these are valid.

**Table 2-3** Void fraction correlations for gas-liquid systems.

| Author/source | Correlation | Experimental condition |
|---|---|---|
| **Homogeneous** | $\varepsilon_g = \beta = \frac{j_g}{j_g + j_\ell}$ | - |
| **Armand [108]** | $\varepsilon_g = 0.833 \cdot \beta$ | $\beta < 0.9$ |
| **Triplett et. al. [76]** | $\varepsilon_g = \left(0.28 \cdot \left(\frac{1-\beta}{\beta}\right)^{0.64} \cdot \left(\frac{\rho_g}{\rho_\ell}\right)^{0.36} \cdot \left(\frac{\mu_g}{\mu_\ell}\right)^{0.07} + 1\right)^{-1}$ | Air-water<br>ID=1.1, 1.45mm (C)<br>ID=1.09, 1.49mm (R)<br>$j_G$= 0.022-80 m/s<br>$j_L$= 0.02-8 m/s |
| **Serizawa et al. [71]** | $\varepsilon_g = 0.69 \cdot \beta + 0.0858$ | Air-water<br>ID= 0.02-0.1 mm (C)<br>$j_G$= 0.0012-295.3 m/s<br>$j_L$= 0.003-17.52 m/s |
| **Kawahara et al. [78]** | $\varepsilon_g = \frac{0.69 \cdot \beta^{0.5}}{1 - 0.97 \cdot \beta^{0.5}}$ | $N_2$- water<br>ID=0.1 mm (C)<br>$j_G$ = 0.1-60 m/s<br>$j_L$ = 0.02-4 m/s |
| **Saisorn et al. [109]** | $\varepsilon_g = \frac{0.036 \cdot \beta^{0.5}}{1 - 0.945 \cdot \beta^{0.5}}$ | Air-water<br>ID=0.15 mm (R) |

C: circular, R: rectangular, $\beta$ : volumetric quality.

One of the simplest and most commonly used correlations for the calculation of the void fraction of a multiphase system in capillaries is the homogenous model (2.13) which is based on the assumption that there is no slip between the gas-liquid two phases.

$$\varepsilon_g = \beta = \frac{j_g}{j_g + j_\ell} \quad \textbf{(2.13)}$$

where $\beta$ is the volumetric quality of the system defined as $j_g/(j_g + j_\ell)$.

This assumption is valid mainly for homogeneous flows. Bubbly flow is a typical example of a homogeneous flow, as discrete gas bubbles are entrained in a continuous liquid phase. On the other hand, this correlation cannon be applied with confidence in non-homogeneous flows such as slug, churn and annular flows, where bubbles rise with higher velocities than the liquid phase.

Indeed, when Triplett et al. [76] measured the void fraction of and air/water system in circular and rectangular microchannels for bubbly, slug and annular flow, found that the homogenous model predicted satisfactory their data only in the case of bubbly and slug flow, while overpredicted them in the case of annular flow. For this reason, they developed a correlation (2.14) that can describe the full set of their data for bubbly, slug and annular flow in circular and rectangular microchannels.

$$\varepsilon_g = \left(0.28 \cdot \left(\frac{1-\beta}{\beta}\right)^{0.64} \cdot \left(\frac{\rho_g}{\rho_\ell}\right)^{0.36} \cdot \left(\frac{\mu_g}{\mu_\ell}\right)^{0.07} + 1\right)^{-1} \quad \textbf{(2.14)}$$

In order to take into account the slip effect, other researchers [71,78,108] introduced a prefactor A in the homogeneous model (2.13) to develop void fraction correlations that can describe their data, as shown in (2.15),

$$\varepsilon_g = A\frac{j_g}{j_g + j_\ell} = A \cdot \beta \quad \textbf{(2.15)}$$

where A is an empirical numerical prefactor that can be estimated based on experimental observations that ranges between 0 and 1. All of these models show linear relationship between the void fraction and the volumetric quality and are valid for microchannels with inner diameters larger than 250μm. One of the most commonly used models for void fraction prediction is that of Armand [108] in which A=0.833.

There are several studies in the literature [71,72,110] where researchers have measured the void fraction of gas-liquid systems in microchannels by means of flow observation and have confirmed that Armand's correlation is in good agreement with their experimental data for slug flow.

On the contrary, the relationship between the void fraction and the flow quality β seems to become non-linear for very small microchannels (ID<250μm) [72,78,109].

Chung and Kawaji [72] studied the effect of the channel diameter on the two-phase flow of a nitrogen-water system in circular capillaries and observed this non-linear relationship between the void fraction and the flow quality in small capillaries (ID<250μm).

### 2.3.4 Experimental Techniques for Void Fraction and Residence Time Distribution Studies

Various methods have been demonstrated in literature to measure experimentally the void fraction and other flow characteristics of gas-liquid systems in microchannels. The most common techniques researchers used in the past are flow observation [70-72,78], other optical techniques [111], residence time distribution experiments and electrical impedance [112]. All these techniques, their benefits and applications are discussed below.

#### 2.3.5.1 Flow Observation

The most common technique to estimate the void fraction of a gas-liquid system is by analysing pictures of the two-phase flow recorded in the microchannel [70-72,78]. The benefit of this method is its simplicity as its main requirement is a good quality high speed camera or microscope to produce high quality images in the smooth and well-define interface configuration microchannels provide. The instantaneous void fraction is computed as the ratio of the gas volume to the total channel volume within the viewing window. For example, the images are assigned a void fraction of zero when they show only the liquid flowing alone in the entire view window or a void fraction of unity when they show a continuous gas core with a ring-shaped liquid film. The time-averaged void fraction is then obtained by averaging the instantaneous void fraction values from the total amount of images taken [70]. The drawback of this technique is that images of fast moving gas plugs are blurred at the nose and tail, which results in uncertainty when analysing the images and defining the sizes of the gas plugs. Furthermore, this technique requires a transparent microchannel to

allow the observation of the flow, which is not always feasible (e.g at high pressure systems metal channels are commonly used). Finally, this technique cannot be applied in conditions in which intermittent phenomena occur.

#### 2.3.5.2 Other Optical Techniques

Ide et al. [111] used multiple optical fiber probes to measure the gas plug size, velocity and void fraction for a water/nitrogen system in 100μm circular microchannels. Based on the electrical signals from photodiodes the presence of gas or liquid phase was identified at the measurement location in the microchannel. In addition, the use of multiple fiber probes installed in different points across the microchannel allowed the determination of the speed and consequently the length of gas bubbles and liquid plugs. This technique offers great accuracy on the measurements of flow characteristics compared to flow observation where the shutter speed of the imaging equipment must be very high to capture sharp images of the two-phase flow.

Paranjape et al. [112] used electrical impedance to measure the void fraction of an air/water system in microchannels with a hydraulic diameter of 780μm. The practical implementation of the electronic circuit measures the net electrical admittance (i.e. the inverse of the electrical impedance), which is a function of the void fraction and the flow pattern of the system when it is appropriately normalised for a given geometry of electrodes.

#### 2.3.5.3 Residence time distribution

Another non-intrusive void fraction measurement technique is based on residence time distribution experiments (RTD). For a single-phase flow system, the mean residence time is defined as,

$$\tau = \frac{V_r}{\upsilon} \tag{2.16}$$

where $V_r$ is the volume of the channel and υ is the volumetric flow rate of the fluid.

When considering a gas-liquid system, the mean residence time of the liquid is calculated based on (2.17).

$$\tau = \left(1 - \varepsilon_g\right)\frac{V_r}{\upsilon_\ell} \tag{2.17}$$

where $\upsilon_\ell$ is the liquid volumetric flowrate and $\varepsilon_g$ is the gas void fraction of the system. Hence, by performing RTD experiments and measuring the liquid mean residence time of the system one can then determine the void fraction of the system.

Danckwerts [113] first presented a methodology to study the RTD of a fluid by a step or a pulse change in one of the properties of the fluid (e.g. colour, concentration) in the inlet of the channel and monitoring then this change in the outlet. Consider a fluid flowing at a volumetric flowrate through a vessel of volume V. At time t=0 the main fluid is switched to a tracer of concentration $C_{max}$ (step-input change). The transition of the measured concentration, $C_{step}$, against time is shown in Figure 2.6 [8]. The dimensionless form of the $C_{step}$ curve is called the F curve.

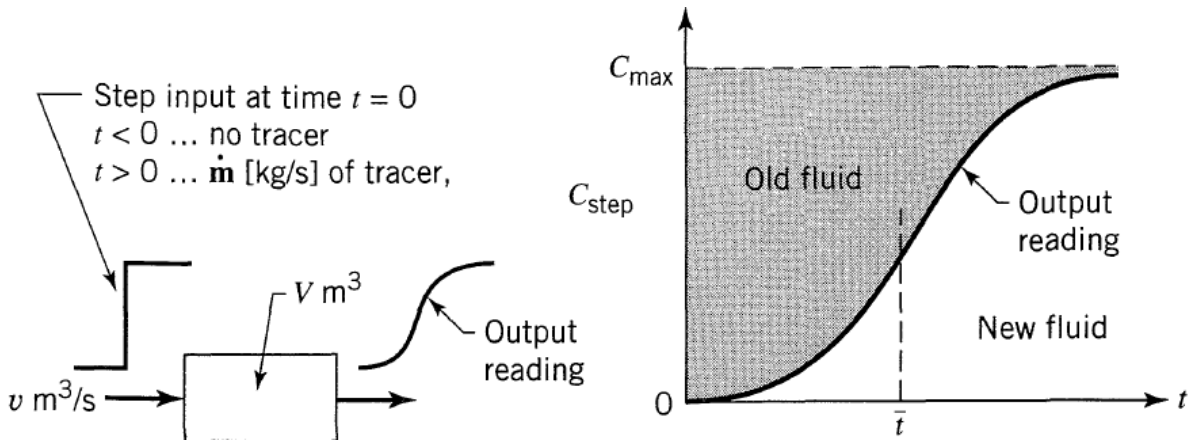


**Figure 2.6** *Residence time distribution experiment based on an step-input change [8].*

The mean residence time of the fluid is then calculated based on (2.18),

$$\tau = \frac{\int_0^{C_{max}} t\, dC_{step}}{\int_0^{C_{max}} dC_{step}} = \frac{1}{C_{max}} \int_0^{C_{max}} t\, dC_{step} \tag{2.18}$$

In cases where the tracer input deviates largely from the assumption of a perfectly sharp step (for a step-input experiment), the fact that the concentration of the tracer in the inlet is a function of time should be taken into account. The concentration of the tracer in the outlet needs to be modified in order to take into account this deviation from the perfect tracer input by the convolution integral [8]. This type of problem is often faced during experimentation and while is quite straightforward to convolute, it is quite hard to deconvolute and requires extensive modelling.

Apart from the mean residence time and residence time distribution of a system, information about dispersion along the reactor can be obtained from RTD experiments. When considering a fluid that flows through a vessel in a continuous process, the most common assumption that is taken for simplification of the problem is either that the fluid is completely mixed in the vessel or that there is plug flow behaviour [113]. The mixing quality of the system can be studied by analysing how much the shape of the concentration curve changes between the inlet and the outlet- the steeper the curve in the outlet the more plug-flow behaviour the system presents.

More specifically, for a flow system that behaves like an open vessel the characterization of the spread of the tracer along the channel can be studied by analysing the dispersion number, $\frac{D}{uL}$, where D is the dispersion coefficient. A large dispersion coefficient number shows fast tracer spread in the fluid, while a zero value indicates plug-flow behaviour.

Experimentally the dispersion number can be determined by the shape of the E curve (Figure 2.7) and (2.19),

$$\sigma_\theta{}^2 = 2\frac{D}{uL} \qquad \textbf{(2.19)}$$

where $\sigma_\theta{}^2$is the variance which can be determined from the tracer response curve and θ is the dimensionless time (θ=t/τ). It should be noted that (2.19)

can only be used for systems with small range of dispersion ($\frac{D}{uL} < 0.01$). For systems with large range of dispersion ($\frac{D}{uL} > 0.01$) (2.20) should be used.

$$\sigma_\theta{}^2 = 8\left(\frac{D}{uL}\right)^2 + 2\frac{D}{uL} \tag{2.20}$$

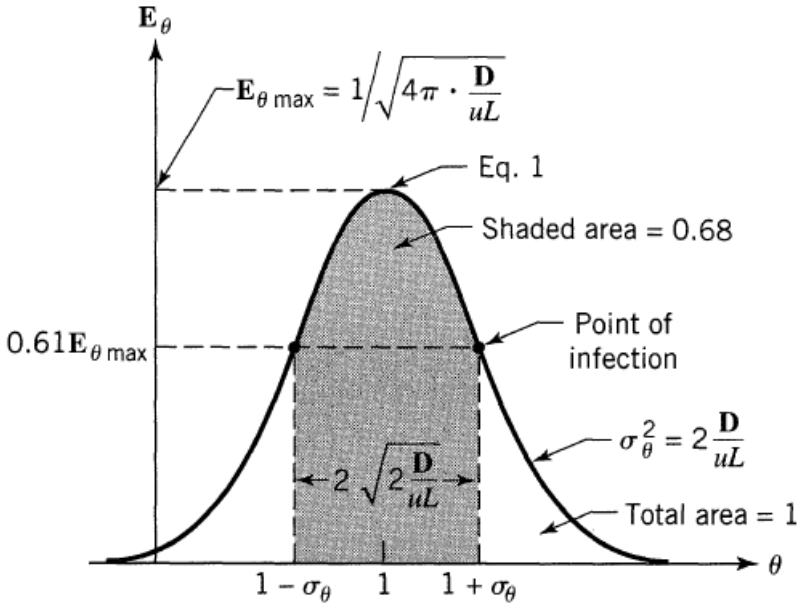


**Figure 2.7** *Typical tracer response curve for 'open vessels' and relationship with the dispersion number,* $\frac{D}{uL}$ *[8].*

In order this analysis to be valid one should ensure that the system is in the dispersion and not the convection region based on Figure 4.5.

The criterion to evaluate how much a flow deviates from plug flow behaviour is based on the vessel dispersion number, $D/uL$ [8]. If $D/uL < 0.01$, the deviation from plug flow is small while if $D/uL > 0.01$, the flow deviates largely from plug flow.

RTD experiments have been widely used in the literature to characterize hydrodynamic characteristics in microchannels such as the residence time, the void fraction and the axial dispersion in a single phase and multiphase systems in microreactors. Many researchers [114-119] have evaluated the performance of microreactors with different designs by studying the RTD of of the system using different techniques of injecting the tracer. Gunther et al.

[120] measured the RTD in test tube reactors and a micromixer using a pulse marking with a dye tracer and applying the axial dispersion model and the tracer was detected by analysing the transmittance by a self-developed transmittance sensor. Lohse et al. [121] developed a RTD measurement technique for microreactors based on a tracer 'injection' using the optical activation of a caged fluorescent dye creating this way ideal signals at arbitrary positions even in complex-structured microreactors. Trachsel et al. [116] presented a piezoelectrically activated tracer injection technique that produces almost perfect pulse signals. The distribution of the tracer was monitored with fluorescence microscopy. Cantu-Perez et al.[114] studied numerically and experimentally the RTD in rectangular channels with and without herringbone structures. For the numerical study particle tracking with random walk diffusion was used while for the experimental study the concentration of the tracer dye was monitored by a LED-photodiode system.

Only a few studies however are available in the literature for RTD measurements of gas-liquid systems under reaction conditions. Zhang et al. [118] studied recently the RTD of gas-liquid systems (cyclohexane or toluene-nitrogen) in minichannels (Stainless Steel tubing with ID=2mm and L=32.45m) under reaction conditions (165$^{o}$C, 1MPa) under slug and under annular flow. The RTD of the liquid phase was determined using the pulsing tracer method and the tracer concentration was measured in the exit using gas chromatography. They found that the RTD of the liquid phase under high temperature was different than that at room temperature due to the evaporation and condensation of the liquid inside the channel. They also observed that their RTD curves became wider by increasing the gas flowrate or by decreasing the liquid flowrate. This was due to the backmixing of the liquid phase at higher gas flowrates resulting in a significant dispersion of the tracer.

## 2.4 Homogeneous Catalysis: Methoxycarbonylation of Ethylene

Catalysis plays a crucial role in today's chemical industry as more than 85% of its products made in catalytic processes. Catalysts are widely used for the production of fuels, bulk and fine chemicals and polymers and are indispensable in preventing pollution by avoiding formation of unwanted products and hence waste. A catalyst accelerates a chemical reaction by offering an alternate mechanism for the reactants to become products with lower activation energy.

Homogeneous catalysis is a sequence of reactions that involve a catalyst in the same phase as the reactants, usually in liquid phase. During the last decades many homogenous catalytic processes use organometallic complexes as catalysts. Organometallic catalysts consist of a central metal surrounded by organic and inorganic ligands and their success is based on the easy modification of their environment by ligand exchange. Once the ligands are coordinated the reactivity of the metals may change significantly. Palladium is one of the most widely used metals in organometallic chemistry as due to its versatility, catalyses a large number of organic reactions such as polymerization of alkenes, carbonylation of alkenes, Heck reaction, Suzuki reaction, alkylic alkylation, etc. [122].

### 2.5.1 Carbonylation reactions in microreactors

Carbonylation reactions are homogeneously catalysed reactions that involve the introduction of C=O into an organic molecule such as alkenes, alkynes, or dienes. The nucleophile can be water, alcohol or acid and the products are acids, esters or anhydrides. Traditionally, these reactions have been carried out glass batch flasks or stainless steel autoclave reactors. However, the rapid development of microreactor technology over the past two decades has brought significant benefits to chemical synthesis over batch reactors, such as large surface to volume ratio, high heat and mass transfer rates and high

operational safety. Specifically for the carbonylation reactions, the small reaction volumes in microreactors allow the use of high CO pressure with great safety compared to batch reaction systems. Moreover, due to the efficient mixing, the environmental impact is also improved as significant smaller amounts of carbon monoxide (and other toxic substances) are required. On the contrary in autoclave reactors, two third of the vessel typically needs to be filled with waste CO. Nowadays, a wide range of carbonylation reaction has been demonstrated in microstructured reactors.

Long et al. [123] studied the palladium catalysed carbonylation of iodobenzene in a microchannel and reported higher yield of the aminocarbonylation product compared to batch operation even with a longer reaction time.

Murphy et al. [44] constructed microreactors capable of reaching pressures exceeding 100bar and demonstrated its advantages on Heck carbonylation reactions. They studied the palladium catalysed carbonylation of p-iodocyanobenzene and reported the ease in handling toxic or air sensitive compounds such as carbon monoxide and palladium as another advantage of closed and small reaction volume systems.

Fukuyama and co-workers studied radical [124], metal-catalysed carbonylation [123,125] and radical-based carbonylation reactions [126] using microstructured devices and highlighted the precise control of reaction temperature and residence time compared to batch systems that lead in greater reaction yields and operation safety. They also demonstrated the mixing efficiency due to the gas-liquid segmented flow that resulted to large gas-liquid interphase and facilitated carbon monoxide diffusion in the liquid slugs, leading to much lower CO pressures required in the system for the satisfactory yields [125].

Takebayashi et al. [127] demonstrated also the importance of the segmented flow in the reductive carbonylation of nitrobenzene. They reported higher

yields of phenylisocyanate when the reactions were carried out in smaller inner diameter tubing (0.5mm instead of 1mm), attributed to the shorter liquid slugs resulting in larger interfacial area.

Keybl et al. [47] demonstrated a microreactor system for the study of homogenous catalysis at high temperature and pressure conditions (<350$^{o}$C and 100bar) under continuous flow by studying the hydroformylation of 1-octene. They reported that segmented gas-liquid flow reduced the axial dispersion and isothermal operation was easily established. The only benefit of batch reactors they reported compared to flow reactors was that the efficiency and ease of the former when collecting time series data.

Miller et al. [128,129] developed a glass microfabricated device for rapid catalyst screening of the aminocarbonylation of iodobenzene in a range of temperatures (75-150$^{o}$C). They highlighted that for the catalyst screening in microreactors only small quantities of catalyst and reagents were needed compared to batch systems.

### 2.5.2 Methoxycarbonylation of ethylene

Methoxycarbonylation of ethylene is a homogeneous palladium catalysed reaction for the production of methyl propionate (2.21), an intermediate for the production of methyl methacrylate.

$$C_2H_4 + CO + CH_3OH \rightarrow C_2H_5COOCH_3 \quad \textbf{(2.21)}$$

The reaction between carbon monoxide, ethylene and methanol can also give rise to other products such as polyketones, materials with very high mechanical strength and flexibility. A possible route for the production of polyketones or methyl propionate is the use of palladium catalysts as discovered by Gouch et al [130]. However, very harsh conditions are required and the process only produced very small amounts of products. Sen et al. [131] observed that use of palladium together with weakly coordinated anion, phosphine and ligands results to more stable and active catalyst

complexes for the formation of polyketones from carbon monoxide, ethylene in alcohol solvents under milder conditions. Drent et al. [132] discovered that cationic palladium complexes containing tertiary phosphines and weakly coordinated anions in methanol are very efficient for producing methyl propionate from carbon monoxide and ethylene. However, when using catalysts containing bidentate tertiary phosphine ligands no methyl propionate is formed but only high molecular weight polyketones [133]. Hence, it was concluded that monodentate phosphines are the most suitable for the production of methyl priopionate. However, later several bidentate ligands were found to be highly selective for the production of methyl propionate with high reaction rates [134]. It is hence clear that the ligand's choice is very important as different ligands can result to significantly different products. It was concluded that the most suitable ligand for the production of methyl propionate is the 1,2-bis[(di-tert-butylphosphino)methyl]benzene or dtbpx.

Another factor that was found to affect largely both the reaction rate and the molecular weight of the product (polyketones) is the amount and the nature of the acid whose main role in these catalysts is to introduce the anion. It was observed that the reaction rate increased significantly when using weakly coordinating anions as they favour coordination of the monomer [135]. Considering the effect of the acid amount added it was found that significant excess of acid leads to higher reaction rates [135]. However, at high acid concentrations the acid found to act as a poison and the anion found to start competing with the monomers for the coordination sites of the metal.

In the Lucite process, the catalyst is formed in situ via the reaction of [Pd(d$^t$bpx)(dba)] (dba = *trans,trans*-(PhCH=CH)$_2$CO] with $CH_3SO_3H$ in MeOH. The catalyst is capable of converting ethylene, carbon monoxide and methanol to methyl propionate at a rate of 50,000 mol of product per mol of catalyst per hour with a selectivity of 99.98% under very mild conditions

(80°C, 10atm of $C_2H_4$/CO)[1,132]. The large selectivity and yield at such mild conditions make this process very attractive industrially.

Different catalysts based on [Pt(d$^t$bpx)(dba)] and $RSO_3H$ (R = $CF_3$, $CH_3$) have been studied for the production of methyl propionate but they were found much less active than the palladium analogue [136]. Other bidentate ligands have been also investigated for the same process, but it was found that d$^t$bpx gave the best results [137].

### 2.5.3 Proposed Mechanisms for Polyketones/Methyl Propionate Formation

There are two mechanistic pathways proposed to describe the mechanism of palladium catalysed methoxycarbonylation of ethylene [134] for the production of both methyl propionate and polyketones as shown in Figure 2.8. Methyl propionate formation and polyketone formation share the initiation and termination steps, however for the former termination occurs after a single turnover [138]. This suggests that only one cycle; either hydride or methoxy is operative in the formation of methyl propionate.

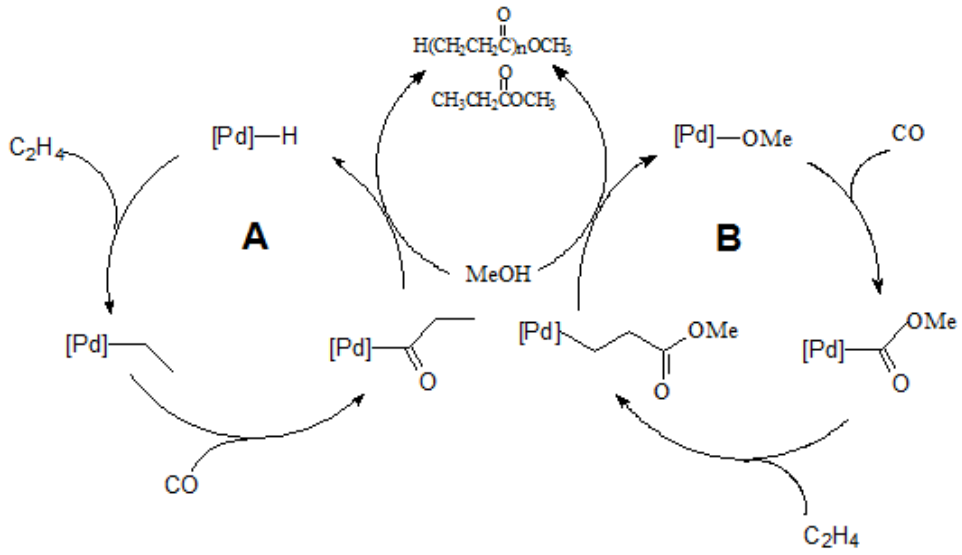


**Figure 2.8** *Proposed mechanisms for the formation of polyketones and methyl propionate.*

The methoxy cycle (B) starts with insertion of carbon monoxide in the palladium methoxy bond. Then, ethylene is added in the Pd-carbon bond of the alkoxycarbonyl-palladium complex. The final step is the addition of methanol that produces methyl propionate and generates the initial alkoxy palladium complex.

The hydride cycle (A) starts with insertion of ethylene in the palladium hydride bond forming an alkyl complex. Then, insertion of carbon monoxide is followed to produce an acyl complex. Last step is addition of methanol that produces methyl propionate and regenerates the palladium hydride.

Extensive studies of Clegg et al. [139] have shown that the methoxycarbonylation of ethylene using Alpha process follows a hydride catalytic cycle based on characterisation of all the intermediates which was also confirmed with another study based on isotope scrambling experiments [140].

# CHAPTER 3. Reactor Model Development and Validation

## 3.1 Introduction

Reactor model is a mathematical model that is able to describe the phenomena happening in a reactor. It is an essential tool in chemical reactor engineering and is used widely for the design of new reactors but also for the kinetic study of reaction systems. There are reactor models available in the literature for some main reactor designs such as the ideal plug flow and continuously stirred reactors. However, for reactors deviating from this ideal-behaviour, one should develop a customised reactor model for the specific reaction system. Then, the validity of the developed reactor model should be confirmed with experimental data of a model system, a system with known kinetics. In our case, a simplified one-dimensional plug flow reactor model was developed in order to be then used for the kinetic study of an homogenous catalysed gas-liquid system, the methoxycarbonylation of ethylene (Chapter 5-Chapter 6). The reactor model was first validated with experiments with a model reaction system, the carbon dioxide absorption in buffer solutions, a well-studied reaction system with simple kinetics in order to ensure its validity to describe gas-liquid reaction systems in capillary reactors.

## 3.2 Reaction System

The validity and suitability of a reactor model should be demonstrated by choosing a well-studied reaction system with kinetics that has been previously described in detail. An ideal model reaction system has simple kinetics and its main characteristics are similar to the main reaction system one wants to study. In our case, the main goal is the kinetic study of the methoxycarbonylation of ethylene, hence it is essential to ensure that there are no mass transfer resistances and therefore the experimental results are

intrinsic data. Therefore, the model reaction should operate in the slow regime in order to fulfil this criterion. A suitable model reaction for our system is the absorption of carbon dioxide in buffer solutions.

Carbon dioxide in alkaline solutions is a reaction system that has been studied to a large extent by several authors [5,141-152] in the past and the kinetics of this reaction system has been described in detail.

When $CO_2$ is absorbed by a $HCO_3^-/CO_3^{2-}$ solution, two reactions may occur,

$$CO_2 + OH^- \overset{k_1}{\rightarrow} HCO_3^- \quad \textbf{(3.1)}$$

$$CO_2 + H_2O \overset{k_2}{\rightarrow} HCO_3^- + H^+ \quad \textbf{(3.2)}$$

According to Nysing et al [141], the reaction (3.1) predominates over the reaction (3.2), which is of comparable importance only when pH<8. In addition, reaction (3.1) can be considered reversible only when pH>10. Both reactions are accompanied by the following instantaneous reactions,

$$CO_3^{2-} + H^+ \rightarrow HCO_3^- \quad \textbf{(3.3)}$$

$$CO_3^{2-} + H_2O \overset{K_4}{\leftrightarrow} HCO_3^- + OH^- \quad \textbf{(3.4)}$$

The overall reaction is,

$$CO_2 + CO_3^{2-} + H_2O \rightarrow 2HCO_3^- \quad \textbf{(3.5)}$$

Astarita [5] showed that the kinetics of reaction (3.5) can be expressed by,

$$r = (k_2 + k_1 \cdot C_{OH^-}) \cdot C_{CO_2} \quad \textbf{(3.6)}$$

where the concentration $C_{OH^-}$ in the buffer solution is derived by the equilibrium reaction (3.4),

$$C_{OH^-} = K_4 \cdot \frac{C_{CO_3^{2-}}}{C_{HCO_3^-}} = K_4 \cdot \beta_c \quad \textbf{(3.7)}$$

and where $\beta_c$ is the carbonate-to-bicarbonate ratio, $\frac{C_{CO_3^{2-}}}{C_{HCO_3^-}}$.

In addition, Astarita [5] reported that for any solution which is not completely converted to bicarbonate, $k_2$ may be neglected. Consequently, the reaction may be considered as a pseudo first order with kinetic equation,

$$r = k \cdot CO_2 \quad \textbf{(3.8)}$$

where,

$$k = k_1 \cdot K_4 \cdot \beta_c \quad \textbf{(3.9)}$$

Pinsent *et al* [142] reported that the activation energy of $k_1$ is 13,250 cal while Nysing *et al* [141] measured the product $k_1 \cdot K_4$ in different temperatures and in different concentrations of sodium and potassium bicarbonate in a wetted wall column, where it appears that the value of k for potassium buffer solutions is higher than for sodium buffer solutions. The assumptions that they made were that the reaction product is not volatile, the diffusivity is constant, there is no heat effect and the concentration of hydroxide ions is constant. In addition, Nysing *et al* [141] reported that in order to keep the concentration of hydroxide ions constant, there should be small partial pressure of $CO_2$, small contact time of $CO_2$, low temperature, high carbonate concentration and low ratio of carbonate and bicarbonate concentrations. It should be noted that, from their results, it appears that the bicarbonate concentration does not affect significantly the value of k but it affects the solubility of $CO_2$.

Furthermore, Astarita [5] concluded that at low carbonate-to-bicarbonate concentrations the reaction takes place in the slow reaction regime when studying this reaction system in a packed tower.

### 3.2.1 Operating Conditions of Reaction System

As it was mentioned earlier, the main criterion that the reaction should fulfil in order to be suitable for a kinetic study is to take place in the slow regime.

Danckwerts [7], using some past experimental data of carbon dioxide absorption in carbonate/bicarbonate solutions in a bubble plate, showed that the reaction in the film is negligible and therefore the reaction is slow, calculating the Hatta number for a first order reaction. He concluded that the criterion below is a necessary condition to ensure that the reaction takes place only in the liquid bulk.

$$Ha = \frac{\sqrt{k_r \cdot D_{A\ell}}}{k_\ell} < 0.3 \qquad \textbf{(3.10)}$$

In order to identify the optimum conditions under which the reaction system would be the slowest possible, the reaction rate constant was calculated in different temperature conditions and under various ratios of carbonate to bicarbonate concentrations by means of (3.9**)**. Values of the product $k_1 \cdot K_4$ at different temperatures were given by Nysing *et al*. [141]. The results are presented in Table 3-1. The diffusion coefficient of carbon dioxide in carbonate/bicarbonate buffer solutions was measured by R. Zeebe [153] and found equal to $14 \cdot 10^{-9}$ $m^2/s$. The liquid side mass transfer coefficient, $k_L$, for carbon dioxide in carbonate/bicarbonate buffer solutions in microchannels was reported by Yue et al. [99] equal to $8 \cdot 10^{-4}$ m/s.

**Table 3-1** Reaction rate constant k ($s^{-1}$) under different temperature conditions, T ($^oC$), and ratios of carbonate to bicarbonate concentrations, $\beta_C$.

| **T($^o$C)** | **$k_1K_4$($s^{-1}$)** | **$\beta_C$** | **k($s^{-1}$)** |
|---|---|---|---|
| ***10*** | *0.21* | *1/9* | *0.0238* |
| | | *1* | *0.21* |
| | | *9* | *1.89* |
| **20** | 0.56 | 1/9 | 0.062 |
| | | 1 | 0.56 |
| | | 9 | 5.04 |
| **30** | 1.4 | 1/9 | 0.16 |
| | | 1 | 1.4 |
| | | 9 | 12.6 |

It is clear that when decreasing the temperature the reaction rate constant decreases, resulting to a slower reaction performance. The ratio of carbonate to bicarbonate appears to have similarly a negative effect. Hence, it can be concluded that the optimum conditions in order to operate in the slow regime are low temperature conditions and low ratio of carbonate to bicarbonate concentrations at atmospheric pressure.

### 3.2.2 Effect of Reaction Extent on Reaction Rate Constant

As it was described earlier, the reaction rate constant at 10°C and at 20°C is given by (3.11) and (3.12) respectively,

$$k_r = 0.21 \cdot \beta_c \quad at\ 10\ ^oC \tag{3.11}$$

$$k_r = 0.56 \cdot \beta_c \quad at\ 20\ ^oC \tag{3.12}$$

where $\beta_c$ is the ratio of the carbonate over the bicarbonate concentration. However, along the capillary reactor, as the reaction takes place, carbonate species are being consumed while bicarbonate species are being produced as the stoichiometry of the reaction shows in Table 3-2, where, $F^0_{CO_2}$ is the molar flowrate of the carbon dioxide in the gas phase in the inlet of the reactor, $F^0_{CO_3^{2-}}$ is the inlet flowrate of the carbonate, $F^0_{HCO_3^-}$ the inlet flowrate of the bicarbonate and $X_{CO_2}$ the conversion of $CO_2$ that is defined by (3.13),

$$X_{CO_2} = 1 - \frac{F_{CO_2,\ell} + F_{CO_2,g}}{F^o_{CO_2,g}} \tag{3.13}$$

where $F^0_{CO_2,g}$ is the molar flowrate of the carbon dioxide in the gas phase in the inlet of the reactor.

**Table 3-2** Stoichiometric table of the reaction in the capillary reactor.

| | $\boldsymbol{CO_2}$ + | $\boldsymbol{CO_3^{2-}}$ + | $\mathbf{H_2O}$ → | $\boldsymbol{2HCO_3^-}$ |
|---|---|---|---|---|
| Inlet | $F^0_{CO_2}$ | $F^0_{CO_3^{2-}}$ | | $F^0_{HCO_3^-}$ |
| Reacted | $-F^0_{CO_2} X_{CO_2}$ | $-F^0_{CO_2} X_{CO_2}$ | | $+2F^0_{CO_2} X_{CO_2}$ |
| Outlet | $F^0_{CO_2}(1-X_{CO_2})$ | $F^0_{CO_3^{2-}} - F^0_{CO_2} X_{CO_2}$ | | $F^0_{HCO_3^-} + 2F^0_{CO_2} X_{CO_2}$ |

The ratio, $\beta_c$, is expressed as a function of the conversion of the reacted carbon dioxide by (3.14),

$$\beta_c = \frac{C_{CO_3^{2-}}}{C_{HCO_3^-}} = \frac{\frac{F_{CO_3^{2-}}}{\upsilon_\ell}}{\frac{F_{HCO_3^-}}{\upsilon_\ell}} = \frac{F_{CO_3^{2-}}}{F_{HCO_3^-}} = \frac{F^0_{CO_3^{2-}} - F^{0,\ell}_{CO_2} X_{CO_2}}{F^0_{HCO_3^-} + 2F^{0,\ell}_{CO_2} X_{CO_2}} \quad \textbf{(3.14)}$$

Considering a gas-liquid stream of 0.1ml/min 20% $CO_2$ and 0.02ml/min $Na_2CO_3$:$NaHCO_3$ (1:9) flowing together through a capillary reactor of 0.5mm inner diameter at 10°C, the ratio, $\beta_c$, and the reaction rate of the system is plotted against carbon dioxide conversion based on equations (3.11), (3.14) and (3.13). Due to the excess of carbon dioxide, the assumption that there is always equilibrium in the gas-liquid interphase and the slow nature of this reaction, it was assumed that the liquid phase is always saturated to carbon dioxide. The results are shown in Figure 3.1 and Figure 3.2, where it is shown that the change of the carbonate-to-bicarbonate ratio, $\beta_c$, against carbon dioxide conversion is significant due to the reaction that leads to consumption of carbonate species and production of bicarbonate species.

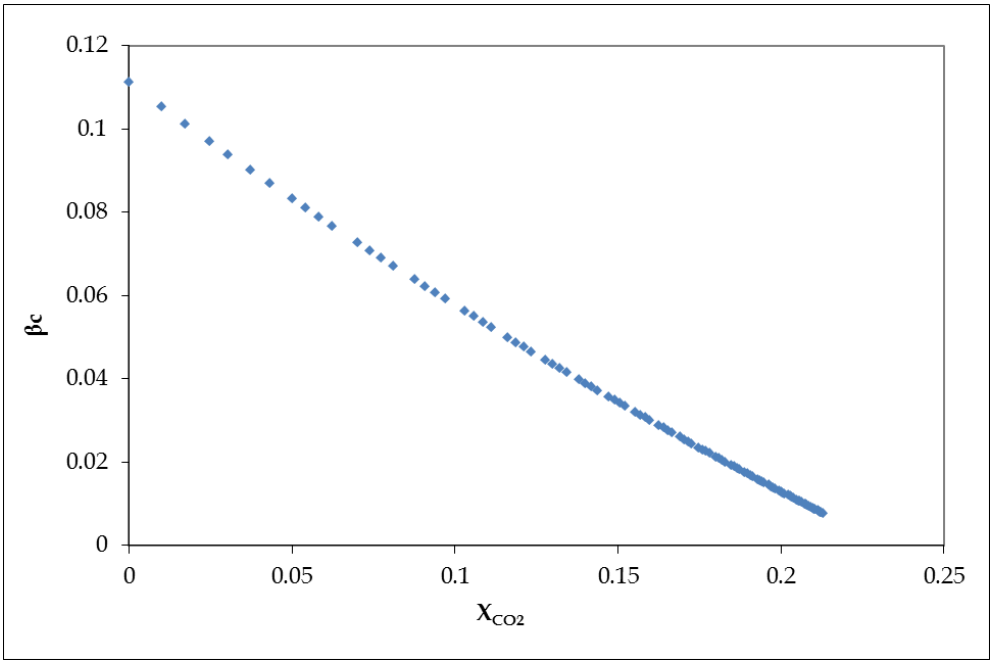


**Figure 3.1** *Effect of reaction extent on carbonate: bicarbonate ratio, $\boldsymbol{\beta_c}$, along a capillary reactor (L=1m, ID=0.5mm) for an initial 0.1M sodium carbonate: bicarbonate (1:9) solution.*

Moreover, the decrease of the ratio, $\beta_c$, as the reaction proceeds has a consequent effect on the reaction rate expression as expected by (3.11). This is also demonstrated in Figure 3.2, where the reaction rate decreases as a function of carbon dioxide conversion. In addition, it is noteworthy that while the reaction proceeds it becomes slower because of the decrease on the ratio, $\beta_c$.

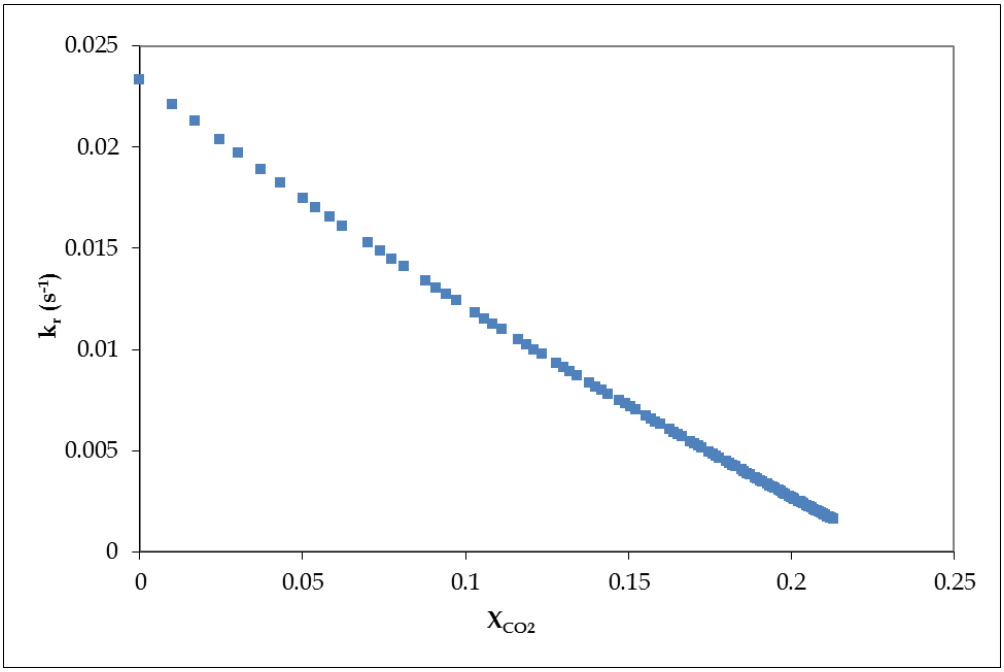


**Figure 3.2** *Effect of reaction extent on reaction rate constant, $k_r$, along a capillary reactor (L=1m, ID=0.5mm) when $k_{r,0}$=0.0233 (T=10°C and βc=0.111).*

It can be concluded that the reaction rate constant expression does not remain constant but is a function of carbon dioxide conversion. Hence, all the relevant equations should be included in the reactor model for an accurate simulation of this reaction system.

### 3.2.3 Effect of Reaction Extent on Solubility of Carbon Dioxide

Solubility of carbon dioxide is a very important parameter as it defines the amount of carbon dioxide that will be dissolved in the liquid phase and hence it will be available for reaction. There are correlations available in the literature [7] that calculate the solubility of various gases in electrolyte solutions such as this system. In general, the solubility of a gas in an

electrolyte solution is affected largely by the temperature as well as the ionic strength of the solution. Schumpe [154] proposed a correlation to describe the effect of dissolved salts on the solubility of a gas.

$$\log\left(\frac{H_0}{H}\right)=\sum_i\left(h_i+h_g\right)\cdot C_i \qquad \textbf{(3.15)}$$

where $\frac{H_0}{H}$ is the ratio of the gas solubility in water to that in a salt solution, $h_i$, $h_g$ are referred in the literature as Sechenov constants and $C_i$ is the concentration of the ion in the solution. The parameters $h_i$ which are specific to each ion present in the solution and the parameter $h_g$ which is characteristic to the absorbed gas ($CO_2$) in the solution are available in the literature [154] at 298K and are given in Table 3-3.

However, according to Schumpe [154] due to the weak effect of the temperature on the Sechenov constants, these values can be applied in a wider temperature range with confidence, by using the gas solubility in water at the respective temperature. For higher accuracy, Schumpe *et al [155]* proposed also a correlation to describe the temperature effect on the Sechenov constants and concluded that there is an approximately linear decrease of them with temperature. Furthermore, the solubility of $CO_2$ in water is available in a wide temperature range in the literature [156] and it was found equal with $0.053 kmol/\left(m^3 atm\right)$ at 283K.

**Table 3-3** Values of Sechenov constants $h_i$ and $h_g$ at 298K [154].

| ion | $h_i$ ($m^3$/kmol) | gas | $h_g$ ($m^3$/kmol) |
|---|---|---|---|
| **$Na^+$** | 0,1171 | $CO_2$ | -0,0183 |
| **$HCO_3^-$** | 0,1372 | | |
| **$CO_3^{2-}$** | 0,1666 | | |

Consequently, in the present work the calculated by (3.15) value of the equilibrium solubility of carbon dioxide in a sodium carbonate/bicarbonate

buffer solution at 283K and at 293K is $0.05\,mol/(Latm)$ and $0.037\,mol/(Latm)$ respectively. These values are correct when assuming that the ratio of carbonate-bicarbonate remain constant along the reactor. However, it was shown earlier that in reality this ratio is changing along the reactor, as the reaction proceeds and carbon dioxide conversion increases, due to the reaction between carbon dioxide and carbonate species. The effect of the reaction extent on the solubility of carbon dioxide due to the ratio change is studied in Figure 3.3, where its solubility is plotted against carbon dioxide conversion.

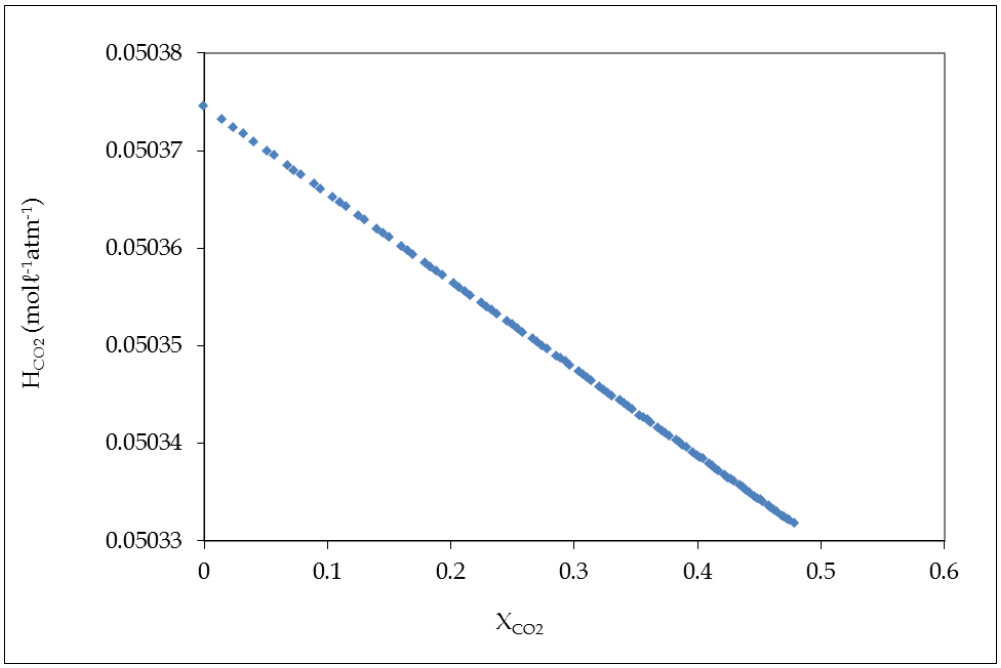


**Figure 3.3** *Effect of carbon dioxide conversion on carbon dioxide solubility in a carbonate-bicarbonate solution in a capillary reactor at 10°C.*

In Figure 3.3, it is shown that even for a 40% conversion, the solubility change is insignificant (<0.6%). Hence, it can be concluded that the change of carbon dioxide solubility along the reactor is insignificant and therefore it can be considered constant along the reactor.

## 3.3 Experimental Set-Up: Reaction and Analysis System

The schematic diagram of the experimental set-up used for the study of the model system is shown in Figure 3.4. A syringe pump (kdScientific) is used

to deliver the liquid fluid (sodium carbonate: bicarbonate buffer solution, 1:9), through a pulse dampener, then a liquid filter (for particles above 10μm) to the tee-junction where it meets the gas mixture (2% $CO_2$, 98% $N_2$). This T-junction has a low swept volume of 2.9μL with thru-hole of 0.5mm. The first gas stream is a 20 vol% $CO_2$, 80 vol% $N_2$ mixture and its flowrate is controlled by a mass flow controller (Bronkhorst LTD, 0-1ml/min). Then, it is mixed with a second gas stream ($N_2$), which is controlled by another mass flow controller (Brooks 5850, 0-3ml/min) and dilutes the 20% $CO_2$ mixture to a 2% $CO_2$ mixture. The gas mixture (2% $CO_2/N_2$) passes through a non-return valve, a pressure relief valve (up to 17bar) and then mixes with the liquid. Following this, the gas-liquid mixture passes through the capillary microreactor.

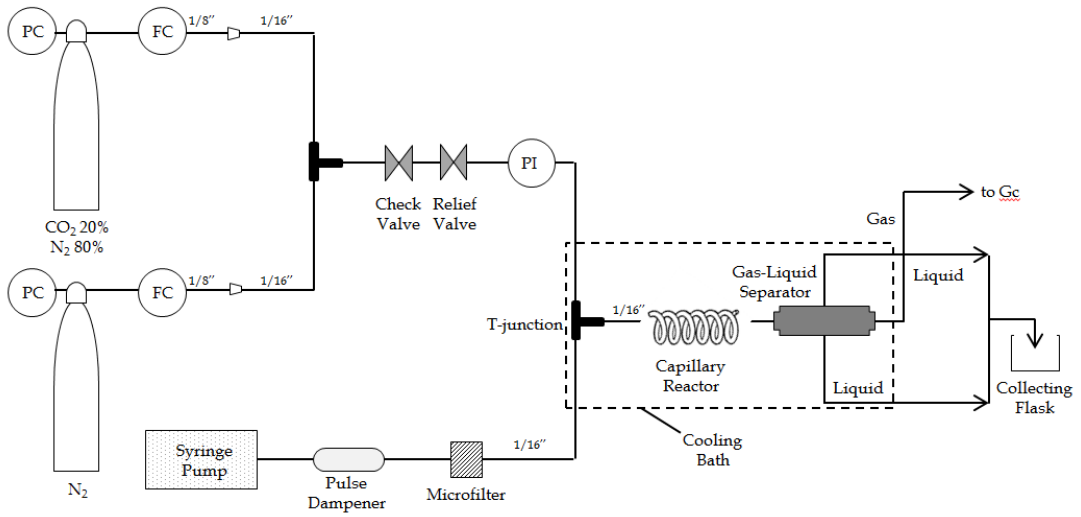


**Figure 3.4** *Schematic diagram of the experimental set-up for the study of the carbon dioxide absorption in a carbonate-bicarbonate buffer solution.*

Two capillary reactors made of glass were used with 1m length and internal diameter 1mm and 0.5mm respectively. After the microreactor, the gas-liquid mixture enters a glass microseparator (Figure 3.5) from which the liquid is being collected in a flask while the gas is being analysed online by the GC. More photos of the experimental set-up can be found in the Appendix B.

Experiments with the model reaction were conducted at two different temperature conditions (20°C and 10°C). A water bath (Polystat cc2) was used to cool the microreactor down to 10°C and control the temperature. Leak test was conducted by pressuring the system and no leaks were found. In the beginning of every run, the microseparator was primed with the liquid solution. Generally, the glass separator was separating effectively the gas-liquid stream. Rarely some bubbles were going to the liquid phase but this was not crucial because the goal was to prevent liquid flow to the gas exit as after the separator the gas was being analyzed online with GC analysis. To ensure that no liquid flows into the GC, a liquid trap with small volume was placed after the gas exit of the separator.

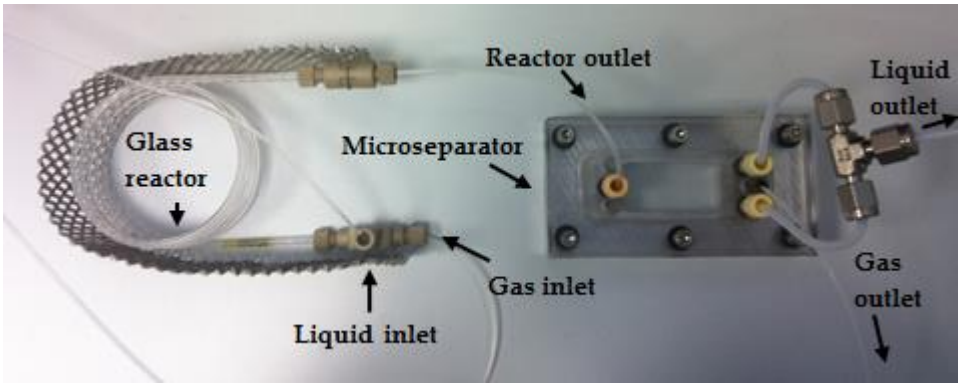


**Figure 3.5** *Picture of the glass reactor (L=1m, ID=1mm) and the glass microseparator where gas is being separated from the liquid and is analysed by GC.*

The two mass flow controllers (MFC) were calibrated using a bubble meter at NTP conditions (20°C, 1bar). The calibration results were also corrected for the moisture effect and the temperature effect based on (3.16**)**.

$$F_{real} = \frac{V}{t} \cdot \frac{T_{\exp}}{T_{cal}} \cdot \frac{P_{cal} - P_s}{P_{cal}} \qquad \textbf{(3.16)}$$

where t (min) is the time that the bubble needs to cover a volume V (ml), $T_{cal}$ (K) and $T_{exp}$ (K) are the temperature conditions of the calibration and of the experiment respectively, $P_{cal}$ (atm) is the pressure conditions during the calibration (i.e. atmospheric pressure) and $P_s$ (atm) is the saturation pressure of water at the temperature conditions of the experiment. The calibration

lines of the two mass MFCs are shown in the Appendix (Figure A. 1-Figure A. 2).

Analysis of the gas stream was performed online by means of gas chromatography. Specifically, a capillary column HP-PLOT Q was used for the analysis of the gas stream ($CO_2/N_2$). GC conditions with this column were optimised in order to achieve a good separation of the components and the final conditions chosen are shown in the Appendix (Table A. 1).

The calibration of carbon dioxide was performed, using a 20 vol% $CO_2/N_2$ and a $N_2$ cylinder. The concentrations of the gases were calculated by means of the two calibrated mass flow controllers. The calibration curve of $CO_2$ is shown in the Appendix (Figure A. 9). It should be noted that in order to produce accurate experimental results, the GC was calibrated for the carbon dioxide every day with reproducibility approximately 7%.

### 3.3.1 Reaction Quench

As the reaction can take place at room temperature and at atmospheric pressure, quick quench of the reaction is required in order to avoid reaction downstream of the reactor, so that analysis is accurate. Quench of the reaction is based on the quick separation of the gas-liquid mixture that exits the reactor, ensuring also that the extent of the reaction inside the separator is negligible.

In reaction systems where a basic reactant is involved (e.g. carbon dioxide into a sodium hydroxide solution), a common way to quench the reaction is with adding a strong acid (e.g. hydrochloric acid). In this way, salt (from the reaction between the base and the acid) and water will be produced and the reaction will stop. However, quenching the carbon dioxide absorption in a buffer solution of sodium carbonate-bicarbonate with hydrochloric acid was found to be ineffective. The quench was producing carbon dioxide and consequently was impossible to identify how much carbon dioxide was

consumed due to the reaction and how much was produced due to the quench. Hence, it was impossible to analyse accurately the reaction system with this kind of quench.

Different types of gas-liquid separators were also evaluated. Initially, an open-phase separator (Figure 3.6) was added after the reactor to separate the exiting gas-liquid stream. This type of separator has been used by many researchers in the literature [99,157,158] for the same reaction system. The gas was escaping to the atmosphere, while the liquid was being collected and analysed by titration with standardised hydrochloric acid.

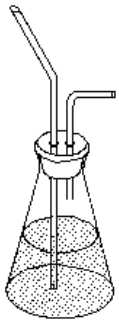

**Figure 3.6** *Schematic of open-phase gas-liquid separator.*

The disadvantage of this method is that is not a continuous way of analysis and because the liquid flowrates were very small ($U_l$<0.03ml/min), it was taking too long to collect an appreciable amount of liquid sample. This led to further inaccuracies due to interaction of the liquid with the atmosphere.

Another way to separate the gas-liquid stream after the reactor was to use a glass separator, which consists of a filter disk with small pores. As the two-phase fluid enters the separator, the gas is repelled by the hydrophilic pores while the liquid is forced through the pores via pressure gradient. A glass separator with a filter disk with pores in a range of 10-16μm was installed after the capillary reactor. The volume inside the separator (above the filter) is approximately 2.5ml and its design characteristics are shown in Figure 3.7.

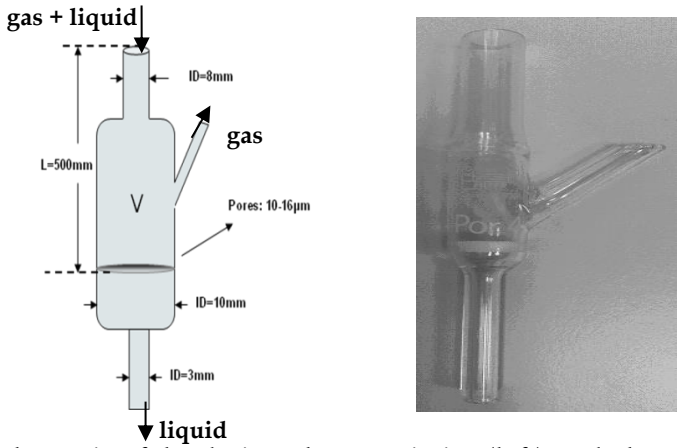


**Figure 3.7** *Schematic of the design characteristics (left) and photograph (right) of the glass gas-liquid separator with a porous filter inside.*

After the separator, the gas was analyzed by means of the GC. It was found that the gas-liquid stream is separated effectively for gas and liquid flowrates 1-3ml/min and 0.003-0.05ml/min respectively. However, results of some blank tests with water showed that physical absorption of carbon dioxide in water taking place inside the separator was underpredicted by the corresponding Henry's constant available in the literature. Consequently, it was not feasible to close the carbon balance of the system as the amount of dissolved carbon dioxide in water couldn't be neither measured nor calculated based on theory. This was not caused due to leaks in the system, as leak test was conducted by pressuring the system and no leaks were found. Therefore, it was impossible to quantify accurately the extent of the reaction inside this type of separator. Consequently, when using gas-liquid separators for the analysis of a gas-liquid reaction system, it is of crucial importance to ensure that no reaction takes place inside the separator.

Another way to analyse carbon dioxide absorption in a carbonate: bicarbonate buffer solution is to monitor the pH of the liquid phase after the reactor. As the reaction proceeds, carbonate is being consumed while bicarbonate is being produced, resulting to a decrease in the pH of the liquid phase. The stoichiometry of the model reaction can be found in Table 3.1. In this method the pH of the liquid phase is measured initially ($pH_0$) and then

is monitored after the reactor ($pH_1$). The pH difference is related to the conversion of carbon dioxide via (3.17)-(3.18).

$$\beta_c = \frac{F^0_{CO_3^{2-}} - F^{0,\ell}_{CO_2} X_{CO_2}}{F^0_{HCO_3^-} + 2F^{0,\ell}_{CO_2} X_{CO_2}} \Rightarrow X_{CO_2} = \frac{\beta^0_c - \beta_c}{2\beta_c + 1} \cdot \frac{F^0_{CO_3^{2-}}}{\beta^0_c} \cdot \frac{1}{F^{0,\ell}_{CO_2}} \quad \textbf{(3.17)}$$

$$\beta_c = \frac{[OH^-]}{K_f} = \frac{\frac{1}{10^{pOH}}}{K_f} = \frac{\frac{1}{10^{14-pH}}}{K_f} \Rightarrow \beta_c = \frac{1}{K_f \cdot 10^{14-pH}} \quad \textbf{(3.18)}$$

Where $\beta_c$ is the ratio of the carbonate over the bicarbonate concentration, $F^0_{CO_3^{2-}}$ is the inlet molar flowrate of the carbonate, $F^0_{HCO_3^-}$ the inlet molar flowrate of the bicarbonate, $F^{0,\ell}_{CO_2}$ the inlet molar flowrate of carbon monoxide in the liquid, $X_{CO_2}$ the conversion of $CO_2$. Finally, $K_f$ is the equilibrium constant for the reaction between the carbonate and the bicarbonate, which can be also defined as the ratio of the second dissociation constant of carbonic acid and the dissociation constant of water. At 20°C the value of $K_f$ is $1.7 \cdot 10^{-4}$ $mol/\ell$ [5].

The accuracy of this method of analysis depends on the accuracy of the pH meter. The pH meter used had ±0.01 accuracy, which is translated to conversion accuracy up to ±2%.

However, separation of the gas-liquid stream and then analysis of the gas stream with gas chromatography would be a much more accurate method and hence we focused finding the most suitable gas-liquid separator, which in our case seemed to be microseparators, due to the small volume used in our system. One of its advantages is the very small gas-liquid interfacial area it provides due to its small dimensions. Therefore, the extent of the reaction inside this type of separator can be considered negligible which is very important for the accurate study of the model reaction.

#### 3.3.1.1 Experimental Evaluation of Glass-Silicon Microseparators

Microseparators are devices that have been used widely the last decade for the separation of gas/liquid and liquid/liquid phases based on surface forces and associated with capillary phenomena [159-169]. Typically they consist of a main microchannel that is connected to series of small capillaries. Based on the capillary pressure the non-wetting phase (gas) does not pass through the capillaries but leaves the microseparator through the main channel while the wetting phase (liquid) fills the capillaries leading to efficient separation of the two phases.

In this study, preliminary testing of silicon-glass microseparators was performed to ensure efficient and stable separation of the gas-liquid stream exiting the reactor. The efficiency of separation in these devices was tested in a range of inlet flowrates by controlling the pressure difference across the capillaries. A detailed study on the performance of these silicon-glass microseparators was presented recently by Roydhouse et al. [170].

Gas/liquid mixture was entering from the inlet into a 300μm deep microchannel and then the liquid was being sucked by the 70 capillaries of 40μm wide and 100μm length from both sides (each side consists of 35 capillaries) while the gas was passing across them and was exiting from the gas outlet (Figure 3.8).

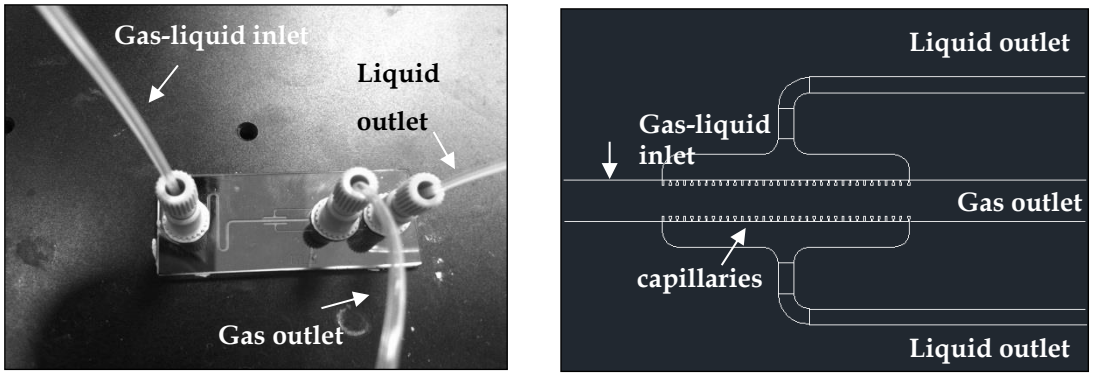


**Figure 3.8** P*hotograph (left) and schematic (right) of the silicon gas-liquid microseparator with etching depth 300μm.*

Details on the fabrication procedure of the microseparators used are given in the Appendix H.

For the control of the differential pressure across the capillaries, two metering valves were used at the outlet of the gas and the liquid phase. After the separator the gas stream was analyzed by gc analysis. The schematic of the set-up used for the evaluation of the microseparator is shown in Figure 3.9. Separation was evaluated for gas and liquid flowrates 2ml/min and 6μl/min respectively.

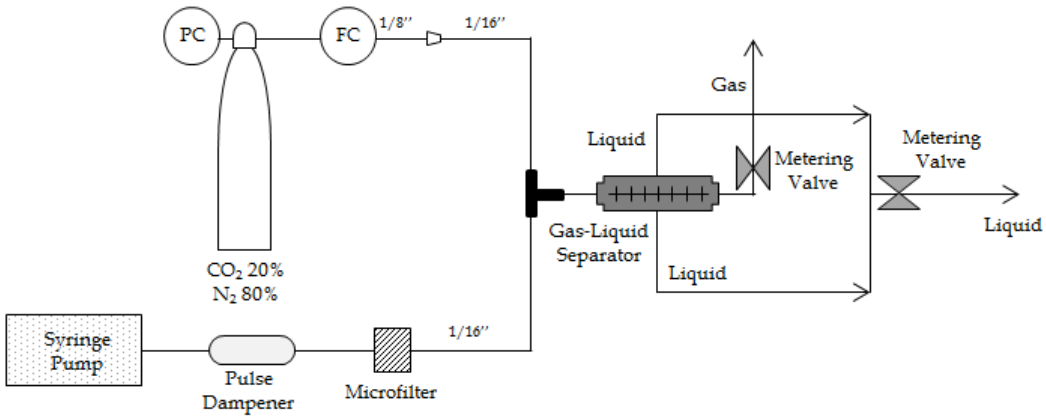


**Figure 3.9** *Schematic diagram of the experimental set-up for the test of the performance of the glass microseparator (Mikroglas).*

Microseparators with different etching depths (40, 100, 300, 480μm) were tested. Wafers with the small etching depth (40, 100μm) were found not suitable, as they were leaking from the fitting of the inlet, possibly due to high pressure drop that was developed. Wafers with large etching depth 480μm were also found to be inappropriate as they were leaking from the bottom of the wafer, because of the thin remaining thickness of the wafer (Figure 3.10). It was concluded that the separator with etching depth 300μm is the most suitable in our case.

Using the glass-silicon microseparator with the 300μm etching depth numerous attempts were conducted to separate a 20%$CO_2$-carbonate/bicarbonate solution.

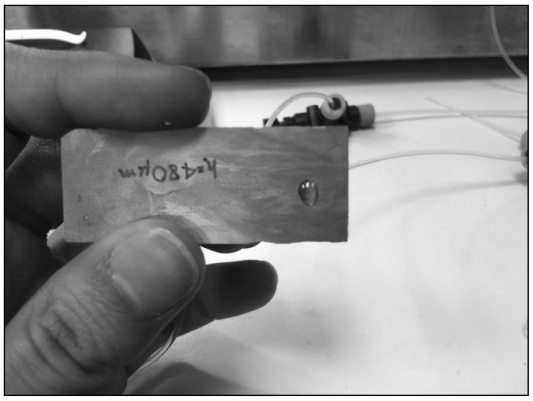

**Figure 3.10** *Photograph of the microseparator when it was leaking from the bottom of the silicon wafer with etching depth 480μm.*

In the beginning of every run, the microseparator was primed with liquid in order the capillaries to be filled with liquid. Initially, attempts of separating the gas-liquid stream were performed without reaction (bypassing the reactor). The gas and liquid flowrates used were 0.3ml/min and 0.003ml/min respectively. After adjusting gradually the metering valves it was possible to separate the gas and the liquid phases although sometimes small bubbles were seen in the liquid phase. However, this was not important because the goal was to prevent liquid flow to the gas exit, since after the separator the gas was analyzed. Higher gas flowrates were also used (up to 2ml/min) and the separation was also successful after slight decrease of the pressure in the gas phase. It was observed that the system needed around 10min for the flow to stabilize after every adjustment of the metering valves. However, in all cases instabilities in the performance of the glass-silicon microseparator over time were observed. These instabilities are possibly due to instabilities of the pump and due to fluctuations in the backpressure on the gas outlet created when i.e. liquid was flowing to the gas outlet.

Another design of the microseparator was also tried, similar with the one presented earlier but with only one arm for the liquid stream, hence containing only 35 capillaries, but its behaviour was similar with the previous one and the separation was still unstable. Therefore, due to the instabilities this type of microseparators was not pursued further.

### 3.3.1.2 Design and Evaluation of Glass Microseparator

A glass microseparator was manufactured by Mikroglas (Mainz, Germany) and its separation efficiency was tested for different gas and liquid flowrates. Specifically, the aim of this study was to establish operating conditions under which complete and stable separation of the gas-liquid mixture exiting the reactor can be achieved. The set-up used for the evaluation of the glass microseparator was the same as the one used in Chapter 3.3.1.1 (Figure 3.9).

The gas/liquid mixture enters from the inlet into a 200μm deep and 600μm wide microchannel and then the liquid (DI water) is being sucked due to capillary forces by the 80 rectangular capillaries of 50μm wide, 200μm deep and 7700μm length from both sides (each side consists of 40 capillaries) while the gas (20% $CO_2$) passes across them and exits from the gas outlet (Figure 3.11). For the precise control of the differential pressure between the two phases, two metering valves were used at the outlet of the gas and the liquid phase (Figure 3.9).

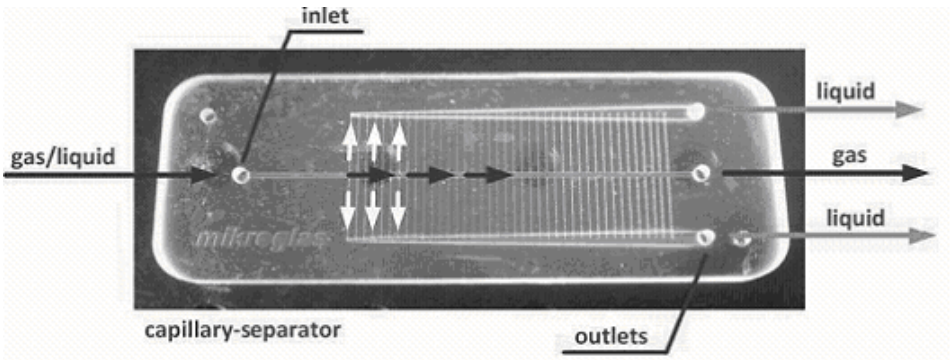


**Figure 3.11** P*hotograph of the glass gas-liquid microseparator (mikroglas).*

The design characteristics of the microseparator are shown in Figure 3.12. More photos of the experimental set-up can be found in the Appendix B.

Gas (20% $CO_2$) and liquid (DI water) flowrates ranged between 0.06-2ml/min and 0.005-0.2ml/min respectively (Table 3-4). A differential manometer (up to 200kPa) was used in order to monitor the pressure difference between the gas and the liquid phase and was placed in the gas and liquid exits before the corresponding metering valves.

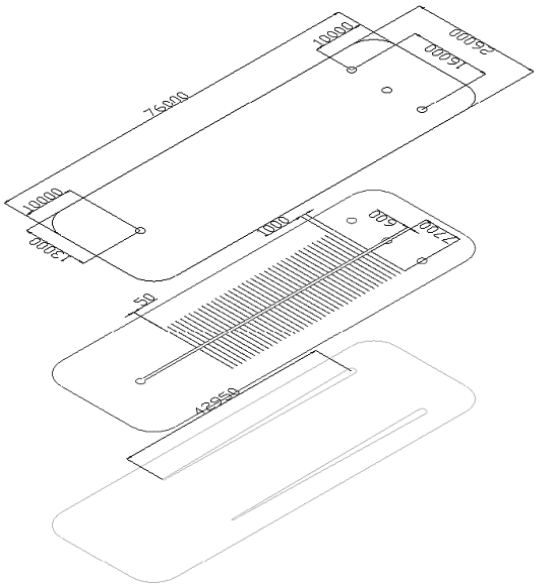


**Figure 3.12** *Technical drawing of the glass microseparator (Mikroglas) showing its design characteristics*

**Table 3-4** Operating conditions of the glass microseparator test and observations.

| $F_g$ (ml/min) | $F_\ell$ (ml/min) | Observations |
|---|---|---|
| 2 | 0.005 | Complete separation at $\Delta P=P_{gas}-P_{liquid}$=1kPa |
| 0.06 | 0.02 | Successful separation at ΔP=0.5-1.5kPa |
| | | Rarely pressure fluctuates and bubbles enter the liquid phase (≈1bubble/10min) |
| | | No liquid in the gas phase |
| | | Gas breakthrough at ΔP≈2.2kPa |
| 0.06 | 0.03 | Constant separation (ΔP>0.32kPa) |
| | | Gas breakthrough at ΔP≈2.49kPa |
| 0.2 | 0.02 | No liquid in the gas phase |
| | | Rarely bubbles enter the liquid phase |

Furthermore, in the beginning of every run, the microseparator was primed with liquid in order the capillaries to become wet and consequently the liquid to be able to flow through.

In Figure 3.13 the limits of applied pressure difference required for an efficient separation of a 20%$CO_2$-DI water mixture for certain flowrates at 10$^o$C in the glass microseparator are presented. Specifically, the pressure

differences limits were highlighted outside which incomplete separation was observed. Moreover, these experimentally observed operation limits were also compared with the theoretically expected ones.

The capacity of a separator is based on the number of the capillaries, their cross sections and their lengths. Therefore, theoretically independently of the flow regime, as long as the applied pressure difference does not exceed the capillary pressure ($P_b$) in the individual capillaries and the flow rates are below the design limit, complete separation can be achieved. The breakthrough pressure ($P_b$) can be calculated using Young-Laplace equation (3.19), where γ is the interfacial surface tension between the two fluids (N/m), and $R_1$, $R_2$ are the radii of curvature for each point at the interface.

$$P_b = \gamma\left(\frac{1}{R_1}+\frac{1}{R_2}\right) \quad \textbf{(3.19)}$$

For cylindrical pores ($R_1 = R_2 = r/\cos\theta$) (3.19) becomes (3.20),

$$P_b = \frac{2\gamma\cos\theta}{r} \quad \textbf{(3.20)}$$

where θ is the wetting angle and r is the pore radius (m). In addition, for the case of the breakthrough of the gas (non-wetting phase) to the liquid (wetting phase) θ=0 and (3.20) becomes,

$$P_b = \frac{2\gamma}{r} \quad \textbf{(3.21)}$$

However, for irregular geometries $2/r$ can be substituted for $p/A$ as it is shown in (3.25), where p is the perimeter (m) and A the area ($m^2$) of the pore opening [159] and $\gamma_{H2O}$=0.7197N/m at 20°C.

$$P_b = \frac{p\gamma}{A} \quad \textbf{(3.22)}$$

Amador *et al.* [167] studied the stability and the position of an interfacial meniscus in cylindrical and polygonal pores and they proposed a model for the description of this phenomenon. According to them, the position of the meniscus is moving inside the capillary until the pressure difference across the meniscus interface becomes equal to $P_b$.

The second design limit (lower limit) of a microseparator is determined by the maximum possible flowrate through the capillaries and can be found using Hagen-Poiseuille's law which calculates the pressure drop due to the laminar flow of Newtonian fluid along a length of tubing of known geometry (3.23),

$$\Delta P = \frac{\alpha \eta Q L}{A^2} \quad \textbf{(3.23)}$$

where, α is a numerical prefactor related to the geometry of the cross section of the channel, η is the liquid viscosity ($\eta_{H20}=10^{-3}$Pa·s at 20$^o$C_, Q is the liquid flowrate ($m^3/s$), L is the channel length (m) and A the cross-sectional area of the channel ($m^2$). It was reported [171] that α is linearly related to the shape's compactness factor, C (C=perimeter$^2$/area) for a channel of any geometry cross-section. For a pore with rectangular geometry,

$$\alpha = \frac{22}{7} C - \frac{65}{3} \quad \textbf{(3.24)}$$

Significant deviation was observed between the theoretically predicted gas-to-liquid breakthrough pressures (by Young-Laplace equation) and the experimentally observed ones. This behaviour was also observed by Roydhouse et al. [170] who studied the breakthrough pressures of capillary microseparators. They showed that at low flowrates the experimental gas-to-liquid pressures were in qualitatively agreement with the theoretical ones, while at higher flowrates deviations were significant. TeGrotenhuis *et al.* [161] also observed gas breakthrough at pressure differences below the Young-Laplace pressure limit, $P_b$, of the pore throat when studying the gas-liquid separation in a single-channel microchannel which employs a pore

throat within it. The deviation in that case was explained due to fluctuations in the backpressure in the gas outlet that were significant when liquid was flowing to the gas outlet.

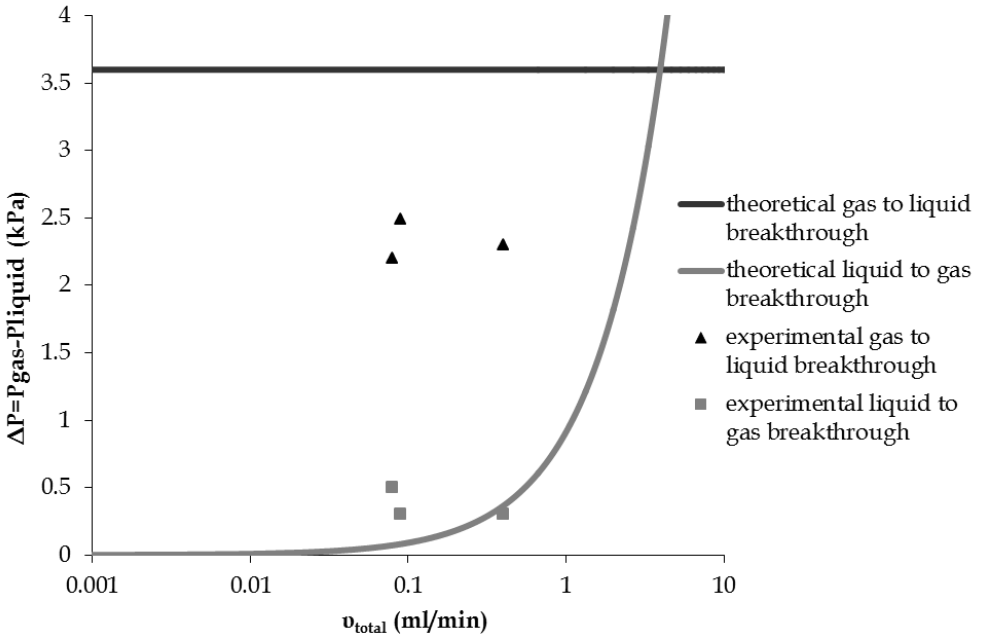


**Figure 3.13** *Operating conditions of the glass microseparator consisting of 80 capillaries, illustrating minimum applied pressure difference required to remove all the liquid from the gas-liquid stream (grey line), applied pressure difference at which gas breakthrough occurs (black line) and experimentally observed gas (black dots) and liquid (grey dots) breakthrough.*

It was concluded that for small liquid flowrates (up to 0.3ml/min) complete and stable separation is possible even for very high gas to liquid ratios (e.g. flowrates gas: liquid=400) after adjusting the pressure difference between the gas and the liquid phase ($\Delta P=P_{gas}-P_{liquid}$) by means of two metering valves between 0.3-2kPa. For $\Delta P$ below 0.3kPa, the capillaries were not able to suck all the liquid. Therefore, liquid was observed flowing to the gas exit. On the other hand, for $\Delta P$ above 2.5kPa, gas was breaking through the capillaries and was flowing to the liquid exit. For larger liquid flowrates (bigger than 0.3ml/min) pressure fluctuations were observed, resulting to an unstable system (either gas or liquid breakthrough). In conclusion, the glass microseparator seems the most promising way to separate the gas-liquid reaction mixture for the study of quench of the reaction as only small liquid flowrates are needed.

### 3.3.2 Hydrodynamic Study of Gas-Liquid Flow

For the kinetic study of a system the hydrodynamic study of the system is essential as it provides information on the mass transfer characteristics of the system, the reaction volume and time and the mixing quality of the system. This is crucial especially in gas-liquid systems where depending on the gas and liquid flowrates different flow patterns are observed and depending on the flow pattern, the system presents very different hydrodynamic and mass transfer characteristics.

Observation of the gas-liquid flow system was performed by means of a high-speed camera (Phantom Miro 4) under different gas (20%$CO_2$-$N_2$) and liquid (sodium carbonate: bicarbonate buffer solution) flowrates in two circular glass tubing with inner diameters 1mm and 0.5mm. The corresponding schematic of the experimental set-up is shown in Figure 3.14.

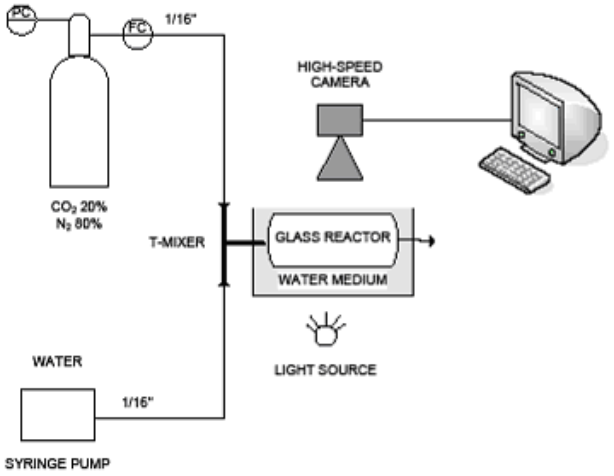


**Figure 3.14** *Schematic diagram of the experimental set-up for flow observation of the gas-liquid flow by means of a high-speed camera.*

It should be mentioned that the part of the tubing that was recorded by the camera was immersed in water medium to minimise the beam steering effect of the curved tube wall [78].

In Figure 3.15 it is clear that when the tubing is not immersed into the water medium, is difficult to determine the wall thickness and therefore the use of

a water medium to immerge the tubing is quite crucial for the accuracy of the flow observation.

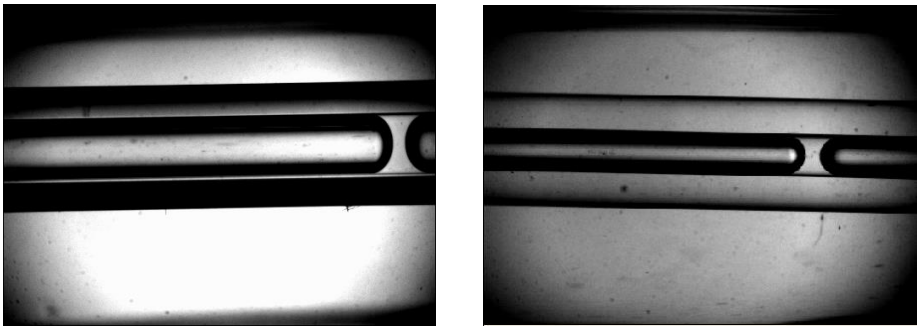

**Figure 3.15** *Images of the glass circular tubing (ID=1mm) without water medium (left picture) and with water medium (right picture) under $F_g$=1.6ml/min and $F_l$=0.006ml/min).*

The operating conditions of the flow observation experiments together with the results are shown in Table 3-5.

**Table 3-5** Conditions and results of flow observation and calculation of mass transfer coefficient, $k_l a$ and Hatta number at 0.03ml/min liquid flowrate.

| Exp | T °C | ID mm | $\upsilon_g$ ml/min | $L_{bubble}$ cm | $L_{liquid\ slug}$ cm | Film thickness μm | $k_l a$ $s^{-1}$ | $Ha_0$ | $Ha_f$ |
|---|---|---|---|---|---|---|---|---|---|
| 1 | 20 | 1 | 0.3 | 0.8-1 | 0.035-0.038 | <<30 | 0.36 | 0.08 | 0.05 |
| 2 | 20 | 1 | 0.5 | 1.1-1.2 | 0.03-0.04 | 30 | 0.37 | 0.08 | 0.05 |
| 3 | 20 | 1 | 1 | 2.5-2.6 | 0.029-0.038 | 36 | 0.36 | 0.08 | 0.05 |
| 4 | 20 | 1 | 2 | 5.8-6.3 | 0.018-0.030 | 45 | 0.37 | 0.08 | 0.05 |
| 5 | 10 | 1 | 0.3 | 0.8-0.1 | 0.035-0.038 | <<30 | 0.35 | 0.05 | 0.04 |
| 6 | 10 | 1 | 0.5 | 1.1-1.2 | 0.03-0.04 | 30 | 0.36 | 0.05 | 0.04 |
| 7 | 10 | 1 | 1 | 2.5-2.6 | 0.029-0.038 | 36 | 0.35 | 0.05 | 0.04 |
| 8 | 10 | 1 | 2 | 5.8-6.3 | 0.018-0.030 | 45 | 0.35 | 0.05 | 0.04 |
| 9 | 20 | 0.5 | 0.3 | 4-5 | 0.1-0.2 | - | 0.67 | 0.08 | 0.07 |
| 10 | 20 | 0.5 | 0.5 | 9-11 | 0.1-0.2 | - | 0.68 | 0.08 | 0.07 |
| 11 | 20 | 0.5 | 1 | 15-17 | 0.1-0.2 | - | 0.7 | 0.08 | 0.07 |
| 12 | 20 | 0.5 | 2 | 30-35 | 0.1-0.2 | - | 0.71 | 0.08 | 0.07 |

The gas and the liquid flowrates ranged between 0.1-3ml/min and 0.006-0.01ml/min respectively. Under these gas and liquid flowrates, slug and slug annular flow were observed, as defined in Chapter 2.3.1.

It can be seen that as the gas flowrate increases the bubble length increases significantly while the liquid slug length slightly decreases. Bubble lengths found also to increase when capillary size decreases. These observations have found to be in good agreement with the literature [172,173].

Furthermore, the liquid film around the gas bubble flowing at 20$^{o}$C found to become thicker when the gas flowrate increases (and hence as the capillary number increases in a range between 0.001-0.003). This is consistent with previous observations of Taylor's and Bretherton's first experiments [174,175]. Due to limitation of the current equipment, it was not feasible to measure the film thickness at very small flowrates and using the capillary with 0.5mm inner diameter.

The mass transfer coefficient was estimated by means of van Baten and Krishna's correlation for long contact times (3.22), as it was found that under these operating conditions Fo>1 based on (3.26).

$$k_\ell \alpha = k_{\ell,cap}\alpha_{cap} + k_{\ell,film}\alpha_{film} = 2\frac{\sqrt{2}}{\pi}\sqrt{\frac{Du_B}{d}}\frac{4}{L_{UC}} + 3.41\frac{D}{\delta_{film}}\frac{4\varepsilon_g}{d} \qquad \textbf{(3.25)}$$

$$Fo = \frac{D \cdot t}{d^2} \qquad \textbf{(3.26)}$$

where D is the diffusion coefficient of the gas in the liquid, t is the contact time between the two phases and d is the diffusion path length of the liquid which in our case is equal with the film thickness.

Hatta number was calculated based on (2.4), assuming that the gas film resistance is negligible,

$$Ha = \frac{\sqrt{k_r \cdot D_{A\ell}}}{k_\ell} \qquad \textbf{(3.27)}$$

where $k_r$ is the reaction rate constant of the reaction, $D$ is the reactant A diffusivity into the liquid and $k_\ell$ the mass transfer coefficient of A in the liquid phase.

Hatta number was calculated both in the inlet ($Ha_0$) and outlet of the reactor ($Ha_f$) as it was shown that the reaction rate constant changes along the reactor and hence Hatta number changes as well along the reactor. It was found that $k_\ell\alpha$ in this range of conditions is between 0.35-0.71$s^{-1}$ depending on the gas and the liquid flowrates. Moreover, Hatta number was found that ranges between 0.04-0.08, indicating that the mass transfer resistances in this system are negligible based on Hatta criterion (Ha<<0.3, as explained in Chapter 2.1.3).

### 3.3.3 Residence Time Distribution Experiments

Residence time distribution experiments were performed in order to measure the liquid residence time and the liquid volume fraction of the system under conditions similar to reaction experiments. Experimental RTD measurements were performed by monitoring the concentration of a tracer dye by means of a LED-photodiode system. Experiments were performed with pure nitrogen and a 0.1M sodium carbonate: bicarbonate (1:9) solution in a glass capillary with 1m length and 1mm inner diameter.

The set-up used (Figure 3.16) has been described by Cantu-Perez et. al [114] in the past. The tracer pulse (Parker Blue dye) was introduced by a 6-port sample injection valve (Rheodyne 7725(i)) equipped with 0.3ml sample loop and an internal position signal switch that indicated the time of injection. The piping among all components was PFA 1mm ID. Tracer detection was performed by light absorption in the inlet and in the outlet of the glass reactor. Illumination was provided by two square LEDs (Kingbright L-1553IDT). To seal the system from ambient light it was placed in a dark box. The detection system was based on a linear diode array detector (TSL, 1401R-LF) which had 128 diodes each of dimensions 63.5μm by 55.5μm. This was driven using the manufacturer's recommended circuit. A scan of all diodes would take 128μs and the interval between successive scans was 5.12μs.

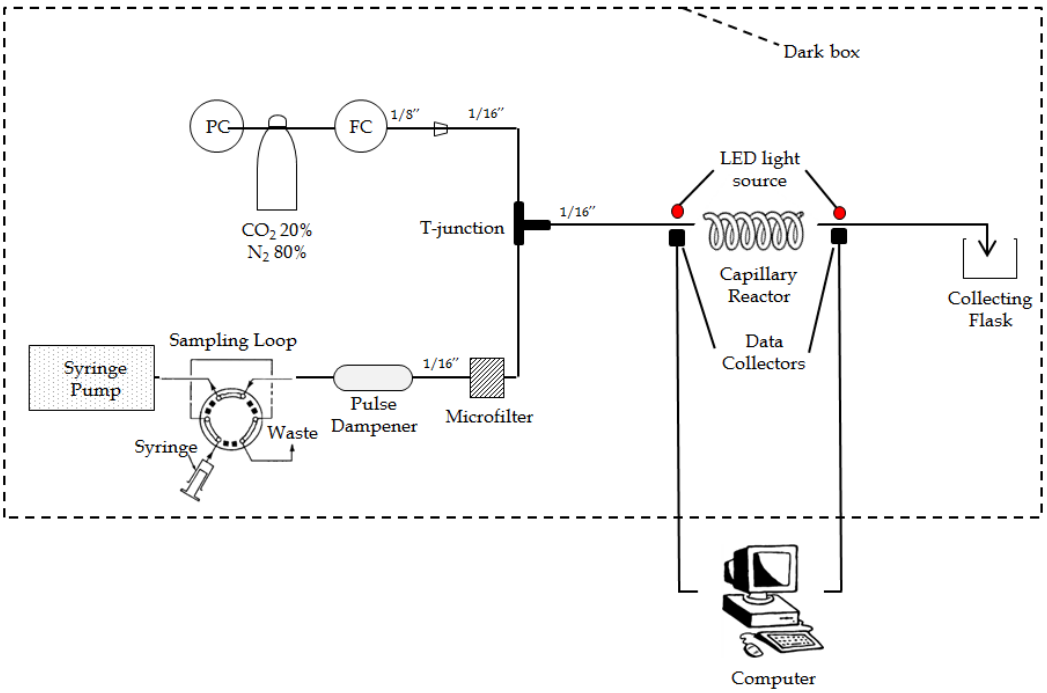


**Figure 3.16** *Schematic of experimental set-up for RTD study of model system.*

Data from the sensor was collected using a National instruments PCI-6010 data acquisition card before being analysed and displayed on a computer using a program written in Labview. Every 100ms the computer would average the previous two scans, calculate the absorbance for each diode and display the result.

Validation of the method used for the analysis of the RTD experiments can be found in the Appendix (Appendix D) where the analysis methodology of the signal is also demonstrated. The method was firstly validated by analysing the RTD curves of liquid-only flows where the residence time of the fluid was known ($\tau = {}^{V}/_{\upsilon_\ell}$).

The RTD curves for various gas-to-liquid ratios are presented in Figure 3.17 where by decreasing the gas-to-liquid ratio the RTD curve becomes sharper indicating a plug-like behaviour.

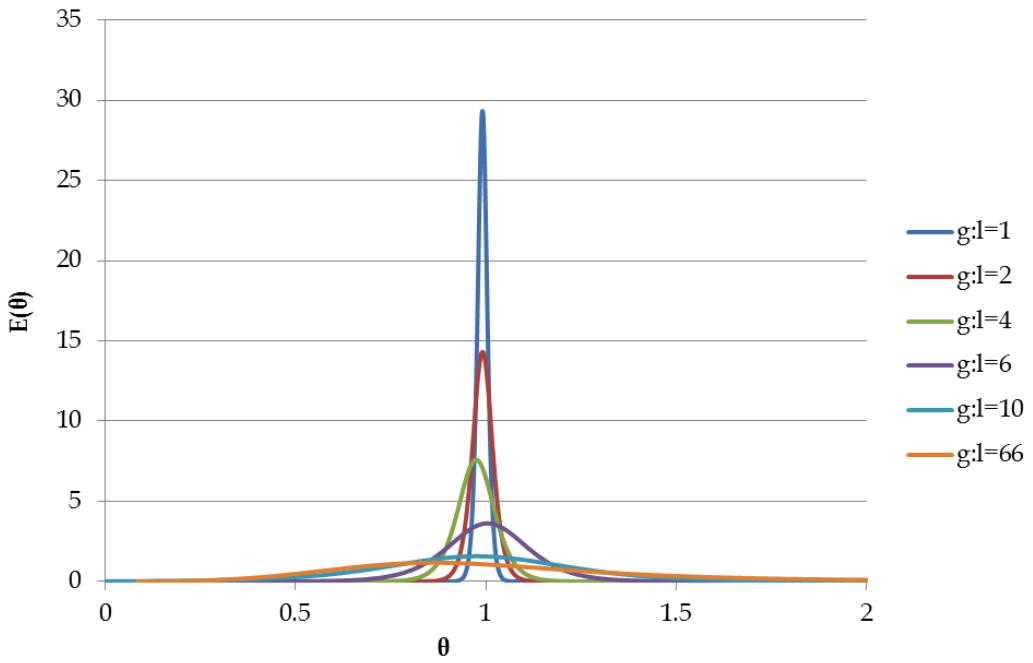


**Figure 3.17** *RTD curves for a range of gas-to-liquid ratios.*

All the finding of the RTD experiments are summarised in Table 3-6.

**Table 3-6** Results of RTD experiments for various gas-to-liquid ratios conditions.

| $\upsilon_g$ (ml/min) | $\upsilon_\ell$ (ml/min) | gas-liquid ratio | $\tau_\ell$ (s) | D/uL | A |
|---|---|---|---|---|---|
| **0.5** | 0.5 | 1 | 53.4 | 0.00006 | 0.8 |
| **1** | 0.5 | 2 | 39.5 | 0.0004 | 0.83 |
| **2** | 0.5 | 4 | 28.4 | 0.005 | 0.85 |
| **3** | 0.5 | 6 | 17.7 | 0.005 | 0.88 |
| **0.3** | 0.03 | 10 | 254 | 0.02 | 0.91 |
| **2** | 0.03 | 66 | 118 | 0.08 | 0.93 |

In Table 3-6 $\upsilon_g$, $\upsilon_\ell$ are the gas and the liquid flowrates, $\tau_\ell$ is the experimentally measured liquid residence time, D/uL is the dispersion number and A is the numerical prefactor found to satisfy (3.28),

$$\varepsilon_g = A \cdot \frac{j_g}{j_g + j_\ell} \tag{3.28}$$

Factor A in the case of Armand's model is equal to 0.833 while in the case of homogenous model is equal to 1. The reproducibility of the system was satisfactorily with uncertainty of ±3% concerning the mean residence time of the liquid.

As the gas to liquid ratio increases the dispersion number, $D/uL$, is also increasing (Table 3-6), behaviour which was also observed by Zhang et al. [118]. They studied the effect of temperature, pressure and flow pattern on the observed RTD of a toluene/nitrogen and a cyclohexane/nitrogen system at gas-to-liquid-ratios between 0.3-0.005 in a stainless steel tube with 2mm inner diameter and reported increasing deviation from plug flow behaviour when increasing the gas flowrate or decreasing the liquid flowrate. Higler et al. [176] observed also the same effect of the gas-to-liquid ratio on the RTD curves when measuring the liquid-phase residence time of an air-water system in structured packed columns of 10-24cm inner diameter.

Moreover, in our system it was observed that when the ratio becomes 10 then $D/uL < 0.01$ indicating that the flow starts deviating from the ideal plug flow behaviour.

Another point worth noting in Table 3-6 is that as the gas to liquid ratio increases the factor A gradually increases. For gas-to-liquid ratios below 3 Armand's model can be used while for ratios above 10 it would be better to use the homogenous model. However, these results highlight the necessity of actually measuring the residence time and the void fraction of a gas-liquid system experimentally instead of using correlations. One should be very careful when using these void fraction correlations if using a channel with different geometrical characteristics, different fluids or different gas-to-liquid ratios.

## 3.4 Reactor Model

### 3.4.1 Reactor Model Development

A simple one-dimensional plug-flow reactor model was developed to simulate the carbon dioxide absorption in buffer solutions in capillary reactors and it will be further used for the kinetic study of methoxycarbonylation of ethylene. It was aimed to keep the reactor model at a lower level of complexity in order to reduce the time required to run the simulation and the number of parameters which need to be determined. The differential volume element considered for the modelling is shown in Figure 3.18 and consists of a cylindrical part with outer diameter equal with the inner diameter of the capillary, d, thickness equal with the liquid film thickness, δ, and length equal with a distance element dx.

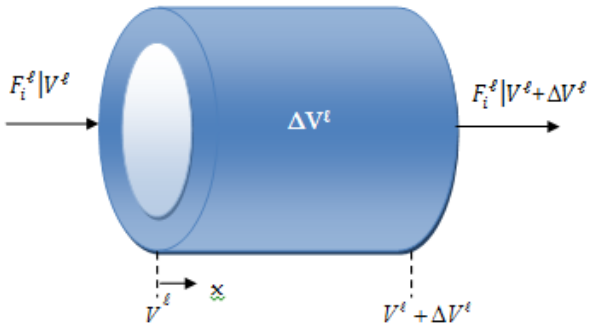


**Figure 3.18** *A volume element $\Delta V^{\ell}$ in the liquid phase in a gas-liquid reactor*

An annular-type flow is assumed where the liquid is flowing along the walls of the tube while the gas is flowing in the core. In the gas-liquid interphase it is assumed that vapour-liquid equilibrium is established between the two phases for each component. The reaction takes place only in the liquid phase. The reactor model considers the mass balances in the gas and the liquid phase.

The assumptions considered are the following:

- Plug flow in the gas and the liquid phase
- Steady state, isothermal reactor
- Reaction takes place only in the liquid phase

- Equilibrium at the gas-liquid interface
- Constant gas and liquid volumetric flowrates along the reactor

The mass balance for the $CO_2$ in the liquid phase for a volume element $\Delta V^{\ell}$ in the liquid phase can be written as,

$$liq.flow,in - liq.flow,out + in\ by\ absorption - reaction = 0 \quad \textbf{(3.29)}$$

$$F^{\ell}_{CO_2|V^{\ell}} - F^{\ell}_{CO_2|V^{\ell}+\Delta V^{\ell}} + N^{\ell}_{CO_2}\Delta A - r_{CO_2}\Delta V^{\ell} = 0 \quad \textbf{(3.30)}$$

By defining the volume fraction of the liquid, $\varepsilon^{\ell}$, as well as the ratio, α,

$$\varepsilon^{\ell} = \frac{\Delta V^{\ell}}{\Delta V^{r}} = \frac{liquid\ volume\ element}{reactor\ volume\ element} \quad \textbf{(3.31)}$$

$$\alpha = \frac{\Delta A}{\Delta V^{r}} = \frac{interfacial\ contact\ area}{reactor\ volume} \quad \textbf{(3.32)}$$

Equation (3.30) can be written as,

$$F^{\ell}_{CO_2|V^{\ell}+\Delta V^{\ell}} - F^{\ell}_{CO_2|V^{\ell}} = N^{\ell}_{CO_2}.\alpha \cdot \Delta V^{r} - r_{CO_2} \cdot \varepsilon \cdot \Delta V^{r} = 0 \quad \textbf{(3.33)}$$

After division by the reactor volume element $\Delta V^{r}$ and allowing $\Delta V^{r} \to 0$,

$$\frac{dF^{\ell}_{CO_2}}{dV^{r}} = N^{\ell}_{CO_2} \cdot \alpha - r_{CO_2} \cdot \varepsilon \quad \textbf{(3.34)}$$

The molar flowrate of $CO_2$ in the liquid phase $F^{\ell}_{CO_2}$ and the volume element $V^{\ell}$ can be expressed by,

$$F^{\ell}_{CO_2} = j^{\ell} \cdot A_c \cdot C^{\ell}_{CO_2} \quad \textbf{(3.35)}$$

$$dV^{\ell} = A_c dx \quad \textbf{(3.36)}$$

where $j^{\ell}$ is the superficial velocity of the liquid, $A_c$ is the tube cross section area.

Equation (3.34) is now transformed to,

$$j^{\ell}\frac{dC_{CO_2}^{\ell}}{dx} = N_{CO_2}^{\ell}\alpha - r_{CO_2}.\varepsilon^{\ell} \quad \textbf{(3.37)}$$

The reaction $r_{CO_2}$ can be expressed by (3.38) (see Chapter 3.2),

$$r_{CO_2} = k_r \cdot C_{CO_2}^{\ell} \quad \textbf{(3.38)}$$

The reaction rate constant $k_r$ depends on the reaction temperature and the ratio of carbonate and bicarbonate concentrations.

The flux of $CO_2$ from the liquid film to the liquid bulk $N_{CO_2}^{\ell}$ is obtained by (3.39),

$$N_{CO_2}^{\ell} = k_{\ell}\left(C_{CO_2}^{\ell,i} - C_{CO_2}^{\ell}\right) \quad \textbf{(3.39)}$$

where $k_{\ell}$ is the mass transfer coefficient in the liquid phase, $C_{CO_2}^{\ell,i}$ is the concentration of the liquid $CO_2$ in the gas-liquid interface and $C_{CO_2}^{\ell}$ is the concentration of the liquid $CO_2$ in the bulk of the liquid.

The boundary condition of (3.37) is that in the inlet of the reactor all the carbon dioxide is in the gas phase and hence,

$$x = 0 \rightarrow C_{CO_2}^{\ell} = 0 \quad \textbf{(3.40)}$$

Similarly, the mass balance for the $CO_2$ in the gas phase for a volume element $\Delta V^g$ (

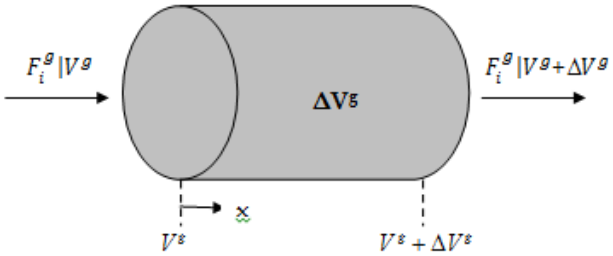


Figure 3.19) in the gas phase is expressed by,

$$gas\ flow, in - gas\ flow, out - out\ by\ absorption = 0 \quad \textbf{(3.41)}$$

$$F_{CO_2}^{g}\Big|_{V^g} - F_{CO_2}^{g}\Big|_{V^g+\Delta V^g} - N_{CO_2}^{g}\Delta A = 0 \qquad \textbf{(3.42)}$$

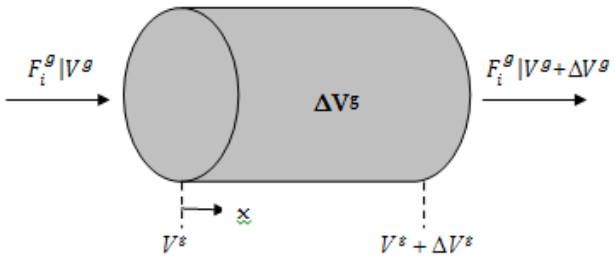


**Figure 3.19** *A volume element $\Delta V^g$ in the gas phase in a gas-liquid reactor.*

Substituting (3.32**)** into (3.42**)**,

$$F_{CO_2}^{g}\Big|_{V^g+\Delta V^g} - F_{CO_2}^{g}\Big|_{V^g} = -N_{CO_2}^{g}\alpha\Delta V^r \qquad \textbf{(3.43)}$$

Where $V^g$ is the volume occupied by the gas phase while $V^r$ is the total volume of the reactor.

After division by the reactor volume element $\Delta V^r$ and allowing $\Delta V^r \to 0$,

$$\frac{dF_{CO_2}^{g}}{dV^r} = -N_{CO_2}^{g}\alpha \qquad \textbf{(3.44)}$$

Substituting for gas superficial velocity, equation (3.44**)** becomes,

$$j^g \frac{dC_{CO_2}^{g}}{dx} = -N_{CO_2}^{g}\alpha \qquad \textbf{(3.45)}$$

The flux of $CO_2$ from the gas bulk to the gas film $N_{CO_2}^{g}$ is defined by (3.46**)**,

$$N_{CO_2}^{g} = k_g\left(C_{CO_2}^{g} - C_{CO_2}^{g,i}\right) \qquad \textbf{(3.46)}$$

where $k_g$ is the mass transfer coefficient in the gas phase, $C_{CO_2}^{g,i}$ is the concentration of the gas $CO_2$ in the gas-liquid interface and $C_{CO_2}^{g}$ is the concentration of the gas $CO_2$ in the bulk of the gas.

The boundary condition at the inlet is,

$$x = 0 \rightarrow C_{CO_2}^{g} = C_{CO_2}^{g,0} = \frac{y_{CO_2} P}{RT} \quad \textbf{(3.47)}$$

At the gas-liquid interface, a chemical equilibrium is assumed to exist and the concentrations of the carbon dioxide in the gas and in the liquid phase are related to each other by (3.48**)**, where $K_{CO_2}$ is the equilibrium constant [177].

$$K_{CO_2} = \frac{C_{CO_2}^{g,i}}{C_{CO_2}^{\ell,i}} \quad \textbf{(3.48)}$$

The unknown concentration of carbon dioxide in the interface can be calculated by (3.49**)**.

$$N_{CO_2}^{g} = N_{CO_2}^{\ell} \Rightarrow$$

$$k_g \left( C_{CO_2}^{g} - K_{CO_2} C_{CO_2}^{\ell,i} \right) = k_\ell \left( C_{CO_2}^{\ell,i} - C_{CO_2}^{\ell} \right) \quad \textbf{(3.49)}$$

Assuming that the resistance in the gas film is negligible compared to that in the liquid film, the fluxes of carbon dioxide in the gas and the liquid film are expressed by (3.50**)**. This assumption is valid as the diffusion coefficient of carbon dioxide in the gas phase is much bigger than that in the liquid phase.

$$N_{CO_2}^{\ell} = k_\ell \left( \frac{C_{CO_2}^{g}}{K_{CO_2}} - C_{CO_2}^{\ell} \right) = N_{CO_2}^{g} \quad \textbf{(3.50)}$$

At the interface the Henry's law is given by (3.51**)**,

$$\frac{C_i^{\ell}}{C_i^{g}} = K_i = \frac{RT}{H_i} \quad \textbf{(3.51)}$$

where *K* is the Henry's law constant defined as the ratio of liquid to gas concentrations [7] and H is solubility.

The model equations (3.37)-(3.40),(3.45)-(3.47) and (3.50) were solved using Polymath software. The parameters involved in the model are listed in Table

3-7 together with the correlations used for their determination or reference values.

**Table 3-7** Model parameters and relevant correlations

| Parameter | Units | Correlation/Value |
|---|---|---|
| $k_\ell\alpha$ | $s^{-1}$ | van Baten and Krishna [105]: $k_\ell\alpha = k_{\ell,cap}\alpha_{cap} + k_{\ell,film}\alpha_{film} = 2\frac{\sqrt{2}}{\pi}\sqrt{\frac{Du_B}{d}}\frac{4}{L_{UC}} + 3.41\frac{D}{\delta_{film}}\frac{4\varepsilon_g}{d}$ |
| $\varepsilon^{\ell}$ | - | Armand [108]: $\varepsilon_g = A\frac{j_g}{j_g + j_\ell}$ |
| $K_{CO_2}$ | $mol/L \cdot atm$ | $K_{CO_2}$ = 0.05 at 10°C<br>$K_{CO_2}$ = 0.037 at 20°C [156] |
| $k_r$ | - | $k_r = 0.21 \cdot \beta_c$ at 10 °C<br>$k_r = 0.56 \cdot \beta_c$ at 20 °C [141] |

3.4.1.1 Model Sensitivity on Mass Transfer Coefficient

The effect of the mass transfer coefficient on the overall performance of the model system was studied using the suggested reactor model. Keeping the gas flowrate constant ($U_g$=0.1ml/min), different cases were studied with different liquid flowrates and operating conditions. In all cases, the corresponding reactor had a length of 1m and an inner diameter of 0.5mm and the operating conditions of the carbon dioxide (20 vol% $CO_2/N_2$) absorption in a 0.1M sodium carbonate bicarbonate solution were 10°C and 1atm. Different values of $k_\ell\alpha$ were used while keeping all the other parameters the same.

In Figure 3.20 the effect of the mass transfer on the conversion of carbon dioxide is shown. It can be seen that the effect of the mass transfer on the reaction rate is insignificant and it only starts affecting the reaction rate when $k_\ell\alpha$ is lower than $0.1s^{-1}$. It should be noted that during experiments, $k_\ell\alpha$ was calculated to be around $0.35s^{-1}$, as shown in Chapter 3.3.2. Therefore, it can is ensured that the experimental results of the model reaction were intrinsic kinetic data.

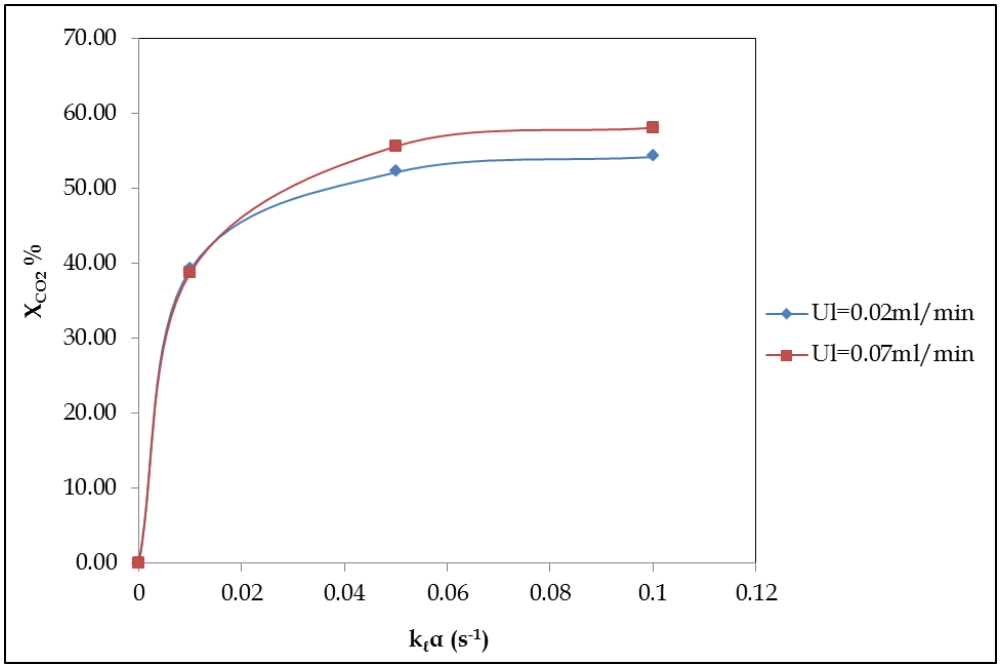


**Figure 3.20** *Conversion of carbon dioxide reaction against volumetric liquid mass transfer coefficient for different liquid ($Na_2CO_3$:$NaHCO_3$ (1:9)) flowrates under constant gas (20% $CO_2$) flowrate (Ug=0.1ml/min) at 10°C, at atmospheric pressure in a capillary reactor with L=1m, ID=0.5mm.*

### 3.4.1.2 Liquid Volume Fraction

In Figure 3.21 the effect of the liquid volume fraction, $\varepsilon_\ell$, on the predicted conversion of carbon dioxide is shown under the same operating conditions as previously. The model uses Armand correlation to calculate the liquid volume fraction and under these conditions ($U_l$=0.02ml/min, $U_g$=0.1ml/min at 10°C) the predicted value was 0.305. Two different values of $\varepsilon_\ell$ (0.25 and 0.35) were used to investigate the effect of a small deviation from the Armand correlation on the accuracy of the model. In Fig.3.5 it is shown that a moderate deviation (~15%) from the Armand correlation produces a noticeable change (~10%) in the predicted conversion. Since it was shown earlier that Armand correlation cannot be applied for gas-to-liquid ratios larger than 2, the importance of measuring experimentally the liquid void fraction is highlighted, so it is determined with better accuracy.

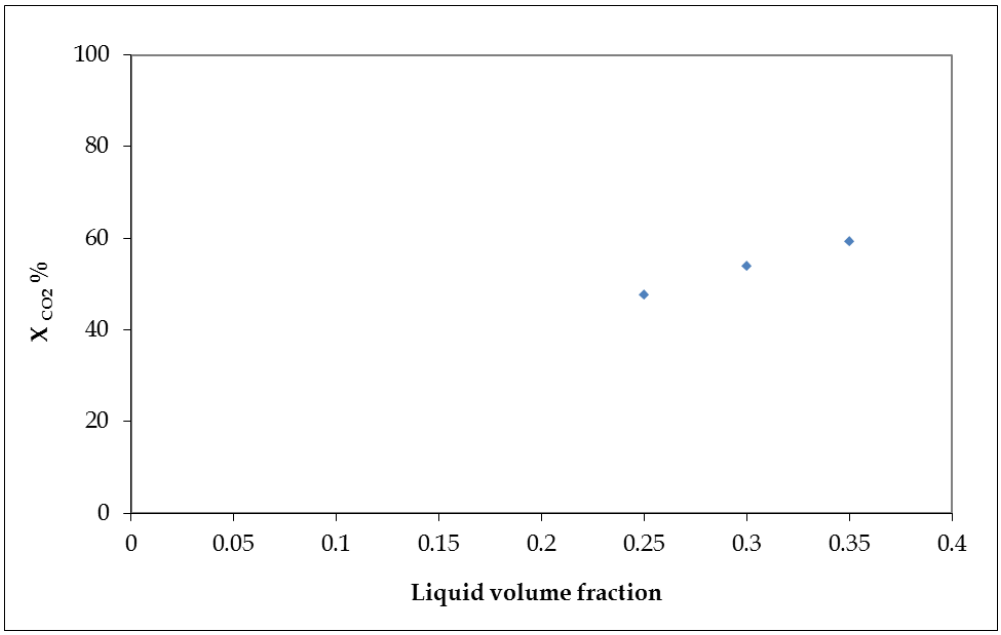


**Figure 3.21** *Effect of liquid volume fraction on conversion of carbon dioxide predicted from the model ($U_g$=0.1ml/min 20% $CO_2$, $U_l$=0.02ml/min $Na_2CO_3$:$NaHCO_3$ (1:9) at 10$^o$C) in a capillary reactor (L=1m, ID=0.5mm).*

### 3.4.2 Comparison of Model with Experimental Results

Initially blank tests were conducted using 2% $CO_2$/DI water in order to compare the experimental measured physical absorption with the theoretical one. As $CO_2$ solubility into water at 20$^o$C is 0.039kmol/m$^3$atm, for gas and liquid flowrates 0.5ml/min and 0.03ml/min the maximum expected absorption of $CO_2$ is around 6.1%. Under the same conditions, the experimental measured absorption of $CO_2$ was found to be 5.05% ±0.23 in good agreement with the model.

Reaction experiments were performed and the corresponding operating conditions are shown in Table 3-8 together with the experimental results and the corresponding predictions of the reactor model.

**Table 3-8** Experimental results of the model reaction and corresponding model predictions under different operating conditions when inlet liquid flowrate was constant at 0.03ml/min.

| No. | T | Reactor | | $\upsilon_g$ | $\varepsilon_\ell$ | Conversion % | |
|---|---|---|---|---|---|---|---|
| Exp. | (°C) | ID (mm) | L (m) | (ml/min) | | model | experiment |
| 1 | 20 | 1 | 1 | 0.3 | 0.17 | 69.31 | 73.33 |
| 2 | 20 | 1 | 1 | 0.5 | 0.13 | 46.9 | 40.62 |
| 3 | 20 | 1 | 1 | 1 | 0.10 | 25.15 | 22.97 |
| 4 | 20 | 1 | 1 | 2 | 0.08 | 12.92 | 13.1 |
| 5 | 10 | 1 | 1 | 0.3 | 0.17 | 53.28 | 49.405 |
| 6 | 10 | 1 | 1 | 0.5 | 0.13 | 34.67 | 30.33 |
| 7 | 10 | 1 | 1 | 1 | 0.10 | 18.16 | 19.83 |
| 8 | 10 | 1 | 1 | 2 | 0.08 | 9.23 | 10.48 |
| 9 | 20 | 0.5 | 1 | 0.3 | 0.17 | 36.76 | 40.75 |
| 10 | 20 | 0.5 | 1 | 0.5 | 0.13 | 23.05 | 25.15 |
| 11 | 20 | 0.5 | 1 | 1 | 0.10 | 11.75 | 12.79 |
| 12 | 20 | 0.5 | 1 | 2 | 0.08 | 5.71 | 6.21 |

In Figure 3.22 the experimentally observed carbon dioxide conversion in a glass reactor of 1m length and 1mm inner diameter at 20°C is plotted against the liquid residence time (as measured in residence time experiments). The residence time varied between 2-4.5min by decreasing the gas flowrate while keeping the liquid flowrate fixed (Table 3-8).The conversion of carbon dioxide increases when liquid residence time increases as more time is available for the reaction to take place. The experimental results of carbon dioxide conversion are also compared with the corresponding predictions of the reactor model (bold line in Figure 3.22) and a good fit between the two is shown. Any deviations between the model predictions and the experimental results can be attributed to the experimental error observed (≈8%).

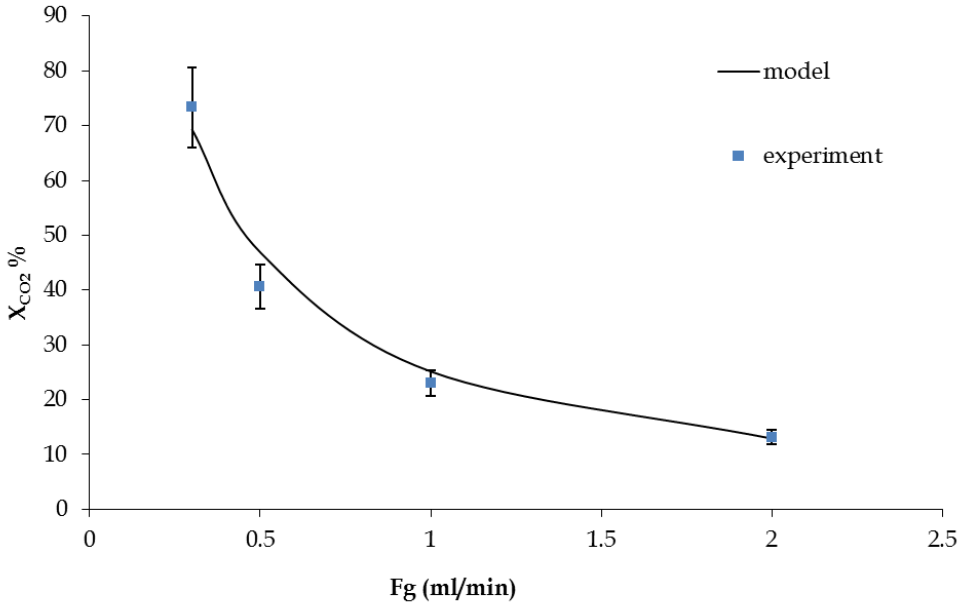


**Figure 3.22** *Experimental results and model predictions for $F_g$=0.3-2ml/min, $F_l$=0.03ml/min at 20°C in a glass reactor of 1m length and 1mm inner diameter (No. experiments=1-4).*

Similarly, in Figure 3.23 the experimentally observed carbon dioxide conversion in a glass reactor of 1m length and 1mm inner diameter at 10°C is plotted against the liquid residence time.

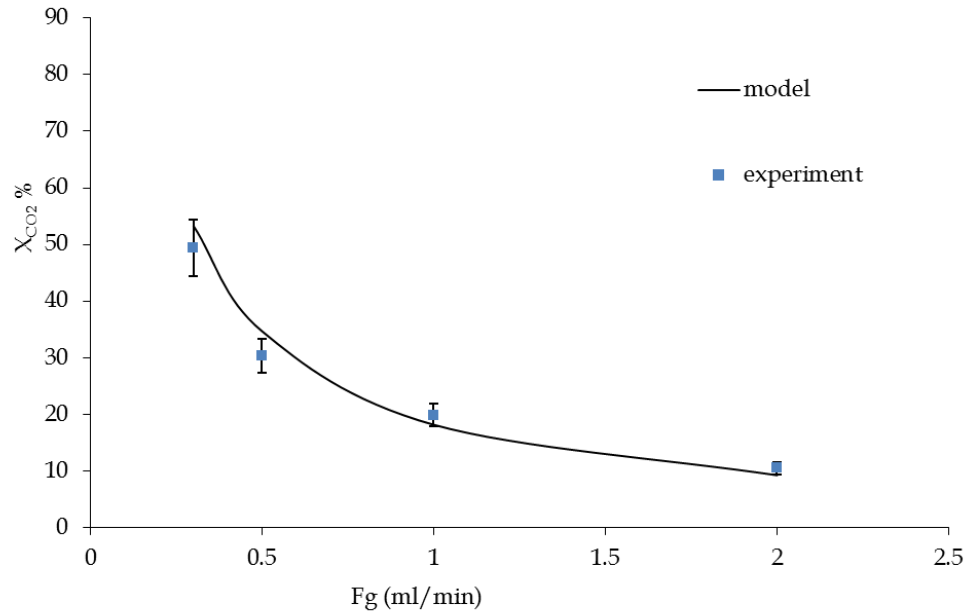


**Figure 3.23** *Experimental results and model predictions for $F_g$=0.3-2ml/min, $F_l$=0.03ml/min at 10°C in a glass reactor of 1m length and 1mm inner diameter (No. experiments=5-8).*

Lower carbon dioxide conversion is observed at higher gas flowrate due to the smaller liquid residence time at higher gas flowrate. Moreover, due to the lower temperature conditions in this series of experiments, lower conversions were observed in total compared to those at 20°C in Figure 3.22. This is due to the higher reaction rate constant at higher temperatures. Moreover, model predictions provide a good fit of the experimental data in all cases.

In Figure 3.24 the experimentally observed carbon dioxide conversion in a glass reactor of 1m length and 0.5mm inner diameter at 20°C is plotted against the liquid residence time.

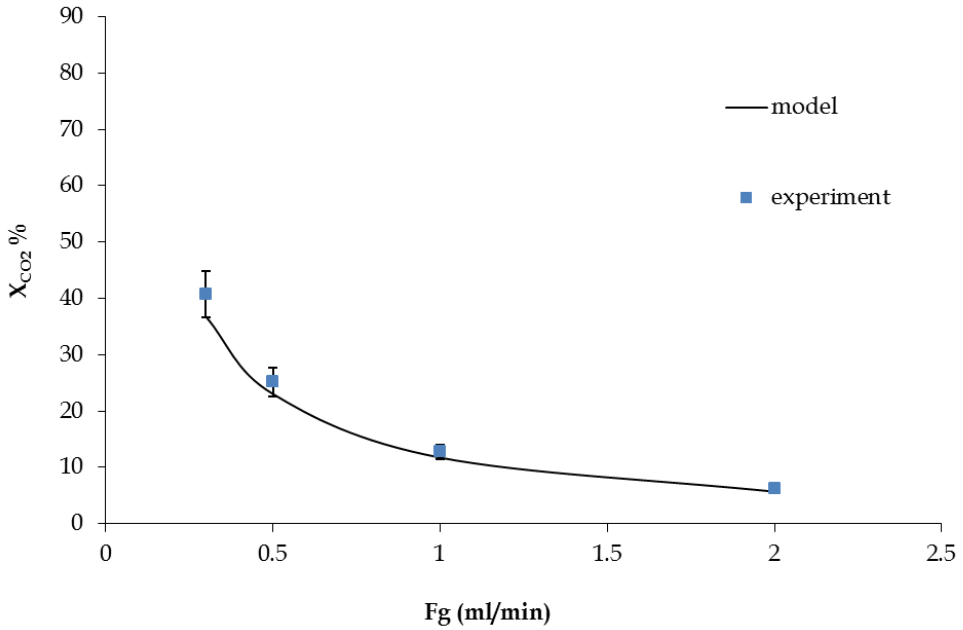


**Figure 3.24** *Experimental results and model predictions for $F_g$=0.3-2ml/min, $F_l$=0.03ml/min at 20°C in a glass reactor of 1m length and 0.5mm inner diameter (No. experiments=9-12).*

For the same gas and liquid flowrate, lower carbon dioxide conversions are observed in Figure 3.24 compared to the corresponding experiments in the glass reactor with 1mm inner diameter (Figure 3.22). This is due to the smaller reactor volume that led to smaller residence time of the liquid and hence less time for reaction to take place resulting to smaller conversions of

carbon dioxide. The experimental data are also compared with the corresponding model predictions presenting satisfactorily fit.

Furthermore, the accuracy of the reactor model to predict the reaction performance is highlighted in the following parity plot (Figure 3.25) where the experimentally measured conversions of carbon dioxide for exps.1-12 (Table 3-8) are plotted together with the corresponding model predictions.

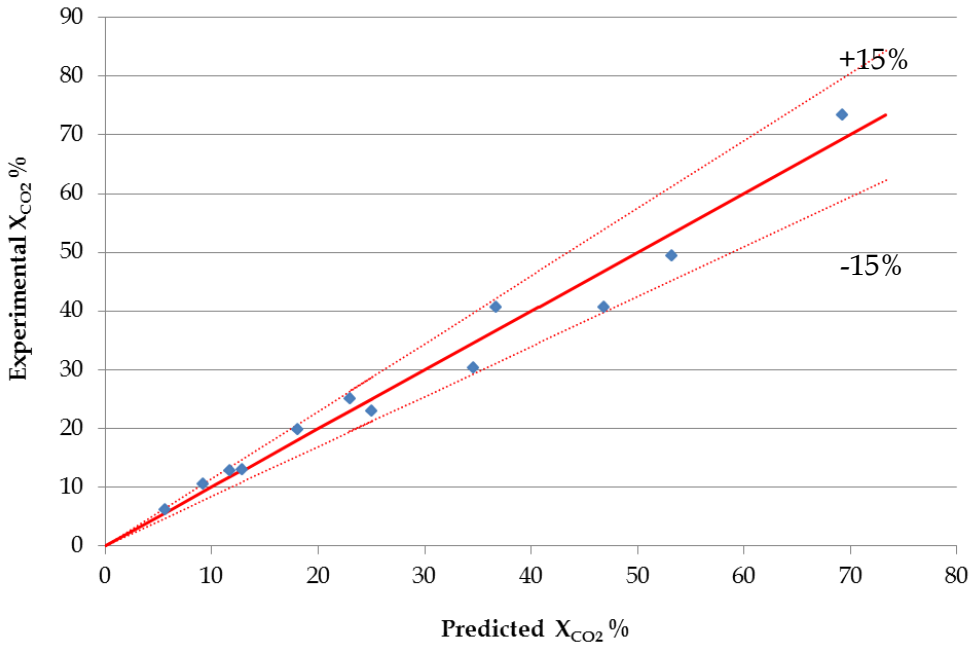


**Figure 3.25** *Parity plot of carbon dioxide conversions for exps.1-12 (Table 3-8) and model predictions.*

It is observed that model is satisfactorily predictive in the whole range of operating conditions as the deviation from the experimental results is always less than 15%. Hence, it can be concluded that the model is able to predict satisfactorily the behaviour of the model reaction in different designs of capillary microreactors as well as at different reaction temperatures and different residences times.

## 3.5 Conclusions

The performance of carbon dioxide absorption in a 0.1M carbonate:bicarbonate (1:9) buffer solution was studied in glass capillary microreactors of 0.5mm and 1mm inner diameter at different temperature

conditions and different residence times (by varying the gas flowrate and keeping the liquid flowrate constant). Reaction analysis was based on the analysis of the gas stream with gc, after quenching the reaction and separating the gas-liquid flow using a glass microseparator. Results showed that carbon dioxide conversion decreases with increasing gas flowrate (while keeping the liquid flowrate constant) due to the decrease of the liquid volume fraction (and hence the reaction volume as the reaction takes place only in the liquid phase). At constant gas and liquid flowrates, higher conversion of carbon dioxide was observed at higher temperatures due to the higher reaction rate constant at higher temperature.

Hydrodynamic study of the flow system was also performed and the flow characteristics, the residence time and the void fraction of the system were determined based on flow observation and residence time distribution experiments. The flow pattern under the operated conditions found to be slug-annular flow with long gas bubbles and thin liquid slugs in between. Bubble length found to increase with increase of the gas flowrate or with decrease of the capillary size. Moreover, the liquid film around the gas bubble found to become thicker when the gas flowrate increases (and hence as the capillary number increases), consistent with previous observations of Taylor's and Bretherton's first experiments [174,175]. Based on the flow observation results, the mass transfer characteristics of the system were determined based on van Baten and Krishna's correlation and it was concluded that the system does not suffer from mass transfer limitations (based on Hatta criterion) but is under kinetic control under the operated conditions. Furthermore, RTD experiments under different gas-to-liquid ratios showed that the dispersion number, $D/uL$, increases with gas-to-liquid ratio, consistent to previous studies [118], [176]. Another point worth noting is that as the gas to liquid ratio increases the factor A, required for the theoretical estimation of the void fraction of the system gradually increases. Specifically, it was found that Armand correlation can be accurately used

only for gas-to-liquid ratios below 3 while for higher ratios experimental measurement of the void fraction is necessaire.

Furthermore, a mathematical model was developed to simulate the reaction in the capillary reactor and its validity was confirmed with comparison with experimental results. The model predicted satisfactorily the experimental results in the whole range of operating conditions with deviations always smaller than 15%. Hence, it can be concluded that the reactor model can be further used for the simulation of other gas-liquid catalytic reaction in capillary reactors under slug-annular flow.

# CHAPTER 4. Hydrodynamic Study of Gas-Liquid Flow Systems in Microcapillaries

## 4.1 Introduction

When studying multiphase reaction systems, knowledge of the hydrodynamics of the system is essential as they affect significantly both the mass transfer and the heat transfer of the system, determining the reaction yield. The last decade many researchers [68-92] have focused on studying the hydrodynamics of multiphase systems in microchannels giving significant insight on the flow patterns, the void fraction and the pressure drop of the studied systems as well as the factors that affect these. In Table 2-2, hydrodynamic studies available in the literature on two phase-flow systems in micro and mini-channels are listed. However, these studies mainly focused in multiphase systems with moderate gas and liquid flowrates ($j_g$,$j_\ell$>0.4m/s), while no studies were found for lower gas and liquid velocities.

The objective of this study is to investigate experimentally the hydrodynamics of gas-liquid flow systems with very small gas and liquid superficial velocities (Figure 4.1) in circular microcapillaries. Gas and liquid superficial velocities were varied between 0.004-0.068m/s and 0.0001-0.102m/s respectively. Hydrodynamic characteristics such as the flow pattern, the void fraction and the residence time distribution were experimentally measured and their dependence on the fluid properties, the capillary diameter and the gas-to-liquid ratio was investigated. For this purpose, flow observation and residence time distribution measurements of various gas-liquid systems such as $N_2$/methanol, $N_2$/water and $N_2$/glycerol were conducted at a range of gas-to liquid ratios ($j_g$:$j_\ell$=0.66-40) in circular PFA capillaries with various inner diameters (ID=0.25, 0.5, 1mm).

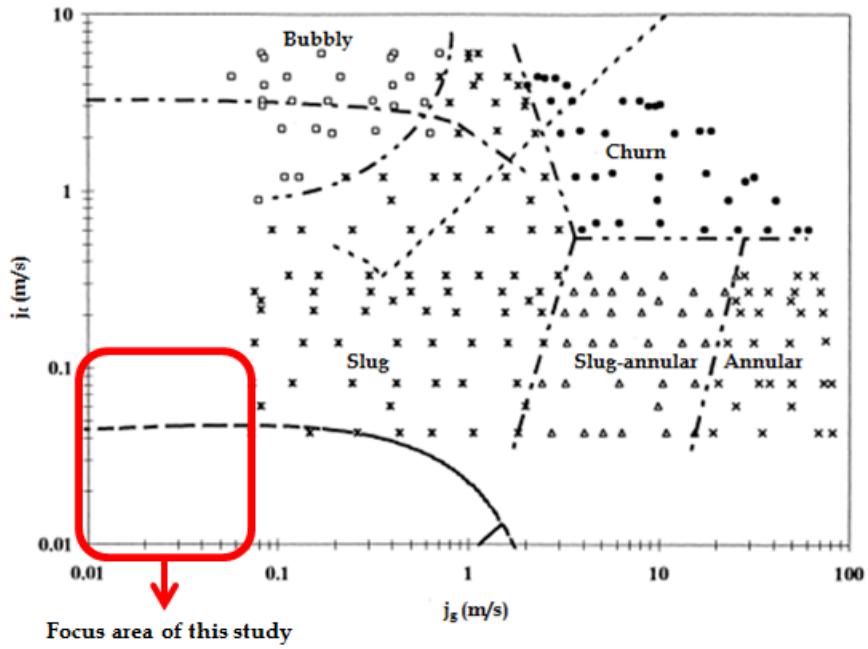


**Figure 4.1** *Range of gas and liquid superficial velocities used in this study compared to Triplett et al. [69]study in a 1mm circular capillary.*

The experimentally measured void fractions were then compared with published hydrodynamic models and a new correlation is suggested for the void fraction of $N_2$/water systems in circular capillaries with inner diameter 0.25-1mm.

## 4.2 Experimental Set-Up and Operating Conditions

A schematic diagram of the experimental set-up used for the hydrodynamic study is shown in Figure 4.2. The experiments conducted in circular PFA tubes with various inner diameters (0.25, 0.5, 1mm) under different gas to liquid ratios ($j_g$:$j_\ell$=0.66-40) in order to investigate different flow patterns. Gas was controlled by a mass flow controller (Brooks, T67438/001) while the liquid was delivered by a syringe pump. A pressure indicator (Comark, C9555, 0-30psi) was added in the inlet gas side to monitor the pressure during the experiments. Flow observation of the system was conducted by means of a microscope camera and the flow characteristics of the gas-liquid systems such as the liquid slug and the gas bubble length were recorded.

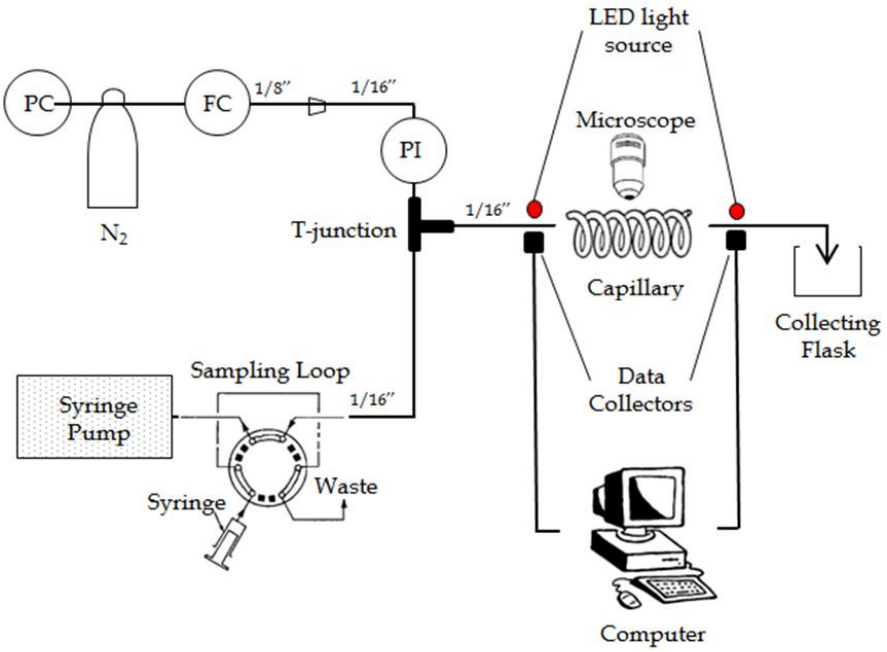


**Figure 4.2** *Schematic of the experimental set-up used for the hydrodynamic study of gas-liquid systems in circular microcapillaries.*

Furthermore, residence time distribution (RTD) experiments were conducted by introducing a step-input change on the liquid feed concentration and monitoring this change in the inlet and outlet of the reactor. The inlet step-input change on the liquid feed concentration was created by injecting a tracer with a syringe via a 6-port valve which was installed after the syringe pump. The concentration change was being monitored in the inlet and the outlet of the reactor by two infrared optical sensors. A great benefit of using IR sensors is that there is no sensitivity to the ambient light hence it is very easy to use compared to other sensors (e.g. linear diode array detectors) sensitive to ambient light, where the set-up has to be installed inside a box that prevents light transmittance (e.g wooden box used in Chapter 3.3.3) making the handling difficult. In this way, RTD experiments can be performed simultaneously with reaction experiments, measuring in that way the real residence time and reaction volume of a system under reaction. This has many advantages, as it takes into account changes in the flow behaviour along the reactor due to reaction (e.g decrease of gas flowrate) or flow anomalies along the reactor (e.g waves), which are not taken into account

when studying the hydrodynamics of a system off-line or when using relative hydrodynamic correlations.

All experiments were conducted at room temperature and atmospheric pressure. A picture of the experimental set-up is shown in Figure 4.3.

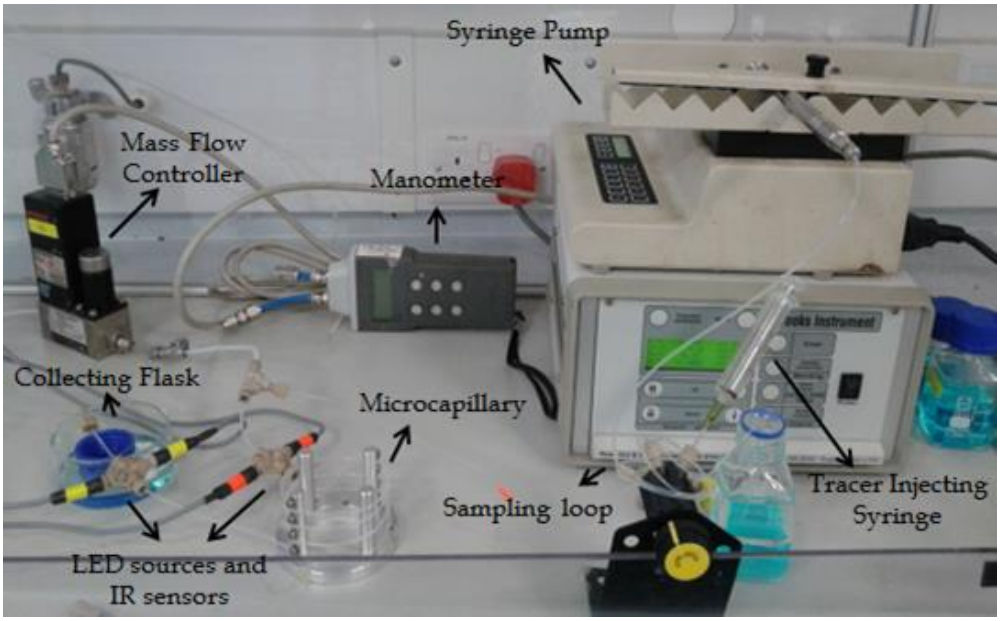


**Figure 4.3** *Picture of the experimental set-up for the hydrodynamic study of gas-liquid systems in circular microcapillaries.*

During the hydrodynamic study working fluids were nitrogen, deionised water, methanol and 10% aqueous glycerol which physical properties are shown in Table 4-1.

**Table 4-1** Physical properties of working fluids

| **Fluid** | **Density** $\rho(kg/m^3)$ | **Viscosity** $\mu(Pa \cdot s)$ | **Surface Tension** $\gamma(N/m)$ |
|---|---|---|---|
| **Deionized water** | 997 | 0.899 | 0.0720 |
| **Methanol** | 782 | 0.256 | 0.0221 |
| **Glycerol (10%)** | 1021 | 1.147 | 0.0705 |
| **Nitrogen** | 1.2 | 0.0179 | |

The gas mass flow controller was calibrated with nitrogen using a bubble meter at NTP conditions (20$^{o}$C, 1bar). The calibration results were also corrected for the moisture effect and the temperature effect based on (3.16**)**.

The calibration line of the mass flow controller is shown in the Appendix (Figure A. 3).

For the residence time distribution experiments, the choice of the tracer was based on the sensitivity of the optical sensors on the specific fluid. For this purpose, the sensors sensitivity for various fluids was plotted against the refractive index of these fluids. Refractive index is a dimensionless number and is characteristic to the fluid describing how light propagates through that fluid (Figure 4.4). A suitable tracer would be one for which the difference in detector's output between the main fluid and the tracer is significantly different.

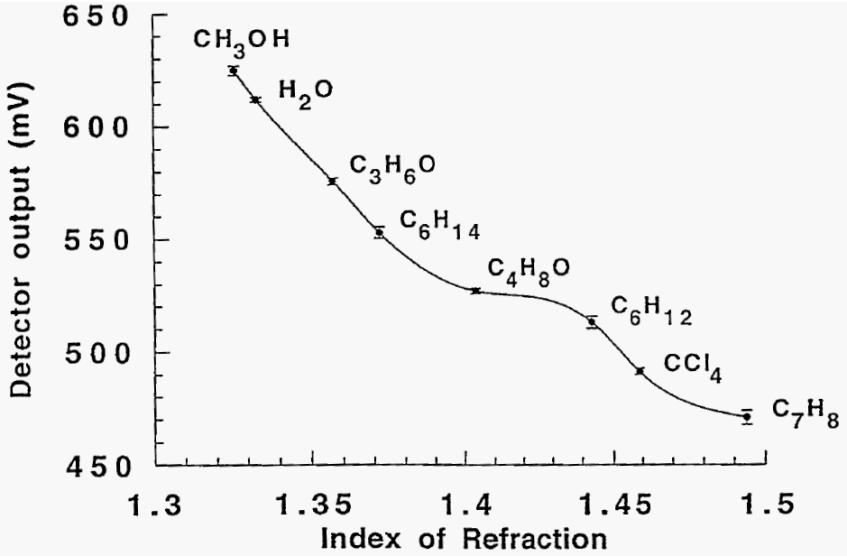


**Figure 4.4** *Sensitivity of optical sensor to different components [178].*

In order to obtain a clean step signal, toluene was chosen as the tracer when methanol was the working fluid and 0.3M $CuCO_4$ when 10% aqueous glycerol was the working fluid.

### 4.2.1 Residence Time Distribution Experiments: Method Analysis and Validation

The methodology followed for the analysis of the RTD signal has been described in detail in Chapter 2.3. In order the analysis methodology followed to be valid one should ensure that the system is in the dispersion

and not the convection region based on Figure 4.5. For this purpose, we consider the equivalent single phase (liquid only system) with inner diameter equal with the film thicken and fluid velocity the superficial velocity of the liquid. Hence, in Figure 4.5 L represents the length of the reactor (≈80-270cm in this study), dt is the liquid film thickness (≈30·10$^{-4}$cm), u is the superficial velocity of the liquid (≈0.01-0.2cm/s) and D is the dispersion coefficient of the liquid (1-5·10$^{-5}$cm$^2$/s). In our case it was found that the axial dispersion model can be used as shown in Figure 4.5.

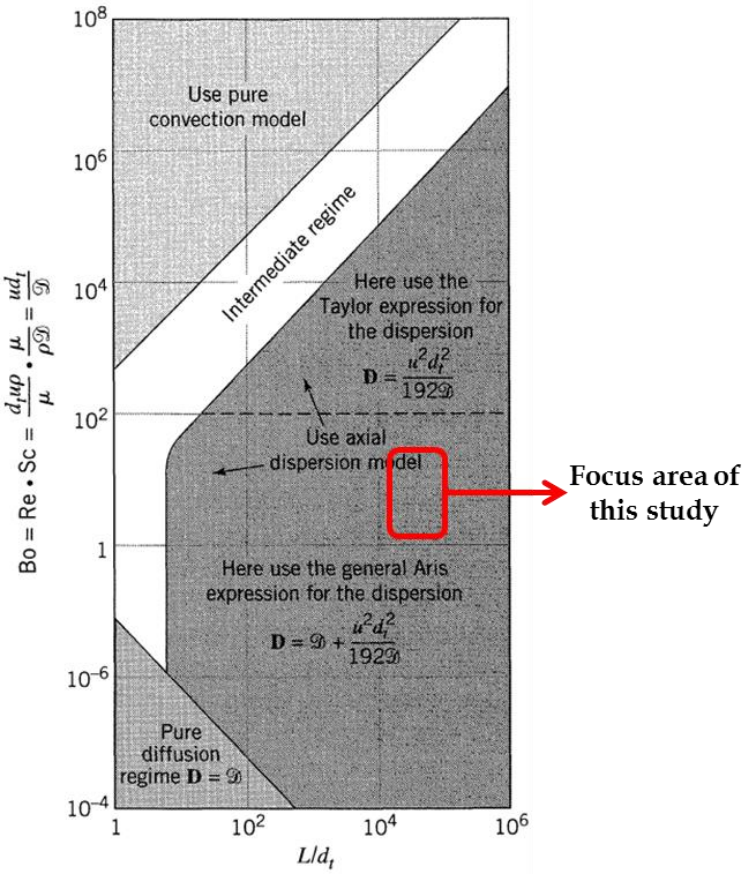


**Figure 4.5** *Flow model selection based on fluid properties, flow conditions and vessel geometry [8].*

Furthermore, it should be noted that this RTD study was based on the assumption that the inlet signal of the tracer is a very sharp step and hence no convolution of the inlet data was needed. This assumption enables a quicker and simpler data analysis and in the same time it was found that affected only slightly our results. Due to this simplification, the dispersion factor would be slightly smaller in reality than the one calculated from the

experiment. So this assumption results to the worst case scenario. However, it should be noted that the step-change in liquid concentration was monitored in the inlet of the capillary as well in order to define the time zero, the time when the tracer was reaching the inlet sensor.

Validation of the analysis methodology followed for the RTD experiments was conducted by performing single-phase experiments with only liquid flowing along the reactor. The volumetric flowrate of the liquid was set in the inlet (via the pump) and hence the liquid residence time was calculated based on (4.1).

$$\tau = \frac{V}{v} \tag{4.1}$$

The calculated residence time of the liquid was then compared with the experimentally measured one. This was repeated for a range of liquid flowrates and it was found that in all cases the deviation between the calculated and the experimental residence time of the liquid was always less than 5%, confirming the validity of this methodology.

## 4.3 Results

### 4.3.1 Flow Patterns

Flow observation of gas-liquid flow systems was conducted by means of a microscope camera in a PFA circular capillary of 1mm inner diameter. Firstly the effect of the fluid properties on the observed flow pattern was studied by observing two different gas-liquid systems, $N_2$/DI water and $N_2$/methanol. Water and methanol present different surface tension and viscosity as shown in Table 4-1. It should be also noted that PFA is highly wetted to methanol while only marginally wetted to water. Moreover, these two flow systems were studied at various gas-to-liquid ratios in order to investigate the effect of the gas-to-liquid ratio on the flow pattern. However, the amount of data collected was not enough to form a flow regime map.

In Figure 4.6 the observed flow patterns of the $N_2$/DI water system are presented for two gas-to-liquid ratios, 0.4 and 40 respectively.

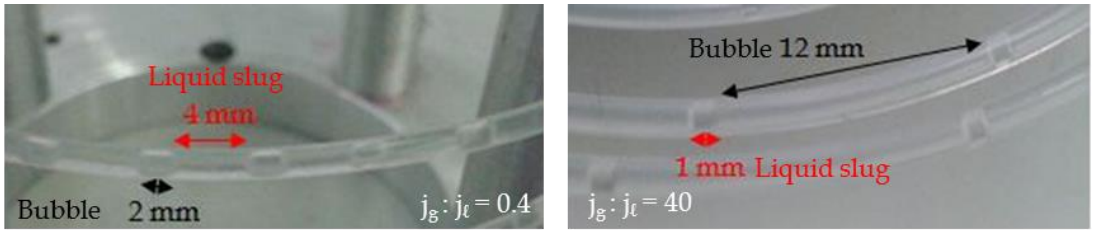


**Figure 4.6** *Observed flow patterns of the $N_2$/DI water system at different gas-to-liquid ratios ($v_g$=0.2ml/min, $v_\ell$=0.5ml/min on the left and $v_g$=0.2ml/min, $v_\ell$=0.005ml/min on the right) in a circular PFA capillary of 1mm inner diameter.*

When increasing the gas-to-liquid ratio, the flow pattern gradually changes from slug flow to slug-annular flow as these are defined in Chapter 2.3.1. More specifically, when the liquid flowrate decreases, while the gas flowrate remains constant, the liquid slug length decreases and the gas bubble length increases significantly.

In Figure 4.7 the observed flow patterns of the $N_2$/methanol system are presented for two gas-to-liquid ratios, 0.4 and 40 respectively. Slug-annular was the observed flow pattern in both cases with thin liquid slugs and very long gas bubbles.


**Figure 4.7** *Observed flow pattern of the $N_2$/methanol system at different gas-to-liquid ratios ($v_g$=0.2ml/min, $v_\ell$=0.5ml/min on the left and $v_g$=0.2ml/min, $v_\ell$=0.005ml/min on the right) in a circular PFA capillary of 1mm inner diameter.*

It was observed that as the gas-to-liquid ratio increases (by decreasing only the liquid flowrate), there is no flow pattern change even for a 100 times change in the gas-to-liquid ratio. However, as the gas-to-liquid ratio increases, the liquid slugs become thinner and less frequent. Flow patterns such as churn or annular flow were not observed in the range of velocities

used in this study as significantly larger gas velocities are required for the formation of these inertia-dominated flow regimes [93].

At high gas-to-liquid ratios, the $N_2$/methanol system showed much larger gas bubbles compared to the $N_2$/water system. This is due to the increased contact angle of water on the PFA surface that prevents the further spreading of the liquid on the wall and leads to the formation of frequent, short slugs, which was also observed by Barajas [73].

Furthermore, it was observed that the transition from slug flow to slug-annular flow moved to lower gas-to-liquid ratios (lower liquid superficial velocity when keeping constant gas superficial velocity) with decreasing surface tension ($\gamma_{methanol} = 0.0221 N/m < \gamma_{water} = 0.072 N/m$), in agreement with previous hydrodynamic studies in microchannels [82,96,179-181].

Hence, in the $N_2$/water system slug flow was observed for smaller gas-to-liquid ratios than in the $N_2$/methanol system, which is expected as when the surface tension of the system is large, the system in an attempt to minimise the energy, lowers the interfacial area between the gas and the liquid. In other words, earlier transition from slug to slug-annular is observed in decreasing surface tension as liquid is easier to break through in this case.

### 4.3.2 Residence Time Distribution Experiments

#### 4.3.2.1 Effect of Gas-to-Liquid Ratio on Dispersion Number

In order to study the effect of gas-to liquid ratio on the RTD and the dispersion of the liquid, RTD experiments of a N2/water system were performed at different gas-to-liquid ratios in circular PFA capillary of 1mm. The gas-to-liquid ratio was adjusted by increasing the liquid flowrate while keeping the gas flowrate constant. The F(t) curve in Figure 4.8 represents the normalised data of the original signal of the step-change in liquid concentration as recorded by the IR sensor in the outlet of the capillary. It should be noted that the F(t) curve in Figure 4.8 is plotted against the

normalised time for each experiment, using as basis the residence time of each experiment.

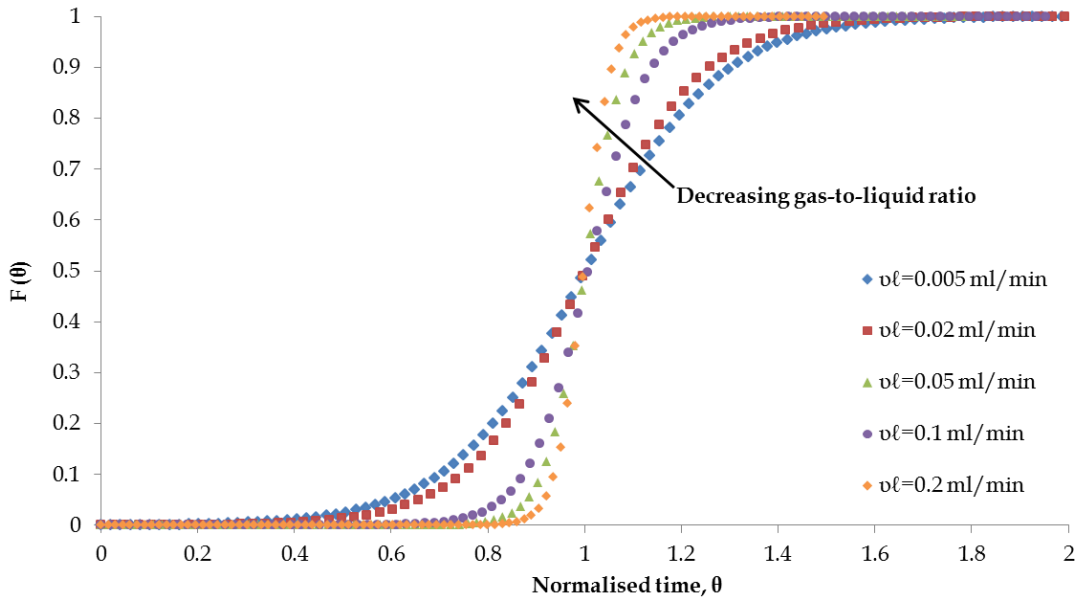


**Figure 4.8** *Experimental F curves for different liquid flowrates (vl) at constant gas flowrate ($\upsilon_g$=0.2ml/min) for a $N_2$/water system in a circular PFA capillary of 1mm inner diameter.*

In Figure 4.8, as the gas-to-liquid flowrate ratio decreases the curves become steeper indicating that the flow approaches plug flow behaviour. The dispersion number was calculated for each curved based on (4.2) [8],

$$dispersion\ number = \left(\frac{D}{j_\ell L}\right) \tag{4.2}$$

Where D is the dispersion coefficient, $j_\ell$ the superficial liquid velocity and L is the channel length. The flow can be considered plug when the dispersion number is smaller than 0.01 [8]. In the case of the $N_2$/water system, dispersion number found to be smaller than 0.01 for gas-to-liquid ratios smaller than 5. When the dispersion number is larger than 0.01, in the case of $N_2$/water for gas-to-liquid ratios above 5, axial dispersion becomes noticeable.

In Figure 4.9 the dispersion number of the system is shown as a function of the liquid flowrate (while the gas flowrate was kept constant) and as a function of the gas-to-liquid ratio.

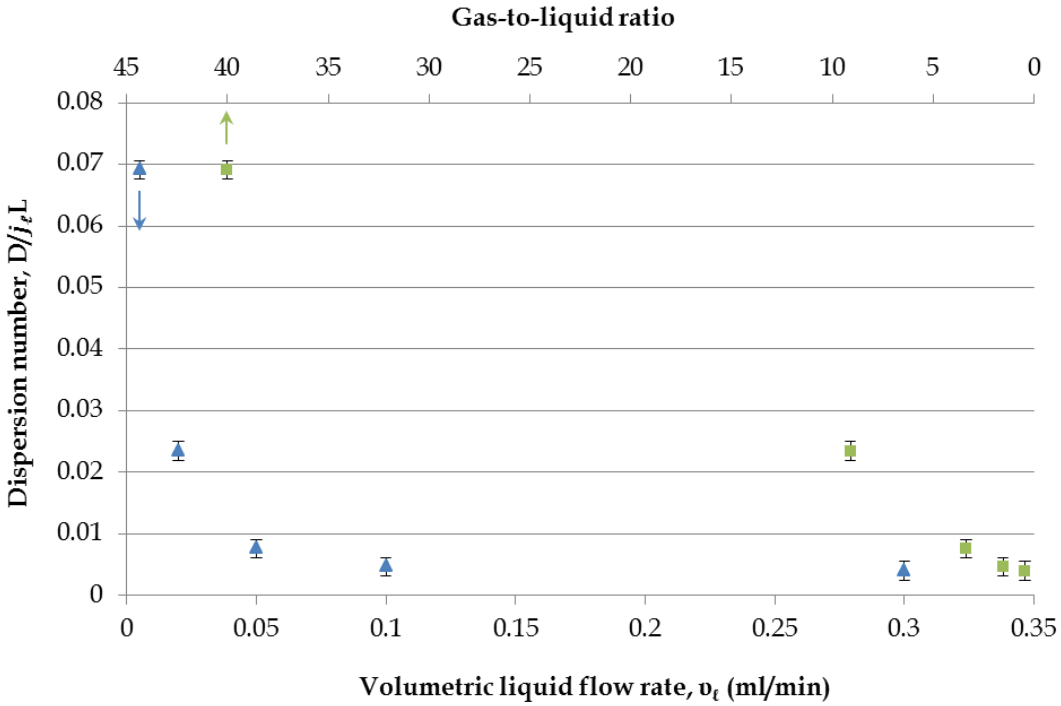


**Figure 4.9** *Dispersion number for different liquid flowrates at 0.2ml/min gas flowrate for a $N_2$/water system in a circular PFA capillary of 1mm inner diameter.*

The dispersion number increases sharply when decreasing the liquid flowrate, hence increasing the gas-to-liquid ratio. This could be explained by the fact that when the gas-to-liquid ratio is very large, the liquid slugs are very short and are followed by very long gas bubbles. This is leading to incomplete mass-exchange with the stagnant liquid film causing excessive broadening of the step change.

This behaviour has been observed also by Kreutzer et al. [182] who studied the effect of segmentation on dispersion in microchannels. They observed that dispersion is small when gas-to-liquid ratio is small, although their range of gas-to-liquid ratios was smaller, ranging between 0.1-2.1.

In this study the range of gas-to-liquid ratios was much wider ranging between 0.4-40 and it was observed that the dispersion number of the $N_2$/water system becomes significant ($D/j_\ell L>0.01$) for gas-to-liquid ratios

above 5, above which the flow starts deviating from the ideal plug flow behaviour.

Similar behaviour has been also reported in larger systems, when studying the hydrodynamic performance of gas-liquid systems related to residence time distribution in static mixers with inner diameter around 4cm [183]. They reported larger dispersion numbers when decreasing the liquid-side Reynolds number at constant gas-side Reynolds number. They attributed this behaviour to the lower liquid holdup at smaller liquid-side Reynolds numbers resulting in large dispersion numbers. At high gas velocities a competitive phenomenon it taking place as the average liquid velocities will increase resulting to smaller dispersion numbers.

#### 4.3.2.2 Effect of Fluid Properties on Dispersion Number

To study the effect of fluid properties on the dispersion, residence time distribution experiments were performed using two different fluids, DI water and a 10% aqueous solution of glycerol together with nitrogen in both cases. These fluids were chosen as they have similar surface tensions but different viscosities (Table 4-1).

The RTD curves of the two systems are shown in Figure 4.10. In both cases the liquid flowrate was equal to 0.3ml/min while the gas flowrate was set at 0.2ml/min and the capillary used for this study was made of PFA and its inner diameter was 1mm. It is clear that the $N_2$/glycerol system presents a steeper F-curve indicating a more plug flow behaviour than the $N_2$/water system. This is due to the increased viscosity of glycerol, as when nitrogen breaks through the glycerol slug (more viscous than water), more driving force is needed. Hence a thicker film of glycerol is formed around the nitrogen bubble compared to the $N_2$/water system at same velocities which results a lower dispersion number for the system. In other words, due to the increased viscosity, the capillary number of the system increases (Ca=0.079 for $N_2$/water system and Ca=0.105 for $N_2$/glycerol system), hence the film

thickness of the gas-liquid system increases [174,184] which leads to a smaller dispersion number for the system [185].

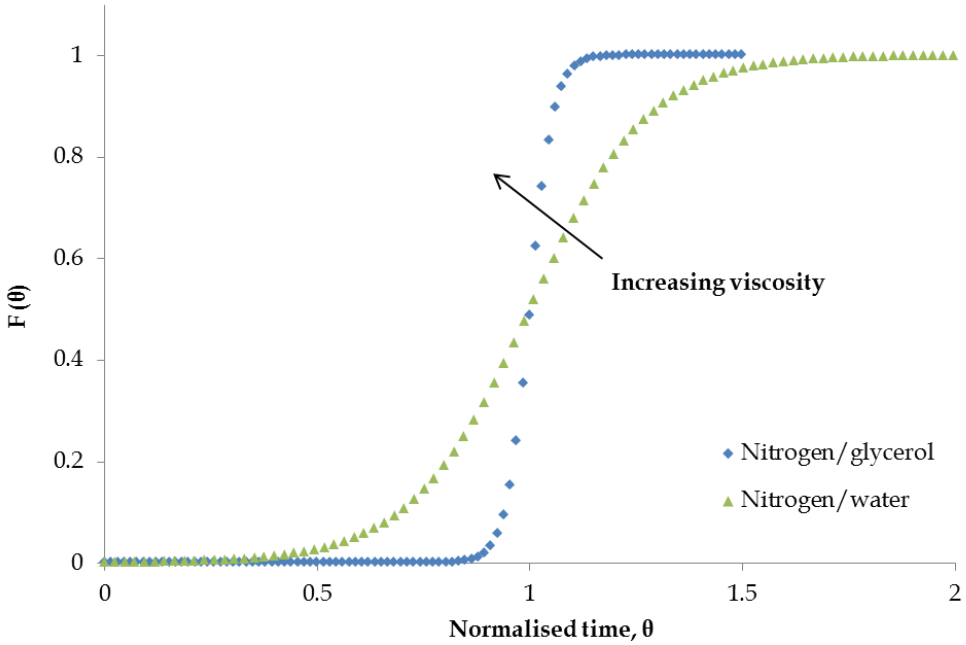


**Figure 4.10** *Experimental F curves for $N_2$/water (green line) and $N_2$/10% aqueous glycerol (blue line) at 0.3ml/min liquid flowrate and 0.2ml/min gas flowrate in a circular PFA capillary of 1mm inner diameter.*

This behaviour is in agreement with previous observations of Zhang et al. [179] who studied the effect of physical properties on gas-liquid hydrodynamics in glass microchannels with inner diameters ranging between 302-916μm. They found that the liquid film around the bubbles becomes thicker by increasing the fluid's viscosity or by decreasing its surface tension leading to less dispersion in the system.

Figure 4.11 shows the effect of liquid flowrate on the dispersion number for the two systems of different viscosity when keeping the gas flowrate constant. Glycerol shows smaller dispersion numbers for every liquid flowrate due to its larger viscosity compared to water that causes thicker films around the gas bubbles. This difference on dispersion numbers between the two fluids becomes bolder for smaller liquid flowrates, hence at large gas-to-liquid ratios. This is because at large gas-to-liquid flowrates the flow pattern moves to a more annulus-type flow pattern where the film

thickness becomes a more critical parameter for mass transfer in the capillary. On the contrary, as the gas-to-liquid ratio decreases (i.e. as the liquid flowrate increases in Figure 4.11) and moves to a more slug-type flow, the effect of viscosity gradually fades away.

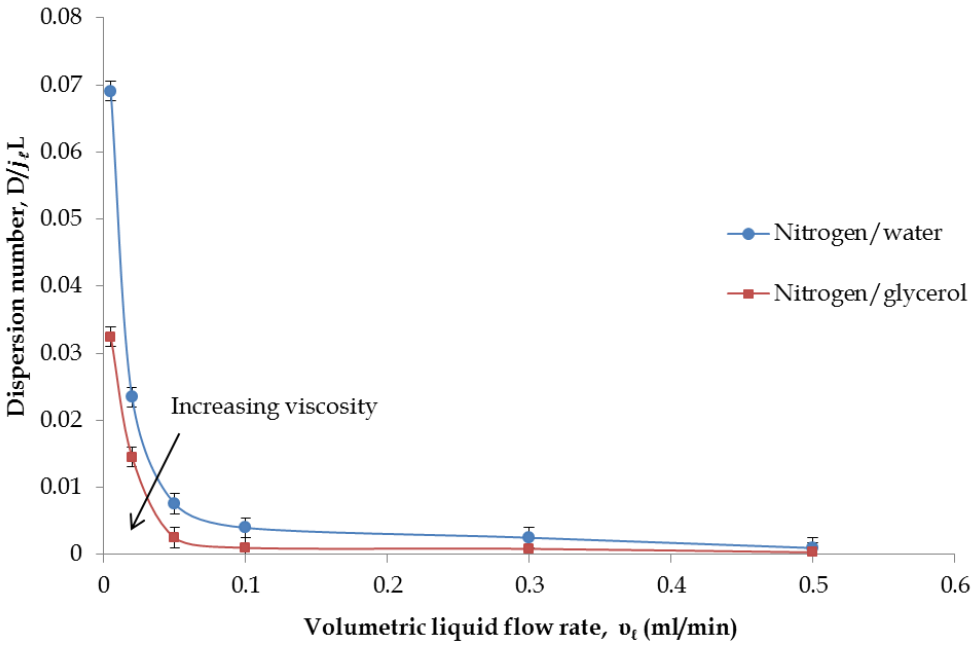


**Figure 4.11** *Dispersion number against liquid flowrate for $N_2$/water (blue line) and $N_2$/10% aqueous glycerol (red line) at 0.2ml/min gas flowrate in a PFA circular capillary of 1mm inner diameter.*

#### 4.3.2.3 Effect of Channel Size on Dispersion Number

The effect of the capillary diameter on the dispersion was studied by performing RTD experiments with a $N_2$/water system in capillaries of different inner diameters (Figure 4.12). Three capillary diameters were tested varying from 0.25, 0.5 and 1mm. The liquid and gas flowrates were kept constant in all cases at 0.1 and 0.2ml/min respectively.

Increasing the tube diameter, F curves become steeper, hence less dispersion is observed and the flow approaches a more plug flow type behaviour. This is because in larger tubes the velocities are smaller resulting to lower Reynolds numbers. And lower Reynolds numbers lead to decrease of the film thickness in slug-annular flow and consequently decrease of the dispersion in the system.

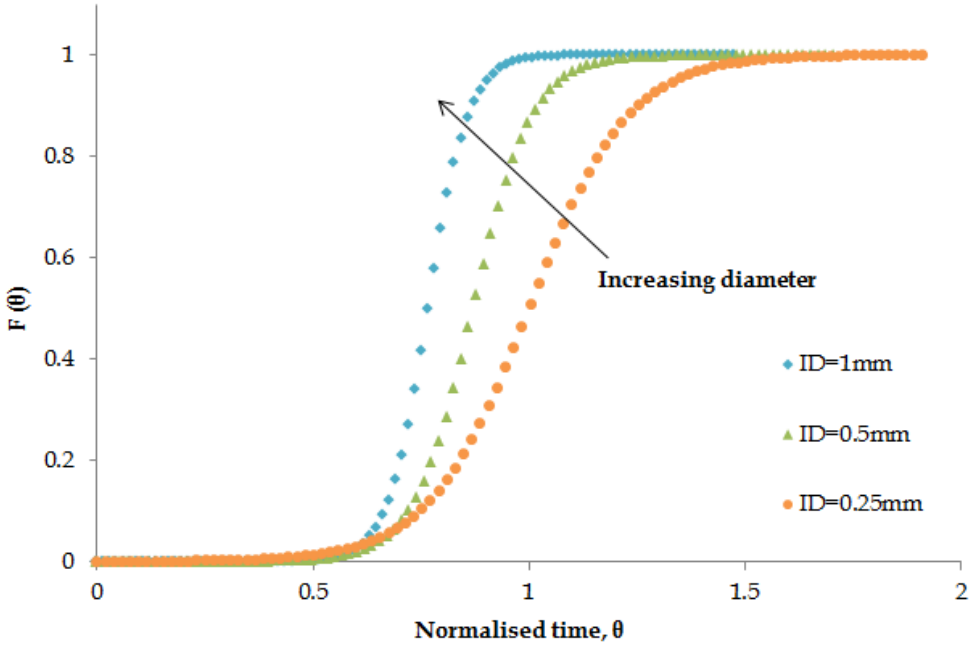


**Figure 4.12** *Experimental F curves of a $N_2$/water system in PFA circular capillaries of different inner diameters at 0.2ml/min gas flowrate and 0.1ml/min liquid flowrate.*

#### 4.3.2.4 Effect of Channel Size on Void Fraction

The effect of capillary diameter on void fraction was tested by performing RTD experiments for a $N_2$/water system in circular capillaries with inner diameters of 0.25, 0.5 and 1mm. The liquid flowrate was varied between 0.005-0.5ml/min while the gas flowrate was kept constant at 0.2ml/min. The void fraction of the system was estimated based on equation (4.3).

$$\varepsilon_g = 1 - \frac{\tau_\ell \cdot \upsilon_\ell}{V_{total}} \tag{4.3}$$

where $\tau_\ell$ is the liquid mean residence time calculated from the RTD experiments, $\upsilon_\ell$ is the liquid volumetric flowrate and $V_{total}$ is the reactor's volume.

Figure 4.13 shows the void fraction results for the different circular capillaries. The void fraction is plotted against a homogenous void fraction ($\beta = j_g/j_g + j_\ell$) with different symbols used for the different capillaries.

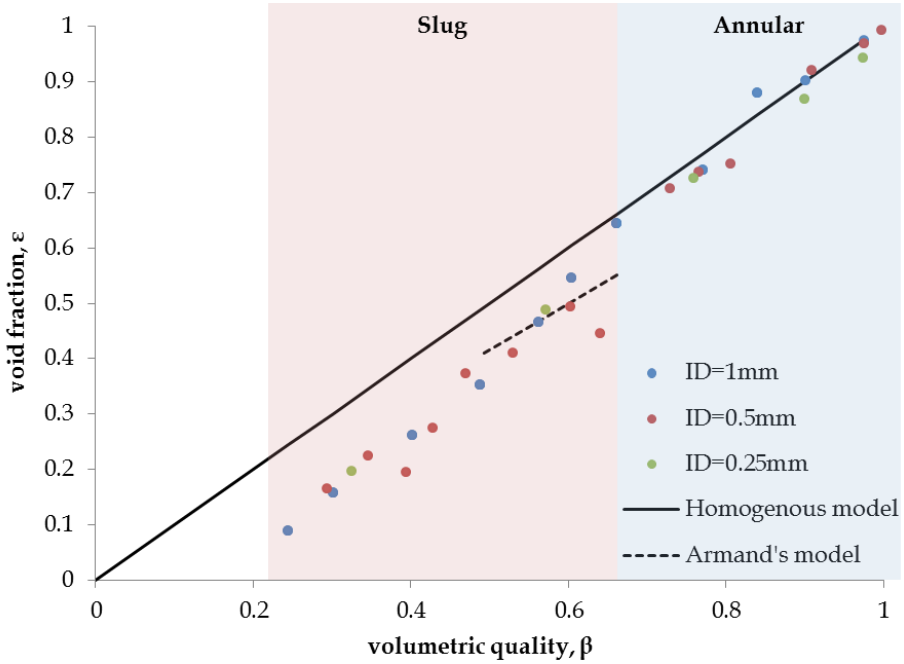


**Figure 4.13** *Void fraction of $N_2$/water against volumetric quality at 0.2ml/min gas flowrate in circular PFA capillaries of 0.25, 0.5 and 1mm inner diameter.*

It is clear that the void fraction is not strongly dependent on the diameter of the capillary.

The bold line in the figure represents homogenous model ($\varepsilon_g = \beta$ ) while the dashed curve corresponds to Armand's model [108] ($\varepsilon_g = 0.833 \cdot \beta$). Both homogenous and Armand's model provide linear relation for the void fraction. The void fraction in the present system seems to be well described by homogenous model for high volumetric qualities (β>0.65). As the volumetric quality decreases below 0.7, the void fraction deviates largely from homogenous model and can be better predicted by Armand's model. This behaviour can be explained by assuming that flow pattern changes from annular to slug flow (for β<0.65). Armand's model though is only applicable in a small range of volumetric qualities (0.65>β>0.45) [108]. Comparison with more hydrodynamic models available in the literature was performed but overall, no previous hydrodynamic model can describe our experimental data in the whole operating range (see Appendix, Figure A. 30).

For this reason, a new correlation was developed to fit the void fraction behaviour of a $N_2$/water system in the whole range of volumetric qualities in

circular capillaries of 0.25-1mm inner diameter. The correlation as shown in (4.4) is only a function of the volumetric quality, β.

$$\varepsilon_G = \frac{2\beta^{2.11}}{1+\beta^{2.11}} \quad \textbf{(4.4)}$$

In Figure 4.14 the void fraction predictions of the suggested correlation is plotted together with the experimental data of the $N_2$/water system.

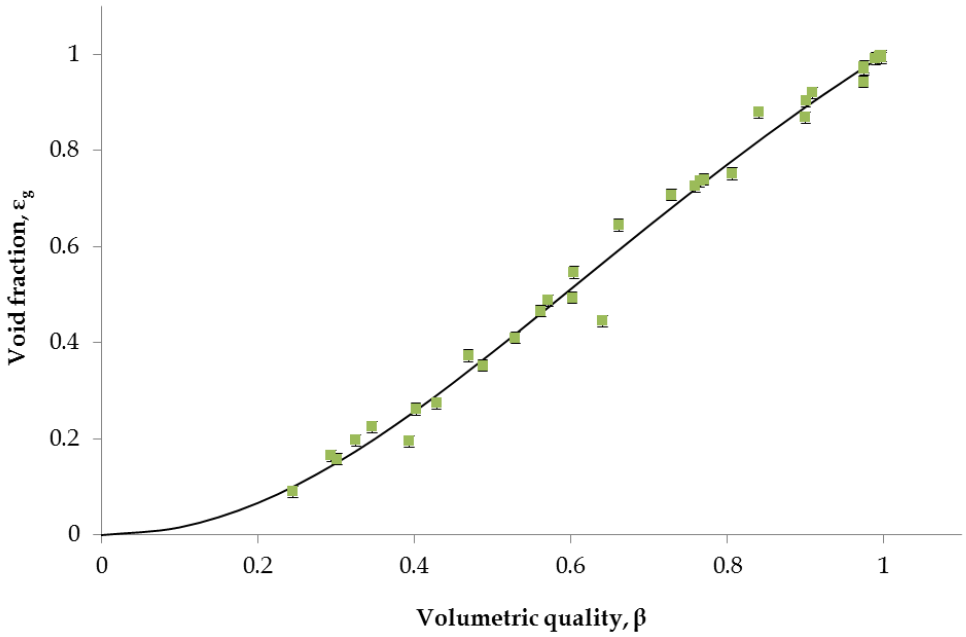


**Figure 4.14** *Fit of proposed correlation for the void fraction of $N_2$/water systems in circular PFA capillaries with inner diameter 0.25-1mm.*

The proposed correlation can fit the full set of the experimental void fraction data with great accuracy. This indicates that this correlation (4.4) can be used with confidence to predict the void fraction of a $N_2$/water system in circular capillaries with inner diameter 0.25-1mm.

#### 4.3.2.5 Effect of Fluid Properties on Void Fraction

The effect of fluid properties on void fraction was investigated by performing a series of RTD experiments with three different gas-liquid systems, $N_2$/water and $N_2$/methanol and N2/10% glycerol (in water). The liquid flowrate was varied between 0.005-0.8ml/min while the gas flowrate

was kept constant at 0.2ml/min. A circular PFA capillary was used in all experiments with 1mm inner diameter.

Figure 4.15 shows the void fraction results for the two different systems. The void fraction is plotted against liquid volumetric flowrate with different symbols used for the different gas-liquid systems.

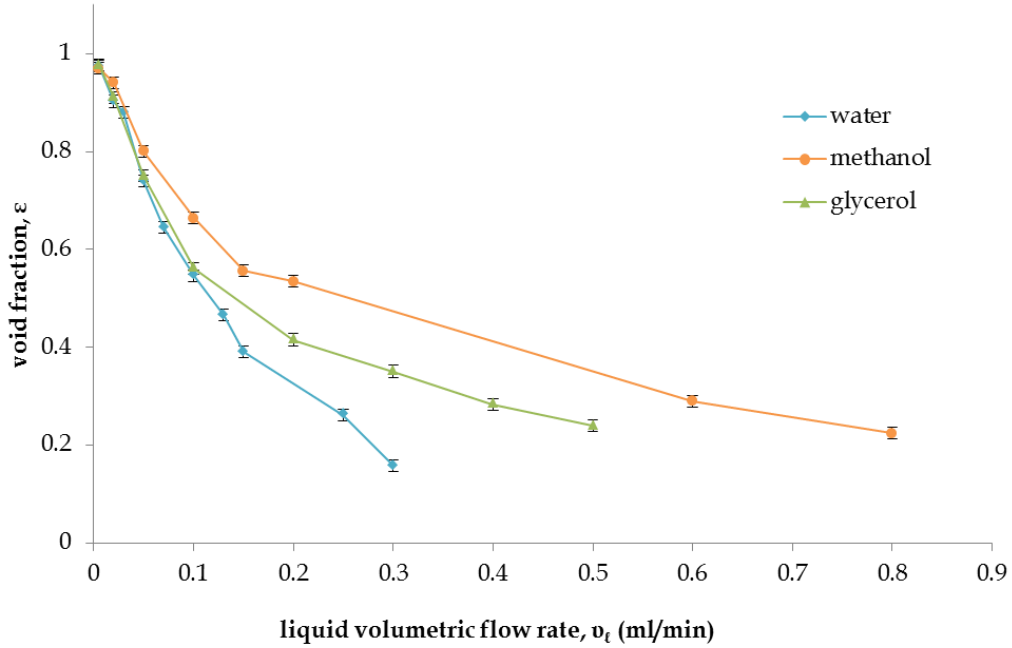


**Figure 4.15** *Void fraction of $N_2$/water (blue line), $N_2$/glycerol (green line) and $N_2$/methanol (orange line) against liquid flowrate at 0.2ml/min gas flowrate in a circular PFA capillary of 1mm.*

At very large void fractions (or very small liquid flowrates) the nature of the liquid does not seem to affect the void fraction of the system significantly. This is because the volume of liquid in the system in this case is very small and hence its effect is insignificant. However, when increasing the liquid flowrate (or decreasing the void fraction), the dependence of the fluid's nature on the void fraction becomes larger. Specifically, for a certain liquid flowrate, the void fraction of the $N_2$/methanol system is larger than the void fraction of the $N_2$/glycerol system which in turn is larger than the void fraction of the $N_2$/water system. The surface tension of methanol is much smaller of glycerol and water ($\gamma_{Methanol}$ =0.0221N/m, $\gamma_{Glycerol}$ =0.0705N/m, $\gamma_{Water}$ =0.072N/m). Hence, it appears that the lower the surface tension of

the fluid, the larger the void fraction of the system will be for certain gas and liquid velocities. This can be explained by the fact that when the surface tension of a system decreases, the dispersion number of the system decreases as well (as we observed earlier in Chapter 4.3.2.2). This effect becomes bolder at higher liquid flowrates (smaller void fractions) due to the increased amount of liquid in that case.

## 4.4 Conclusions

Hydrodynamic study of gas-liquid systems was performed experimentally in circular microcapillaries at very small gas and liquid superficial velocities. The capillaries were made of PFA and their diameter ranged between 0.25-1mm. Gas and liquid superficial velocities were varied between 0.004-0.068m/s and 0.0001-0.102m/s respectively. Hydrodynamic characteristics such as the flow pattern, the void fraction and the residence time distribution were experimentally measured and their dependence on the fluid properties, the capillary diameter and the gas-to-liquid ratio was investigated.

For this purpose flow observation of $N_2$/methanol and $N_2$/water was performed at a range of gas-to-liqiud ratios ($j_g$:$j_\ell$=0.66-40) in a circular PFA capillaries of 1mm inner diameter. It was found that at high gas-to-liquid ratios, the $N_2$/methanol system showed much larger gas bubbles compared to the $N_2$/water system. This was due to the increased contact angle of water on the PFA surface that prevented the further spreading of the liquid on the wall and led to the formation of frequent, short slugs, phenomenon which was also observed by Barajas [73]. Furthermore, it was observed that the transition from slug flow to slug-annular flow moved to lower gas-to-liquid ratios with decreasing surface tension, in agreement with previous studies [82,96,179-181].

Moreover, residence time distribution measurements of various gas-liquid systems such as $N_2$/methanol, $N_2$/water and $N_2$/ 10% glycerol (in water) were conducted at a range of gas-to liquid ratios ($j_g$:$j_\ell$=0.66-40) in circular

PFA capillaries with various inner diameters. It was found that as the gas-to-liquid flowrate ratio increases, axial dispersion in the system increases, behaviour also reported by Kreutzer et al. [182]. This was explained by the fact that when the gas-to-liquid ratio is very large, the liquid slugs are very short and followed by very long gas bubbles. This is leading to incomplete mass-exchange with the stagnant liquid film causing excessive broadening of the step change. In the case of the $N_2$/water system, it was found that axial dispersion becomes noticeable for gas-to-liquid ratios above 5.

Moreover, when increasing the viscosity of the liquid, less axial dispersion was observed in the system, behaviour also reported by Zhang et al. [179]. This was explained by the thicker film that was formed around the bubble, as the driving force of the gas to break through a more viscous liquid was larger leading to a smaller dispersion number [174,184,185]. This difference on dispersion numbers between two fluids with different viscosities found to become larger for smaller liquid flowrates, hence at large gas-to-liquid ratios. This is because at large gas-to-liquid flowrates the flow pattern moves to a more annulus-type flow pattern where the film thickness becomes a more critical parameter for mass transfer in the capillary. On the contrary, as the gas-to-liquid ratio decreases (i.e. as the liquid flowrate increases in Figure 4.11) and moves to a more slug-type flow, the effect of viscosity gradually fades away.

Furthermore, it was found that by increasing the tube diameter, less dispersion is observed in the system and the flow approaches a more plug flow type behaviour. This is because for the same gas and liquid flowrates, the superficial velocities are smaller in capillaries with larger diameters resulting to smaller Reynolds and capillary numbers leading to smaller dispersion numbers [183,185].

Moreover, experimental data of void fraction of a $N_2$/water system in capillaries with various inner diameters (0.25-1mm) in a range of gas-to

liquid ratios (0.3-400) showed that the void fraction is not strongly dependent on the inner diameter of the capillary in this range of diameters. The void fraction data of this system were well described by homogenous model at high volumetric qualities ($\beta>0.65$) and by Armand model for moderate volumetric qualities ($0.65>\beta>0.45$). As the volumetric quality decreased below 0.45, the void fraction deviated largely from both models and no other hydrodynamic model was well predictive either. For this purpose, a new correlation was developed which found to fit the full set of void fraction data with great accuracy.

Finally, it was observed that the nature of the liquid affect the void fraction only in very small gas-to-liquid ratios, when the amount of liquid in the system is hence not very small. It was found that the lower the surface tension of the liquid, the larger the void fraction of the system will be for certain gas and liquid velocities, due to the increased dispersion number in that case.

# CHAPTER 5. Methoxycarbonylation of Ethylene: Set-up Design and Preliminary Experiments

## 5.1 Introduction

In this chapter the design of the set-up for the kinetic study of methoxycarbonylation of ethylene is presented. The set-up can withstand elevated temperature and pressure conditions required for this reaction system and safety precautions are taken due to the poisonous nature of the reactants. The design of the reactor is discussed focusing on the material's choice, its permeability, reactivity and isothermality.

Residence time distribution studies were performed in order to determine the hydrodynamic characteristics of the system such as the void fraction and the residence time distribution under reaction conditions.

A reactor model was developed to describe the phenomena of reaction and mass transfer in the capillary reactor. Due to the high pressure of the system it was not feasible to collect experimental data directly at the inlet and outlet of the reactor. Instead experimental data for the outlet side for example were collected downstream after the gas and liquid were separated at ambient pressure and temperature conditions. A vapour-liquid equilibrium model was used to convert the experimental data to the conditions in the inlet and outlet of the reactor.

Blank experiments without catalyst in the feed and experiments at standard operating conditions were performed to validate the accuracy of the analysis methods and the system for an accurate kinetic study.

## 5.2 Experimental Set-Up Design for Kinetic Experiments

A flow set-up (Figure 5.1) that can withstand elevated temperature and pressure conditions (up to 12bara and 120$^{o}$C) was built for the kinetic study of methoxycarbonylation of ethylene by a homogenous Palladium based catalyst.

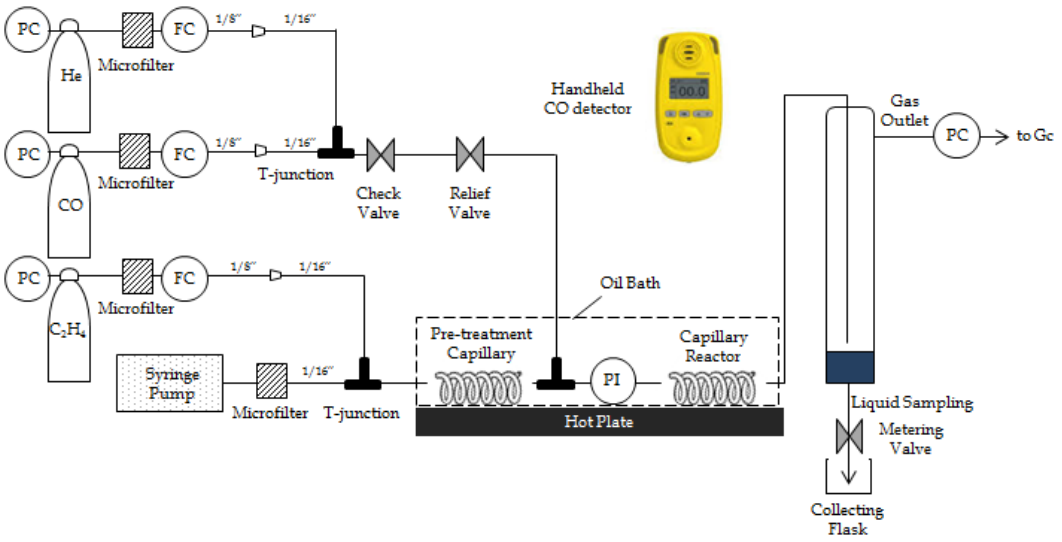


**Figure 5.1** *Schematic of the flow set-up for the kinetic study of methoxycarbonylation of ethylene at elevated temperature and pressure conditions.*

The gases were controlled by three mass flow controllers (up to $1ml_{25oC,1bar}/min$ for CO, up to $3ml_{25oC,1bar}/min$ for $C_2H_4$ and He) that can operate at pressures up to 12bar. Upstream of each mass flow controller particle microfilters were installed to prevent any particles from the cylinders to enter the set-up. In addition, downstream of each mass flow controller check valves were installed to prevent any liquid backflush. The mass flow controllers were calibrated by means of a bubble meter and equation (3.16) and their calibration line can be found in the Appendix (Figure A. 4-Figure A. 6).

A catalytic liquid mixture was prepared on site by diluting a 99:1 v/v MeP:MeOH catalytic solution (provided by Lucite International) with methanol and methyl propionate to the desired concentration. The final catalytic mixture contained 5.86ppm Palladium and had a molar ratio of

1:5:450 in Pd:Alpha ligand:Methanesulfonic acid. The mixture was prepared in a glove box under argon atmosphere to prevent catalyst deactivation by oxygen poisoning (Appendix J). Then, the liquid was added in a stainless steel syringe of 8ml and was delivered to the reactor after passing a liquid filter for particles above 10μm.

The liquid stream was added to the ethylene stream via a T-junction and flowed through a pre-treatment section at 100$^{o}$C. The pre-treatment section consisted of a 2m long Hastelloy capillary with 1.75mm inner diameter and 1/8in outer diameter. After the pre-treatment section, carbon monoxide was introduced to the system via a T-junction and the gas-liquid mixture entered the reactor at 100$^{o}$C where the reaction begun. The pressure was always kept constant at 10bara via a back pressure regulator.

The reactor was a 6m long Hastelloy capillary with 1mm inner diameter and 1/16in outer diameter. The reactor was tested for its isothermality and permeability as well as its surface reactivity (Appendix J). It was concluded that no fluoropolymer tubing (i.e. PFA, ETFE, PEEK, Halar, ECTFE) was suitable for the kinetic study of the MeP system as they are permeable to ethylene at elevated temperature. Hastelloy however found to be suitable for this kinetic study, as it is not permeable to any of the reactants even at elevated temperature and it provides an inert and hence non-reactive internal surface.

Both capillaries for pre-treatment and reaction were placed in an oil bath with a stirrer on a hot plate to control the temperature.

After the reactor the gas-liquid mixture entered a gravity-based separator made of stainless steel. The liquid exited from the bottom of the separator, where a metering valve helped to achieve a more controlled and smooth liquid sampling without sudden pressure drops. The gas exited from the top of the separator and passed through the back pressure regulator (BPR, Brooks 5866) that maintained the pressure of the system at the desired value.

The gas exiting the separator was analysed online using gas chromatography (GC). A liquid trap was placed before the GC in order to prevent any liquid entering the GC. The gas flowrate in the outlet was measured by a bubble meter. More details on the analysis methodology and calibration can be found in the Appendix J. Reproducibility of the gas phase analysis found equal to 0.5%, while for the liquid phase analysis equal to 2%.

The pressure of the system was monitored by means of a pressure transducer installed at the inlet of the reactor. The calibration of the pressure transducer can be found in the Appendix (Figure A. 7). The set-up was regularly checked for leaks by pressurising the set-up at 12bar with helium in order to ensure that the system is not leaking.

The standard operating procedure employed for the experiments can be found in the Appendix (Appendix J).

Blank experiments without catalyst in the feed and experiments at standard operating conditions were performed (Appendix J). The carbon balance closed within 3% difference, validating the accuracy of the analysis methods and the system for an accurate kinetic study.

## 5.3 Residence Time Distribution Studies under Reaction Conditions

Residence time distribution (RTD) studies of the gas-liquid system were conducted under reaction conditions. Based on residence time distribution experiments, information for the mean residence time of the liquid, the void fraction and the mixing quality of the system were collected under reaction conditions. In this way, effects such as changes in the flow behaviour along the reactor due to reaction (e.g decrease of gas flowrate) or flow anomalies along the reactor (e.g waves) were taken into account, which would be

impossible to do if studying the hydrodynamics of the system under non-reactive conditions or if using relative hydrodynamic correlations.

Residence time distribution (RTD) experiments were performed by means of two optical (IR) sensors (Chapter 4.2) that were installed just before and after the reactor. A step-change of the liquid feed concentration was introduced to the reactor by a 6-port valve (that was installed just after the syringe pump) and the change of this step-change was monitored by the two optical sensors in the inlet and the outlet of the reactor. More information about the methodology followed and the underlying theory can be found in Chapter 4.2.1 where the same methods were used for the hydrodynamic analysis of a much simpler, non-reactive gas-liquid system.

For the step-change of the liquid feed concentration methanol was used as the tracer which will not disturb the system as it is already present as one of the reactants in the system. The effect of the tracer on the RTD results has been studied further and the results can be found in Appendix J.

RTD experiments were conducted under different gas to liquid ratios. Gas to liquid ratios ranged from 23 to 222. The reactor design and operating conditions are the same as previously. The purpose of these experiments was to investigate the hydrodynamics of the MeP system in order to decide the conditions for the kinetic study. The main criteria were the gas-liquid system to present plug flow behaviour, no mass transfer resistances and liquid residence time enough for accurate measurement of reaction performance.

Four different sets of gas, liquid flowrates and gas-liquid ratios were tested (Table 5-1).

**Table 5-1** Gas and liquid flowrates at reactor's conditions (100°C, 10bara) for the different cases tested.

| Case | A | B | C | D |
|---|---|---|---|---|
| **$\upsilon_g$ (ml/min)** | 0.178 | 0.277 | 0.271 | 0.182 |
| **$\upsilon_\ell$ (ml/min)** | 0.0077 | 0.0083 | 0.00144 | 0.00082 |
| **g/ℓ ratio** | 23 | 33 | 188 | 222 |
| **Flow pattern** | Slug-annular | Slug-annular | Annular | Annular |
| **Liquid slug length (mm)** | <2 | <2 | - | - |
| **Bubble length (cm)** | 20 | 30 | 600 | 600 |

For case A, the observed flow pattern was slug-annular with $L_{bubble}$>20cm and $L_{slug}$<2mm. The flow for case B was slug-annular with elongated bubbles ($L_{bubble}$>30cm) and relatively short liquid slugs ($L_{slug}$<2mm), while for cases C and D, the observed flow pattern was pure annular flow with no appearance of liquid slugs. It should be noted that the flow observation was performed at 25°C and that at reaction conditions (100°C) it is expected the flow to be closer to annular flow in all cases. The results of the RTD experiments for cases A-D are shown in Table 5-2.

**Table 5-2** Results of RTD experiments for different gas-liquid ratios.

| Case | Gas-liquid ratio | Mean liquid residence time, $\tau_\ell$ (min) | Dispersion factor, D/uL | Void fraction, ε | Film Thickness (μm) | Void fraction prefactor, A |
|---|---|---|---|---|---|---|
| **A** | 23 | 45.2 | 0.003 | 0.926 | 19 | 0.949 |
| **B** | 33 | 30.5 | 0.006 | 0.946 | 14 | 0.956 |
| **C** | 188 | 63.9 | 0.023 | 0.98 | 5 | 0.979 |
| **D** | 222 | 89 | 0.026 | 0.984 | 4 | 0.985 |

Liquid residence time (reaction time) up to ca. 90min was obtained with the current reactor design, enough for accurate reaction performance measurements during the kinetic study. For cases A and B the flow satisfied the plug flow criterion ($D/uL<0.01$) while for cases C and D the flow deviated from plug flow behaviour.

The void fraction, $\varepsilon$, found to increase as the gas-to-liquid ratio increases, due to the increase of the gas volume and/or decrease of liquid volume. The liquid film thickness was calculated for each case based on the RTD results and found to decrease as the gas-to-liquid ratio increases. This is because as the gas-to-liquid ratio increases, the gas moves faster (in comparison with the liquid), pushing the liquid towards the walls, creating a thinner liquid film around the bubbles. Moreover, it is worth noting that the void fraction prefactor, A, does not remain constant as the gas-to-liquid ratio increases but increases. Specifically, as the gas-to-liquid ratio increases, the void fraction prefactor approaches the homogenous model prediction.

It was concluded that the flowrates of case A are the most suitable for the kinetic study as it fulfils all the criteria and is the quicker one.

## 5.5 Analysis Methodology and Reactor Model

In Figure 5.2 a simplified schematic of the experimental set-up for the kinetic experiments is shown that highlights where the composition of the gas and liquid streams change either because of a temperature change (resulting to a new vapour-liquid equilibrium) or because of reaction.

For the kinetic study, the gas and liquid composition and the flowrates are required at the inlet and outlet of the reactor (point 1 and 2 in Figure 5.2). However, in our flow set-up it was not feasible to analyse the gas and liquid streams directly at these points due to the elevated pressure. Instead, experimental data were collected in the feed of the set-up (point 0 in Figure 5.2) and in the outlets of the gas and the liquid (point 4 and point 5 in Figure

5.2), based on which the conditions in the separator (point 3 in Figure 5.2) were determined.

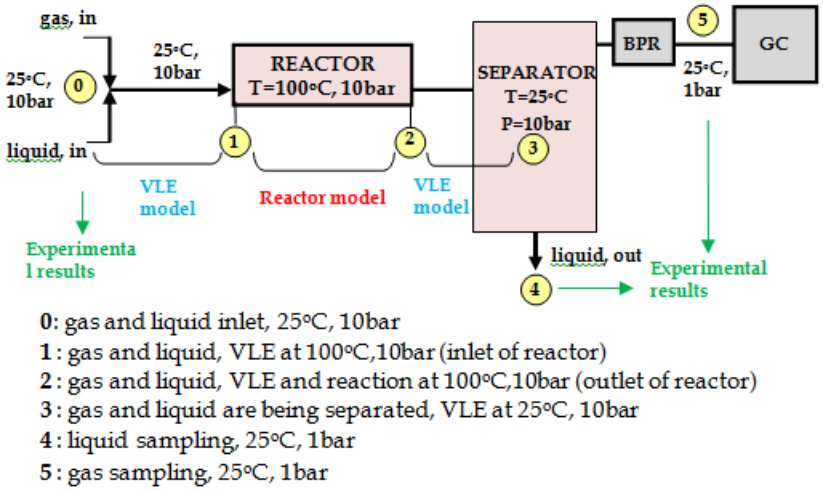


**Figure 5.2** *Simplified schematic of the experimental set-up for kinetic experiments demonstrating the main points where gas and liquid composition changes either because of temperature change (new VLE) or because of reaction.*

In order to estimate the compositions of the gas and liquid streams in the inlet and outlet of the reactor (at point 1 and 2) based on experimental data at point 0 and 3 a vapour-liquid equilibrium (VLE) model was used as new VLE was established due to the different temperature conditions between these points. More details on the VLE model can be found in the Appendix J.

The reactor model previously developed and validated with a model system (carbon dioxide absorption in buffer solutions-Chapter 3), is now applied for the MeP system to be able to describe the change of the molar flowrates of all components (CO, $C_2H_4$, MeOH, MeP) in both gas and liquid phases along the reactor. The reactor model was based on (5.1) and (5.2) which were solved using gPROMS.

$$\frac{1}{A_c}\frac{dF_i^{\ell}}{dx} = v_i \cdot rxn(z) \cdot \varepsilon^{\ell} + k_{\ell}a \cdot \left(\frac{C_i^{g}}{K_i} - C_i^{\ell}\right) \tag{5.1}$$

$$\frac{1}{A_c}\frac{dF_i^{g}}{dx} = -k_{\ell}a\left(\frac{C_i^{g}}{K_i} - C_i^{\ell}\right) \tag{5.2}$$

where, $C_i^\ell$ and $C_i^g$ and $F_i^\ell$ and $F_i^g$ are the concentrations (mol/ml) and the molar flowrates (mol/min) of component i (MeOH, MeP, CO, $C_2H_4$) in the liquid and in the gas phase respectively, x is the axial coordinate, $A_c$ is the cross sectional area ($cm^2$), $v_i$ is the reaction stoichiometric coefficient (equal with -1 for the reactants and with 1 for the products), $rxn(z)$ is the reaction rate (mol/ml min), $\varepsilon^\ell$ is the liquid volume fraction of the system, $k_\ell\alpha$ is the mass transfer coefficient ($min^{-1}$) of the system and $K_i$ is the gas-liquid equilibrium constant. The actual reactor model in gPROMS is given in Appendix E. The boundary conditions for (5.1) and (5.2) were the known molar flowrates of all components in the inlet of the reactor (point 1, Figure 5.2) calculated by means of the VLE model and the experimental results in the inlet of the set-up (point 0, Figure 5.2).

The liquid side volumetric mass transfer coefficient $k_\ell\alpha$ was estimated by van Baten and Krishna [105] model shown in (5.3).

$$k_\ell\alpha = k_{\ell,cap}\alpha_{cap} + k_{\ell,film}\alpha_{film} = 2\frac{\sqrt{2}}{\pi}\sqrt{\frac{Du_B}{d}}\frac{4}{L_{UC}} + 3.41\frac{D}{\delta_{film}}\frac{4\varepsilon_g}{d} \qquad \textbf{(5.3)}$$

The system found to be under kinetic control (Appendix J). It is worth noting that as the reaction is very slow, the value of the mass transfer coefficient does not affect the results.

The value of $\varepsilon^\ell$ was determined by residence time distribution experiments. The value of the equilibrium constant $K_i$ was calculated by (5.4) for carbon monoxide and ethylene and (5.5) for methanol and methyl propionate by means of the VLE model at the inlet conditions of the reactor.

$$K_i = \frac{\gamma_i \cdot He_i \cdot v^\ell}{F_i^\ell \cdot R \cdot T} \qquad \textbf{(5.4)}$$

$$K_i = \frac{\gamma_i \cdot P_i^{vap} \cdot v^\ell}{F_i^\ell \cdot R \cdot T} \qquad \textbf{(5.5)}$$

where $\gamma_i$ is the activity coefficient (-), $He_i$ is the Henry's constant (bar), $P_i^{vap}$ is the vapour pressure (bar) of component i, $\upsilon^{\ell}$ is the total liquid volumetric flowrate (ml/min) and $F_t^{\ell}$ is the total molar flowrate (mol/min) of the liquid phase. It was assumed that $K_i$ remains constant along the reactor, as the liquid volumetric flowrate, the temperature and the pressure of the system did not change significantly along the reactor.

## 5.6 Conclusions

The design of a high-pressure set-up for the kinetic study of methoxycarbonylation of ethylene was discussed in detail. Methods for the analysis of gas and liquid phase by gas chromatography were developed and validated. The design of the reactor was discussed focusing on the material's choice, its permeability, reactivity and isothermality.

Residence time distribution (RTD) studies were performed at different gas-to-liquid ratios under reaction conditions to determine the residence time of the liquid, the void fraction and the mixing quality of the system under reaction. Liquid residence time (reaction time) up to ca. 90min was obtained with the current reactor design, enough for accurate reaction performance measurements during the kinetic study. The flow found to satisfy the plug flow criterion for gas-to-liquid ratios below 33 while for larger ratios the flow deviated from lug flow behaviour.

The void fraction of the system found to increase as the gas-to-liquid ratio increased, due to the increase of the gas volume and/or decrease of liquid volume. The liquid film also decreased as the gas-to-liquid ratio increased. Moreover, the void fraction prefactor did not remain constant as the gas-to-liquid ratio increases but increased. It was concluded that a gas-to-liquid ratio of 23 is the most suitable for the kinetic study as it provides enough residence time for the reaction and results to plug flow behaviour.

The reactor model that will be applied to describe the phenomena of reaction and mass transfer in the capillary reactor in this kinetic study was presented. A vapour-liquid equilibrium model will be used to convert the experimental data to the conditions in the inlet and the outlet of the reactor.

# CHAPTER 6. Kinetic Study of Methoxycarbonylation of Ethylene: Experiments and Modelling

## 6.1 Introduction

In this chapter, the kinetic study of methoxycarbonylation of ethylene is presented in a flow system. The main aim is the development of a rate expression that describes accurately the effect of methanol, ethylene and carbon monoxide concentration and of temperature over a wide range of conditions. Experiments are performed in a Hastelloy capillary microreactor of 1mm inner diameter and 6m length. The experimental conditions include a temperature range of 80-120$^{o}$C, gas inlet molar ratio ethylene-to-carbon monoxide range of 1.25-10 and a liquid inlet concentration range of 22-90% wt. methanol-to-methyl propionate while pressure is kept constant at 10bara. The catalyst used in this study is the homogeneous [Pd(d$^{t}$bpx)(dba)] (dba=trans, trans-(PhCH=CH)$_2$CO) that was developed by Lucite International is capable of converting ethylene, carbon monoxide and methanol to methyl propionate at a rate of 50000 mol of product per mol of catalyst per hour with a selectivity of 99.98% [132,134].

A mechanistic kinetic model that can describe satisfactorily the system's behaviour is developed based on the Palladium hydride catalytic cycle. Parameter estimation of the kinetic model is performed in order to achieve good fit of the experimental data. The accuracy of the estimation is evaluated using statistical tools. Information analysis is also performed to evaluate how informative the experimental data were for the model parameters estimation.

## 6.2 Experimental

### 6.2.1 Experimental Set-up

A series of kinetic experiments of methoxycarbonylation of ethylene were performed in a flow set-up in order to study. The purpose of these experiments was to study the effect of various parameters, such as the reactants concentration and temperature effect on the kinetics of the system.

The flow set-up used for these experiments is shown in Figure 6.1 and can withstand elevated temperature and pressure conditions (up to 12bara and 120$^{o}$C). The gases were controlled by three mass flow controllers (up to 1ml$_{25oC,1bar}$/min for CO, up to 3ml$_{25oC,1bar}$/min for $C_2H_4$ and He) that can operate at pressures up to 12bar. Upstream of each mass flow controller particle microfilters were installed to prevent any particles from the cylinders to enter the set-up. In addition, downstream of each mass flow controller check valves were installed to prevent any liquid backflush. The mass flow controllers were calibrated by means of a bubble meter and equation (3.16) and their calibration line can be found in the Appendix (Figure A. 4-Figure A. 6).

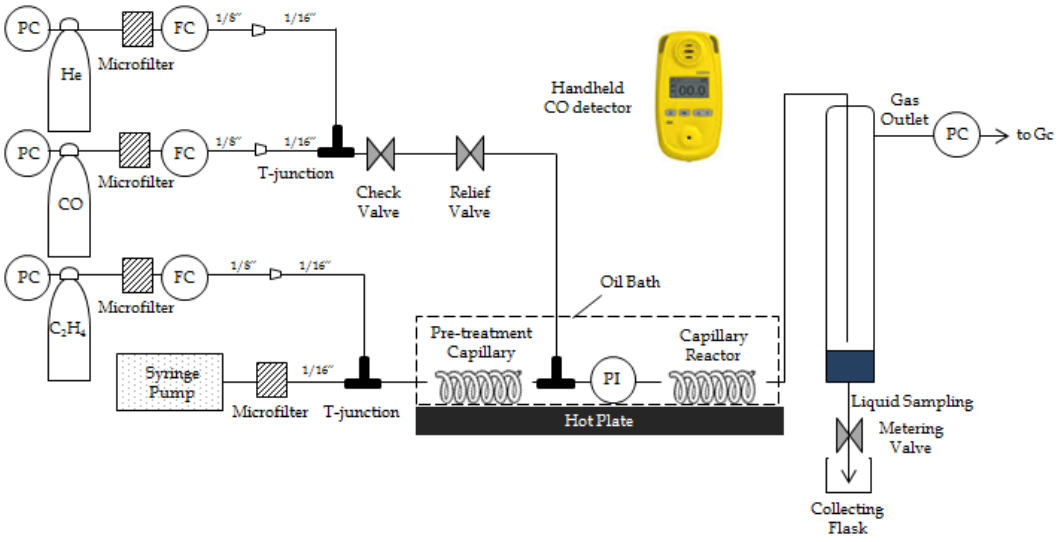


**Figure 6.1** *Schematic of the flow set-up for the kinetic study of methoxycarbonylation of ethylene at elevated temperature and pressure conditions.*

The liquid feed was added in a stainless steel syringe of 8ml and was delivered to the reactor after passing a liquid filter for particles above 10μm.

The liquid stream was added to the ethylene stream via a T-junction and flowed through a pre-treatment section at 100$^{o}$C. The pre-treatment section consisted of a 2m long Hastelloy capillary with 1.75mm inner diameter and 1/8in outer diameter. After the pre-treatment section, carbon monoxide was introduced to the system via a T-junction and the gas-liquid mixture entered the reactor at 100$^{o}$C where the reaction begun. The pressure was always kept constant at 10bara via a back pressure regulator. The reactor was a 6m long Hastelloy capillary with 1mm inner diameter and 1/16in outer diameter. Both capillaries for pre-treatment and reaction were placed in an oil bath with a stirrer on a hot plate to control the temperature.

After the reactor the gas-liquid mixture entered a gravity-based separator made of stainless steel. The liquid exited from the bottom of the separator, where a metering valve helped to achieve a more controlled and smooth liquid sampling without sudden pressure drops. The gas exited from the top of the separator and passed through the back pressure regulator (BPR, Brooks 5866) that maintained the pressure of the system at the desired value. The gas exiting the separator was analysed online using gas chromatography (GC). A liquid trap was placed before the GC in order to prevent any liquid entering the GC. The gas flowrate in the outlet was measured by a bubble meter.

The pressure of the system was monitored by means of a pressure transducer installed at the inlet of the reactor. The calibration of the pressure transducer can be found in the Appendix (Figure A. 7).

The set-up was regularly checked for leaks by pressurising the set-up at 12bar with helium in order to ensure that the system is not leaking.

The standard operating procedure employed for the experiments can be found in the Appendix (Appendix E).

### 6.2.2 Operating Conditions

The kinetic study of methoxycarbonylation of ethylene was performed at 100$^{o}$C and at 10bara. Gas and liquid flowrates were kept constant in all cases at 0.1ml$_{25oC,10bara}$/min and 0.005ml/min respectively. A 99:1 v/v MeP:MeOH catalytic solution was provided by Lucite International and consists of the catalyst [Pd(d$^{t}$bpx)(dba)] (dba=trans, trans-(PhCH=CH)$_2$CO). This catalyst was developed by Lucite International and is capable of converting ethylene, carbon monoxide and methanol to methyl propionate at a rate of 50000 mol of product per mol of catalyst per hour with a selectivity of 99.98% [132,134]. The catalyst solution was then diluted with methanol and methyl propionate to the desired concentration in %wt. MeP:MeOH. This preparation was performed in a glove box under Argon atmosphere to avoid any catalyst deactivation with contact with air. This is because its preparation under air atmosphere results to deactivation of the catalyst due to the oxygen from the atmosphere dissolving in the liquid mixture, oxidising and deactivating the catalyst. For the same reason, the solutions of methanol and methyl propionate used for the catalyst solution were first degassed with Argon to remove any dissolved oxygen. The final catalytic mixture contained 5.86ppm Palladium and had a molar ratio of 1:5:450 in Pd:Alpha ligand:Methanesulfonic acid. The catalyst concentration was equal to $1.3 \cdot 10^{-3}$ mol/L in all cases.

## 6.3 Kinetic Experiments

### 6.3.1 Dependence of Reaction Rate on Methanol Concentration

In order to study the effect of methanol concentration on the reaction rate liquid solution concentrations in the feed ranged between 22-90%wt. MeOH:MeP. Gas concentration in the feed was kept constant at 10%v/v

$CO:C_2H_4$ in all cases. Gas and liquid flowrates were kept constant in all cases at $0.1ml_{25oC,10bara}/min$ and 0.005ml/min respectively. The experimental conditions for the methanol series experiments are shown in Table 6-1.

**Table 6-1** Experimental conditions for the methanol series experiments.

| | |
|---|---|
| **Temperature:** | 100°C |
| **Pressure:** | 10bara |
| **CO feed partial pressure:** | 1bara |
| **Ethylene feed partial pressure:** | 9bara |
| **Liquid feed concentration:** | 22-90%wt. MeOH: MeP |
| **Pd catalyst concentration:** | $1.3 \cdot 10^{-3}$ mol/L |
| **Gas feed volumetric flowrate** | $0.1ml_{25oC,10bara}/min$ |
| **Liquid feed volumetric flowrate** | 0.005ml/min |

The results of the methanol series experiments are shown in Figure 6.2.

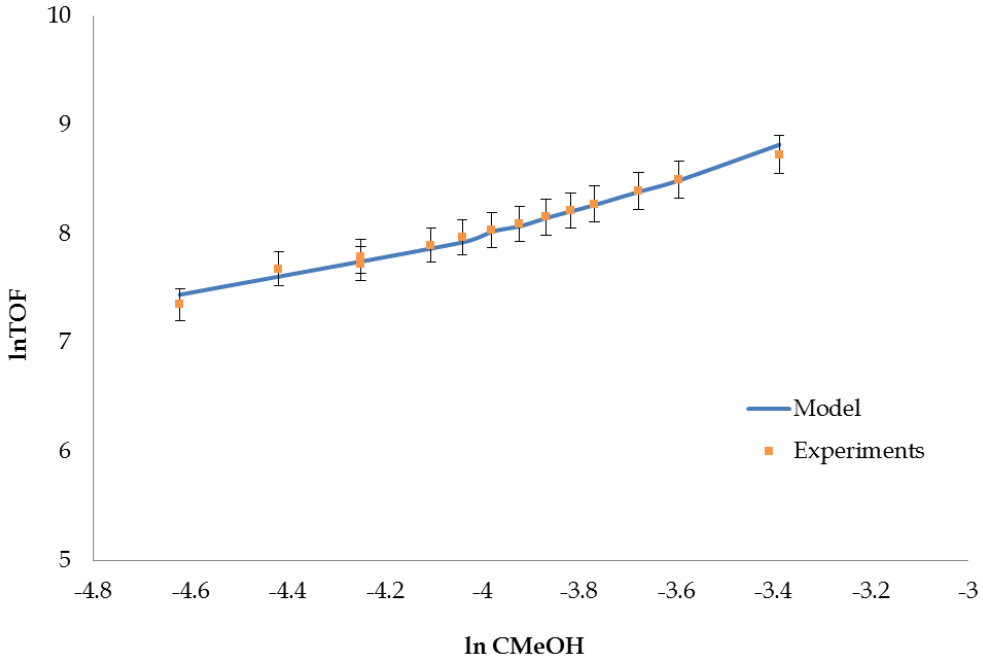


**Figure 6.2** *Effect of methanol concentration on turnover frequency for a gas feed stream of 10%v/v $CO:C_2H_4$ at 100°C, 10bara.*

The observed reaction was measured by means of the turn over frequency (TOF) which is defined by (6.1),

$$TOF = \frac{mol\ MeP\ produced}{mol\ Pd\ inlet\ \cdot hr} \quad \textbf{(6.1)}$$

The data are presented as classical log-log plots for methanol concentration at the outlet of the reactor. It was assumed that there was not significant change of concentration along the reactor length due to the small conversions observed. Conversions data for the experiments reported in this chapter can be found in the Appendix J. The error stated in the graph is based on the reproducibility of the liquid analysis and corresponds to 95% confidence.

Although methanol was in excess in these experiments, it has a great effect on the observed reaction rate. This may indicate that methanol attack of the ethyl carbonylated complex is not very fast or favoured. In this case a higher concentration in solution increases the chance of an attack of methanol on the complex and influences the overall reaction rate in this way. As the sensitivity to methanol concentration appears high, this probably indicates that it is the slowest step. This was also observed by Zacchini who carried out NMR spectroscopic studies for the methoxycarbonylation of ethylene promoted by the Palladium catalyst, [Pd(d$^t$bpx)(dba)] [136]. This observation is supported by other researchers as well who studied the methoxycarbonylation of higher α-olefins [186-188] or the hydroformulation of alkenes [189,190].

The analysis of these data has been completed by carrying out a regression of the reaction rate against methanol concentration. The data provided an order in methanol concentration close to unity. This correlation is only valid between methanol concentrations of 22-90%wt. MeOH:MeP.

### 6.3.2 Dependence of Reaction Rate on Ethylene Concentration

For the ethylene series experiments ethylene concentration in the feed ranged between 23-83%vol. by means of helium acting as the diluting inert

gas. Carbon monoxide concentration in the feed was always constant at 10%vol. by means of helium as the diluting gas. The liquid concentration in the feed was kept constant at 30%wt. MeOH:MeP. The main reason for this choice of reaction mixture composition is that it has been shown that decomposition of the catalyst is slower when the level of methanol in the reaction mixture is low. Gas and liquid flowrates were kept constant in all cases at $0.1ml_{25oC,10bara}/min$ and 0.005ml/min respectively. The experimental conditions are shown in Table 6-2.

**Table 6-2** Experimental conditions for the ethylene series experiments.

| | |
|---|---|
| **Temperature:** | 100°C |
| **Pressure:** | 10bara |
| **CO feed partial pressure:** | 1bara |
| **Ethylene feed partial pressure:** | 2.3-8.3bara |
| **Liquid feed concentration:** | 30%wt. MeOH: MeP |
| **Pd catalyst concentration:** | $1.3 \cdot 10^{-3}$ mol/L |
| **Gas feed volumetric flowrate** | $0.1ml_{25oC,10bara}/min$ |
| **Liquid feed volumetric flowrate** | 0.005ml/min |

The results are shown in Figure 6.3 where the lnTOF is plotted against the concentration of ethylene in the outlet of the reactor. In this range of operating conditions ethylene appears to have no significant effect on the reaction rate. The lack of any effect with ethylene concentration is attributed to its high solubility and the fast mass transfer of the system. Typical concentration of carbon monoxide in the liquid phase at reaction conditions are ca. 0.04% while of ethylene ca. 2.4%. Hence, it is expected that the concentration of ethylene in the solution is not changing very much since it is always saturated and in excess. Similar behaviour has been also reported by Seayad [191] who studied the carbonylation of styrene using a homogenous Pd-complex catalyst and observed zero-order with respect to the styrene.

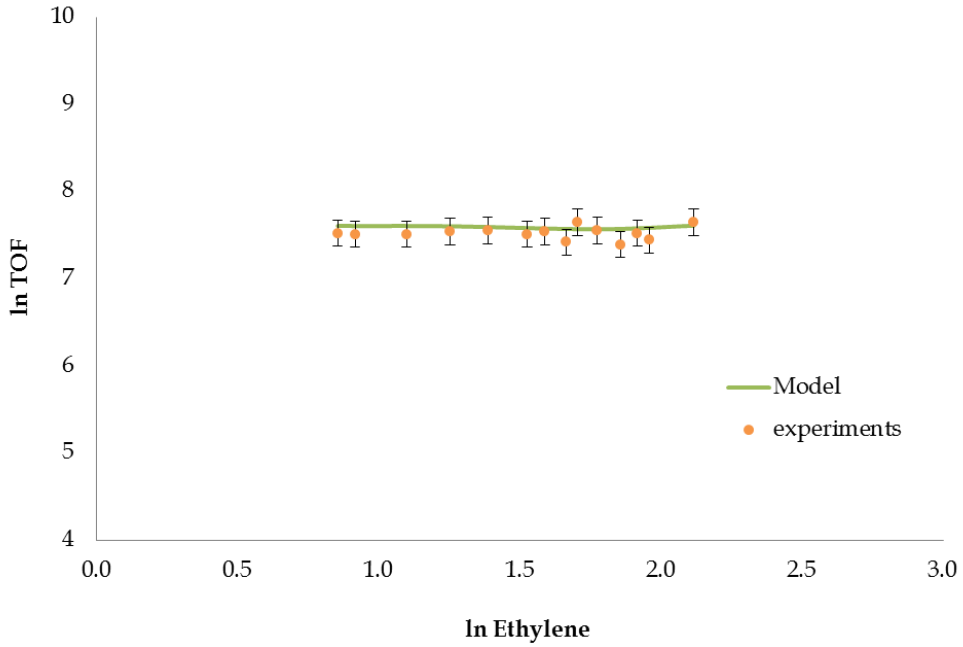


**Figure 6.3** *Effect of ethylene concentration on turnover frequency for a liquid feed stream of 30%wt. MeOH:MeP and 10%vol. CO in the gas feed at 100°C, 10bara.*

### 6.3.3 Dependence of Reaction Rate on Carbon Monoxide Concentration

The effect of carbon monoxide concentration on the reaction rate was investigated by keeping constant the liquid concentration in the feed at 30%wt. MeOH:MeP while ethylene concentration in the feed was always constant at 50%vol. Carbon monoxide concentration in the feed was ranged between 5-40%vol. by means of an inert diluting gas, helium. Gas and liquid flowrates were kept constant in all cases at $0.1ml_{25oC,10bara}/min$ and 0.005ml/min respectively. The experimental conditions for the carbon monoxide series experiments are shown in Table 6-3.

In Figure 6.4 the data which reflect the measured dependence of reaction rate on carbon monoxide concentration in the outlet of the reactor are presented graphically.

**Table 6-3** Experimental conditions for the carbon monoxide series experiments.

| | |
|---|---|
| **Temperature:** | 100°C |
| **Pressure:** | 10bara |
| **CO feed partial pressure:** | 0.5-4bara |
| **Ethylene feed partial pressure:** | 5bara |
| **Liquid feed concentration:** | 30%wt. MeOH: MeP |
| **Pd catalyst concentration:** | $1.3 \cdot 10^{-3}$ mol/L |
| **Gas feed volumetric flowrate** | $0.1 ml_{25oC,10bara}$/min |
| **Liquid feed volumetric flowrate** | 0.005ml/min |

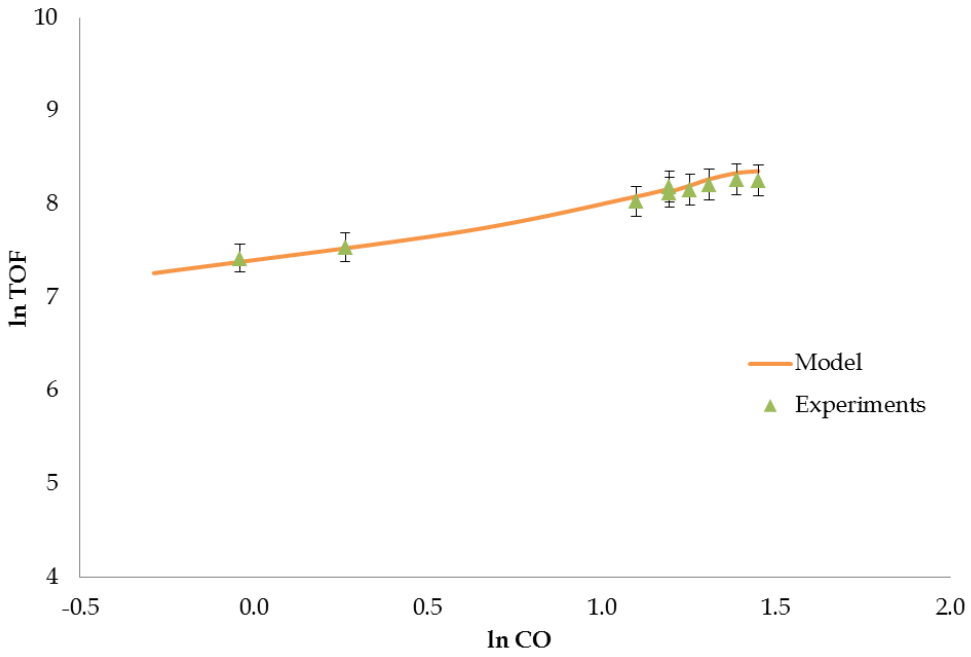


**Figure 6.4** *Effect of carbon monoxide concentration on turnover frequency for a liquid feed stream of 30%wt. MeOH:MeP and 50%vol. $C_2H_4$ in the gas feed at 100°C, 10bara.*

In previous studies of this reaction system, negative effect of carbon monoxide concentration on reaction rate has been observed at high carbon monoxide concentrations due to poisoning of the catalyst by carbon monoxide species [192,193]. The decomposition reaction is believed to occur

when carbon monoxide reacts with the palladium hydride complex before ethylene addition as shown in equations (6.2)-(6.5).

$$(L-L)Pd(H)]^{+} + CO \overset{K_1}{\leftrightarrow} (L-L)Pd(H)(CO) \quad \textbf{(6.2)}$$

$$(L-L)Pd(H)(CO) + CO \overset{K_2}{\leftrightarrow} (L-L)Pd(CO)_2 + H^{+} \quad \textbf{(6.3)}$$

$$(L-L)Pd(CO)_2 + CO \overset{K_3}{\leftrightarrow} (L-L)Pd(CO)_3 \quad \textbf{(6.4)}$$

$$(L-L)Pd(CO)_3 + CO \overset{K_4}{\leftrightarrow} Pd(CO)_4 \downarrow \quad \textbf{(6.5)}$$

This rapidly leads to reduction of the palladium to palladium (0) which has a greater tendency to form clusters. Similar deactivation of the catalyst by carbon monoxide molecules has been reported in other reactions such as the hydroformulation of ethylene using a Rd-complex catalyst [194,195], the hydroformulation of 1-decane using a Rd-complex catalyst [190].

However no sign of catalyst poisoning by carbon monoxide appeared in our study most probably because of the very high catalyst concentrations used in this study (about 10 times larger than in previous studies [192,193]. This means that if there were any loss of catalyst due to poisoning it would be unlikely to impact the rate very much.

### 6.3.4 Dependence of Reaction Rate on Temperature

A series of experiments was conducted in order to establish the temperature effect on the reaction rate. The experimental conditions for the carbon monoxide series experiments are shown in Table 6-4. The reactor temperature range investigated was between 80-120$^{o}$C. In all cases the liquid feed composition was 30:70%wt. MeOH:MeP while the gas feed composition was 10%wt. CO:$C_2H_4$. Gas and liquid flowrates were kept constant in all cases at $0.1ml_{25oC,10bara}$/min and 0.005ml/min respectively.

**Table 6-4** Experimental conditions for the temperature series experiments.

| **Temperature:** | **80-120°C** |
|---|---|
| **Pressure:** | 10bara |
| **CO feed partial pressure:** | 1bara |
| **Ethylene feed partial pressure:** | 9bara |
| **Liquid feed concentration:** | 30%wt. MeOH: MeP |
| **Pd catalyst concentration:** | $1.3 \cdot 10^{-3}$ mol/L |
| **Gas feed volumetric flowrate** | $0.1ml_{25oC,10bara}/min$ |
| **Liquid feed volumetric flowrate** | 0.005ml/min |

The results of the temperature effect series are shown in Figure 6.5.

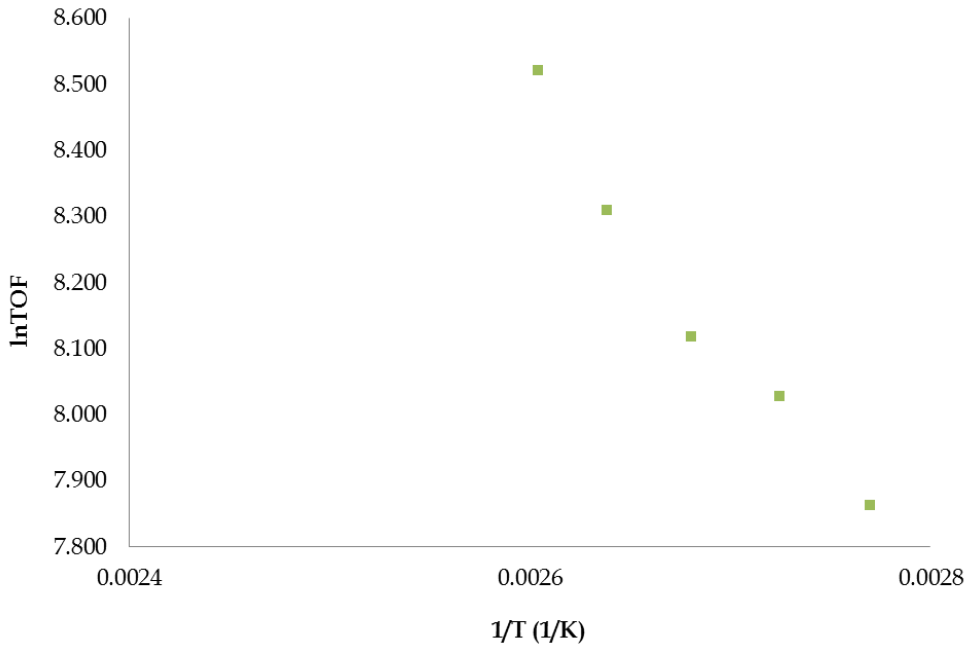


**Figure 6.5** *Effect of temperature on turnover frequency for a liquid and gas feed stream of 30%wt. MeOH:MeP and 10%vol.CO:$C_2H_4$ respectively at 10bara.*

The turnover frequency increases when increasing the temperature of the reactor (and hence decreasing 1/T). However, it should be noted that when the temperature changes the composition in the gas and the liquid changes according to the new vapour liquid equilibrium. Hence, these observations

are a result of the temperature change as well as the gas and liquid composition change.

## 6.4 Kinetic Modeling and Parameter Estimation

### 6.1 Reaction Mechanism and Kinetic Models Discretisation

There are three possible kinetic models for the formation of methyl propionate based on the Pd-Hydride cycle (Figure 6.6) [196].

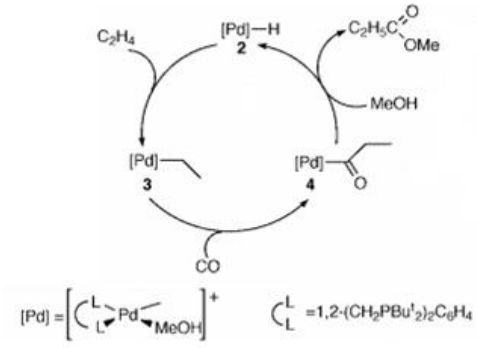


**Figure 6.6** *Palladium-Hydride catalytic cycle for the formation of methyl propionate.*

This depends on which reaction step (i.e the methanolysis step, the addition of ethylene or the addition of carbon monoxide) we consider as the rate determining step. All three kinetic models will be developed and examined with respect to how well they fit the experimental observations and data of the system.

The main assumptions for these models are the following:

- The Pd-Hydride cycle (Figure 6.6) is the predominant cycle [196].
- The reverse reaction of the MeP decomposition resulting in the formation of CO, C2H4 and MeOH is negligible.
- The quasi-state approximation was used for the analysis which assumes that the intermediate complexes formed are very reactive and they never accumulate to considerable amounts compared to the

concentrations of the main reactants (i.e. carbon monoxide, ethylene and methanol).

#### 6.4.1.1 Carbon Monoxide Addition the Rate Determining Step

First we examine the case of carbon monoxide addition being the rate limiting step. Below the suggested reaction scheme is presented where the various complexes were named with letters (i.e. a-c) for simplicity.

$$[(L-L)Pd(H)]^+ + C_2H_4 \overset{K_1}{\leftrightarrow} [(L-L)Pd(CH_2CH_3)]^+ \quad \textbf{(6.6)}$$

(a) (b)

$$[(L-L)Pd(CH_2CH_3)]^+ + CO \overset{k_2}{\rightarrow} [(L-L)Pd(CO)(CH_2CH_3)]^+ \quad \textbf{(6.7)}$$

(b) (c)

$$[(L-L)Pd(CO)(CH_2CH_3)]^+ + CH_3OH \overset{K_3}{\leftrightarrow} [(L-L)Pd(H)]^+ + CH_3CH_2COOCH_3 \quad \textbf{(6.8)}$$

(c) (a)

Analysis using the steady state approximation for reactions (6.28)-(6.30) gives,

$$K_1 = \frac{[b]}{[a]\cdot[C_2H_4]} \quad \textbf{(6.9)}$$

$$K_3 = \frac{[a]}{[c]\cdot[CH_3OH]} \quad \textbf{(6.10)}$$

$$R = k_2\cdot[b]\cdot[CO] \quad \textbf{(6.11)}$$

$$[Pd] = [a] + [b] + [c] \quad \textbf{(6.12)}$$

where [a], [b] and [c] are the concentrations of species (a), (b) and (c) of reactions (6.28)-(6.30) and [Pd] is the concentration of Palladium catalyst in

the system. After rearranging and combining equations (6.31)-(6.34) the following reaction rate expression is formed,

$$R = \frac{k_2 \cdot K_1 \cdot K_3 \cdot [Pd] \cdot [CO] \cdot [C_2H_4] \cdot [CH_3OH]}{1 + K_3 \cdot [CH_3OH] + K_1 \cdot K_3 \cdot [CH_3OH] \cdot [C_2H_4]} \quad \textbf{(6.13)}$$

When setting $z = K_3 \cdot [CH_3OH] + K_1 \cdot K_3 \cdot [CH_3OH] \cdot [C_2H_4]$ in the denominator, two cases are possible for equation (6.13). If z>>1, equation (6.13) becomes,

$$\begin{aligned} R &= \frac{k_2 \cdot K_1 \cdot K_3 \cdot [Pd] \cdot [CO] \cdot [C_2H_4] \cdot [CH_3OH]}{K_3 \cdot [CH_3OH] + K_1 \cdot K_3 \cdot [CH_3OH] \cdot [C_2H_4]} \\ &= \frac{k_2 \cdot K_1 \cdot K_3 \cdot [Pd] \cdot [CO] \cdot [C_2H_4]}{K_3 + K_1 \cdot K_3 \cdot [C_2H_4]} \end{aligned} \quad \textbf{(6.14)}$$

In this case, the effect of methanol on the reaction rate is cancelled out. However, this is not in agreement with the experimental observations where a positive effect of methanol on the reaction rate was observed.

If z<<1, , equation (6.13) becomes,

$$R = \frac{k_2 \cdot K_1 \cdot K_3 \cdot [Pd] \cdot [CO] \cdot [C_2H_4] \cdot [CH_3OH]}{1} \quad \textbf{(6.15)}$$

In this case, the model suggests a positive ethylene effect on the reaction rate. However, experimentally no effect of ethylene on the reaction rate was reported. Hence, it can be concluded that this kinetic expression is not suitable for the representation of this system and consequently, the addition of carbon monoxide is not the rate determining step based on the experimental data.

#### 6.4.1.2 Ethylene Addition the Rate Determining Step

When considering the case of ethylene addition being the rate limiting step, the reaction scheme is the following:

$$[(L-L)Pd(H)]^+ + C_2H_4 \overset{k_1}{\rightarrow} [(L-L)Pd(CH_2CH_3)]^+ \quad \textbf{(6.16)}$$

(a) (b)

$$[(L-L)Pd(CH_2CH_3)]^+ + CO \overset{K_2}{\leftrightarrow} [(L-L)Pd(CO)(CH_2CH_3)]^+ \quad \textbf{(6.17)}$$

(b) (c)

$$[(L-L)Pd(CO)(CH_2CH_3)]^+ + CH_3OH \overset{K_3}{\leftrightarrow} [(L-L)Pd(H)]^+ + CH_3CH_2COOCH_3 \quad \textbf{(6.18)}$$

(c) (a)

Analysis using the steady state approximation for reactions (6.16)-(6.18) gives,

$$K_2 = \frac{[c]}{[b]\cdot[CO]} \quad \textbf{(6.19)}$$

$$K_3 = \frac{[a]}{[c]\cdot[CH_3OH]} \quad \textbf{(6.20)}$$

$$R = k_1 \cdot [a] \cdot [C_2H_4] \quad \textbf{(6.21)}$$

$$[Pd] = [a] + [b] + [c] \quad \textbf{(6.22)}$$

Where [a], [b] and [c] are the concentrations of species (a), (b) and (c) of reactions (6.16)-(6.18) and [Pd] is the concentration of Palladium catalyst in the system. After rearranging and combining equations (6.19)-(6.22) the following reaction rate expression is formed,

$$R = \frac{k_1 \cdot K_2 \cdot K_3 \cdot [Pd] \cdot [CO] \cdot [C_2H_4] \cdot [CH_3OH]}{1 + K_2 \cdot [CO] + K_2 \cdot K_3 \cdot [CO] \cdot [CH_3OH]} \quad \textbf{(6.23)}$$

This is not a suitable rate expression as it suggests positive effect of ethylene while experimentally ethylene found to have no effect on the reaction rate.

Hence, it can be concluded that the addition of ethylene is not the rate determining step based on the experimental data.

#### 6.4.1.3 Methanolysis the Rate Determining Step

Assuming that the methanolysis is the rate limiting step, the corresponding reaction scheme is,

$$[(L-L)Pd(H)]^+ + C_2H_4 \overset{K_1}{\leftrightarrow} [(L-L)Pd(CH_2CH_3)]^+ \quad \textbf{(6.24)}$$

(a) (b)

$$[(L-L)Pd(CH_2CH_3)]^+ + CO \overset{K_2}{\leftrightarrow} [(L-L)Pd(CO)(CH_2CH_3)]^+ \quad \textbf{(6.25)}$$

(b) (c)

$$[(L-L)Pd(CO)(CH_2CH_3)]^+ + CH_3OH \overset{k_3}{\rightarrow} [(L-L)Pd(H)]^+ + CH_3CH_2COOCH_3 \quad \textbf{(6.26)}$$

(c) (a)

Analysis using the steady state approximation for reactions (6.24)-(6.26) gives,

$$K_1 = \frac{[b]}{[a]\cdot[C_2H_4]} \quad \textbf{(6.27)}$$

$$K_2 = \frac{[c]}{[b]\cdot[CO]} \quad \textbf{(6.28)}$$

$$R = k_3\cdot[c]\cdot[CH_3OH] \quad \textbf{(6.29)}$$

$$[Pd] = [a] + [b] + [c] \quad \textbf{(6.30)}$$

Where [a], [b] and [c] are the concentrations of species (a), (b) and (c) of reactions (6.24)-(6.26) and [Pd] is the concentration of Palladium catalyst in the system. After rearranging and combining equations (6.27)-(6.30) the following reaction rate expression is formed,

$$R = \frac{k_3 \cdot K_1 \cdot K_2 \cdot [Pd] \cdot [CO] \cdot [C_2H_4] \cdot [CH_3OH]}{1 + K_1 \cdot [C_2H_4] + K_1 \cdot K_2 \cdot [C_2H_4] \cdot [CO]} \quad \textbf{(6.31)}$$

This is a suitable rate expression as it is in agreement with the experimental observation such as the positive effect of methanol.

## 6.2 Parameter Estimation

Using the kinetic model (6.31), the validated reactor model (Chapter 5.5) and the experimental data, parameter estimation of the kinetic model was performed using gPROMS. However, it was not possible to identify the model parameters of the kinetic model in the current form. A model is practically identifiable when each set of model parameters can be uniquely determined by each set of experiments [197,198]. For this purpose, the kinetic model was reparametrised to (6.32) in order to decrease the number of parameters and cancel any correlation problems.

$$R = \frac{C \cdot [Pd] \cdot [CO] \cdot [C_2H_4] \cdot [CH_3OH]}{1 + A \cdot [C_2H_4] + B \cdot [C_2H_4] \cdot [CO]} \quad \textbf{(6.32)}$$

where, $A=K_1$, $B=K_1 \cdot K_2$, $C=K_1 \cdot K_2 \cdot k_3$.

Even after the reparametrisation numerical problems prevented the parameter estimation to reach a solution. A possible reason for these numerical problems is the fact that we are dealing with very small numbers ($\sim 10^{-15}$) due to the small concentrations in the liquid phase. In addition, it is noteworthy that gPROMS considers numbers smaller than $10^{-22}$ equal with zero. Hence, in order to prevent any numerical problems, it was decided to replace the concentrations in (6.32) with molar fractions ($C_i = x_i \cdot C_{total}$) resulting to (6.33).

$$R = \left( \frac{C \cdot Pd \cdot x_{CO} \cdot x_{C_2H_4} \cdot x_{CH_3OH}}{A \cdot x_{C_2H_4} + B \cdot x_{C_2H_4} \cdot x_{CO} \cdot \left(\frac{F_{\ell,total}}{v_\ell}\right) + \left(\frac{v_\ell}{F_{\ell,total}}\right)} \right) \cdot \left(\frac{F_{\ell,total}}{v_\ell}\right)^2 \quad \textbf{(6.33)}$$

Furthermore, in order to work with even larger numbers which would result in a smoother simulation, the reparametrised reaction rate, RR, was used for the parameter estimation (6.34).

$$R = 10^{-9} \cdot RR \quad \textbf{(6.34)}$$

It should be clarified that this reparametrisation did not affect the actual results of the parameter estimation of the kinetic model as the kinetic expression, R, remained the same. It was only a modification to help the parameter estimation solver work more efficiently by avoiding working with very small numbers.

Another similar modification of the parameter estimation system was the reparametrisation of the parameters under estimation in order their values to be close to 1. This reparametrisation helps greatly the solver for a better performance by avoiding working with very small numbers. Hence, instead of estimating parameter A, B and C, the new parameter for estimation were theta1, theta2 and theta3 according to (6.35)-(6.37).

$$A = AA_n \cdot theta1 \quad \textbf{(6.35)}$$

$$B = BB_n \cdot theta2 \quad \textbf{(6.36)}$$

$$C = CC_n \cdot theta3 \quad \textbf{(6.37)}$$

where $AA_n=10^5$, $BB_n=10^{15}$, $CC_n=2\cdot10^{18}$.

After these modifications, estimation of the parameters theta1, theta2 and theta3 was performed by means of the collected kinetic data, the reactor model and (6.33)-(6.37). Statistically satisfactory fit of the experimental data

was obtained based on the parameter estimation. The parity plot of the data fit is shown in Figure 6.7. The fit between the experimental data of reaction rate and the corresponding predictions based on the suggested kinetic model in the whole design space is satisfactory. Detailed comparison of the model predictions with the experimental data can be found in the Appendix J.

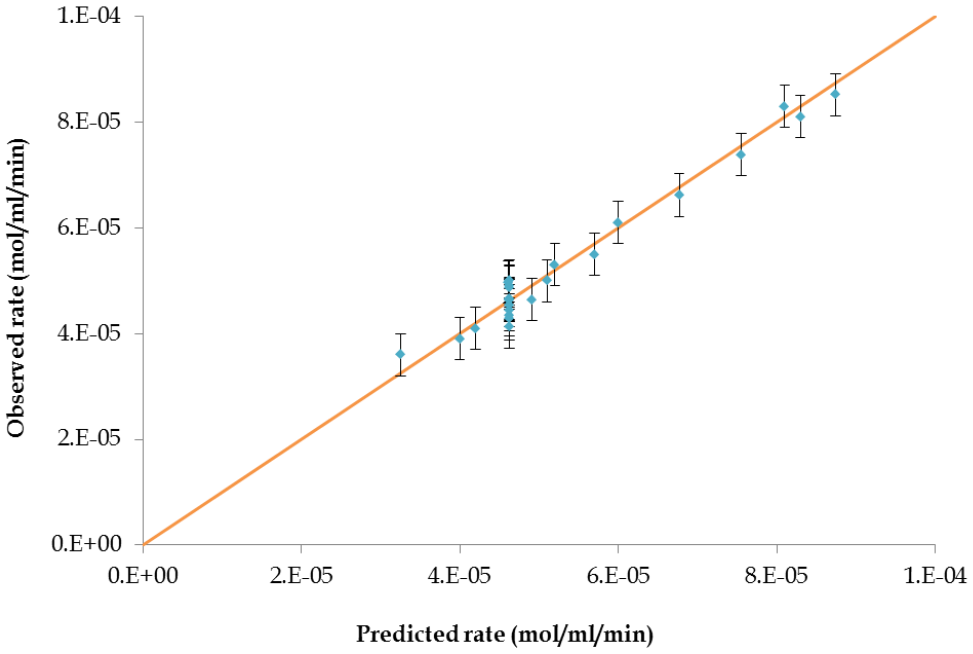


**Figure 6.7** *Parity plot of experimental and predicted from the kinetic model reaction rate data.*

In order to statistically assess the reliability and adequacy of the model and of the new parameter estimates, a $\chi^2$-test was performed considering the sum of the weighted residuals [199],

$$SWR = \sum_{i=1}^{N} \left[ (y_i - \hat{y}_i) \sum_{i}^{-1} (y_i - \hat{y}_i) \right] \quad \textbf{(6.38)}$$

,where $y_i$is the measured data and $\hat{y}_i$ is the predicted ones.

This SWR value was compared with a reference $\chi^2$distribution with (n-p) degrees of freedom (n is the total number of data, p is the total number of parameters). If the $SWR$ value < $\chi^2$distribution implies an adequate fit of the model to the experimental data. This is because it indicates that any deviations between the predictions and the experimental data can be solely

attributed to measurement errors. In that case the model can adequately describe the physical system under investigation. In our case, the SWR value and $\chi^2$distribution were calculated automatically in gPROMS in the end of the parameter estimation process by a built-in statistical tool. It was found that SWR value was much smaller than the $\chi^2$distribution, confirming the excellence of the data fit.

The corresponding estimated values of the kinetic model parameters, theta1, theta2 and theta3 are shown in Table 6-5.

**Table 6-5** Estimation results of parameters of kinetic model.

| Parameter | Final Value | Standard Deviation | 95% t-value |
|---|---|---|---|
| **theta1** | $9.798 \cdot 10^{-6}$ | $5 \cdot 10^{-6}$ | 1.701 |
| **theta2** | 0.1049 | 0.0048 | 10.88 |
| **theta3** | 0.0041 | 0.0002 | 10.94 |
| | | **Reference t-value (95%)** | 1.680 |

The standard deviation of each model parameter was calculated based on,

$$\sigma_i = \sqrt{\frac{\sum_{j=1}^{N}(X_i - x)^2}{N-1}} \quad \textbf{(6.39)}$$

where N is the number of experiments, $X_i$ is the simulation response and x is the measured response. In the fourth column, the t-value of the estimation results is shown for 95% confidence.

The t-values are a common way to measure the confidence of the model parameter estimates and are evaluated as,

$$t_i = \frac{\widehat{\theta_i}}{\sqrt{V_{ii}}} \quad \textbf{(6.40)}$$

where $V_{ii}$ is variance of the i-th element (the i-th element of the diagonal element of the variance-covariance matrix) and $\theta_i$ is the vector of the current parameter estimates. The t-values are compared to a reference t-value, usually given by a Student t-distribution with (n-p) degrees of freedom (n is

the total number of data, p is the total number of parameters). If the t-value of a given model parameter is higher than the reference t-value, the estimate is reliable. Very high t-values usually indicate a high confidence in the estimation of the parameters [200].

In our case, the t-values of all model parameters were calculated by means of a built-in statistical tool of gPROMS. The estimation of all parameters appears to be satisfactory as their t-value is larger than the reference t-value.

Based on the estimated parameters in Table 6-5, the equilibrium constants $K_1$, $K_2$ and the kinetic constant $k_3$ were calculated in Table 6-6.

**Table 6-6** Estimation results of original parameters of kinetic model.

| Parameter | Value |
|---|---|
| **$K_1$ (ml/mol)** | $9.79 \cdot 10^4$ |
| **$K_2$ (ml/mol)** | $1.071 \cdot 10^9$ |
| **$k_3$ (ml/mol/min)** | $7.913 \cdot 10^1$ |

The results show that $K_2 > K_1$ indicating the limited effect of ethylene effect on reaction rate.

## 6.3 Sensitivity Analysis

In kinetic modelling, when the aim is to fit a model to experimental data and to establish the best parameter estimates, it is essential to evaluate how much a variation of the estimated parameter vector affects the predicted measured response of the model. For this process the sensitivity analysis of the system is the ideal analysis tool as it gives the effect of a variation of a model parameter on a measured response based on the sensitivity coefficients matrix, $q_i$, defined in (6.41) [200].

$$q_i = \left[\frac{\partial x_i}{\partial \theta_i}\right] \quad \textbf{(6.41)}$$

where x are the measured responses and θ are the model parameters.

The sensitivity analysis of a parameter shows how important this parameter is in the calculation of a response and how easy it is to estimate this parameter. A large effect of the variation of a model parameter on the response indicates that this parameter can be easily estimated.

Sensitivity analysis of parameter theta1 was done by varying the value of parameter theta1 relatively to its actual value (while keeping theta2 and theta 3 fixed) and measuring the effect of this variation on the reaction rate. Similarly, sensitivity analysis was performed for parameters theta2 and theta3 as well. The results are presented in Figure 6.8.

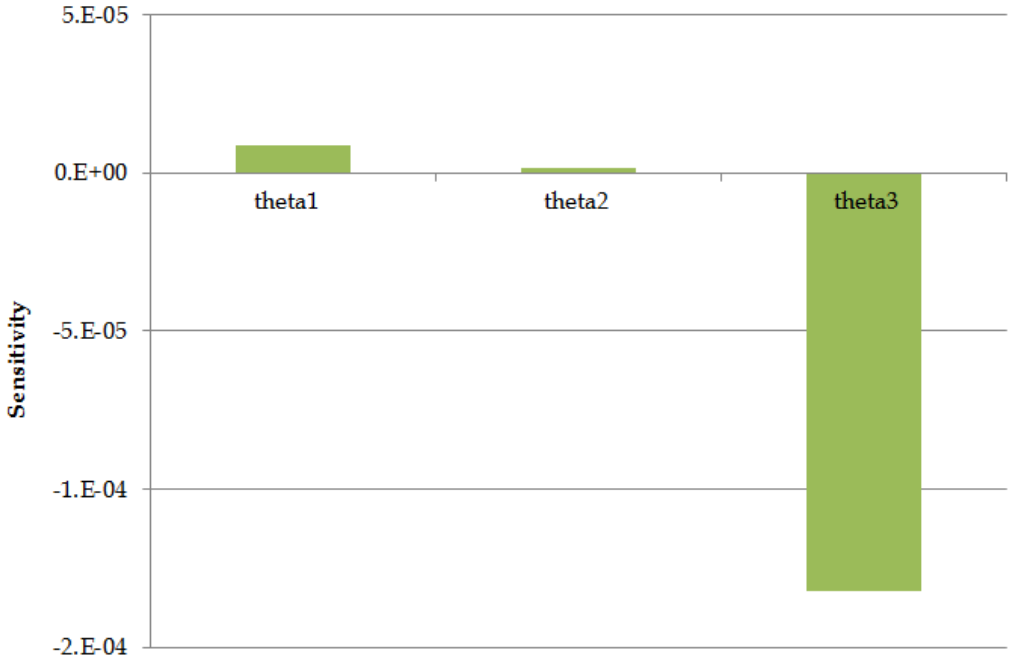


**Figure 6.8** *Sensitivity analysis of parameters theta1, theta2 and theta3 on reaction rate.*

The sensitivities of all three parameters are very small- the largest one is of parameter theta3 and does not exceed $2 \cdot 10^{-4}$. The small values of sensitivities

especially for parameter theta1 and theta2 indicate that their estimation is not very easy as their effect on the measured response (the reaction rate in our case) is not significant. Possible ways to improve the sensitivity of the model parameters is by model reformulation and reparametrisation.

## 6.4 Information Analysis

Another very valuable analysis tool in the kinetic modelling is the information analysis of the system. This consists of the study of the information each experiment provides with regards to the estimation of a parameter in our case. The information which can be acquired by each single experiment can be represented by the measure of Fisher Information Matrix (FIM), $H_\theta$, which is built from the sensitivity matrix and the preliminary information matrix as shown in(6.42) [200].

$$H_\theta(\theta,\varphi) = \left[\sum_{k=1}^{n_{sp}}\sum_{i=1}^{N_y}\sum_{j=1}^{N_y} s_{ijk}\cdot Q_{ik}^T\cdot Q_{jk} + H_\theta^0\right] \qquad \textbf{(6.42)}$$

where θ are the model parameters, φ is the design vector, $s_{ijk}$ is the variance-covariance of measurements errors, $Q_{ik}^T \cdot Q_{jk}$ is the sensitivity matrix, $N_y$ is the number of measured variables, $n_{sp}$ is the number of experiments and $H_\theta^0$ the prior information matrix, taking into account the statistical information about the parametric system before each trial is carried out. The scope of the design procedure is the maximisation of the expected information predicted by minimising a metric ψ of the variance-covariance matrix of model parameters. The most commonly used design criteria are the so called 'alphabetic criteria' [200] (reference: Federico thesis, 2. Kiefer 1959). The geometrical interpretation of the alphabetic design criteria for a two parameters problem is shown in Figure 6.9.

In the case of A-optimality the trace of information matrix is considered while in the case of D-optimal and E-optimal the determinant and the maximum eigenvalue of the FIM are considered respectively [200]. The

information analysis of a system is a very powerful analysis tool as it provides insights on how informative the experiments are and which experiments are more important.

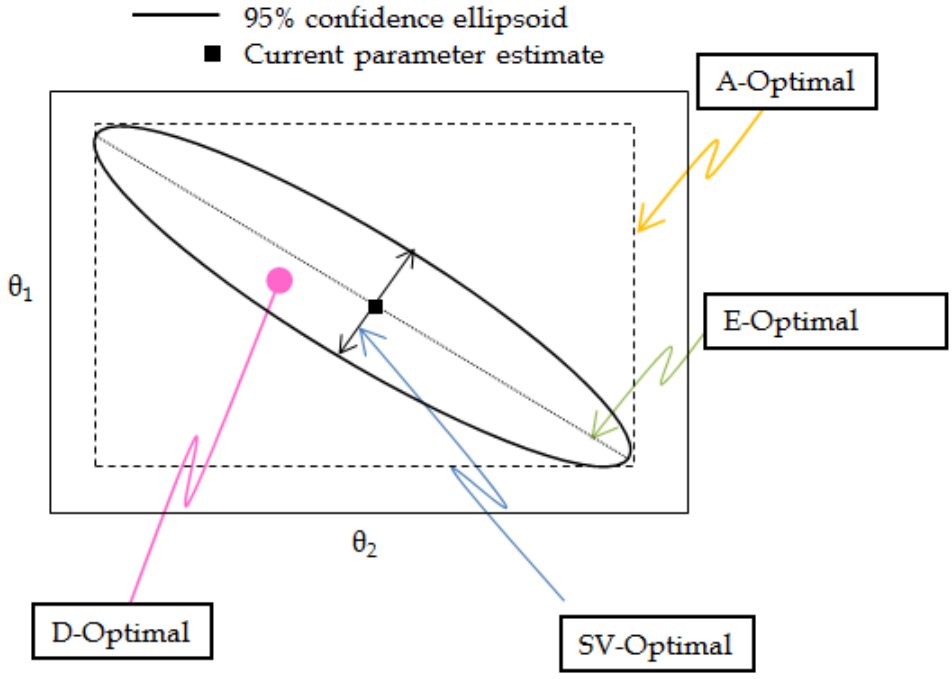


**Figure 6.9** *Design Criteria for model-based design of experiments.*

Information analysis was conducted on the already performed experiments by plotting the trace of Fischer Information Matrix based on the A-optimal design, calculated in gPROMS, for each experiment. The results of the information analysis are presented in Figure 6.10 where the information provided by the different series of experiments for the estimation of the kinetic parameter is given. This is based on (6.42) for one experiment.

The most informative experiments appear to be those studying the carbon monoxide effect (Figure 6.10). Then, the next most informative are those studying the ethylene effect. The least informative experiments are those studying the methanol effect. It is interesting to note also that in all series of experiments there are experiments that provide almost zero information.

These experiments could have been avoided if the experiments were designed based on their information content.

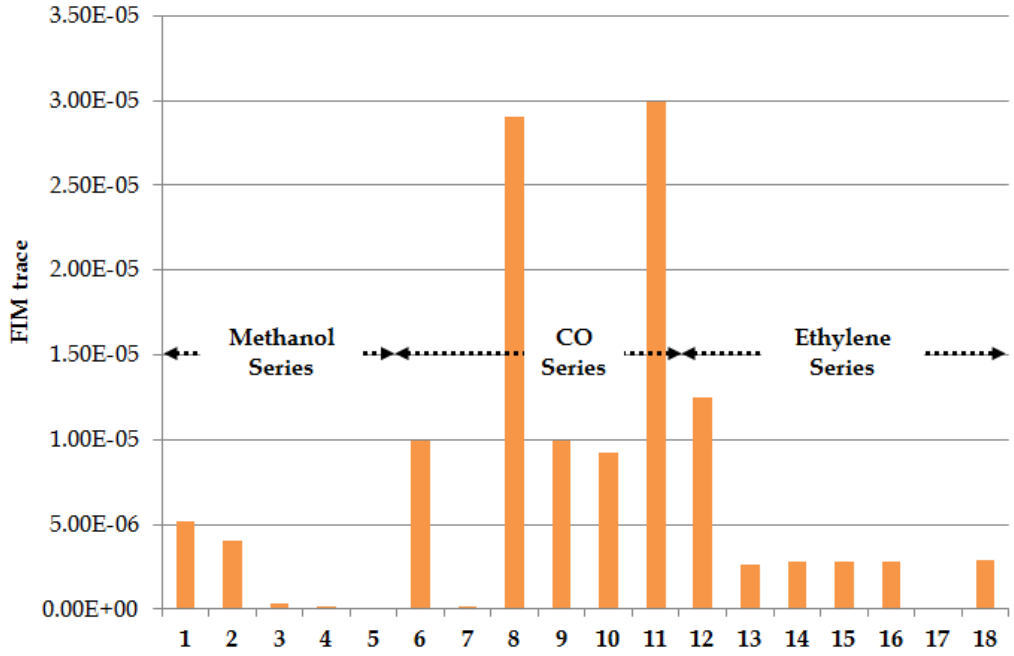


**Figure 6.10** *Information analysis of performed experiments based on Fischer information.*

## 6.5 Conclusions

The kinetics of methoxycarbonylation of ethylene was studied in this chapter using a capillary reactor and the effect of methanol, ethylene and carbon monoxide concentration on the reaction rate was investigated. Methanol found to have a great, positive effect on the observed reaction rate although it was in excess. This may indicate that methanol insertion is not favoured and hence a higher concentration in solution increases the chance of an attack of methanol on the complex and influences the overall reaction rate in this way. On the contrary, ethylene appeared to have no significant effect on the reaction rate. This was attributed to its high solubility and the fast mass transfer of the system. Similar behaviour was also reported by Seayad [191] who studied the carbonylation of styrene using a homogenous Pd-complex

catalyst and observed zero-order with respect to the styrene. Carbon monoxide found to have a positive effect on the reaction rate. This is not in agreement with previous studies, where a negative effect of carbon monoxide was observed for very high carbon monoxide concentrations due to poisoning of the catalyst by carbon monoxide species [192]. However no sign of catalyst poisoning by carbon monoxide appeared in our study most probably because of the very high catalyst concentrations used in this study (about 10 times larger than in previous studies [192,193]. This means that if there were any loss of catalyst due to poisoning it would be unlikely to impact the rate very much. Temperature increase found also to increase the turnover frequency.

A mechanistic kinetic model that can describe satisfactorily the system's behaviour was developed based on the Palladium hydride catalytic cycle. Kinetic model discretisation was performed based on the experimental observations and it was concluded that methanolysis is the rate-controlling step in this reaction system. Parameter estimation of the kinetic model was performed and excellent fit of data was achieved. The results showed that the addition of carbon monoxide is more favourable than the ethylene insertion. The accuracy of the estimation was validated using statistical tools. Information analysis was conducted on the already performed experiments by plotting the trace of Fischer Information Matrix based on the A-optimal design. It was found that the most informative experiments are those studying the carbon monoxide effect, then those studying the ethylene effect and finally, the least informative experiments, those studying the methanol effect.

# CHAPTER 7. Conclusions & Future Developments

The first part of the thesis (Chapter 3) focused on the development of a mathematical model for the simulation of gas-liquid reactions in capillary microreactors. A one-dimensional plug flow reactor model was developed and its validation was performed with experiments with a model system, carbon dioxide absorption in a sodium carbonate/bicarbonate buffer solution, a system with well-studied kinetics. A flow set-up was designed and built for the study of the model reaction and design of the operating condition was conducted in order the system to operate under kinetic control.

Flow observation of the system was performed by means of a high-speed camera and the flow pattern found to be slug-annular with long gas bubbles and thin liquid slugs in between. Bubble length found to increase with increase of the gas flowrate or with decrease of the capillary size. Moreover, the liquid film around the gas bubble found to became thicker when the gas flowrate increased (and hence as the capillary number increases), consistent with previous observations of Taylor and Bretherton [174,175]. Mass transfer resistances in this system were negligible based on Hatta criterion ($Ha<0.3$). The flow was found to deviate slightly from the ideal plug-flow behaviour based on residence time distribution experiments and this deviation increased when increasing the gas-to-liquid ratio. Furthermore, it was observed that the numerical void fraction prefactor A, necessary for the determination of the liquid volume fraction, was not constant as the gas-to-liquid ratio increased, but gradually increased. This highlights the importance of measuring experimentally the void fraction and the residence time of a multiphase system rather than using correlations especially when operating under conditions (channels with different geometrical characteristics, different fluids, or different gas-to-liquid rations) different from those in the studies of these correlations.

Experiments were conducted under different gas-to-liquid ratios and temperatures and using glass microcapillaries with different inner diameters. Results showed that carbon dioxide conversion decreased with increasing gas flowrate (while keeping the liquid flowrate constant) due to the decrease of the volume fraction and residence time. At constant gas and liquid flowrates, higher conversion of carbon dioxide was observed at higher temperatures due to the higher reaction rate constant at higher temperature. Comparison of the obtained results with the corresponding reactor's model predictions showed good agreement, confirming that this reactor model can be used with confidence for the evaluation of the kinetics of other similar gas-liquid catalytic reaction systems in capillary microreactors under slug-annular flow.

In Chapter 4, the hydrodynamic study of gas-liquid systems with very small gas and liquid velocities in capillary microreactors was discussed. Optical sensors were integrated in the flow set-up to perform residence time distribution (RTD) experiments and a microscope camera was used for the flow observation of the gas-liquid systems. Three gas-liquid systems ($N_2$/water, methanol and 10% aqueous glycerol solution) were studied in PFA microcapillaries of various inner diameters (0.25, 0.5 and 1mm) under different gas-to-liquid ratios (0.66-40). Gas and liquid superficial velocities were varied between 0.004-0.068m/s and 0.0001-0.102m/s respectively.

At high gas-to-liquid ratios, the $N_2$/methanol system presented much larger gas bubbles compared to the $N_2$/water system. This was due to the increased contact angle of water on the PFA surface that prevented the further spreading of the liquid on the wall and led to the formation of frequent, short slugs. Moreover, the transition from slug flow to slug-annular flow moved to lower gas-to-liquid ratios with decreasing surface tension, in agreement with previous studies [82,96,179-181]. As the gas-to-liquid flowrate ratio increased, axial dispersion in the system increased, behaviour also reported by Kreutzer et al. [182]. This was explained by the fact that

when the gas-to-liquid ratio was very large, the liquid slugs were very short and followed by very long gas bubbles. This was leading to incomplete mass-exchange with the stagnant liquid film causing excessive broadening of the step change. In the case of the $N_2$/water system, it was found that axial dispersion became noticeable for gas-to-liquid ratios above 5. When increasing the viscosity of the liquid, less axial dispersion was observed in the system, behaviour also reported by Zhang et al. [179]. This was attributed to the thicker film that was formed around the bubble at higher viscosities, as the driving force of the gas to break through a more viscous liquid was larger leading to a smaller dispersion number [174,184,185]. This difference on dispersion numbers between two fluids with different viscosities was found to become larger for smaller liquid flowrates, hence at large gas-to-liquid ratios. This was because at large gas-to-liquid flowrates the flow pattern moved to a more annulus-type flow pattern where the film thickness became a more critical parameter for mass transfer in the capillary. By increasing the tube diameter, less dispersion was observed in the system and the flow approached a more plug flow type behaviour. This was because for the same gas and liquid flowrates, the superficial velocities were smaller in capillaries with larger diameters resulting to smaller Reynolds and capillary numbers leading to smaller dispersion numbers [183,185].

Experimental data of void fraction of a $N_2$/water system in capillaries with various inner diameters (0.25-1mm) in a range of gas-to liquid ratios (0.3-400) showed that the void fraction was not strongly dependent on the inner diameter of the capillary in this range of diameters. The void fraction data of this system were well described by homogenous model at high volumetric qualities ($\beta>0.65$) and by Armand model for moderate volumetric qualities ($0.65>\beta>0.45$). As the volumetric quality decreased below 0.45, the void fraction deviated largely from both models and no other hydrodynamic model was well predictive either. For this purpose, a new correlation was

developed which found to fit the full set of void fraction data with great accuracy.

It was observed that the nature of the liquid affected the void fraction only in very small gas-to-liquid ratios, when the amount of liquid in the system was significant. The lower the surface tension of the liquid, the larger the void fraction of the system found to be for certain gas and liquid velocities.

Future study should include residence time distribution studies of more gas-liquid systems in capillaries with various diameters and at various gas and liquid velocities. This would allow the development of a universal correlation for the void fraction in microcapillaries, independent of the gas-to-liquid ratio or the nature of the fluids. Moreover, flow observation of these systems by means of a high speed camera would allow the creation of universal flow maps which is not available in the literature for small gas and liquid velocities.

Chapter 5 focused on the design of the set-up and the analysis methodology for the study of methoxycarbonylation of ethylene. Design of reactor's material was based on permeability and reactivity experiments. Hastelloy was concluded to be the most suitable reactor's material as it was found to be non-permeable and it provided an inert and hence non-reactive internal surface. Vapour-liquid equilibrium (VLE) of the system was accounted by means of a pre-existing VLE model developed for this system and its validity was tested with experimental data. A gas-to-liquid ratio of 23 was chosen for the kinetic study based on RTD experiments as it provided enough residence time for the reaction and resulted to plug flow behaviour. The system was under kinetic control at these conditions based on Hatta criterion.

Further study should include experimental study of liquid pretreatment with ethylene on the reaction performance and on catalyst poisoning by carbon monoxide. Moreover, the effect of reactor's material on reaction performance is another very interesting topic to investigate by testing the reaction

performance in capillaries of different materials such as stainless steel, titanium and aluminium. This would give us valuable knowledge on the surface effects (e.g. reaction between surface and catalyst, precipitation of catalyst on the surface) of these materials and their implication on catalyst performance.

In Chapter 6, the kinetic study of methoxycarbonylation of ethylene was performed using the experimental set-up and the analysis methodology described in Chapter 5. The reactants' concentrations and temperature effect on the reaction rate was investigated. Methanol was found to have a great effect on the observed reaction rate, with an order close to unity, although it was in excess. This may indicate that in the catalytic cycle methanol insertion is not favoured and hence a higher concentration of methanol increases the chance of an attack of methanol on the catalytic complex and influences the overall reaction rate in this way. On the contrary, ethylene appeared to have no significant effect on the reaction rate. This was attributed to its high solubility and the fast mass transfer of the system. Similar behaviour was also reported by Seayad [191] who studied the carbonylation of styrene using a homogenous Pd-complex catalyst and observed zero-order with respect to the styrene. Carbon monoxide was found to have a positive effect on the reaction rate. This is not in agreement with previous studies, where a negative effect of carbon monoxide was observed for very high carbon monoxide concentrations due to poisoning of the catalyst by carbon monoxide species [192]. However no sign of catalyst poisoning by carbon monoxide appeared in our study most probably because of the very high catalyst concentrations used in this study (about 10 times larger than in previous studies [192,193]). This means that if there were any loss of catalyst due to poisoning it would be unlikely to impact the rate very much. Temperature increase was also found to increase the turnover frequency.

Future work on the kinetics of methoxycarbonylation of ethylene should include a more in-depth investigation of the temperature effect on the

parameters of the kinetic model by performing a number of experiments at different inlet reactants' concentrations at different temperature conditions. Another very interesting topic to investigate further would be that of catalyst deactivation due to carbon monoxide poisoning at high carbon monoxide concentrations using different catalyst concentrations. This would give valuable information on the mechanism related to the catalyst deactivation, essential for further optimisation of the process.

Moreover, in Chapter 6 a kinetic model based on palladium hydride catalytic cycle was suggested to describe the mechanism of this system. Kinetic model discretisation was performed based on the experimental observations and it was concluded that methanolysis is the rate-controlling step in this reaction system. Parameter estimation of the model was performed in gPROMS and excellent fit of data was achieved in the whole design space indicating that it is a suitable model for this system. The accuracy of the estimation was validated using gPROMS built-in statistical tools.

Lucite International can be immediately benefited by the results of this study, especially the knowledge of the kinetic behaviour of this system and the development of a kinetic model that is aligned with the reaction mechanism of the system and the experimental data. These results can be used to understand better the process, redesign the reactors accordingly and optimise further the process.

Moreover, this study can be further used at a higher level as an automated methodology and tool for kinetic analysis of gas-liquid catalytic systems in a much quicker and accurate way. The fidelity of this methodology is based on the combined insight it can provide on the chemistry on the system taking also into account the vapour-liquid equilibrium and the hydrodynamics of the system.

Future study should focus on improving further this methodology by integrating in-situ concentration analysis such as IR analysis in the inlet and

outlet of the capillary reactor and possibly even in more points along the reactor. This would provide information that in this study had to be predicted based on reactor and VLE modelling and downstream experimental measurements, increasing hence the complexity of the analysis. Increase of the measurements would also increase significantly the information content of the experiments which would improve the accuracy of the kinetic study.

Another very interesting tool to further improve the methodology developed in this study is to include Design of Experiments (DoE) techniques to improve the accuracy of the parameters estimation and reduce significantly the number of experiments required [200-203]. This can be done by retrospectively testing all possible combinations of design variables and select those that result in the most informative experiments based on Fisher Information Matrix (FIM), which is built from the sensitivity matrix [200]. The operating conditions may include the temperature and pressure conditions in the reactor, the inlet concentrations but also the reactor design characteristics. A process diagram of the design of optimum experiments is shown in Figure 7.1.

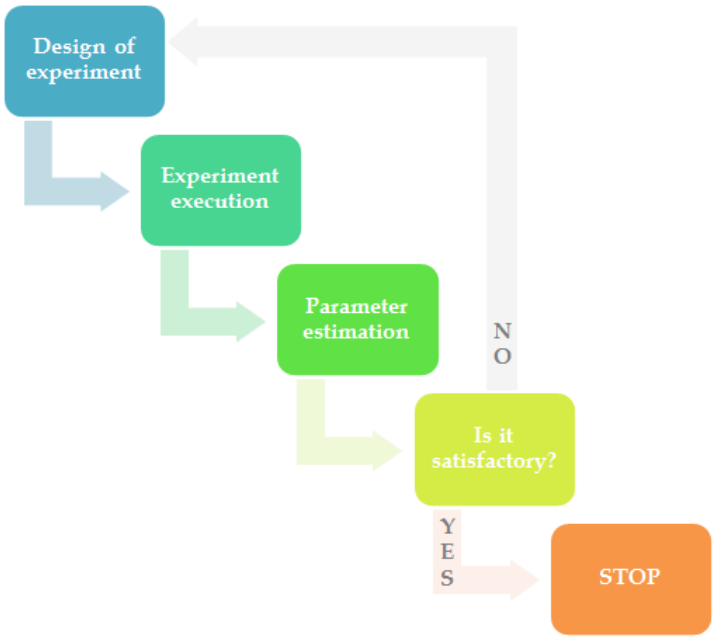


**Figure 7.1** *Process diagram for a design of experiments process.*

# References

[1] W. Clegg, R. J. Elsegood, R. Eastham, P. Tooze, X. Lan Wang, and K. Whiston, Highly active and selective catalysts for the production of methyl propanoate via the methoxycarbonylation of ethene, Chem. Commun., (1999) 1877-1878.

[2] K. F. Jensen, Microreaction engineering -- is small better?, Chemical Engineering Science, 56 (2001) 293-303.

[3] A. Gavriilidis, P. Angeli, E. Cao, K. K. Yeong, and Y. S. S. Wan, Technology and Applications of Microengineered Reactors, Chemical Engineering Research and Design, 80 (2002) 3-30.

[4] G. Charles, T. Roques-Carmes, N. Becheikh, L. Falk, J. M. Commenge, and S. Corbel, Determination of kinetic constants of a photocatalytic reaction in micro-channel reactors in the presence of mass-transfer limitation and axial dispersion, Journal of Photochemistry and Photobiology A: Chemistry, (2011).

[5] Astarita G, Mass transfer with chemical reaction, Elsevier Publishing Company, 1967.

[6] Westerterp K.R., Van Swaaij W.P.M., and Beenackers A.A.C.M., Chemical Reactor Design and Operation, John Wiley &Sons, 1984.

[7] P. V. Danckwerts, Gas-liquid reactions, McGraw-Hill Book Company, 1970.

[8] O. Levenspiel, Chemical Reaction Enginnering, John Wiley & Sons, 1999.

[9] J. R. Bourne, Mixing and the Selectivity of Chemical Reactions, Organic Process Research & Development, 7 (2003) 471-508.

[10] M. S. Lucas, J. A. Peres, B. Y. Lan, and G. Li Puma, Ozonation kinetics of winery wastewater in a pilot-scale bubble column reactor, Water Research, 43 (2009) 1523-1532.

[11] J. Fischer, T. Lange, R. Boehling, A. Rehfinger, and E. Klemm, Uncatalyzed selective oxidation of liquid cyclohexane with air in a microcapillary reactor, Chemical Engineering Science, 65 (2010) 4866-4872.

[12] A. Trusek-Holownia, A membrane phase contactor for enzymatic synthesis of ZAlaPheOMe, the precursor of bitter dipeptide, Biochemical Engineering Journal, 16 (2003) 69-77.

[13] D. A. Waterkamp, M. Engelbert, and J. Thoming, On the Effect of Enhanced Mass Transfer on Side Reactions in Capillary Microreactors during High-Temperature Synthesis of an Ionic Liquid, Chem. Eng. Technol., 32 (2009) 1717-1723.

[14] A.L.Y Tonkovich, J.L.Zilka, M.R.Powell, and C.J.Call, The catalytic partial oxidation of methane in a microreactor, 1998, pp. 45-53.

[15] V.Skelton, G.M.Greenway, S.J.Haswell, P.Styring, D.O.Morgan, B.H.Warrington, and S.Wong, Micro Reaction Technology: Synthetic Chemical Optimisation Methodology of Wittig Synthesis Enabling a Semi-automated microreactor for combinatoial Screening, 2000, pp. 78-88.

[16] O.Wörz, K.P.Jäckel, T. Richter, and A. Wolf, Microreactors, a new efficient tool for optimum reactor design, Chemical Engineering Science, 56 (2001) 1029-1033.

[17] J. R. Burns and C. Ramshaw, The intensification of rapid reactions in multiphase systems using slug flow in capillaries, Lab Chip, 1 (2001) 10-15.

[18] G. Dummann, U. Quittmann, Lothar Gröschel, D. W. Agar, Otto Wörz, and K. Morgenschweis, The capillary-microreactor: a new reactor concept for the intensification of heat and mass transfer in liquid-liquid reactions, Catalysis Today, 79-80 (2003) 433-439.

[19] D. Chambers and C. H. Spink, Microreactors for elemental fluorine, Chem. Commun., (1999) 883-884.

[20] R. D. Chambers, D. Holling, R. C. H. Spink, and G. Sandford, Elemental fluorine Part 13. Gas-liquid thin film microreactors for selective direct fluorination, Lab Chip, 1 (2001) 132-137.

[21] K.Jähnisch, M. Baerns, V. Hessel, W. Ehrfeld, V. Haverkamp, H.Löwe, C. Wille, and A. Guber, Direct fluorination of toluene using elemental fluorine in gas/liquid microreactors, Journal of Fluorine Chemistry, 105 (2000) 117-128.

[22] Y.Önal, M. Lucas, and P. Claus, Application of a Capillary Microreactor for Selective Hydrogenation of a,ß-Unsaturated Aldehydes in Aqueous Multiphase Catalysis, Chem. Eng. Technol., 28 (2005) 972-978.

[23] R. Natividad, R. Kulkarni, K. Nuithitikul, S. Raymahasay, J. Wood, and J. M. Winterbottom, Analysis of the performance of single capillary and multiple capillary (monolith) reactors for the multiphase Pd-catalyzed hydrogenation of 2-Butyne-1,4-Diol, Chemical Engineering Science, 59 (2011) 5431-5438.

[24] A. N. Tsoligkas, M. J. H. Simmons, J. Wood, and C. G. Frost, Kinetic and selectivity studies of gas-liquid reaction under Taylor flow in a circular capillary, Catalysis Today, 128 (2007) 36-46.

[25] A. N. Tsoligkas, M. J. H. Simmons, and J. Wood, Two phase gas-liquid reaction studies in a circular capillary, Chemical Engineering Science, 62 (2009) 5397-5401.

[26] J. F. Ng, Y. Nie, G. K. Chuah, and S. Jaenicke, A wall-coated catalytic capillary microreactor for the direct formation of hydrogen peroxide, Journal of Catalysis, 269 (2010) 302-308.

[27] R. Jevtic, P. A. Ramachandran, and M. P. Dudukovic, Capillary reactor for cyclohexane oxidation with oxygen, Chemical Engineering Research and Design, 88 (2010) 255-262.

[28] Philip W.Miller, Nicholas J.Long, Andrew J.de Mello, R. Vilar, Hélène Audrain, D. Bender, J. Passchier, and A. Gee, Rapid Multiphase Carbonylation Reactions by Using a Microtube Reactor: Applications in Positron Emission Tomography 11C-Radiolabeling, Angewandte Chemie International Edition, 46 (2007) 2875-2878.

[29] L. N. Protasova, E. V. Rebrov, H. E. Skelton, A. E. H. Wheatley, and J. C. Schouten, A kinetic study of the liquid-phase hydrogenation of citral on Au/TiO2 and Pt-Sn/TiO2 thin films in capillary microreactors, Applied Catalysis A: General, 399 (2011) 12-21.

[30] D. I. Enache, G. J. Hutchings, S. H. Taylor, R. Natividad, S. Raymahasay, J. M. Winterbottom, and E. H. Stitt, Experimental Evaluation of a Three-Phase Downflow Capillary Reactor, Industrial & Engineering Chemistry Research, 44 (2005) 6295-6303.

[31] L. Ducry and D. M. Roberge, Controlled Autocatalytic Nitration of Phenol in a Microreactor, Angewandte Chemie International Edition, 44 (2005) 7972-7975.

[32] S. Marre, Y. Roig, and C. Aymonier, Supercritical microfluidics: Opportunities in flow-through chemistry and materials science, The Journal of Supercritical Fluids, 66 (2012) 251-264.

[33] T. Bauer, M. Schubert, R. Lange, and R. Abiev, Intensification of heterogeneous catalytic gas-fluid interactions in reactors with a multichannel monolithic catalyst, Russian Journal of Applied Chemistry, 79 (2006) 1047-1056.

[34] X. Liu, B. Unal, and K. F. Jensen, Heterogeneous catalysis with continuous flow microreactors, Catal. Sci. Technol., 2 (2012) 2134-2138.

[35] J. Kobayashi, Y. Mori, K. Okamoto, R. Akiyama, M. Ueno, T. Kitamori, and S. Kobayashi, A Microfluidic Device for Conducting Gas-Liquid-Solid Hydrogenation Reactions, Science, 304 (2004) 1305-1308.

[36] R. Abdallah, P. Magnico, B. Fumey, and C. de Bellefon, CFD and kinetic methods for mass transfer determination in a mesh microreactor, AIChE J., 52 (2006) 2230-2237.

[37] K. K. Yeong, A. Gavriilidis, R. Zapf, H. J. Kost, V. Hessel, and A. Boyde, Characterisation of liquid film in a microstructured falling film reactor using laser scanning confocal microscopy, Experimental Thermal and Fluid Science, 30 (2006) 463-472.

[38] E. V. Rebrov, E. A. Klinger, A. Berenguer-Murcia, E. M. Sulman, and J. C. Schouten, Selective Hydrogenation of 2-Methyl-3-butyne-2-ol in a Wall-Coated Capillary Microreactor with a Pd25Zn75/TiO2 Catalyst, Organic Process Research & Development, 13 (2009) 991-998.

[39] K. S. Elvira, X. C. Solvas, R. C. R. Wootton, and A. J. deMello, The past, present and potential for microfluidic reactor technology in chemical synthesis, Nat Chem, 5 (2013) 905-915.

[40] I. Dencic, V. Hessel, M. H. J. M. de Croon, J. Meuldijk, C. W. J. van der Doelen, and K. Koch, Recent Changes in Patenting Behavior in Microprocess Technology and its Possible Use for Gas Liquid Reactions and the Oxidation of Glucose, ChemSusChem, 5 (2012) 232-245.

[41] V. R. A. S. J. C. Hessel and J. Yoshida, Micro Process Engineering:

A Comprehensive Handbook, Wiley, 2009.

[42] C. Basheer, S. Swaminathan, H. K. Lee, and S. Valiyaveettil, Development and application of a simple capillary-microreactor for oxidation of glucose with a porous gold catalyst, Chem. Commun., (2005) 409-410.

[43] D. I. Enache, G. J. Hutchings, S. H. Taylor, S. Raymahasay, J. M. Winterbottom, M. D. Mantle, A. J. Sederman, L. F. Gladden, C. Chatwin, K. T. Symonds, and E. H. Stitt, Multiphase hydrogenation of resorcinol in structured and heat exchange reactor systems: Influence of the catalyst and the reactor configuration, Catalysis Today, 128 (2007) 26-35.

[44] E. Murphy, J. Martinelli, N. Zaborenko, S. Buchwald, and K. Jensen, Accelerating Reactions with Microreactors at Elevated Temperatures and Pressures: Profiling Aminocarbonylation Reactions, Angewandte Chemie International Edition, 46 (2007) 1734-1737.

[45] N. Wang, T. Matsumoto, M. Ueno, H. Miyamura, and S. Kobayashi, A Gold-Immobilized Microchannel Flow Reactor for Oxidation of Alcohols with Molecular Oxygen, Angewandte Chemie International Edition, 48 (2009) 4744-4746.

[46] N. de Mas, A. Gunther, M. A. Schmidt, and K. F. Jensen, Increasing Productivity of Microreactors for Fast Gas Liquid Reactions: The Case of Direct Fluorination of Toluene, Industrial & Engineering Chemistry Research, 48 (2008) 1428-1434.

[47] J. Keybl and K. F. Jensen, Microreactor System for High-Pressure Continuous Flow Homogeneous Catalysis Measurements, Industrial & Engineering Chemistry Research, 50 (2011) 11013-11022.

[48] B. Tidona, A. Urakawa, and P. Rudolf von Rohr, High pressure plant for heterogeneous catalytic CO2 hydrogenation reactions in a continuous flow microreactor, Chemical Engineering and Processing: Process Intensification, 65 (2013) 53-57.

[49] M. Al-Rawashdeh, J. Zalucky, C. Muller, T. A. Nijhuis, V. Hessel, and J. C. Schouten, Phenylacetylene Hydrogenation over [Rh(NBD)(PPh3)2]BF4 Catalyst in a Numbered-Up Microchannels Reactor, Industrial & Engineering Chemistry Research, 52 (2013) 11516-11526.

[50] X. Liu and K. F. Jensen, Multistep synthesis of amides from alcohols and amines in continuous flow microreactor systems using oxygen and urea hydrogen peroxide as oxidants, Green Chem., 15 (2013) 1538-1541.

[51] V. Paunovic, V. Ordomsky, M. Fernanda Neira D'Angelo, J. C. Schouten, and T. A. Nijhuis, Direct synthesis of hydrogen peroxide over Au-Pd catalyst in a wall-coated microchannel, Journal of Catalysis, 309 (2014) 325-332.

[52] L. A. Truter, D. M. Perez Ferrandez, J. C. Schouten, and T. A. Nijhuis, TS-1 coated microreactor for selective oxidations, Applied Catalysis A: General, 490 (2015) 139-145.

[53] J. R. Burns and C. Ramshaw, Development of a Microreactor for Chemical Production, Chemical Engineering Research and Design, 77 (1999) 206-211.

[54] M. N. Kashid, F. Platte, D. W. Agar, and S. Turek, Computational modelling of slug flow in a capillary microreactor, Journal of Computational and Applied Mathematics, 203 (2007) 487-497.

[55] W. Verboom, Selected Examples of High-Pressure Reactions in Glass Microreactors, Chem. Eng. Technol., 32 (2009) 1695-1701.

[56] N. de Mas, A. Gunther, M. A. Schmidt, and K. F. Jensen, Microfabricated Multiphase Reactors for the Selective Direct Fluorination of Aromatics, Industrial & Engineering Chemistry Research, 42 (2003) 698-710.

[57] Y. Voloshin, R. Halder, and A. Lawal, Kinetics of hydrogen peroxide synthesis by direct combination of H2 and O2 in a microreactor, Catalysis Today, 125 (2007) 40-47.

[58] S. Maehara, M. Taneda, and K. Kusakabe, Catalytic synthesis of hydrogen peroxide in microreactors, Chemical Engineering Research and Design, 86 (2008) 410-415.

[59] T. Inoue, M. A. Schmidt, and K. F. Jensen, Microfabricated Multiphase Reactors for the Direct Synthesis of Hydrogen Peroxide from Hydrogen and Oxygen, Industrial & Engineering Chemistry Research, 46 (2007) 1153-1160.

[60] R. A. Maurya, K. I. Min, and D. P. Kim, Continuous flow synthesis of toxic ethyl diazoacetate for utilization in an integrated microfluidic system, Green Chem., 16 (2014) 116-120.

[61] S. J. Haswell and P. Watts, Green chemistry: synthesis in micro reactors, Green Chem., 5 (2003) 240-249.

[62] B. Gutmann, J. P. Roduit, D. Roberge, and C. O. Kappe, A Two-Step Continuous-Flow Synthesis of N-(2-Aminoethyl)acylamides through Ring-Opening/Hydrogenation of Oxazolines, Chem. Eur. J., 17 (2011) 13146-13150.

[63] N. Kockmann, M. Gottsponer, B. Zimmermann, and D. Roberge, Enabling Continuous-Flow Chemistry in Microstructured Devices for Pharmaceutical and Fine-Chemical Production, Chem. Eur. J., 14 (2008) 7470-7477.

[64] M. l. M. E. Delville, P. J. Nieuwland, P. Janssen, K. Koch, J. C. M. van Hest, and F. P. J. T. Rutjes, Continuous flow azide formation: Optimization and scale-up, Chemical Engineering Journal, 167 (2011) 556-559.

[65] J. J. Lerou and K. M. Ng, Chemical reaction engineering: A multiscale approach to a multiobjective task, Chemical Engineering Science, 51 (1996) 1595-1614.

[66] C. Amador, A. Gavriilidis, and P. Angeli, Flow distribution in different microreactor scale-out geometries and the effect of manufacturing tolerances and channel blockage, Chemical Engineering Journal, 101 (2004) 379-390.

[67] R. L. Hartman and K. F. Jensen, Microchemical systems for continuous-flow synthesis, Lab Chip, 9 (2009) 2495-2507.

[68] K. Mishima and T. Hibiki, Some characteristics of air-water two-phase flow in small diameter vertical tubes, International Journal of Multiphase Flow, 22 (1996) 703-712.

[69] K. A. Triplett, S. M. Ghiaasiaan, S. I. bdel-Khalik, and D. L. Sadowski, Gas-liquid two-phase flow in microchannels Part I: two-phase flow patterns, International Journal of Multiphase Flow, 25 (1999) 377-394.

[70] M. Kawaji, K. Mori, and D. Bolintineanu, The Effects of Inlet Geometry and Gas-Liquid Mixing on Two-Phase Flow in Microchannels, Journal of Fluids Engineering, 131 (2009) 041302.

[71] A. Serizawa, Z. Feng, and Z. Kawara, Two-phase flow in microchannels, Experimental Thermal and Fluid Science, 26 (2002) 703-714.

[72] K. M. Chung PMY, The effect of channel diameter on adiabatic two-phase flow characteristics in microchannels, International Journal of Multiphase Flow, 30 (2004) 735-761.

[73] A. M. Barajas and R. L. Panton, The effects of contact angle on two-phase flow in capillary tubes, International Journal of Multiphase Flow, 19 (1993) 337-346.

[74] T. Fukano and A. Kariyasaki, Characteristics of gas-liquid two-phase flow in a capillary tube, Nuclear Engineering and Design, 141 (1993) 59-68.

[75] J. W. Coleman and S. Garimella, Characterization of two-phase flow patterns in small diameter round and rectangular tubes, International Journal of Heat and Mass Transfer, 42 (1999) 2869-2881.

[76] K. A. Triplett, S. M. Ghiaasiaan, S. I. bdel-Khalik, A. LeMouel, and B. N. McCord, Gas-liquid two-phase flow in microchannels: Part II: void fraction and pressure drop, International Journal of Multiphase Flow, 25 (1999) 395-410.

[77] T. S. Zhao and Q. C. Bi, Co-current air-water two-phase flow patterns in vertical triangular microchannels, International Journal of Multiphase Flow, 27 (2001) 765-782.

[78] A. Kawahara, P. M. Chung, and M. Kawaji, Investigation of two-phase flow pattern, void fraction and pressure drop in a microchannel, International Journal of Multiphase Flow, 28 (2002) 1411-1435.

[79] W. L. Chen, M. C. Twu, and C. Pan, Gas-liquid two-phase flow in micro-channels, International Journal of Multiphase Flow, 28 (2002) 1235-1247.

[80] P. M. Y. Chung, M. Kawaji, A. Kawahara, and Y. Shibata, Two-Phase Flow Through Square and Circular Microchannels: Effects of Channel Geometry, Journal of Fluids Engineering, 126 (2004) 546-552.

[81] I. Hassan, M. Vaillancourt, and K. Pehlivan, Two-Phase Flow Regime Transitions in Microchannels: A Comparative Experimental Study, Microscale Thermophysical Engineering, 9 (2005) 165-182.

[82] S. Waelchli and P. Rudolf von Rohr, Two-phase flow characteristics in gas-liquid microreactors, International Journal of Multiphase Flow, 32 (2006) 791-806.

[83] N. J. English and S. G. Kandlikar, An Experimental Investigation into the Effect of Surfactants on Air-Water Two-Phase Flow in Minichannels, Heat Transfer Engineering, 27 (2006) 99-109.

[84] H. Ide, A. Kariyasaki, and T. Fukano, Fundamental data on the gas-liquid two-phase flow in minichannels, International Journal of Thermal Sciences, 46 (2007) 519-530.

[85] C. Y. Lee and S. Y. Lee, Influence of surface wettability on transition of two-phase flow pattern in round mini-channels, International Journal of Multiphase Flow, 34 (2008) 706-711.

[86] M. J. F. Warnier, E. Rebrov, M. H. J. M. De Croon, V. Hessel, and J. C. Schouten, Gas hold-up and liquid film thickness in Taylor flow in rectangular microchannels, Chemical Engineering Journal, 135 (2008) S153-S158.

[87] J. Yue, L. Luo, Y. Gonthier, G. Chen, and Q. Yuan, An experimental study of air-water Taylor flow and mass transfer inside square microchannels, Chemical Engineering Science, 64 (2009) 3697-3708.

[88] S. Saisorn and S. Wongwises, An experimental investigation of two-phase air-water flow through a horizontal circular micro-channel, Experimental Thermal and Fluid Science, 33 (2009) 306-315.

[89] A. Kawahara, M. Sadatomi, K. Nei, and H. Matsuo, Experimental study on bubble velocity, void fraction and pressure drop for gas-liquid two-phase flow in a circular microchannel, International Journal of Heat and Fluid Flow, 30 (2009) 831-841.

[90] A. Sur and D. Liu, Adiabatic air-water two-phase flow in circular microchannels, International Journal of Thermal Sciences, 53 (2012) 18-34.

[91] X. Wang, Y. Yong, C. Yang, Z. S. Mao, and D. Li, Investigation on pressure drop characteristic and mass transfer performance of gas-liquid flow in micro-channels, Microfluid Nanofluid, 16 (2014) 413-423.

[92] Xiong Renqiang and Chung J., An experimental study of the size effect on adiabatic gas-liquid two-phase flow patterns and void fraction in microchannels, Physics of Fluids, 19 (2007) 21-28.

[93] N. Shao, A. Gavriilidis, and P. Angeli, Flow regimes for adiabatic gas-liquid flow in microchannels, Chemical Engineering Science, 64 (2009) 2749-2761.

[94] S. Saisorn and S. Wongwises, A review of two-phase gas-liquid adiabatic flow characteristics in micro-channels, Renewable and Sustainable Energy Reviews, 12 (2008) 824-838.

[95] T. Cubaud, U. Ulmanella, and C. M. Ho, Two-phase flow in microchannels with surface modifications, Fluid Dynamics Research, 38 (2006) 772-786.

[96] R. Pohorecki, P. Sobieszuk, K. Kula, W. Moniuk, A. Zielinski, P. Cyganski, and P. Gawinski, Hydrodynamic regimes of gas-liquid flow in a microreactor channel, Chemical Engineering Journal, 135 (2008) S185-S190.

[97] M. K. Akbar, D. A. Plummer, and S. M. Ghiaasiaan, On gas-liquid two-phase flow regimes in microchannels, International Journal of Multiphase Flow, 29 (2003) 855-865.

[98] H. Niu, L. Pan, H. Su, and S. Wang, Flow Pattern, Pressure Drop, and Mass Transfer in a Gas-Liquid Concurrent Two-Phase Flow Microchannel Reactor, Industrial & Engineering Chemistry Research, 48 (2008) 1621-1628.

[99] J. Yue, G. Chen, Q. Yuan, L. Luo, and Y. Gonthier, Hydrodynamics and mass transfer characteristics in gas-liquid flow through a rectangular microchannel, Chemical Engineering Science, 62 (2007) 2096-2108.

[100] M. T. Kreutzer, P. Du, J. J. Heiszwolf, F. Kapteijn, and J. A. Moulijn, Mass transfer characteristics of three-phase monolith reactors, Chemical Engineering Science, 56 (2001) 6015-6023.

[101] C. O. Vandu, H. Liu, and R. Krishna, Mass transfer from Taylor bubbles rising in single capillaries, Chemical Engineering Science, 60 (2005) 6430-6437.

[102] Bercic G. and Pintar A., The role of gas bubbles and liquid slug lengths on mass transport in the Taylor flow through capillaries, Chemical Engineering Science, 52 (1997) 3709-3719.

[103] N. Shao, A. Gavriilidis, and P. Angeli, Mass transfer during Taylor flow in microchannels with and without chemical reaction, Chemical Engineering Journal, 160 (2010) 873-881.

[104] S. Irandoust and B. Andersson, Simulation of flow and mass transfer in Taylor flow through a capillary, Computers & Chemical Engineering, 13 (1989) 519-526.

[105] J. M. van Baten and R. Krishna, CFD simulations of mass transfer from Taylor bubbles rising in circular capillaries, Chemical Engineering Science, 59 (2004) 2535-2545.

[106] R. Pohorecki, Effectiveness of interfacial area for mass transfer in two-phase flow in microreactors, Chemical Engineering Science, 62 (2007) 6495-6498.

[107] P. Sobieszuk, R. Pohorecki, P. Cyganski, and J. Grzelka, Determination of the interfacial area and mass transfer coefficients in the Taylor gas-liquid flow in a microchannel, Chemical Engineering Science, 66 (2011) 6048-6056.

[108] A.A Armand, The resistance during the movement of a two-phase system in horizontal pipes, Izv. Vses. Teplotekh. Inst., 1 (1946) 16-23.

[109] S. Saisorn and S. Wongwises, Two-phase air-water flow in micro-channels: An investigation of the viscosity models for pressure drop prediction, International Communications in Heat and Mass Transfer, 38 (2011) 212-217.

[110] T. S. Zhao and Q. C. Bi, Pressure drop characteristics of gas-liquid two-phase flow in vertical miniature triangular channels, International Journal of Heat and Mass Transfer, 44 (2001) 2523-2534.

[111] H. Ide, R. Kimura, and M. Kawaji, Optical Measurement of Void Fraction and Bubble Size Distributions in a Microchannel, Heat Transfer Engineering, 28 (2007) 713-719.

[112] S. Paranjape, S. N. Ritchey, and S. V. Garimella, Electrical impedance-based void fraction measurement and flow regime identification in microchannel flows under adiabatic conditions, International Journal of Multiphase Flow, 42 (2012) 175-183.

[113] D. P.V., Continuous flow systems. Distribution of residence times, Chemical Engineering Science, 50 (1995) 3857-3866.

[114] A. Cantu-Perez, S. Barrass, and A. Gavriilidis, Residence time distributions in microchannels: Comparison between channels with herringbone structures and a rectangular channel, Chemical Engineering Journal, 160 (2010) 834-844.

[115] A. Cantu-Perez, S. Bi, S. Barrass, M. Wood, and A. Gavriilidis, Residence time distribution studies in microstructured plate reactors, Applied Thermal Engineering, 31 (2011) 634-639.

[116] F. Trachsel, A. Gunther, S. Khan, and K. F. Jensen, Measurement of residence time distribution in microfluidic systems, Chemical Engineering Science, 60 (2005) 5729-5737.

[117] C. H. Hornung and M. R. Mackley, The measurement and characterisation of residence time distributions for laminar liquid flow in plastic microcapillary arrays, Chemical Engineering Science, 64 (2009) 3889-3902.

[118] H. Zhang, S. Tang, and B. Liang, Residence time distribution in two-phase flow mini-channel reactor, Chemical Engineering Journal, 174 (2011) 652-659.

[119] W. Salman, A. Gavriilidis, and P. Angeli, Axial mass transfer in Taylor flow through circular microchannels, AIChE J., 53 (2007) 1413-1428.

[120] M. Gunther, S. Schneider, J. Wagner, R. Gorges, T. Henkel, M. Kielpinski, J. Albert, R. Bierbaum, and J. M. Kohler, Characterisation of residence time and residence time distribution in chip reactors with modular arrangements by integrated optical detection, Chemical Engineering Journal, 101 (2004) 373-378.

[121] S. Lohse, B. T. Kohnen, D. Janasek, P. S. Dittrich, J. Franzke, and D. W. Agar, A novel method for determining residence time distribution in intricately structured microreactors, Lab Chip, 8 (2008) 431-438.

[122] Piet W.N.M van Leeuwen and John C.Chadwick, Homogeneous Catalysts: Activity - Stability - Deactivation, John Wiley & Sons, 2011.

[123] P. W. Miller, N. J. Long, A. J. de Mello, R. Vilar, J. Passchier, and A. Gee, Rapid formation of amides via carbonylative coupling reactions using a microfluidic device, Chem. Commun., (2006) 546-548.

[124] T. Fukuyama, M. Kobayashi, M. Rahman, N. Kamata, and I. Ryu, Spurring Radical Reactions of Organic Halides with Tin Hydride and TTMSS Using Microreactors, Org. Lett., 10 (2008) 533-536.

[125] M. Rahman, T. Fukuyama, N. Kamata, M. Sato, and I. Ryu, Low pressure Pd-catalyzed carbonylation in an ionic liquid using a multiphase microflow system, Chem. Commun., (2006) 2236-2238.

[126] T. Fukuyama, M. Rahman, N. Kamata, and I. Ryu, Radical carbonylations using a continuous microflow system, Beilstein Journal of Organic Chemistry, 5 (2009) 34.

[127] Y. Takebayashi, K. Sue, S. Yoda, T. Furuya, and K. Mae, Direct carbonylation of nitrobenzene to phenylisocyanate using gas-liquid slug flow in microchannel, Chemical Engineering Journal, 180 (2012) 250-254.

[128] P. Miller, L. Jennings, A. deMello, A. Gee, N. Long, and R. Vilar, A Microfluidic Approach to the Rapid Screening of Palladium-Catalysed Aminocarbonylation Reactions, Adv. Synth. Catal., 351 (2009) 3260-3268.

[129] X. Gong, P. W. Miller, A. D. Gee, N. J. Long, A. J. de Mello, and R. Vilar, Gas-Liquid Segmented Flow Microfluidics for Screening Pd-Catalyzed Carbonylation Reactions, Chem. Eur. J., 18 (2012) 2768-2772.

[130] A.Gouch. British Pat. [1,081,304]. 1967.

[131] A. Sen and T. W. Lai, Novel palladium(II)-catalyzed copolymerization of carbon monoxide with olefins, Journal of the American Chemical Society, 104 (1982) 3520-3522.

[132] E. Drent and P. H. M. Budzelaar, Palladium-Catalyzed Alternating Copolymerization of Alkenes and Carbon Monoxide, Chem. Rev., 96 (1996) 663-682.

[133] E.Drent. Patent. 121,965,A2 . 1984.

[134] W. Clegg, R. J. Elsegood, R. Eastham, P. Tooze, X. Lan Wang, and K. Whiston, Highly active and selective catalysts for the production of methyl propanoate via the methoxycarbonylation of ethene, Chem. Commun., (1999) 1877-1878.

[135] A. Vavasori and L. Toniolo, Carbon monoxide-ethylene copolymerization catalyzed by a Pd(AcO)2/dppp/TsOH system: the

promoting effect of water and of the acid, Journal of Molecular Catalysis A: Chemical, 110 (1996) 13-23.

[136] Zacchini, Stefano. Spectroscopic Studies of Palladium Catalysed Reactions between Carbon Monoxide and Ethene. 2001. University of Liverpool.

[137] G.R.Eastham. PhD Thesis. 1996. University of Durham.

[138] J. G. Knight, S. Doherty, A. Harriman, E. G. Robins, M. Betham, G. R. Eastham, R. P. Tooze, M. R. J. Elsegood, P. Champkin, and W. Clegg, Remarkable Differences in Catalyst Activity and Selectivity for the Production of Methyl Propanoate versus COΓêÆEthylene Copolymer by a Series of Palladium Complexes of Related C4-Bridged Diphosphines, Organometallics, 19 (2000) 4957-4967.

[139] W. Clegg, G. R. Eastham, M. R. J. Elsegood, B. T. Heaton, J. A. Iggo, R. P. Tooze, R. Whyman, and S. Zacchini, Synthesis and reactivity of palladium hydrido-solvento complexes, including a key intermediate in the catalytic methoxycarbonylation of ethene to methyl propanoate, J. Chem. Soc. , Dalton Trans., (2002) 3300-3308.

[140] G. R. Eastham, R. P. Tooze, M. Kilner, D. F. Foster, and D. J. Cole-Hamilton, Deuterium labelling evidence for a hydride mechanism in the formation of methyl propanoate from carbon monoxide, ethene and methanol catalysed by a palladium complex, J. Chem. Soc. , Dalton Trans., (2002) 1613-1617.

[141] I. Nysing and I. Kramers, Absorption of CO2 in carbonate bicarbonate buffer solutions in a wetted wall column, Chemical Engineering Science, 8 (1958) 81-89.

[142] B. R. W. Pinsent, L. Pearson, and F. J. W. Roughton, The kinetics of combination of carbon dioxide with hydroxide ions, Trans. Faraday Soc., 52 (1956) 1512-1520.

[143] D. Roberts and P. V. Danckwerts, Kinetics of CO2 absorption in alkaline solutions--I Transient absorption rates and catalysis by arsenite, Chemical Engineering Science, 17 (1962) 961-969.

[144] P. V. Danckwerts, A. M. Kennedy, and D. Roberts, Kinetics of CO2 absorption in alkaline solutions--II : Absorption in a packed column and tests of surface-renewal models, Chemical Engineering Science, 18 (1963) 63-72.

[145] G. M. Richards, G. A. Ratcliff, and P. V. Danckwerts, Kinetics of CO2 absorption--III : First-order reaction in a packed column, Chemical Engineering Science, 19 (1964) 325-328.

[146] G. H. Roper, Absorption of carbon dioxide by carbonate solutions in a disc column, Chemical Engineering Science, 4 (1955) 255-264.

[147] H. Hikita, S. Asai, and T. Takatsuka, Absorption of carbon dioxide into aqueous sodium hydroxide and sodium carbonate-bicarbonate solutions, The Chemical Engineering Journal, 11 (1976) 131-141.

[148] G. Astarita, Absorption of Carbon Dioxide into Alkaline Solutions in Packed Towers, Industrial & Engineering Chemistry Fundamentals, 2 (1963) 294-297.

[149] B. Benadda, M. Prost, S. Ismaily, R. Bressat, and M. Otterbein, Validation of the gas-lift capillary bubble column as a simulation device for a reactor by the study of CO2 absorption in Na2CO3/NaHCO3 solutions, Chemical Engineering and Processing: Process Intensification, 33 (1994) 55-59.

[150] R. H. Perry and R. L. Pigford, Kinetics of Gas-Liquid Reactions, Industrial & Engineering Chemistry, 45 (1953) 1247-1253.

[151] J. W. Payne and B. F. Dodge, Rate of Absorption of Carbon Dioxide in Water and in Alkaline Media, Industrial & Engineering Chemistry, 24 (1932) 630-637.

[152] C. R. Harte, E. M. Baker, and H. H. Purcell, Absorption of Carbon Dioxide in Sodium Carbonate-Bicarbonate Solutions, Industrial & Engineering Chemistry, 25 (1933) 528-531.

[153] R. E. Zeebe, On the molecular diffusion coefficients of dissolved CO2-, HCO3-, and CO32- and their dependence on isotopic mass, Geochimica et Cosmochimica Acta, 75 (2011) 2483-2498.

[154] A. Schumpe, The estimation of gas solubilities in salt solutions, Chemical Engineering Science, 48 (1993) 153-158.

[155] S. Weisenberger and A. Schumpe, Estimation of gas solubilities in salt solutions at temperatures from 273 K to 363 K, AIChE J., 42 (1996) 298-300.

[156] Speight, James G. Lange's Handbook of Chemistry (16th Edition). McGraw-Hill.

[157] J. F. Chen, G. Z. Chen, J. X. Wang, L. Shao, and P. F. Li, High-throughput microporous tube-in-tube microreactor as novel gas-liquid contactor: Mass transfer study, AIChE J., 57 (2011) 239-249.

[158] R. V. Shilimkan and J. B. Stepanek, Effect of tube size on liquid side mass transfer in co-current gas-liquid upward flow, Chemical Engineering Science, 32 (1977) 1397-1400.

[159] O. K. Castell, C. J. Allender, and D. A. Barrow, Liquid-liquid phase separation: characterisation of a novel device capable of separating particle carrying multiphase flows, Lab Chip, 9 (2009) 388-396.

[160] J. G. Kralj, H. R. Sahoo, and K. F. Jensen, Integrated continuous microfluidic liquid-liquid extraction, Lab Chip, 7 (2007) 256-263.

[161] TeGrotenhuis, Ward E., Stenkamp, Victoria S., and McQuillen, John. Normal Gravity Testing of a Microchannel Phase separator for Insitu Resource Utilization. [NASA/CR-2001-210955, E-12809, NAS 1.26:210955]. 2001.

[162] Y. Kikutani, K. Mawatari, A. Hibara, and T. Kitamori, Circulation microchannel for liquid-liquid microextraction, Microchimica Acta, 164 (2009) 241-247.

[163] N. Assmann and P. R. von Rohr, Extraction in microreactors: Intensification by adding an inert gas phase, Chemical Engineering and Processing: Process Intensification, In Press, Corrected Proof.

[164] E. Kolehmainen and I. Turunen, Micro-scale liquid-liquid separation in a plate-type coalescer, Chemical Engineering and Processing, 46 (2007) 834-839.

[165] A. Gunther, M. Jhunjhunwala, M. Thalmann, M. A. Schmidt, and K. F. Jensen, Micromixing of Miscible Liquids in Segmented Gas−Liquid Flow, Langmuir, 21 (2005) 1547-1555.

[166] T. Y. Chan, G. H. Priestman, J. M. MacInnes, and R. W. K. Allen, Development of a micro-channel contactor-separator for immiscible liquids, Chemical Engineering Research and Design, 86 (2008) 65-74.

[167] Amador C. Multiphase flow in micro-reactors. 2005.

[168] K. F. Lam, E. Sorensen, and A. Gavriilidis, Review on gas-liquid separations in microchannel devices, Chemical Engineering Research and Design, 91 (2013) 1941-1953.

[169] E. Y. Kenig, Y. Su, A. Lautenschleger, P. Chasanis, and M. Grunewald, Micro-separation of fluid systems: A state-of-the-art review, Separation and Purification Technology, 120 (2013) 245-264.

[170] M. D. Roydhouse, M. Pradas, N. Al-Rifai, B. Azizi, E. Cao, S. Kalliadasis, and A. Gavriilidis, Operating ranges of gas-liquid capillary microseparators: Experiments and theory, Chemical Engineering Science, 114 (2014) 30-39.

[171] N. A. Mortensen, F. Okkels, and H. Bruus, Reexamination of Hagen-Poiseuille flow: Shape dependence of the hydraulic resistance in microchannels, Phys. Rev. E, 71 (2005) 057301.

[172] P. Sobieszuk, P. Cyganski, and R. Pohorecki, Bubble lengths in the gas-liquid Taylor flow in microchannels, Chemical Engineering Research and Design, 88 (2010) 263-269.

[173] S. Laborie, C. Cabassud, L. Durand-Bourlier, and J. M. Laine, Characterisation of gas-liquid two-phase flow inside capillaries, Chemical Engineering Science, 54 (1999) 5723-5735.

[174] G. I. Taylor, Deposition of a viscous fluid on the wall of a tube, Journal of Fluid Mechanics, 10 (1961) 161-165.

[175] F. P. Bretherton, The Motion of Long Bubbles in Tubes, Journal of Fluid Mechanics, 10 (1961) 166-188.

[176] A. P. Higler, R. Krishna, J. Ellenberger, and R. Taylor, Counter-current operation of a structured catalytically packed-bed reactor: Liquid phase mixing and mass transfer, Chemical Engineering Science, 54 (1999) 5145-5152.

[177] T. O. Salmi, J.-P. Mikkola, and J. P. Warna, Chemical Reaction Engineering and Reactor Technology, CRC Press, 2011.

[178] D.L.Alexoff, K.Hallaba, D.Schlyer, and R.Ferrieri, A simple liquid detector for radiopharmaceutical processing systems, *International workshop on targetry and target chemistry,* 1995.

[179] T. Zhang, B. Cao, Y. L. Fan, Y. Gonthier, L. G. Luo, and S. D. Wang, Gas-liquid flow in circular microchannel. Part I: Influence of liquid physical properties and channel diameter on flow patterns, Chemical Engineering Science, 66 (2011) 5791-5803.

[180] E. V. Rebrov, Two-phase flow regimes in microchannels, Theor Found Chem Eng, 44 (2010) 355-367.

[181] C. Y. Yang and C. C. Shieh, Flow pattern of air-water and two-phase R-134a in small circular tubes, International Journal of Multiphase Flow, 27 (2001) 1163-1177.

[182] M. T. Kreutzer, A. Gunther, and K. F. Jensen, Sample Dispersion for Segmented Flow in Microchannels with Rectangular Cross Section, Anal. Chem., 80 (2008) 1558-1567.

[183] C. M. Madhuranthakam, Q. Pan, and G. L. Rempel, Residence time distribution and liquid holdup in Kenics-« KMX static mixer with hydrogenated nitrile butadiene rubber solution and hydrogen gas system, Chemical Engineering Science, 64 (2009) 3320-3328.

[184] P. Aussillous and D. Quere, Quick deposition of a fluid on the wall of a tube, Physics of Fluids, 12 (2000) 2367-2371.

[185] W. Salman, A. Gavriilidis, and P. Angeli, A model for predicting axial mixing during gas-liquid Taylor flow in microchannels at low Bodenstein numbers, Chemical Engineering Journal, 101 (2004) 391-396.

[186] C. Jimenez Rodriguez, D. F. Foster, G. R. Eastham, and D. Cole-Hamilton, Highly selective formation of linear esters from terminal and internal alkenes catalysed by palladium complexes of bis-(di-tert-butylphosphinomethyl)benzene, Chem. Commun., (2004) 1720-1721.

[187] A. Seayad, S. Jayasree, K. Damodaran, L. Toniolo, and R. V. Chaudhari, On the mechanism of hydroesterification of styrene using an in situ-formed cationic palladium complex, Journal of Organometallic Chemistry, 601 (2000) 100-107.

[188] G. Cavinato and L. Toniolo, Metal in organic synthesis. VI. The solvent effect on the hydrocarbonalkoxylation of propene promoted by a [PdCl2(PPh3)2]-PPh3 catalyst precursor, Journal of Molecular Catalysis, 10 (1981) 161-170.

[189] R. M. Deshpande and R. V. Chaudhari, Kinetics of hydroformylation of 1-hexene using homogeneous HRh(CO)(PPh3)3 complex catalyst, Industrial & Engineering Chemistry Research, 27 (1988) 1996-2002.

[190] S. S. Divekar, R. M. Deshpande, and R. V. Chaudhari, Kinetics of hydroformylation of 1-decene using homogeneous HRh(CO)(PPh3)3 catalyst: a molecular level approach, Catal Lett, 21 (1993) 191-200.

[191] A. Seayad, A. A. Kelkar, R. V. Chaudhari, and L. Toniolo, Kinetics of Carboxylation of Styrene Using a Homogeneous Palladium Complex Catalyst, Industrial & Engineering Chemistry Research, 37 (1998) 2180-2187.

[192] J. Wolowska, G. R. Eastham, B. T. Heaton, J. A. Iggo, C. Jacob, and R. Whyman, The effect of mechanistic pathway on activity in the Pd and Pt catalysed methoxycarbonylation of ethene, Chem. Commun., (2002) 2784-2785.

[193] Apostolopoulou E. Micro-contactors for kinetic estimation of multiphase chemistries. 2013. University College London.

[194] R. M. Deshpande, B. M. Bhanage, S. S. Divekar, S. Kanagasabapathy, and R. V. Chaudhari, Kinetics of Hydroformylation of Ethylene in a Homogeneous Medium:Comparison in Organic and Aqueous Systems, Industrial & Engineering Chemistry Research, 37 (1998) 2391-2396.

[195] G. Kiss, E. J. Mozeleski, K. C. Nadler, E. VanDriessche, and C. DeRoover, Hydroformylation of ethene with triphenylphosphine modified rhodium catalyst: kinetic and mechanistic studies, Journal of Molecular Catalysis A: Chemical, 138 (1999) 155-176.

[196] G. R. Eastham, B. T. Heaton, J. A. Iggo, R. P. Tooze, R. Whyman, and S. Zacchini, Synthesis and spectroscopic characterisation of the intermediates in the Pd-catalysed methoxycarbonylation of ethene, Chem. Commun., (2000) 609-610.

[197] F. Galvanin, C. Ballan, M. Barolo, and F. Bezzo, A general model-based design of experiments approach to achieve practical identifiability of pharmacokinetic and pharmacodynamic models, J Pharmacokinet Pharmacodyn, 40 (2013) 451-467.

[198] M. Hongyu, X. Xiaohua, A. S. Perelson, and W. Hulin, On Identifiability of Nonlinear ODE Models and Applications in Viral Dynamics, SIAM Review, 53 (2011) 3-39.

[199] Galvanin, Federico. Optimal model-based design of experiments in dynamic systems: novel techniques and unconventional applications. 2010. University of Padova.

[200] G. Franceschini and S. Macchietto, Model-based design of experiments for parameter precision: State of the art, Chemical Engineering Science, 63 (2008) 4846-4872.

[201] Fisher R.A., The design of experiments, Oliver and Boyd, Edinburgh 1935.

[202] F. Galvanin, S. Macchietto, and F. Bezzo, Model-Based Design of Parallel Experiments, Industrial & Engineering Chemistry Research, 46 (2007) 871-882.

[203] S. P. Asprey and S. Macchietto, Statistical tools for optimal dynamic model building, Computers & Chemical Engineering, 24 (2000) 1261-1267.

[204] C. R. Wilke and P. Chang, Correlation of Diffusion Coefficients in Dilute Solutions, Aiche Journal, 1 (1955) 264-270.

[205] B.Poling, J.Prausnitz, and J.O'Connell, The properties of gases and liquids, McGraw-Hill, 2001.

[206] Frank P.Incropera and David P.DeWitt, Introduction to Heat Transfer, Jonh Wiley & Sons, USA 1996.

[207] Q. Liu, F. Takemura, and A. Yabe, Solubility and diffusivity of carbon monoxide in liquid methanol, Journal of Chemical and Chemical Engineering Data, 41 (1996).

[208] B. H. C. Chen and S. H. Chen, Diffusion of slightly soluble gases in liquids: Measurement and correlation with implications on liquid structures, Chemical Engineering Science, 40 (2001) 1735-1741.

[209] X. Y. Sun, A. Constantinou, and A. Gavriilidis, Stripping of acetone from isopropanol solution with membrane and mesh gas-liquid contactors, Chemical Engineering and Processing, 50 (2011) 991-997.

[210] Alexandre Torres. In situ measurement of gas concentrations in working catalytic reactors by HPNMR. 2009. University of Liverpool.

# Appendix A

## Calibration Graphs

The calibration lines for the mass flow controllers used in this study are shown below.

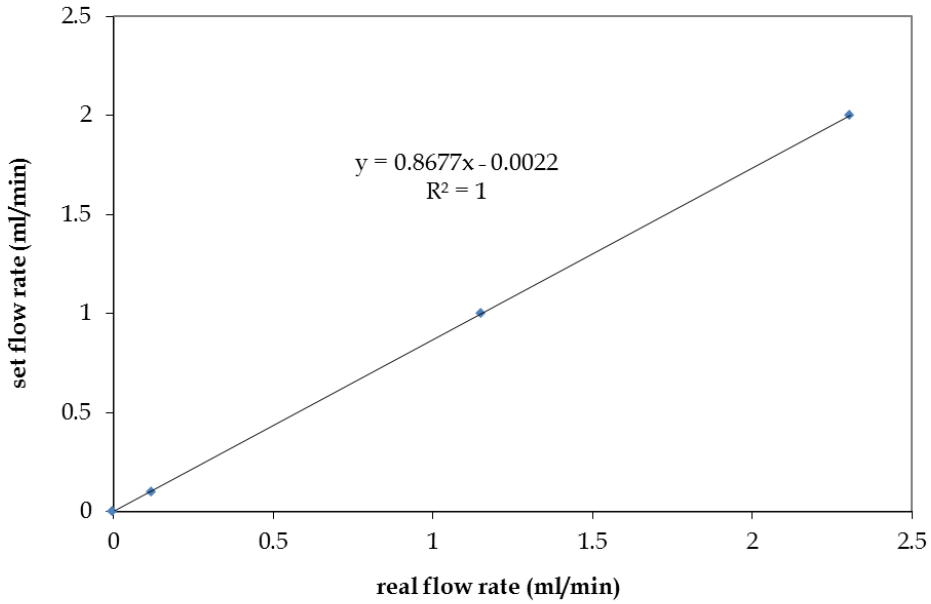


**Figure A. 1** *Calibration line of MFC1 (up to 3ml/min) with $N_2$.*

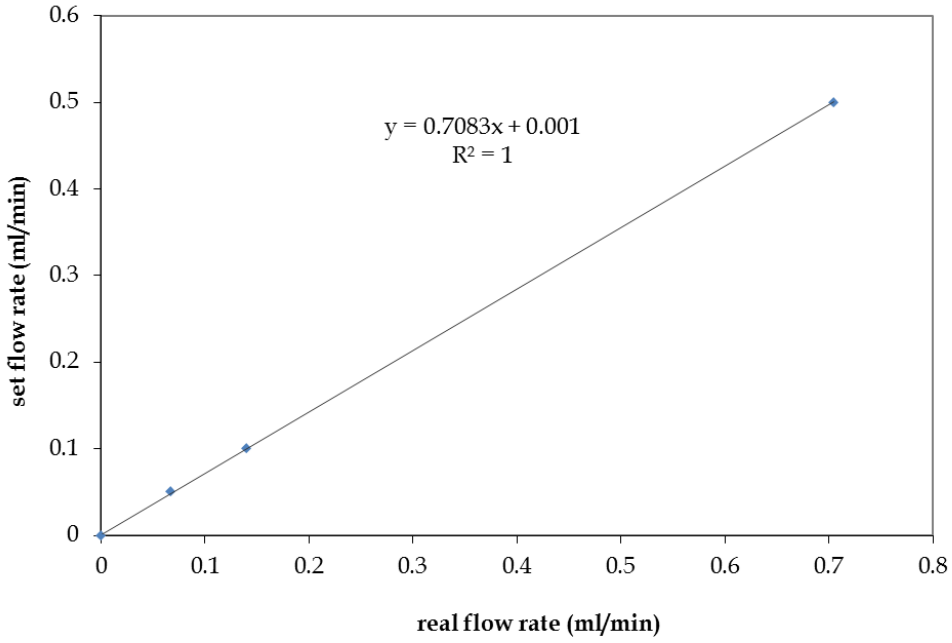


**Figure A. 2** *Calibration line of MFC2 (up to 1ml/min) with 20 vol% $CO_2/N_2$.*

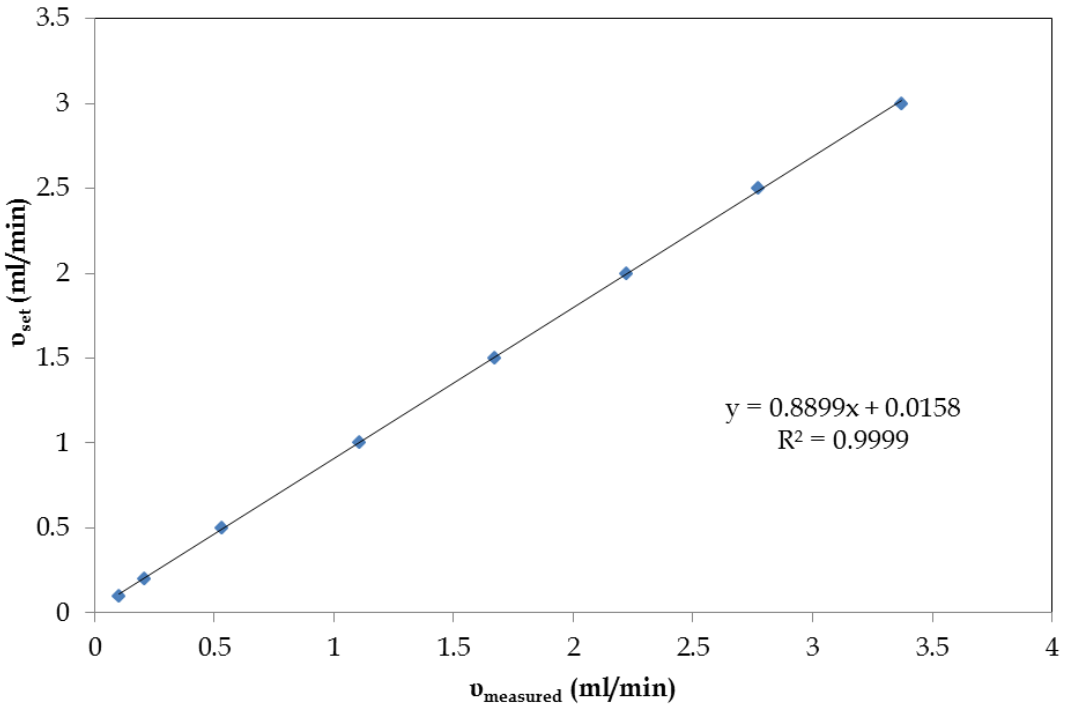


**Figure A. 3** *Calibration line of MFC used with nitrogen for the hydrodynamic study.*

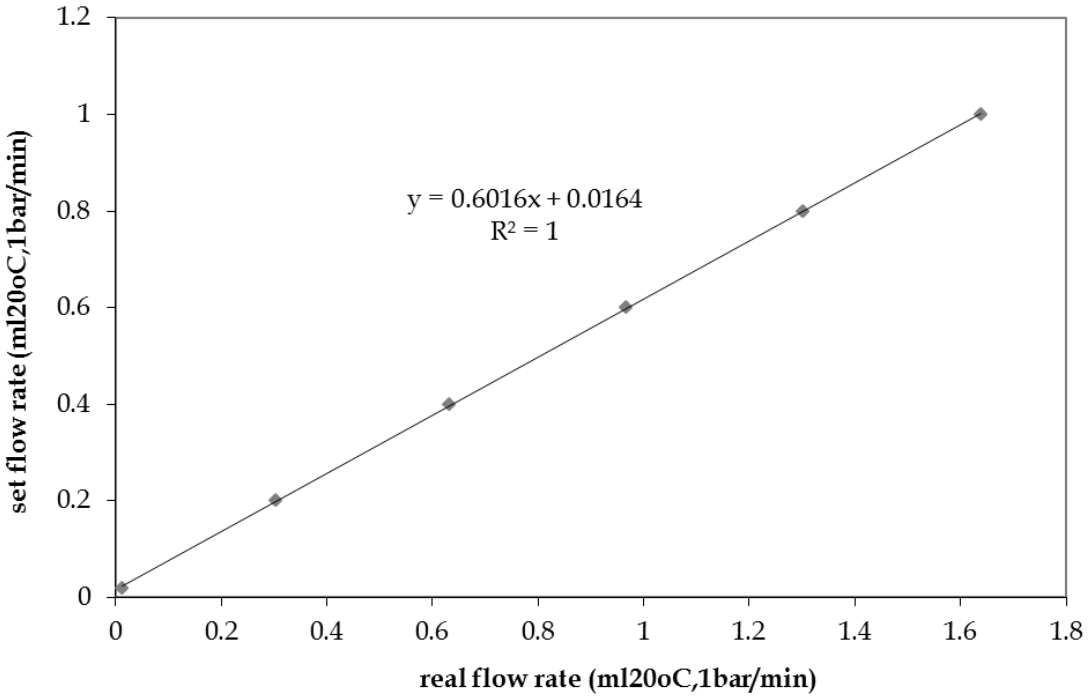


**Figure A. 4** *Calibration line of CO MFC (up to 1ml/min) at NTP conditions (20°C, 1bar).*

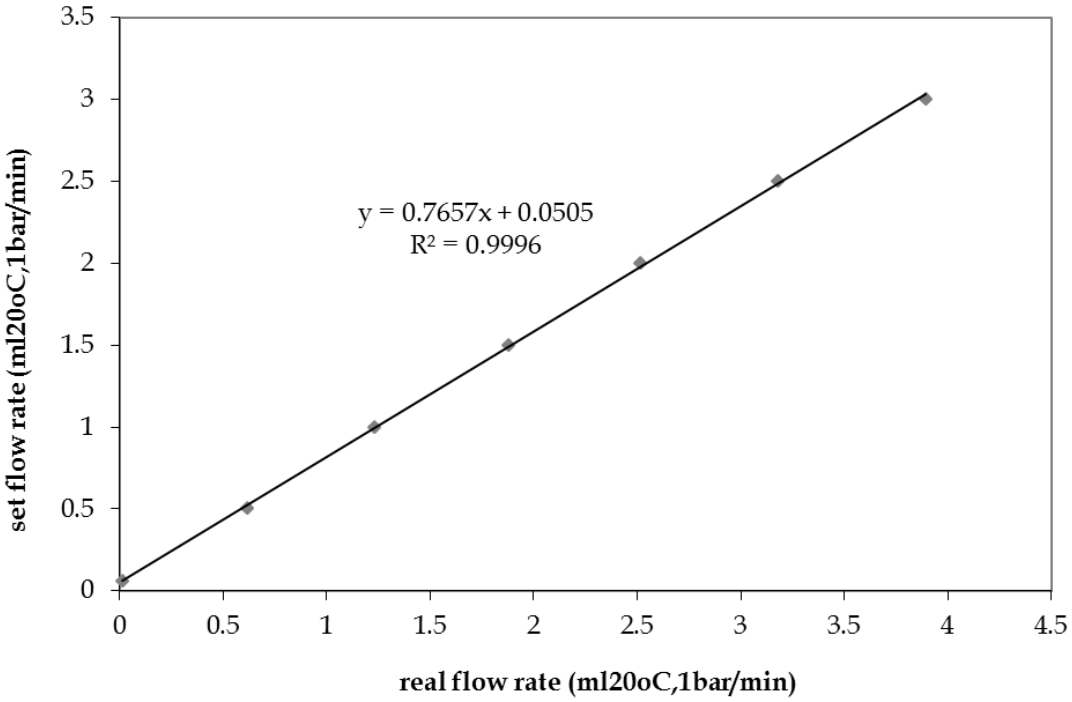


**Figure A. 5** *Calibration line of ethylene MFC (up to 3ml/min) at NTP conditions (20°C, 1bar).*

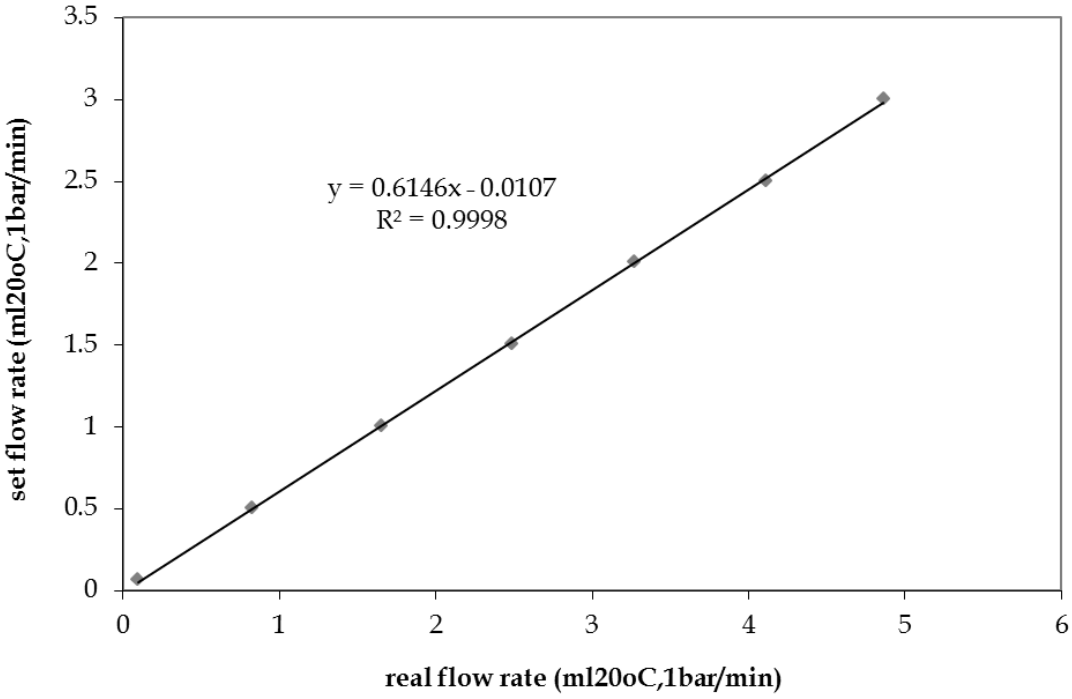


**Figure A. 6** *Calibration line of helium MFC (up to 3ml/min) at NTP conditions*

The calibration line of the pressure transducer used to monitor the pressure in the reactor is presented below.

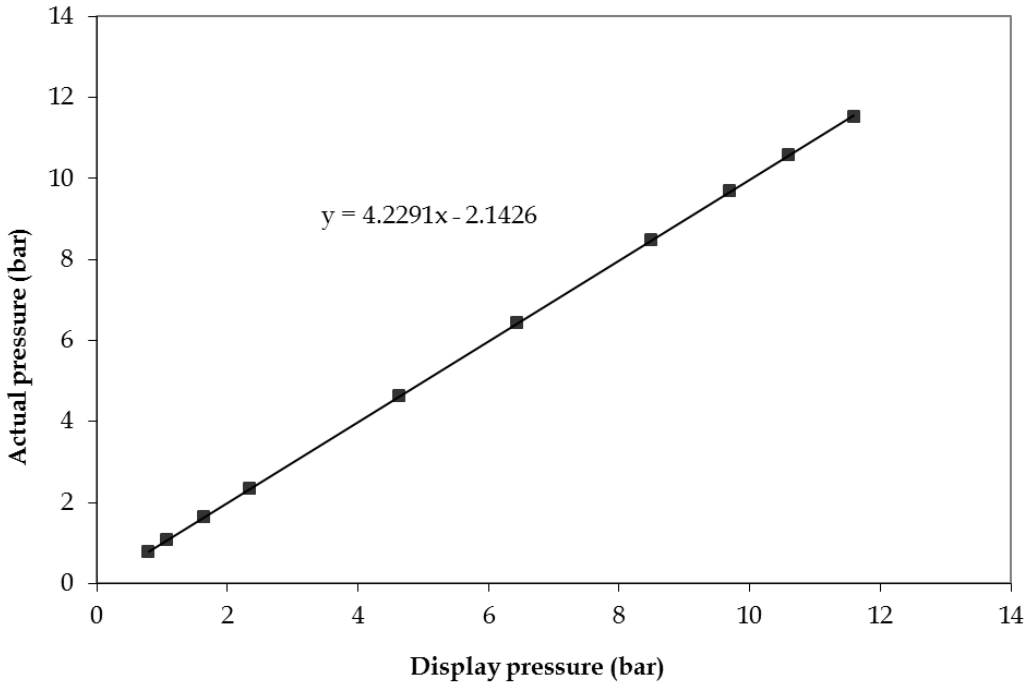


**Figure A. 7** *Calibration line of pressure indicator (up to 17bar) before the reactor using He.*

The final conditions chosen for the analysis of the carbon dioxide absorption in carbonate-bicarbonate buffer solutions are shown in Table A. 1. A typical chromatograph of $CO_2/N_2$ analysis is shown in Figure A. 8, where the first peak is of $N_2$ and the second of $CO_2$.

**Table A. 1** GC operating conditions for the analysis of the model system.

| **Column Name** | HP-PLOT Q |
|---|---|
| **Oven Temperature** | 75°C |
| **Inlet Temperature** | 75°C |
| **Carrier Gas** | Helium |
| **Carrier Flowrate** | 5ml/min |
| **Detector** | TCD |
| **Filament Temperature** | 250°C |
| **Make-up Flowrate** | 5ml/min |
| **Reference Flowrate** | 20ml/min |

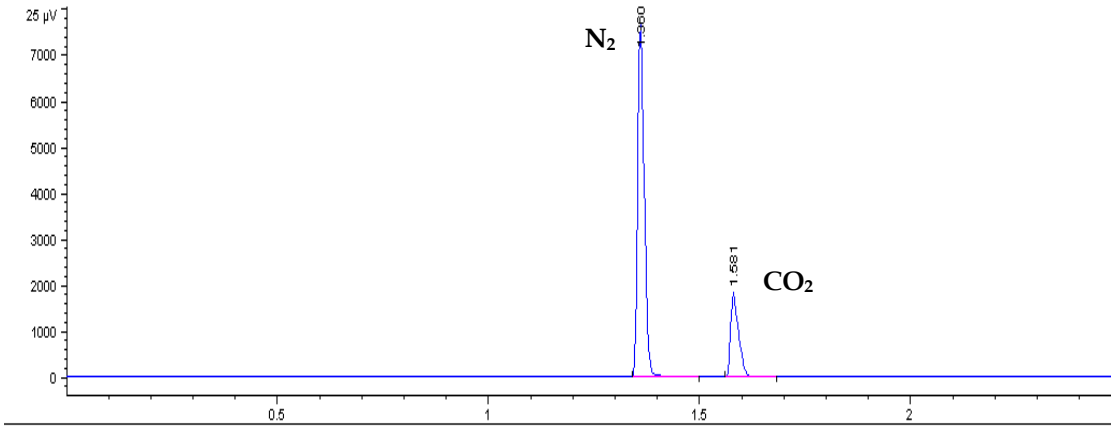


**Figure A. 8** *A typical chromatograph of 20 vol% $CO_2/N_2$.*

The calibration lines of gc for the analysis of various gases are shown below.

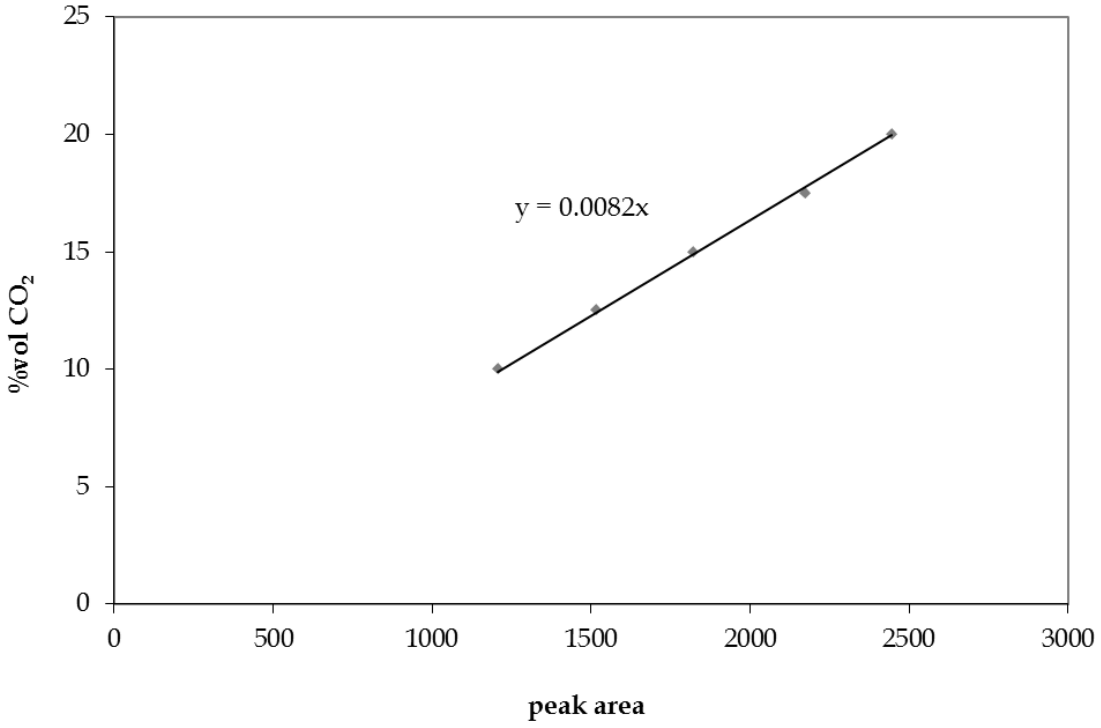


**Figure A. 9** *Calibration line of gc for carbon dioxide analysis.*

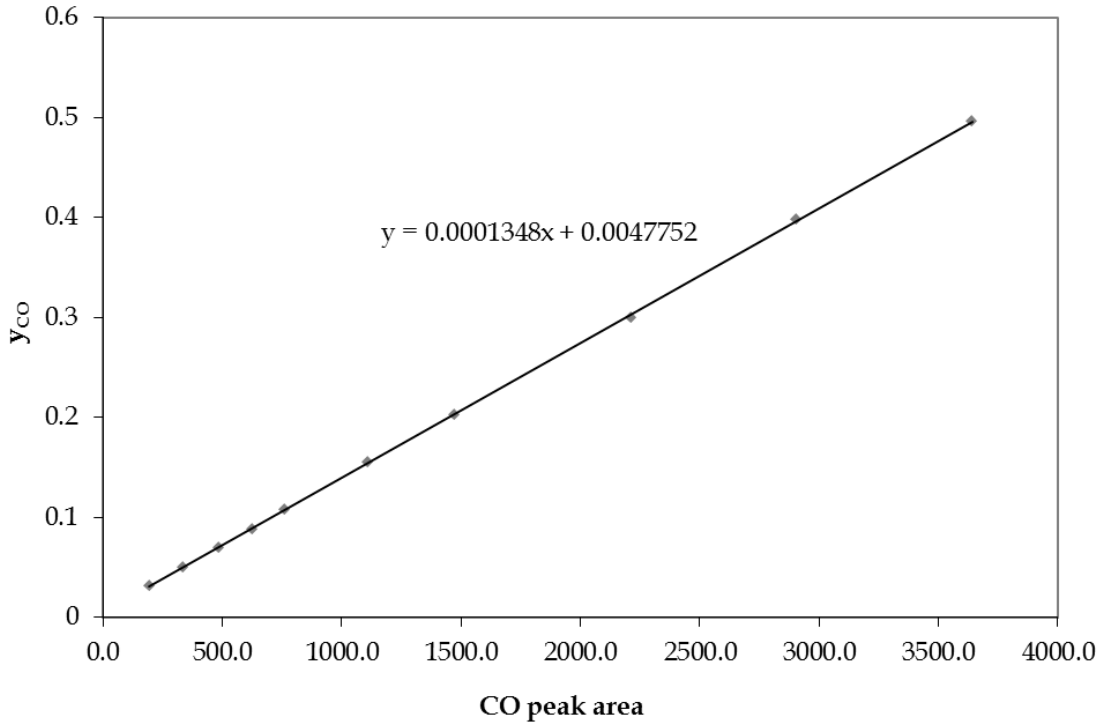


**Figure A. 10** *GC calibration line for analysis of carbon monoxide in gas phase.*

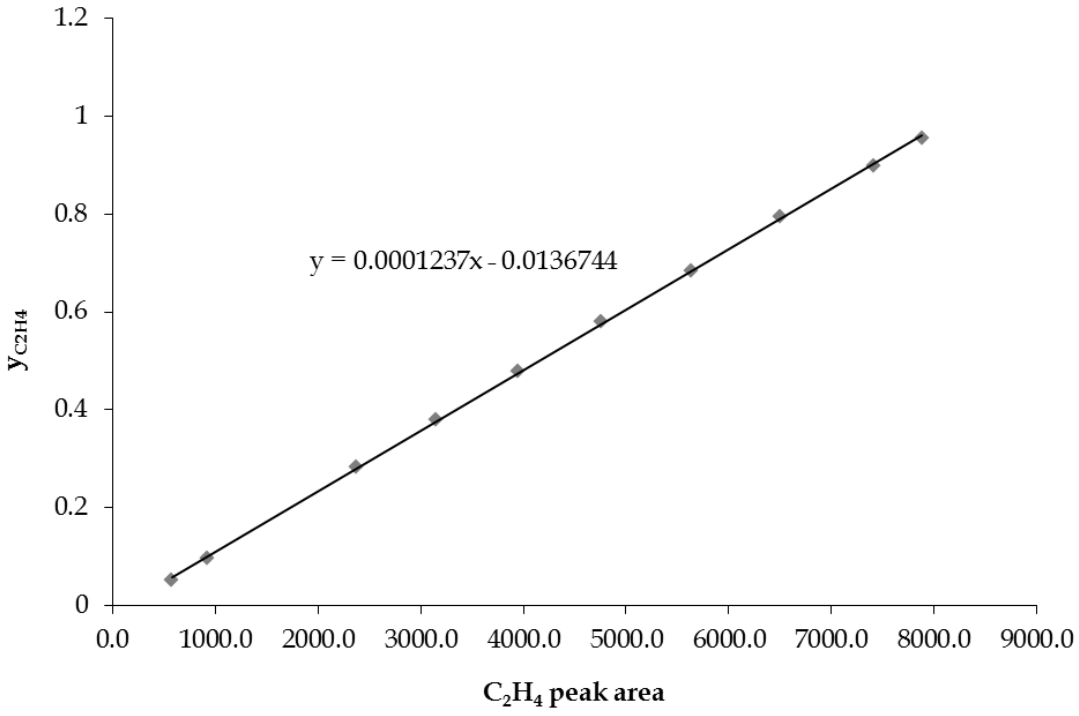


**Figure A. 11** *GC calibration line for analysis of ethylene in gas phase.*

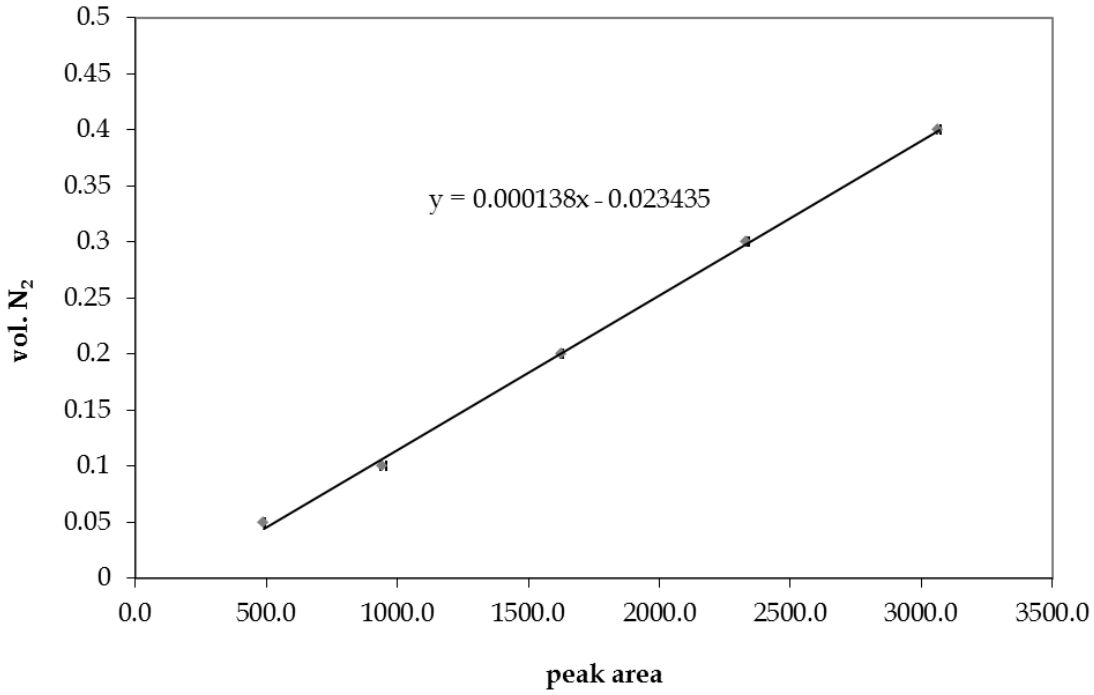


**Figure A. 12** *Gc calibration line for analysis of $N_2$/He mixtures.*

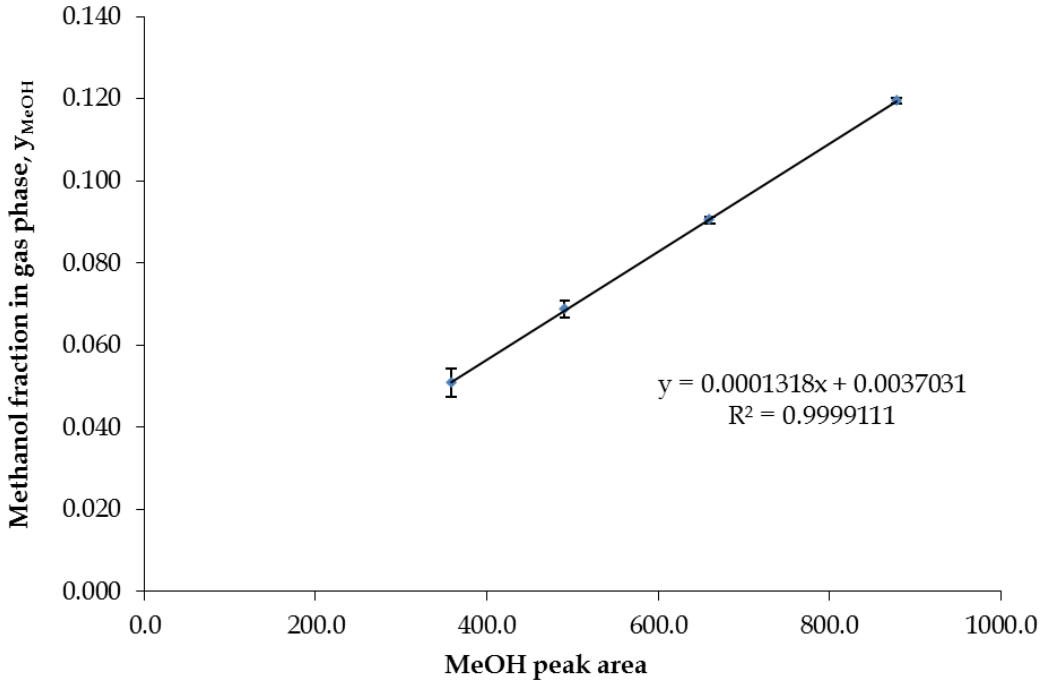


**Figure A. 13** *Gc calibration line for analysis of methanol in gas phase.*

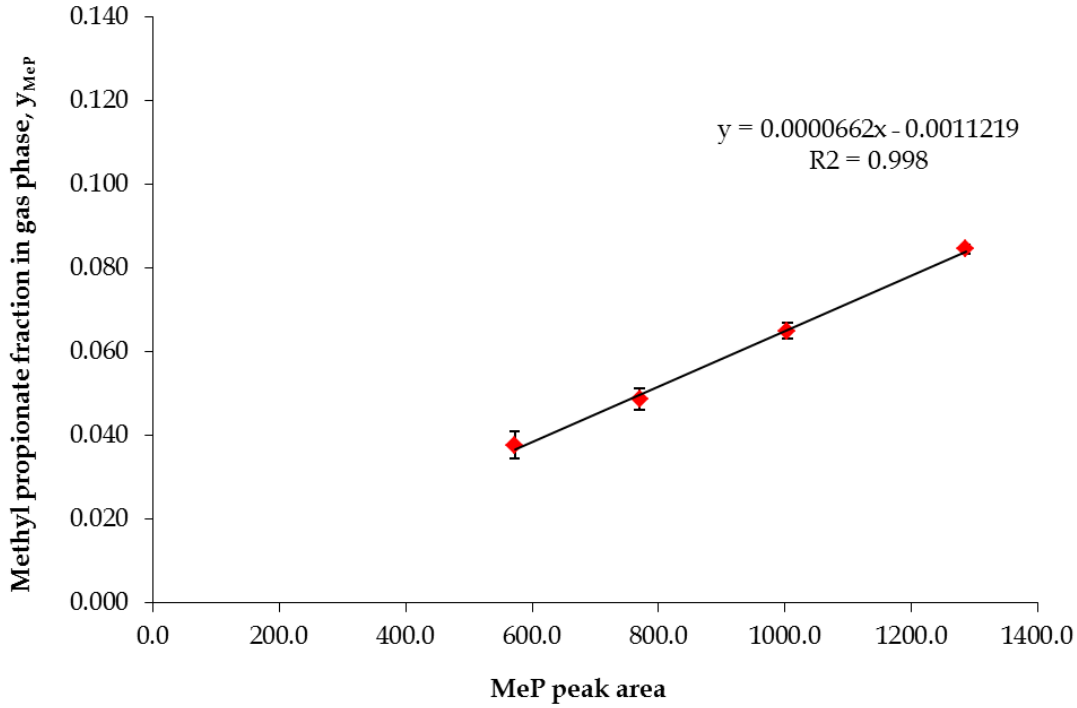


**Figure A. 14** *Gc calibration line for analysis of methyl propionate in gas phase.*

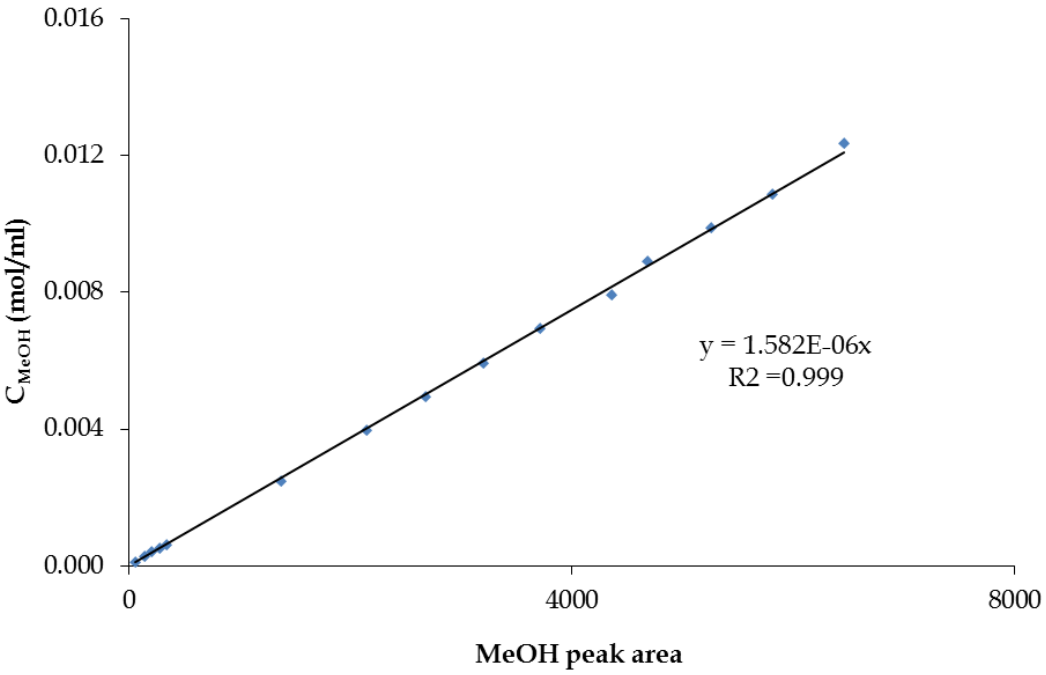


**Figure A. 15** *Gc calibration line for analysis of methanol in liquid phase.*

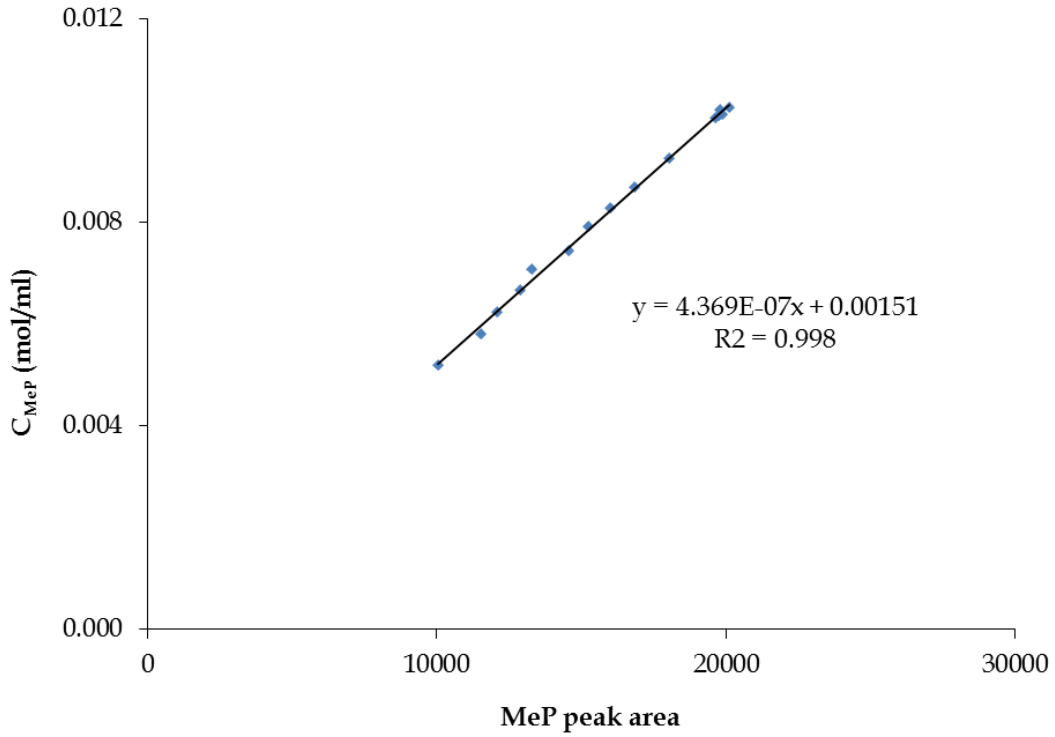


**Figure A. 16** *Gc calibration line for analysis of methyl propionate in liquid phase.*

# Appendix B

## Photos of Experimental Set-Up

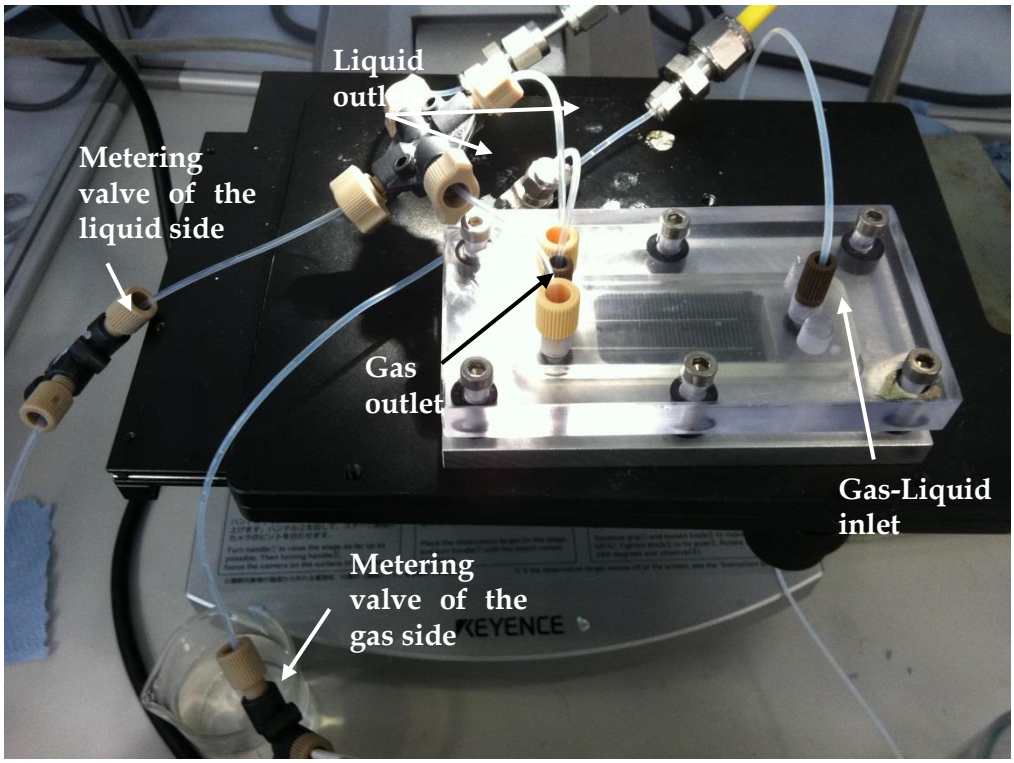


**Figure A. 17** *Experimental set-up for the test of the efficiency of the glass microseparator on separating gas-liquid streams under different gas and liquid flowrates by means of two metering valves in the gas and liquid exit to control the corresponding pressure difference.*

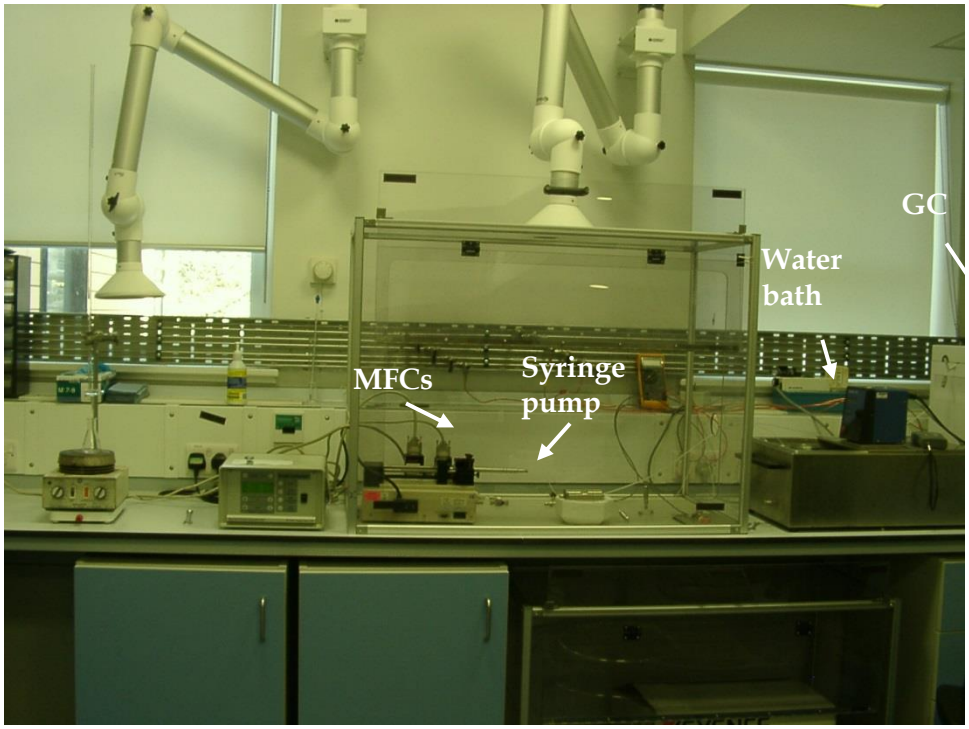


**Figure A. 18** *General view of experimental set-up used for the study of the model system.*

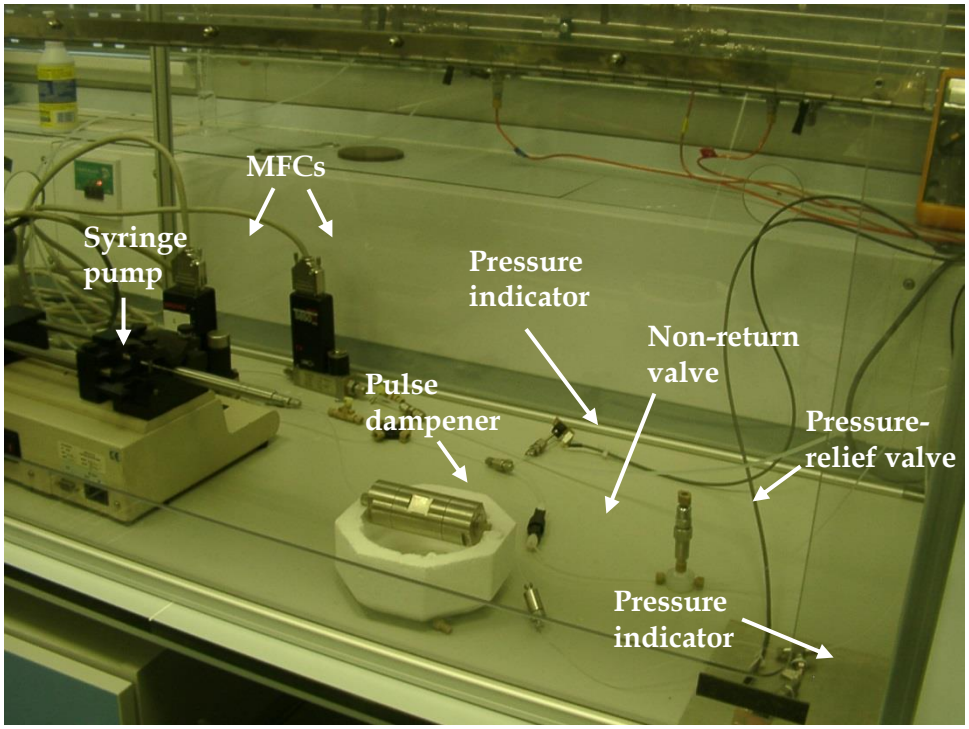


**Figure A. 19** *Closer view of the experimental set-up (upstream) used for the study of the model system .*

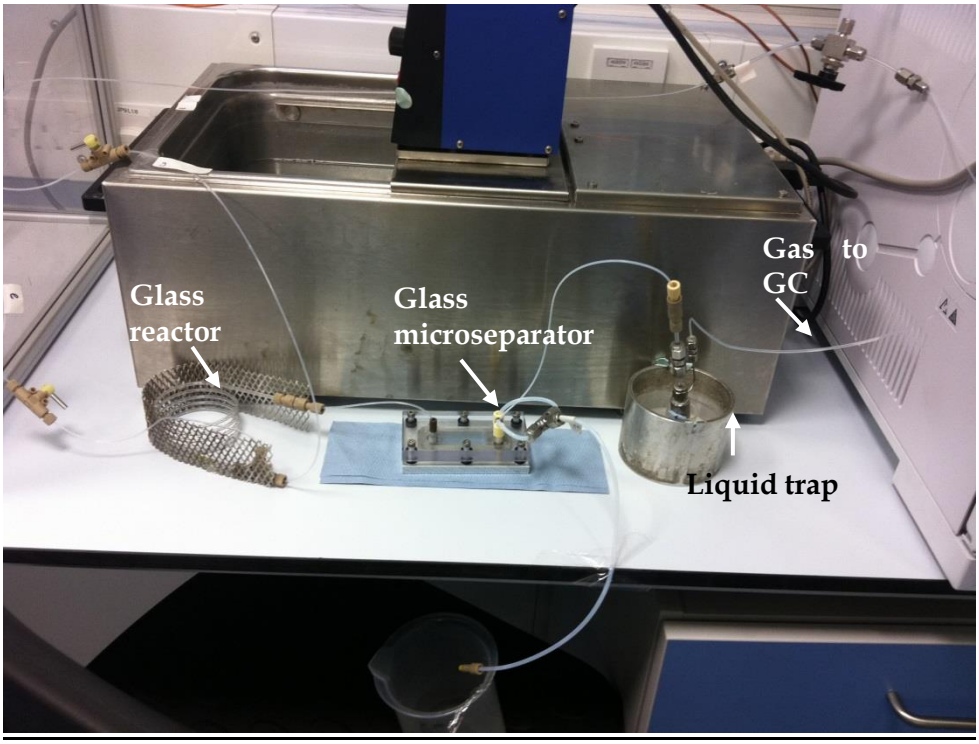


**Figure A. 20** *General view of the experimental set-up (downstream) for the analysis of the model reaction by means of a glass microseparator.*

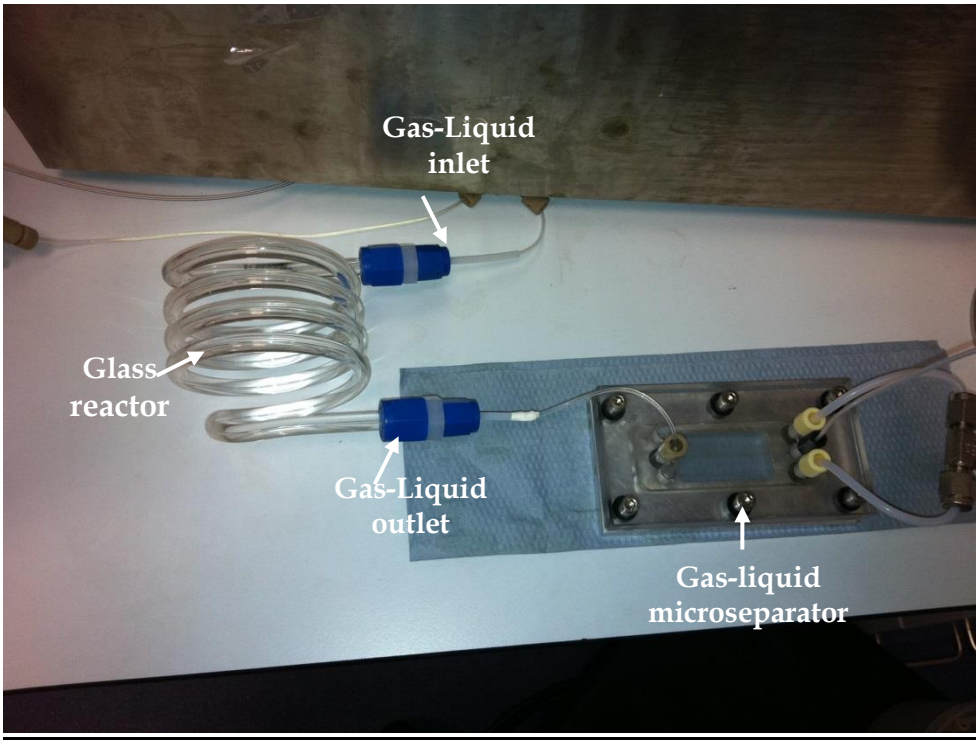


**Figure A. 21** *Closer view of one of the glass reactors (L=1m, ID=0.5mm) used for the model reaction study and the glass microseparator where gas was separated from the liquid and then was analysed by GC.*

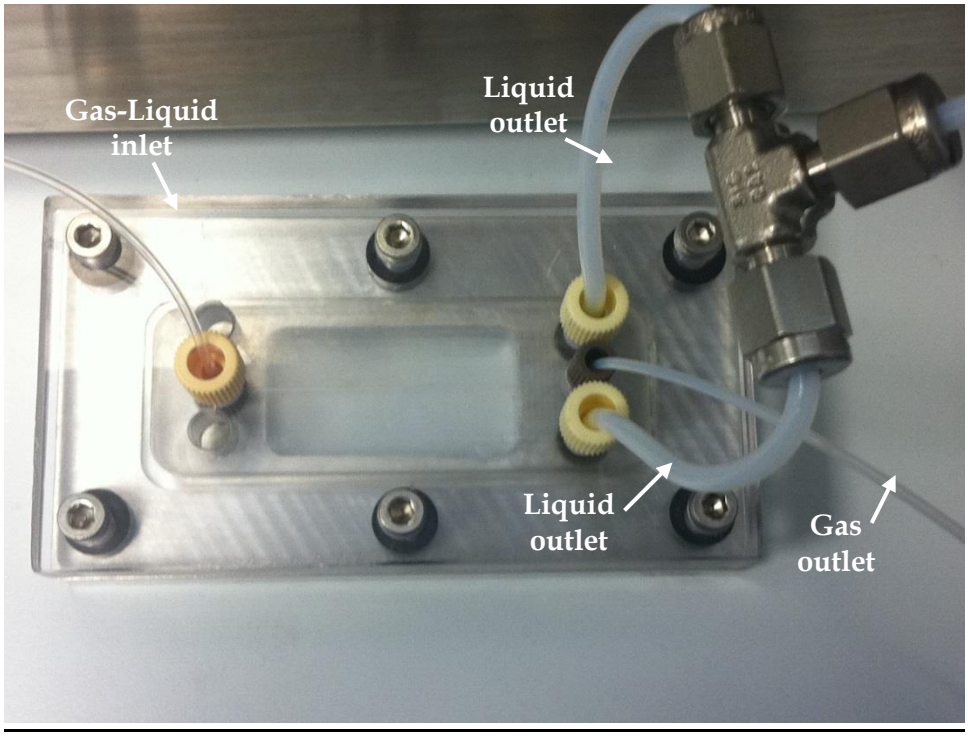


**Figure A. 22** *Closer view of the glass microseparator used for the study of the model reaction.*

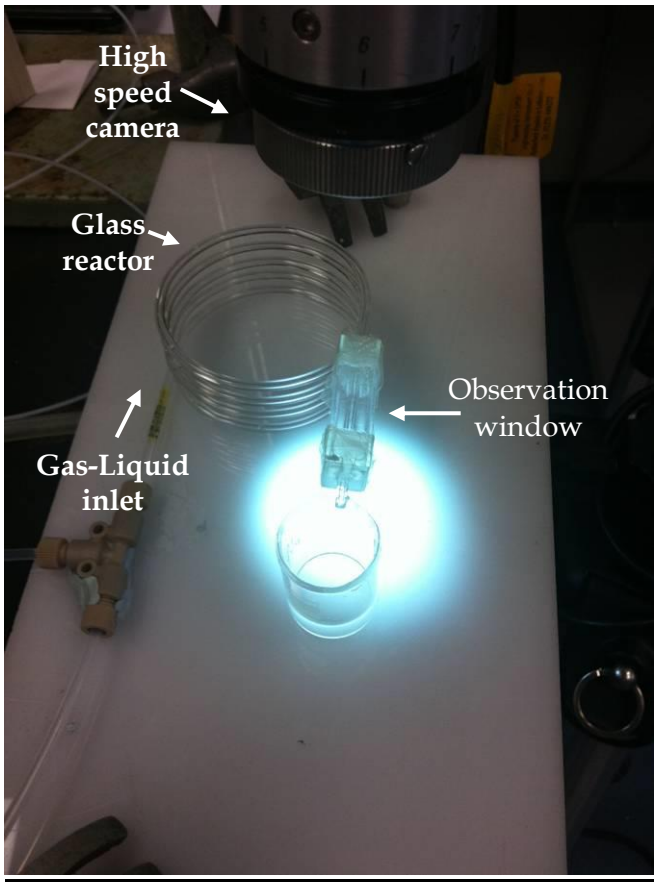


**Figure A. 23** *General view of the experimental set-up for the flow observation by means of a high speed camera.*

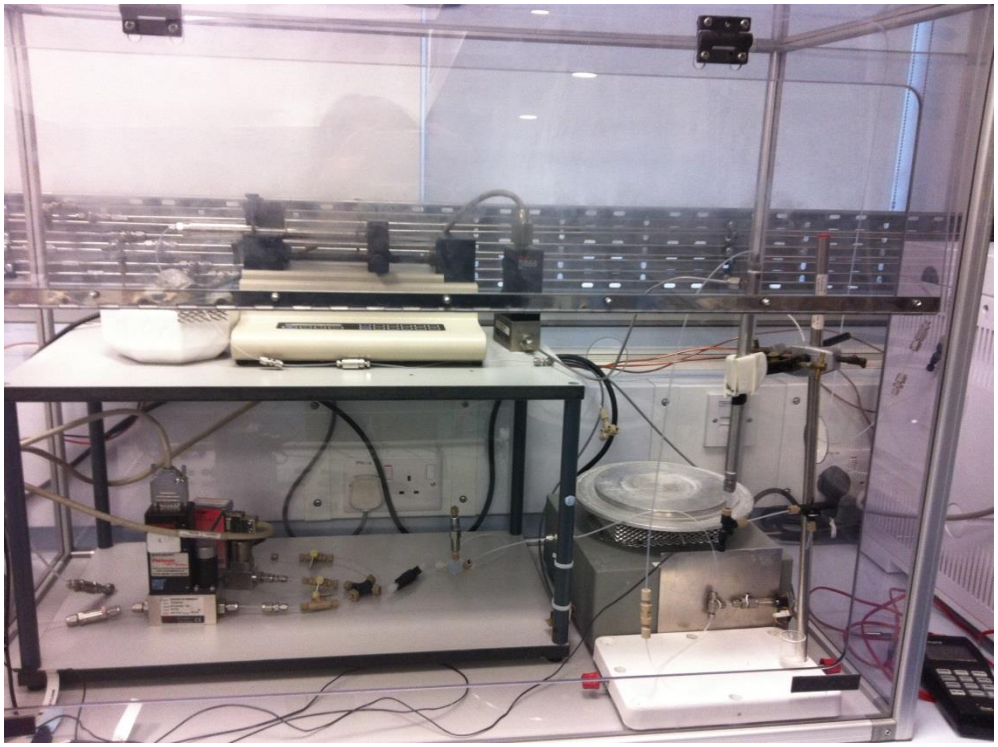

**Figure A. 24** *General view of the experimental set-up used for the study of MeP high pressure system.*

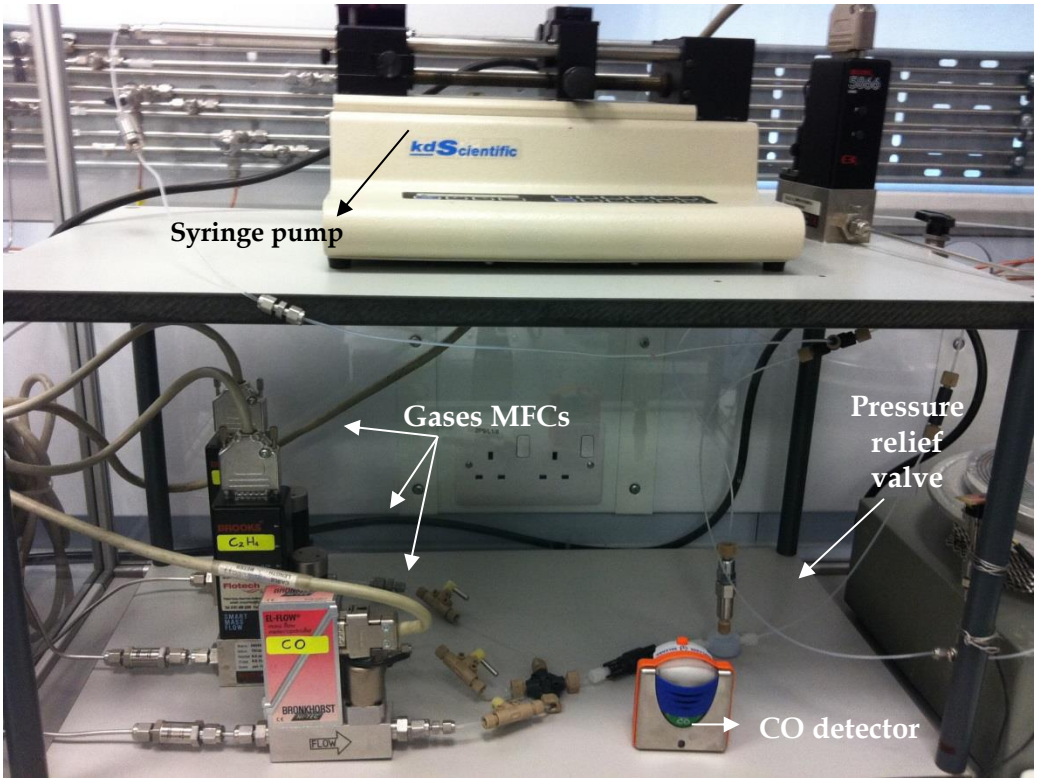


**Figure A. 25** *Closer view of the experimental set-up used for the study of the MeP high pressure system (upstream).*

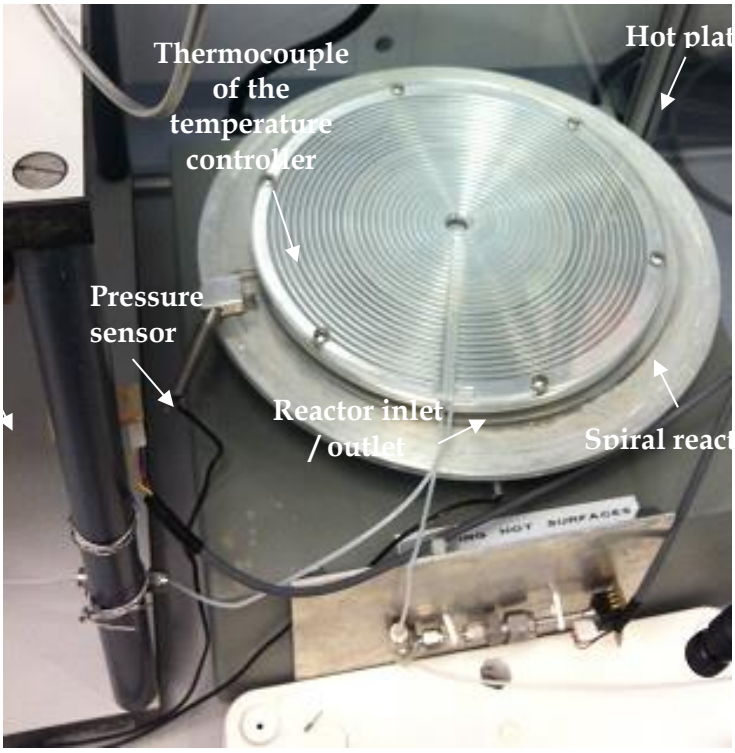


**Figure A. 26** *Spiral reactor tested for the study of the MeP system.*

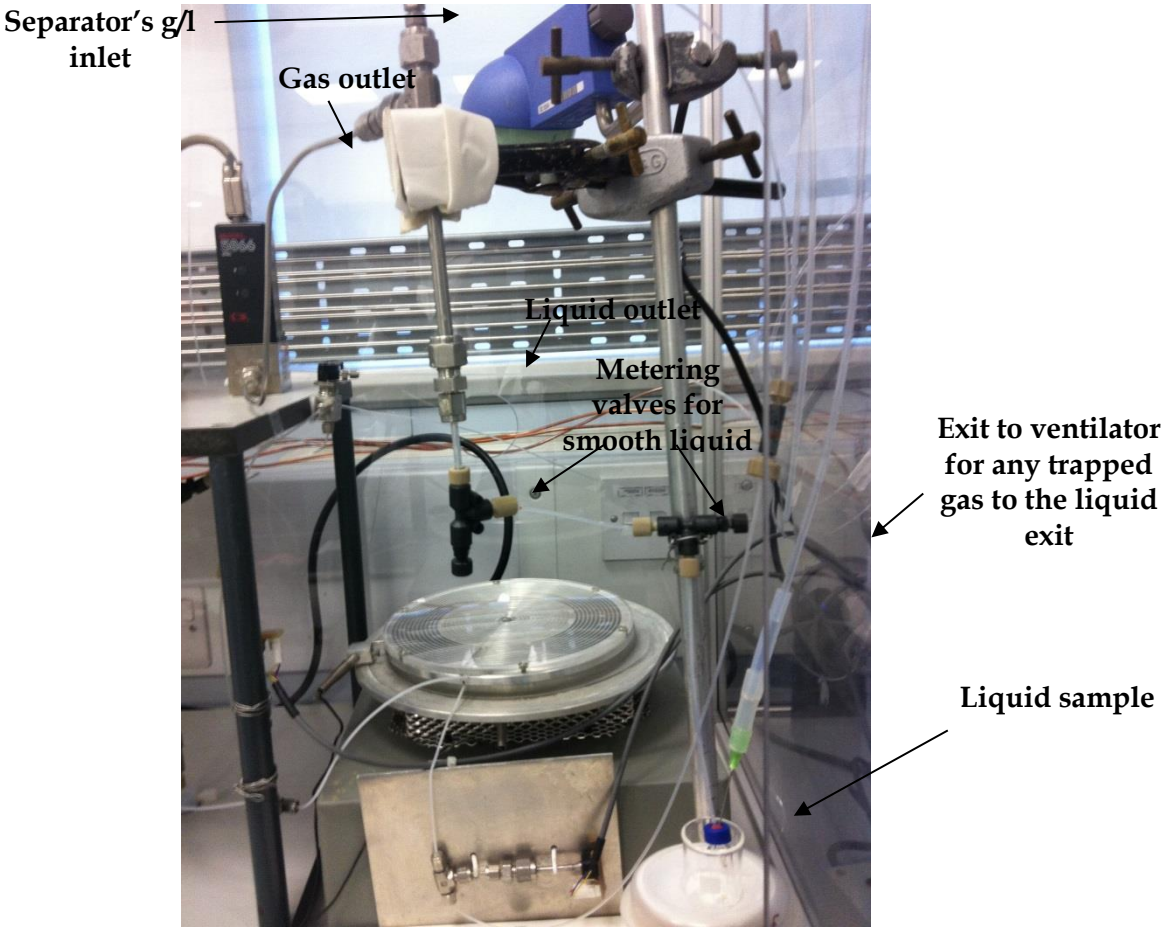


**Figure A. 27** *Closer view of the experimental set-up of the MeP high pressure system (downstream).*

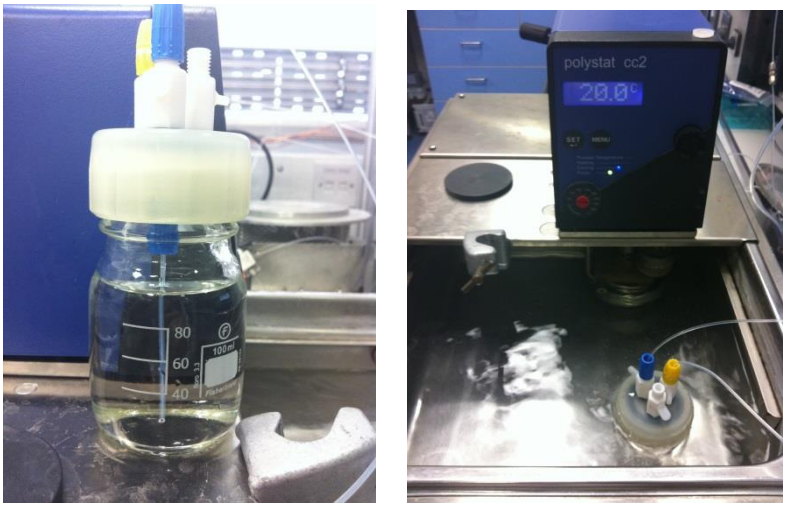


**Figure A. 28** *Photos of the set-up used for gc calibration of vapour MeOH. Bottle with MeOH bubbled with $N_2$/He (on the left) and cooling bath used to maintain the temperature constant (on the right).*

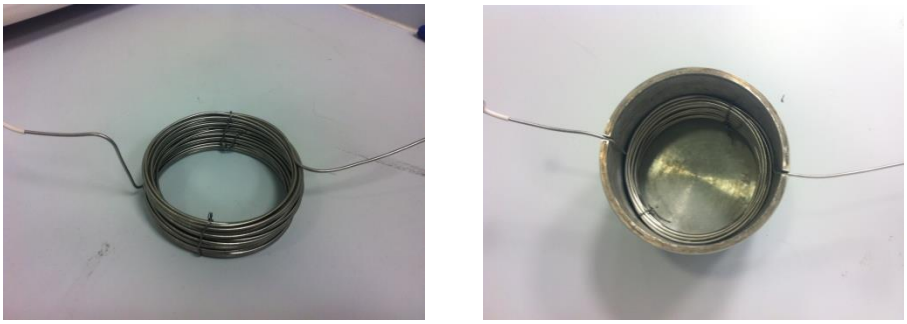

**Figure A. 29** *Stainless steel reactor tested for the study of MeP system and metallic vessel used as an oil bath to heat the reactor.*

# Appendix C

## Experimental Data of Residence Time Distribution Experiments

**Table A. 2** Raw RTD experimental data for $N_2$/DI water system for 0.2ml/min gas flowrate and 0.02ml/min liquid flowrate.

| $t_{norm}$ (s) | $F_{norm}$ | $t_{norm}$ (s) | $F_{norm}$ | $t_{norm}$ (s) | $F_{norm}$ | $t_{norm}$ (s) | $F_{norm}$ | $t_{norm}$ (s) | $F_{norm}$ |
|---|---|---|---|---|---|---|---|---|---|
| 0 | 0 | 0.550718 | 0.020393 | 1.101435 | 0.701899 | 1.652153 | 0.996227 | 2.20287 | 0.999973 |
| 0.026225 | 4.01E-05 | 0.576942 | 0.025451 | 1.12766 | 0.746698 | 1.678378 | 0.996989 | 2.229095 | 0.999973 |
| 0.052449 | 0.000107 | 0.603167 | 0.0317 | 1.153885 | 0.786814 | 1.704602 | 0.997591 | 2.25532 | 0.999987 |
| 0.078674 | 0.000174 | 0.629392 | 0.03942 | 1.180109 | 0.8221 | 1.730827 | 0.998073 | 2.281544 | 0.999987 |
| 0.104899 | 0.000268 | 0.655616 | 0.048907 | 1.206334 | 0.852622 | 1.757051 | 0.998461 | 2.307769 | 0.999987 |
| 0.131123 | 0.000388 | 0.681841 | 0.060522 | 1.232558 | 0.878688 | 1.783276 | 0.998769 | 2.333994 | 0.999987 |
| 0.157348 | 0.000535 | 0.708066 | 0.074679 | 1.258783 | 0.900686 | 1.809501 | 0.999023 | 2.360218 | 1 |
| 0.183573 | 0.000709 | 0.73429 | 0.091807 | 1.285008 | 0.919059 | 1.835725 | 0.999224 | 2.386443 | 1 |
| 0.209797 | 0.000937 | 0.760515 | 0.112387 | 1.311232 | 0.934273 | 1.86195 | 0.999371 | 2.412668 | 1 |
| 0.236022 | 0.001231 | 0.786739 | 0.136861 | 1.337457 | 0.946797 | 1.888175 | 0.999505 | 2.438892 | 1 |
| 0.262246 | 0.001579 | 0.812964 | 0.16567 | 1.363682 | 0.957047 | 1.914399 | 0.999599 | 2.465117 | 1 |
| 0.288471 | 0.002021 | 0.839189 | 0.199136 | 1.389906 | 0.965397 | 1.940624 | 0.999679 | 2.491342 | 1 |
| 0.314696 | 0.002583 | 0.865413 | 0.237432 | 1.416131 | 0.972168 | 1.966849 | 0.999746 | 2.517566 | 1 |
| 0.34092 | 0.003278 | 0.891638 | 0.280505 | 1.442356 | 0.97764 | 1.993073 | 0.999799 | 2.543791 | 1 |
| 0.367145 | 0.004148 | 0.917863 | 0.328034 | 1.46858 | 0.98207 | 2.019298 | 0.999839 | 2.570016 | 1 |
| 0.39337 | 0.005232 | 0.944087 | 0.37935 | 1.494805 | 0.985629 | 2.045523 | 0.99988 | 2.59624 | 1 |
| 0.419594 | 0.006597 | 0.970312 | 0.433517 | 1.52103 | 0.988479 | 2.071747 | 0.999893 | | |
| 0.445819 | 0.008296 | 0.996537 | 0.489329 | 1.547254 | 0.990781 | 2.097972 | 0.99992 | | |
| 0.472044 | 0.01041 | 1.022761 | 0.545395 | 1.573479 | 0.992627 | 2.124197 | 0.999933 | | |
| 0.498268 | 0.013033 | 1.048986 | 0.600324 | 1.599704 | 0.994099 | 2.150421 | 0.999946 | | |
| 0.524493 | 0.016311 | 1.075211 | 0.652858 | 1.625928 | 0.995277 | 2.176646 | 0.99996 | | |

**Table A. 3** Experimental data of residence time distribution experiments for $N_2$/DI water system.

| Exp | Reactor length | D | $V_r$ | $\upsilon_l$ | $\upsilon_g$ | Volumetric quality, β | Mean RT | Void fraction ε | *D/uL* |
|---|---|---|---|---|---|---|---|---|---|
| | cm | cm | ml | ml/min | ml/min | | s | | |
| **31_4** | 87 | 0.1 | 0.704979 | 0.005 | 0.2 | 0.97561 | 217.4199 | 0.974299 | 0.069104 |
| **31_5** | 87 | 0.1 | 0.704979 | 0.005 | 0.5 | 0.990099 | 73.17242 | 0.991351 | 0.235979 |
| **31_6** | 87 | 0.1 | 0.704979 | 0.005 | 1 | 0.995025 | 30.71876 | 0.996369 | 0.64919 |
| **31_7** | 87 | 0.1 | 0.704979 | 0.005 | 1.5 | 0.996678 | 27.75113 | 0.99672 | 0.775928 |
| **31_8** | 87 | 0.1 | 0.704979 | 0.005 | 2 | 0.997506 | 26.89757 | 0.996821 | 1.359412 |
| **31_9** | 93.5 | 0.1 | 0.75765 | 0.02 | 0.181818 | 0.900901 | 221.2285 | 0.902669 | 0.023441 |
| **31_10** | 93.5 | 0.1 | 0.75765 | 0.05 | 0.167926 | 0.770564 | 236.8411 | 0.7395 | 0.007572 |
| **31_11** | 93.5 | 0.1 | 0.75765 | 0.1 | 0.152905 | 0.604595 | 206.2997 | 0.546185 | 0.003983 |
| **31_12** | 93.5 | 0.1 | 0.75765 | 0.3 | 0.12945 | 0.301432 | 127.6534 | 0.15757 | 0.004683 |
| **31_13** | 93.5 | 0.1 | 0.75765 | 0.15 | 0.142857 | 0.487805 | 196.2758 | 0.352353 | 0.000542 |
| **31_14''** | 97.5 | 0.1 | 0.790063 | 0.5 | 0.162075 | 0.244798 | 86.30805 | 0.08965 | 0.000965 |
| **31_15'** | 97.5 | 0.1 | 0.790063 | 0.25 | 0.168209 | 0.402212 | 139.9723 | 0.261808 | 0.001964 |
| **31_16** | 97.5 | 0.1 | 0.790063 | 0.07 | 0.136705 | 0.661354 | 240.6984 | 0.644567 | 0.002236 |
| **31_17** | 97.5 | 0.1 | 0.790063 | 0.03 | 0.157729 | 0.840195 | 190.6332 | 0.879356 | 6.82E-05 |
| **31_18** | 97.5 | 0.1 | 0.790063 | 0.13 | 0.166667 | 0.561798 | 194.8267 | 0.465708 | 0.000617 |
| **31_4** | 87 | 0.1 | 0.704979 | 0.005 | 0.2 | 0.97561 | 217.4199 | 0.974299 | 0.069104 |
| **31_5** | 87 | 0.1 | 0.704979 | 0.005 | 0.5 | 0.990099 | 73.17242 | 0.991351 | 0.235979 |
| **31_6** | 87 | 0.1 | 0.704979 | 0.005 | 1 | 0.995025 | 30.71876 | 0.996369 | 0.64919 |
| **31_7** | 87 | 0.1 | 0.704979 | 0.005 | 1.5 | 0.996678 | 27.75113 | 0.99672 | 0.775928 |
| **31_8** | 87 | 0.1 | 0.704979 | 0.005 | 2 | 0.997506 | 26.89757 | 0.996821 | 1.359412 |
| **31_9** | 93.5 | 0.1 | 0.75765 | 0.02 | 0.181818 | 0.900901 | 221.2285 | 0.902669 | 0.023441 |

**Table A. 3** (continued)

| Exp | Reactor length | D | $V_r$ | $\upsilon_l$ | $\upsilon_g$ | Volumetric quality, β | Mean RT | Void fraction ε | *D/uL* |
|---|---|---|---|---|---|---|---|---|---|
| | cm | cm | cc | cc/min | cc/min | | s | | |
| **31_10** | 93.5 | 0.1 | 0.75765 | 0.05 | 0.167926 | 0.770564 | 236.8411 | 0.7395 | 0.007572 |
| **31_11** | 93.5 | 0.1 | 0.75765 | 0.1 | 0.152905 | 0.604595 | 206.2997 | 0.546185 | 0.003983 |
| **31_12** | 93.5 | 0.1 | 0.75765 | 0.3 | 0.12945 | 0.301432 | 127.6534 | 0.15757 | 0.004683 |
| **31_13** | 93.5 | 0.1 | 0.75765 | 0.15 | 0.142857 | 0.487805 | 196.2758 | 0.352353 | 0.000542 |
| **31_14''** | 97.5 | 0.1 | 0.790063 | 0.5 | 0.162075 | 0.244798 | 86.30805 | 0.08965 | 0.000965 |
| **31_15'** | 97.5 | 0.1 | 0.790063 | 0.25 | 0.168209 | 0.402212 | 139.9723 | 0.261808 | 0.001964 |
| **31_16** | 97.5 | 0.1 | 0.790063 | 0.07 | 0.136705 | 0.661354 | 240.6984 | 0.644567 | 0.002236 |
| **31_17** | 97.5 | 0.1 | 0.790063 | 0.03 | 0.157729 | 0.840195 | 190.6332 | 0.879356 | 6.82E-05 |
| **31_18** | 97.5 | 0.1 | 0.790063 | 0.13 | 0.166667 | 0.561798 | 194.8267 | 0.465708 | 0.000617 |
| **36_1** | 103 | 0.05 | 0.208658 | 0.005 | 2 | 0.997506 | 17.71025 | 0.992927 | 1.325351 |
| **36_2** | 103 | 0.05 | 0.208658 | 0.005 | 0.2 | 0.97561 | 76.78833 | 0.969332 | 0.227085 |
| **36_3** | 103 | 0.05 | 0.208658 | 0.02 | 0.2 | 0.909091 | 49.8353 | 0.920387 | 0.056659 |
| **36_4** | 103 | 0.05 | 0.208658 | 0.05 | 0.163265 | 0.76555 | 66.02941 | 0.736293 | 0.003788 |
| **36_5** | 103 | 0.05 | 0.208658 | 0.1 | 0.151515 | 0.60241 | 63.40049 | 0.493584 | 0.001963 |
| **36_7** | 103 | 0.05 | 0.208658 | 0.3 | 0.125 | 0.294118 | 34.86917 | 0.164441 | 0.006757 |
| **36_8** | 103 | 0.05 | 0.208658 | 0.15 | 0.132802 | 0.469594 | 52.33121 | 0.373002 | 0.002984 |
| **36_9** | 103 | 0.05 | 0.208658 | 0.12 | 0.135135 | 0.529661 | 61.55923 | 0.40995 | 0.007856 |
| **36_6'** | 103 | 0.05 | 0.208658 | 0.2 | 0.12987 | 0.393701 | 50.38296 | 0.195126 | 0.006038 |
| **36_10** | 103 | 0.05 | 0.208658 | 0.06 | 0.161551 | 0.729182 | 60.98144 | 0.707744 | 0.020497 |
| **36_11** | 103 | 0.05 | 0.208658 | 0.04 | 0.166667 | 0.806452 | 77.69802 | 0.751753 | 0.010799 |
| **36_12** | 103 | 0.05 | 0.208658 | 0.08 | 0.142857 | 0.641026 | 86.82808 | 0.445164 | 0.003001 |
| **36_14** | 103 | 0.05 | 0.208658 | 0.25 | 0.13245 | 0.34632 | 38.81996 | 0.224808 | 0.001667 |
| **36_13'** | 103 | 0.05 | 0.208658 | 0.18 | 0.135135 | 0.428816 | 50.47935 | 0.274227 | 0.001078 |
| **38_1** | 265.8 | 0.025 | 0.134615 | 0.005 | 0.190658 | 0.974445 | 92.63664 | 0.942653 | 0.567688 |
| **38_3** | 265.8 | 0.025 | 0.134615 | 0.02 | 0.181159 | 0.900576 | 53.17411 | 0.86833 | 0.182469 |
| **38_4** | 265.8 | 0.025 | 0.134615 | 0.05 | 0.158103 | 0.759734 | 44.34948 | 0.725454 | 0.069201 |
| **38_5** | 265.8 | 0.025 | 0.134615 | 0.1 | 0.133333 | 0.571429 | 41.38256 | 0.487641 | 0.002868 |
| **38_6** | 265.8 | 0.025 | 0.134615 | 0.2 | 0.096618 | 0.325733 | 32.44125 | 0.196688 | 0.010978 |

**Table A. 4** Experimental data of residence time distribution experiments for $N_2$/ pure methanol system.

| Exp | Reactor length | ID | $V_r$ | $\upsilon_l$ | $\upsilon_g$ | Volumetric quality, β | Mean RT | Void fraction ε | *D/uL* |
|---|---|---|---|---|---|---|---|---|---|
| | cm | cm | ml | ml/min | ml/min | | s | | |
| **35_1** | 87 | 0.1 | 0.70498 | 0.005 | 2 | 0.99751 | 355.55 | 0.95797 | 0.03746 |
| **35_2** | 87 | 0.1 | 0.70498 | 0.005 | 0.2 | 0.97561 | 249.947 | 0.97046 | 0.0216 |
| **35_3** | 87 | 0.1 | 0.70498 | 0.02 | 0.2 | 0.90909 | 124.59 | 0.94109 | 0.0068 |
| **35_01** | 87 | 0.1 | 0.70498 | 0.2 | 0.2 | 0.5 | 98.4346 | 0.53457 | 0.00457 |
| **35_02** | 87 | 0.1 | 0.70498 | 0.05 | 0.2 | 0.8 | 168.276 | 0.80109 | 0.00082 |
| **35_03** | 87 | 0.1 | 0.70498 | 0.1 | 0.2 | 0.66667 | 142.331 | 0.66351 | 0.00028 |
| **35_04** | 87 | 0.1 | 0.70498 | 0.15 | 0.2 | 0.57143 | 125.14 | 0.55623 | 0.00166 |
| **35_05'** | 97.5 | 0.1 | 0.79006 | 0.3 | 0.1998 | 0.39976 | 87.3037 | 0.44749 | 7.29E-05 |
| **35_06** | 97.5 | 0.1 | 0.79006 | 0.4 | 0.19685 | 0.32982 | 74.3551 | 0.37258 | 0.00061 |
| **35_07** | 97.5 | 0.1 | 0.79006 | 0.6 | 0.1998 | 0.24981 | 56.1025 | 0.2899 | 1.36E-05 |
| **35_08** | 97.5 | 0.1 | 0.79006 | 0.8 | 0.19802 | 0.19841 | 46.001 | 0.22367 | 0.00025 |
| **37_1** | 103 | 0.05 | 0.20866 | 0.005 | 2 | 0.99751 | 41.8446 | 0.98329 | 0.40335 |
| **37_2** | 103 | 0.05 | 0.20866 | 0.005 | 0.2 | 0.97561 | 66.9985 | 0.97324 | 0.11202 |
| **37_3** | 103 | 0.05 | 0.20866 | 0.02 | 0.2 | 0.90909 | 52.0701 | 0.91682 | 0.05007 |
| **37_4** | 103 | 0.05 | 0.20866 | 0.05 | 0.2 | 0.8 | 49.4608 | 0.80246 | 0.01032 |
| **37_5** | 103 | 0.05 | 0.20866 | 0.1 | 0.2 | 0.66667 | 66.6464 | 0.46766 | 0.00767 |
| **37_6** | 103 | 0.05 | 0.20866 | 0.2 | 0.2 | 0.5 | 32.7534 | 0.47676 | 0.00122 |
| **37_7** | 103 | 0.05 | 0.20866 | 0.3 | 0.2 | 0.4 | 31.529 | 0.24448 | 8.46E-05 |

**Table A. 5** Experimental data of residence time distribution experiments for $N_2$/10% aqueous glycerol system.

| Exp | Reactor length | ID | $V_r$ | $\upsilon_l$ | $\upsilon_g$ | Volumetric quality, β | Mean RT | Void fraction ε | *D/uL* |
|---|---|---|---|---|---|---|---|---|---|
| | cm | cm | ml | ml/min | ml/min | | s | | |
| **39_1** | 97.5 | 0.1 | 0.79006 | 0.005 | 2 | 0.99751 | 6.2159 | 0.99934 | 1.74945 |
| **39_2** | 97.5 | 0.1 | 0.79006 | 0.005 | 0.18433 | 0.97359 | 217.892 | 0.97702 | 0.03246 |
| **39_3** | 97.5 | 0.1 | 0.79006 | 0.02 | 0.11173 | 0.84818 | 210.646 | 0.91113 | 0.01453 |
| **39_4** | 97.5 | 0.1 | 0.79006 | 0.05 | 0.1087 | 0.68493 | 305.924 | 0.67732 | 0.00114 |
| **39_5** | 97.5 | 0.1 | 0.79006 | 0.1 | 0.11933 | 0.54407 | 208.156 | 0.56089 | 3.75E-05 |
| **39_6** | 97.5 | 0.1 | 0.79006 | 0.2 | 0.13605 | 0.40486 | 138.613 | 0.41518 | 0.00039 |
| **39_7'** | 97.5 | 0.1 | 0.79006 | 0.3 | 0.13072 | 0.30349 | 102.612 | 0.35061 | 0.00225 |
| **39_8** | 97.5 | 0.1 | 0.79006 | 0.4 | 0.13289 | 0.24938 | 84.9248 | 0.28339 | 0.00214 |
| **39_9** | 97.5 | 0.1 | 0.79006 | 0.5 | 0.13405 | 0.21142 | 72.1598 | 0.23888 | 0.00309 |

**Table A. 6** Predictions of void fraction from previous hydrodynamic models and our suggested correlation for the $N_2$/DI water system.

| Exp | Volumetric quality | Homogenous | Armand | Chawla | Serizawa | Tripplet | Coleman | Kawahara | Kariyasaki | Saisorn | New correlation |
|---|---|---|---|---|---|---|---|---|---|---|---|
| | | $\varepsilon_g$ | $\varepsilon_g$ | $\varepsilon_g$ | $\varepsilon_g$ | $\varepsilon_g$ | $\varepsilon_g$ | $\varepsilon_g$ | $\varepsilon_g$ | $\varepsilon_g$ | $\varepsilon_g$ |
| **31_4** | 0.97561 | 0.97561 | 0.817374 | 0.080186 | 0.758971 | 0.814182 | 0.860074 | 0.707166 | 0.999875 | 0.533944 | 0.974202 |
| **31_5** | 0.990099 | 0.990099 | 0.839865 | 0.068801 | 0.768968 | 0.887339 | 0.914582 | 0.857448 | 0.999942 | 0.600124 | 0.989602 |
| **31_6** | 0.995025 | 0.995025 | 0.85869 | 0.062262 | 0.772367 | 0.924663 | 0.944518 | 0.923165 | 0.999967 | 0.626121 | 0.994788 |
| **31_7** | 0.996678 | 0.996678 | 0.872192 | 0.059055 | 0.773508 | 0.940864 | 0.958357 | 0.94741 | 0.999977 | 0.63531 | 0.996522 |
| **31_8** | 0.997506 | 0.997506 | 0.88304 | 0.057 | 0.774079 | 0.950314 | 0.966684 | 0.960024 | 0.999982 | 0.640009 | 0.997391 |
| **31_9** | 0.900901 | 0.900901 | 0.749405 | 0.093275 | 0.707422 | 0.629294 | 0.721353 | 0.359 | 0.998197 | 0.331597 | 0.891374 |
| **31_10** | 0.770564 | 0.770564 | 0.639568 | 0.104295 | 0.617489 | 0.472999 | 0.584502 | 0.177317 | 0.989408 | 0.185387 | 0.73418 |
| **31_11** | 0.604595 | 0.604595 | 0.501814 | 0.114704 | 0.50297 | 0.351673 | 0.455314 | 0.094913 | 0.959419 | 0.105547 | 0.517805 |
| **31_12** | 0.301432 | 0.301432 | 0.250188 | 0.134417 | 0.293788 | 0.194445 | 0.245739 | 0.035236 | 0.725201 | 0.041077 | 0.150828 |
| **31_13** | 0.487805 | 0.487805 | 0.404878 | 0.121749 | 0.422385 | 0.28604 | 0.374032 | 0.064966 | 0.912806 | 0.073955 | 0.364766 |
| **31_14''** | 0.244798 | 0.244798 | 0.203182 | 0.135339 | 0.254711 | 0.167359 | 0.20502 | 0.02854 | 0.55026 | 0.033453 | 0.100298 |
| **31_15'** | 0.402212 | 0.402212 | 0.333836 | 0.124258 | 0.363326 | 0.242858 | 0.315635 | 0.049441 | 0.821822 | 0.056981 | 0.259421 |
| **31_16** | 0.661354 | 0.661354 | 0.548924 | 0.113053 | 0.542134 | 0.38815 | 0.496809 | 0.115538 | 0.97673 | 0.126469 | 0.592948 |
| **31_17** | 0.840195 | 0.840195 | 0.697362 | 0.100135 | 0.665534 | 0.544563 | 0.65047 | 0.24801 | 0.99568 | 0.246638 | 0.820025 |
| **31_18** | 0.561798 | 0.561798 | 0.466292 | 0.115841 | 0.47344 | 0.326413 | 0.425075 | 0.08238 | 0.93957 | 0.092505 | 0.461131 |
| **36_1** | 0.997506 | 0.997506 | 0.88304 | 0.052644 | 0.774079 | 0.950314 | 0.966684 | 0.960024 | 0.999891 | 0.640009 | 0.997391 |
| **36_2** | 0.97561 | 0.97561 | 0.817374 | 0.071251 | 0.758971 | 0.814182 | 0.860074 | 0.707166 | 0.999264 | 0.533944 | 0.974202 |
| **36_3** | 0.909091 | 0.909091 | 0.756383 | 0.080186 | 0.713073 | 0.643408 | 0.732554 | 0.380668 | 0.990254 | 0.346791 | 0.900729 |
| **36_4** | 0.76555 | 0.76555 | 0.635407 | 0.090924 | 0.61403 | 0.468511 | 0.580141 | 0.173498 | 0.939299 | 0.181898 | 0.727852 |
| **36_5** | 0.60241 | 0.60241 | 0.5 | 0.099075 | 0.501463 | 0.350342 | 0.453751 | 0.094218 | 0.799151 | 0.104831 | 0.514906 |
| **36_7** | 0.294118 | 0.294118 | 0.244118 | 0.116163 | 0.288741 | 0.190962 | 0.240556 | 0.034329 | 0.302994 | 0.040049 | 0.143823 |
| **36_8** | 0.469594 | 0.469594 | 0.389763 | 0.106337 | 0.40982 | 0.276597 | 0.361598 | 0.061315 | 0.625594 | 0.070001 | 0.341646 |
| **36_9** | 0.529661 | 0.529661 | 0.439619 | 0.103452 | 0.451266 | 0.308435 | 0.402765 | 0.074249 | 0.720127 | 0.083907 | 0.418904 |

**Table A. 6** (continued)

| Exp | Volumetric quality | Homogenous | Armand | Chawla | Serizawa | Tripplet | Coleman | Kawahara | Kariyasaki | Saisorn | New correlation |
|---|---|---|---|---|---|---|---|---|---|---|---|
| | | $\varepsilon_g$ | $\varepsilon_g$ | $\varepsilon_g$ | $\varepsilon_g$ | $\varepsilon_g$ | $\varepsilon_g$ | $\varepsilon_g$ | $\varepsilon_g$ | $\varepsilon_g$ | $\varepsilon_g$ |
| **36_6'** | 0.393701 | 0.393701 | 0.326772 | 0.110215 | 0.357454 | 0.238702 | 0.30981 | 0.048097 | 0.489218 | 0.055492 | 0.249495 |
| **36_10** | 0.729182 | 0.729182 | 0.605221 | 0.092794 | 0.588935 | 0.437931 | 0.549642 | 0.149203 | 0.916021 | 0.159244 | 0.681439 |
| **36_11** | 0.806452 | 0.806452 | 0.669355 | 0.088584 | 0.642252 | 0.507471 | 0.617081 | 0.208982 | 0.959827 | 0.213583 | 0.77892 |
| **36_12** | 0.641026 | 0.641026 | 0.532051 | 0.097995 | 0.528108 | 0.374635 | 0.481723 | 0.107527 | 0.851881 | 0.118421 | 0.566096 |
| **36_14** | 0.34632 | 0.34632 | 0.287446 | 0.112438 | 0.324761 | 0.215848 | 0.277167 | 0.041137 | 0.390768 | 0.047729 | 0.196607 |
| **36_13'** | 0.428816 | 0.428816 | 0.355918 | 0.108036 | 0.381683 | 0.255985 | 0.333801 | 0.053851 | 0.546583 | 0.061846 | 0.29117 |
| **38_1** | 0.974445 | 0.974445 | 0.816059 | 0.064643 | 0.758167 | 0.809505 | 0.856665 | 0.697226 | 0.995501 | 0.529197 | 0.972955 |
| **38_3** | 0.900576 | 0.900576 | 0.74913 | 0.072399 | 0.707198 | 0.628752 | 0.72092 | 0.358187 | 0.940727 | 0.331019 | 0.891002 |
| **38_4** | 0.759734 | 0.759734 | 0.630579 | 0.080187 | 0.610017 | 0.463394 | 0.575134 | 0.169224 | 0.718705 | 0.177972 | 0.720488 |
| **38_5** | 0.571429 | 0.571429 | 0.474286 | 0.088379 | 0.480086 | 0.331956 | 0.43182 | 0.085016 | 0.377643 | 0.095269 | 0.473856 |
| **38_6** | 0.325733 | 0.325733 | 0.270358 | 0.101242 | 0.310556 | 0.206018 | 0.262828 | 0.038356 | 0.112737 | 0.044602 | 0.175039 |

**Table A. 7** Predictions of void fraction from previous hydrodynamic models and our suggested correlation for the $N_2$/ methanol system.

| Exp | Volumetric quality | Homogenous | Armand | Chawla | Serizawa | Triplett | Coleman | Kawahara | Kariyasaki | Saisorn |
|---|---|---|---|---|---|---|---|---|---|---|
| | | $\varepsilon_g$ | $\varepsilon_g$ | $\varepsilon_g$ | $\varepsilon_g$ | $\varepsilon_g$ | $\varepsilon_g$ | $\varepsilon_g$ | $\varepsilon_g$ | $\varepsilon_g$ |
| **35_1** | 0.997506 | 0.997506 | 0.892428 | 0.040596 | 0.774079 | 0.955067 | 0.969315 | 0.960024 | 0.999966 | 0.640009 |
| **35_2** | 0.97561 | 0.97561 | 0.819348 | 0.065836 | 0.758971 | 0.829621 | 0.861675 | 0.707166 | 0.999772 | 0.533944 |
| **35_3** | 0.909091 | 0.909091 | 0.756881 | 0.079239 | 0.713073 | 0.667237 | 0.733288 | 0.380668 | 0.996959 | 0.346791 |
| **35_01** | 0.5 | 0.5 | 0.415 | 0.11078 | 0.4308 | 0.314764 | 0.382489 | 0.067535 | 0.815588 | 0.076724 |
| **35_02** | 0.8 | 0.8 | 0.664 | 0.090276 | 0.6378 | 0.527295 | 0.611415 | 0.202656 | 0.983359 | 0.208052 |
| **35_03** | 0.666667 | 0.666667 | 0.553333 | 0.099926 | 0.5458 | 0.417189 | 0.50102 | 0.117765 | 0.941746 | 0.128689 |
| **35_04** | 0.571429 | 0.571429 | 0.474286 | 0.106125 | 0.480086 | 0.355758 | 0.43197 | 0.085016 | 0.883366 | 0.095269 |
| **35_05'** | 0.39976 | 0.39976 | 0.331801 | 0.117745 | 0.361634 | 0.261521 | 0.31403 | 0.049051 | 0.674298 | 0.056549 |
| **35_06** | 0.329815 | 0.329815 | 0.273747 | 0.12348 | 0.313373 | 0.225882 | 0.265731 | 0.038897 | 0.544228 | 0.045211 |
| **35_07** | 0.249813 | 0.249813 | 0.207344 | 0.130619 | 0.258171 | 0.185172 | 0.208715 | 0.029105 | 0.361584 | 0.034099 |
| **35_08** | 0.198413 | 0.198413 | 0.164683 | 0.13671 | 0.222705 | 0.15822 | 0.17046 | 0.02353 | 0.247146 | 0.027692 |
| **37_1** | 0.997506 | 0.997506 | 0.892428 | 0.036304 | 0.774079 | 0.955067 | 0.969315 | 0.960024 | 0.999801 | 0.640009 |
| **37_2** | 0.97561 | 0.97561 | 0.819348 | 0.055701 | 0.758971 | 0.829621 | 0.861675 | 0.707166 | 0.998656 | 0.533944 |
| **37_3** | 0.909091 | 0.909091 | 0.756881 | 0.065836 | 0.713073 | 0.667237 | 0.733288 | 0.380668 | 0.982331 | 0.346791 |
| **37_4** | 0.8 | 0.8 | 0.664 | 0.074279 | 0.6378 | 0.527295 | 0.611415 | 0.202656 | 0.909262 | 0.208052 |
| **37_5** | 0.666667 | 0.666667 | 0.553333 | 0.081755 | 0.5458 | 0.417189 | 0.50102 | 0.117765 | 0.73272 | 0.128689 |
| **37_6** | 0.5 | 0.5 | 0.415 | 0.090276 | 0.4308 | 0.314764 | 0.382489 | 0.067535 | 0.428562 | 0.076724 |
| **37_7** | 0.4 | 0.4 | 0.332 | 0.095778 | 0.3618 | 0.261645 | 0.314194 | 0.049089 | 0.260006 | 0.056591 |

**Table A. 8** Predictions of void fraction from previous hydrodynamic models and our suggested correlation for the $N_2$/10% aqueous glycerol system.

| Exp | Volumetric quality | Homogenous | Armand | Chawla | Serizawa | Triplett | Coleman | Kawahara | Kariyasaki | Saisorn |
|---|---|---|---|---|---|---|---|---|---|---|
| | | $\varepsilon_g$ | $\varepsilon_g$ | $\varepsilon_g$ | $\varepsilon_g$ | $\varepsilon_g$ | $\varepsilon_g$ | $\varepsilon_g$ | $\varepsilon_g$ | $\varepsilon_g$ |
| **39_1** | 0.997506 | 0.997506 | 0.882158 | 0.066611 | 0.774079 | 0.949182 | 0.966437 | 0.960024 | 0.999976 | 0.640009 |
| **39_2** | 0.973591 | 0.973591 | 0.814954 | 0.089378 | 0.757578 | 0.80242 | 0.85409 | 0.690103 | 0.999826 | 0.525764 |
| **39_3** | 0.848176 | 0.848176 | 0.703986 | 0.108863 | 0.671042 | 0.548312 | 0.658827 | 0.259028 | 0.99649 | 0.25565 |
| **39_4** | 0.684932 | 0.684932 | 0.568493 | 0.118847 | 0.558403 | 0.398863 | 0.514671 | 0.125889 | 0.9804 | 0.136724 |
| **39_5** | 0.54407 | 0.54407 | 0.451578 | 0.12455 | 0.461208 | 0.311295 | 0.412723 | 0.077775 | 0.936656 | 0.087649 |
| **39_6** | 0.404858 | 0.404858 | 0.336032 | 0.129671 | 0.365152 | 0.239805 | 0.317439 | 0.049865 | 0.818527 | 0.057451 |
| **39_7'** | 0.30349 | 0.30349 | 0.251897 | 0.135738 | 0.295208 | 0.191723 | 0.247191 | 0.035494 | 0.671499 | 0.041369 |
| **39_8** | 0.249377 | 0.249377 | 0.206983 | 0.139047 | 0.25787 | 0.166252 | 0.208364 | 0.029056 | 0.547527 | 0.034043 |
| **39_9** | 0.211416 | 0.211416 | 0.175476 | 0.141782 | 0.231677 | 0.148087 | 0.180265 | 0.024899 | 0.44537 | 0.029272 |

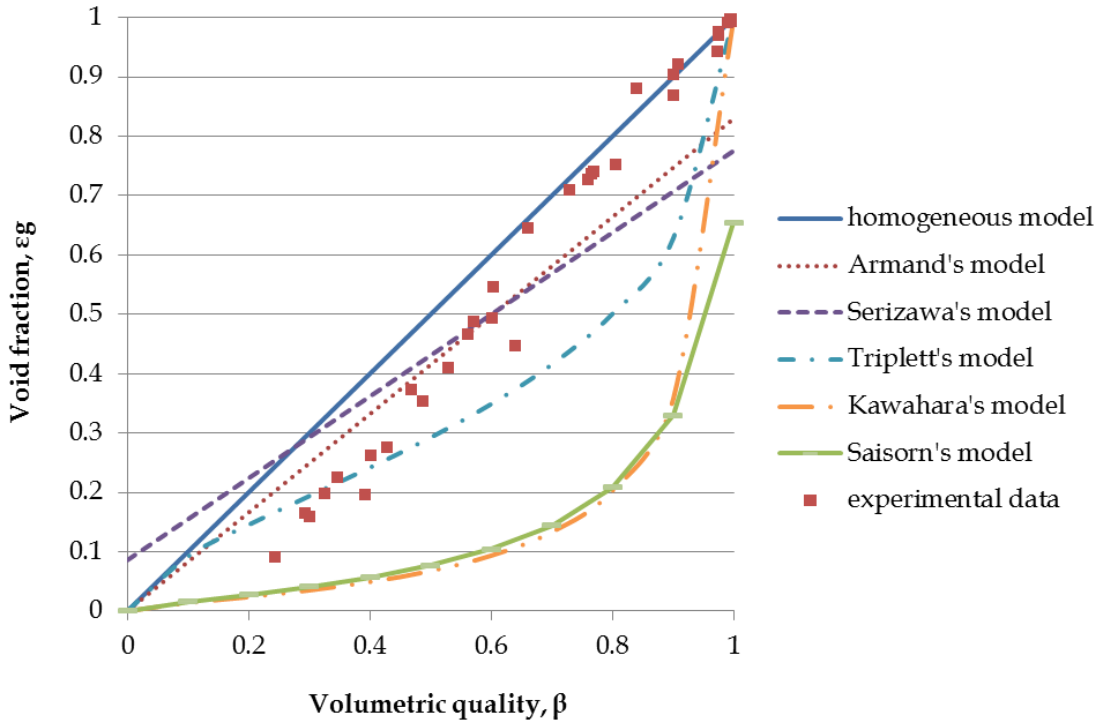


**Figure A. 30** *Comparison of different hydrodynamic models with experimental void fraction data for a $N_2$/water system in circular PFA capillaries of 0.25, 0.5 and 1mm inner diameter.*

# Appendix D

## Validation of RTD Method with Liquid Only Experiments

For the validation of the methodology developed for conducting RTD experiments, initial experiments were performed only with liquid to get familiar with this type of experiment and demonstrate the validity of this methodology. Comparison between the experimentally measured mean time of the liquid and the theoretically expected one was conducted to validate the analysis accuracy of this method. It should be noted that each set of experiments was repeated 2-3 times and the average between the experiments was considered (the deviation between the runs was ranging between 0 and 20%). The liquid used was sodium carbonate:bicarbonate buffer solution (1:9), the same used for the study of the model system.

- **Liquid Flowrate: 0.03ml/min**

In Figure A. 31 the experimental data collected in the outlet of the capillary forming the F(t) curve is shown where t=0 when the tracer dye reaches the detector in the inlet of the reactor. Hence, the signal in the inlet of the reactor was used in order to estimate the time when the tracer dye reaches the detector in the inlet.

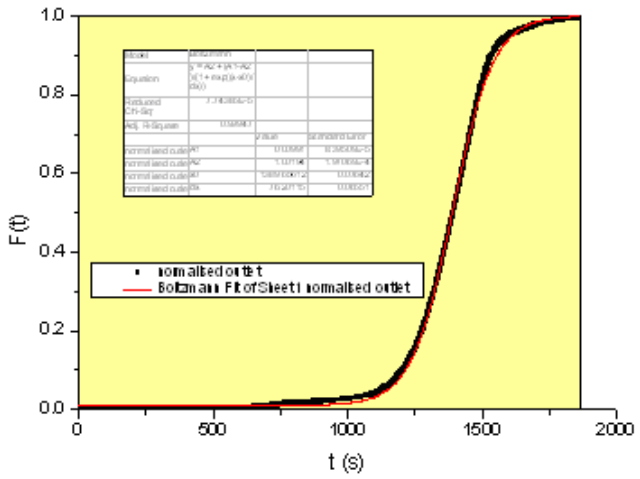


**Figure A. 31** *F curve against t(s) for the case of 0.3ml/min buffer solution.*

At this point, it should be reminded again that the step change in the inlet of the reactor was considered to be sharp enough and therefore the convolution integral was not calculated. After that, the data were fitted as shown in Figure A. 31 by a trend line (found in Origin database of trend lines) which is called 'Boltzmann' and follows the equation below:

$$y = A_2 + \frac{(A_1 - A_2)}{\left(1 + \exp\frac{(x - x_0)}{dx}\right)} \qquad \textbf{(A. 1)}$$

where $A_1$, $A_2$, $x_0$, $dx$ are constants.

Then the trend line was differentiated giving the E(t) (E=dF/dt) curve as it is shown in Figure A. 32.

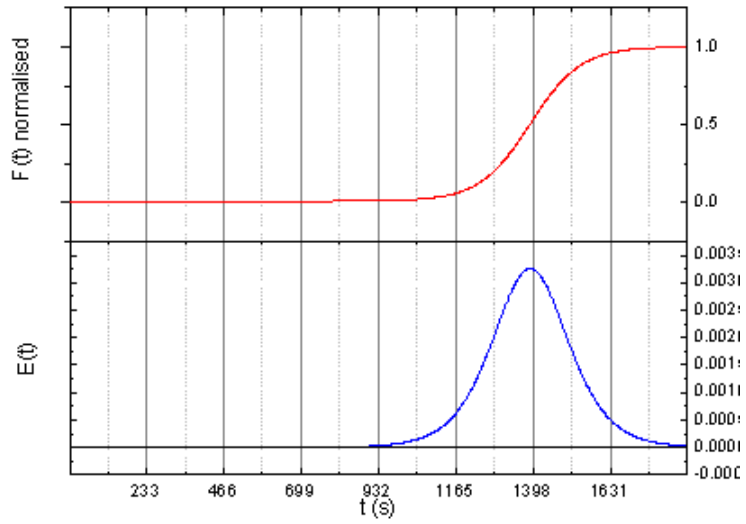


**Figure A. 32** *F,E curves against t(s) for the case of 0.3ml/min buffer solution.*

The mean residence time was found to be $\bar{\tau}$ =1375*s* based on (2.18). The corresponding hydraulic residence time ( $\bar{\tau}_h = V/\upsilon_0$ ) is $\bar{\tau}_h$ =1425s which means that the deviation of the above experimental results with theory is only 3.5% indicating that this method for RTD analysis is valid and hence can be used in multiphase system with confidence.

# Appendix E

## Vapour-liquid Equilibrium and Reactor Models in gPROMS

### 1. Vapour-Liquid Equilibrium Model

**PARAMETER**

no_comp as integer # number of componets [-] 1. methanol / 2.methyl propionate/ 3. carbon monoxide/ 4. ethylene

R as real # gas constant [J/(mol K)]

P_gas_in as real # pressure of gas phase [bar]

temp_in as real # temperature at inlet of set-up [K]

temp_eq as real # temperature at equilibriun (inlet of reactor) [K]

Ug_in, Ul_in as real # gas, liquid volumetric flowrate in the inlet of set-up [ml/min]

x_in, y_in as array(no_comp) of real # concentration in fluid liquid/ gas in the inlet of set-up [mol/mol]

Cl_in as array(no_comp) of real #initial_liquid_concentration

#dens as array(no_comp) of real #concentration of pure components (g/mol)

**VARIABLE**

x_eq, y_eq as DISTRIBUTION(no_comp) of concentration # concentration at inlet of reactor [mol/mol]

P_vap as DISTRIBUTION(no_comp) of pressure # vapoer pressure of pure components [bar] (Torres thesis, p.257,eq.1.39)

He_MeOH as DISTRIBUTION(no_comp) of Henry_constant # Henry's constant for components that xi<=0.03 (CO, C2H4) in pure MeOH at Pv,j (Torres thesis, p.256,eq.1.33)

He_MeP as DISTRIBUTION(no_comp) of Henry_constant # Henry's constant for components that xi<=0.03 (CO, C2H4) in pure MeP at Pv,j (Torres thesis, p.256,eq.1.33)

He_MeOH_p as DISTRIBUTION(no_comp) of Henry_constant # Henry's constant for components that xi<=0.03 (CO, C2H4) in pure MeOH at elevated pressure-Poynting factor correction (Torres thesis, p.257,eq.1.18)

He_MeP_p as DISTRIBUTION(no_comp) of Henry_constant # Henry's constant for components that xi<=0.03 (CO, C2H4) in pure MeP at elevated pressure-Poynting factor correction (Torres thesis, p.257,eq.1.18)

He_mix_p as DISTRIBUTION(no_comp) of Henry_constant # Henry's constant for components that xi<=0.03 (CO, C2H4) in MIXTURE at elevated pressure (Torres thesis, p.256,eq.1.31)

Vinf_MeOH as DISTRIBUTION(no_comp) of volume # partial molar volume of dissolved gas in MeOH-needed for the correction of Henry's constatnt at elevated pressure [ml] (Torres thesis, p.258)

Vinf_MeP as DISTRIBUTION(no_comp) of volume # partial molar volume of dissolved gas in MeP-needed for the correction of Henry's constatnt at elevated pressure [ml] (Torres thesis, p.258)

V_0 as DISTRIBUTION(no_comp) of molar_volume # characteristic volume of substance i [ml/mol] (Torres thesis, p.258, Tab.A.7)

c_MeOH as DISTRIBUTION(no_comp) of constant_neg # constant needed for the calculation of partial molar volume [-] (Torres thesis, p.258)

c_MeP as DISTRIBUTION(no_comp) of constant_neg # constant needed for the calculation of partial molar volume [-] (Torres thesis, p.258)

Z as DISTRIBUTION(no_comp) of fugacity_constant_1 # Rackett compressibility factor for pure component, needed for calulation of fugacity in the vapor phase- (based on Torres thesis-p.251, Tab.A.1)

g as DISTRIBUTION(no_comp) of activity_coefficient # activity coefficient

phi as DISTRIBUTION(no_comp) of activity_constant # constant needed for calculation of activity

q as DISTRIBUTION(no_comp) of activity_constant # constant needed for calculation of activity

theta as DISTRIBUTION(no_comp) of activity_constant # constant needed for calculation of activity

lu as DISTRIBUTION(no_comp) of activity_constant_neg # constant needed for calculation of activity

tau as DISTRIBUTION(no_comp,no_comp) of activity_constant # constant needed for calculation of activity

aa as DISTRIBUTION(no_comp,no_comp) of activity_constant_neg # constant needed for calculation of activity

bb as DISTRIBUTION(no_comp,no_comp) of activity_constant_neg # constant needed for calculation of activity

ro as DISTRIBUTION(no_comp) of activity_constant # constant needed for calculation of activity

ro_total as activity_constant # constant needed for calculation of activity

q_total as activity_constant # constant needed for calculation of activity

sum as DISTRIBUTION(no_comp) of activity_constant # parameter used to simplify activity expression

phi_v as DISTRIBUTION(no_comp) of fugacity # fugacity of component i (based on Torres thesis, p.254, eq.A.2)

bbb as DISTRIBUTION(no_comp) of fugacity_constant # parameter b for pure component needed for calculation of fugacity in the vapor phase- (based on Torres thesis-p.250, eq.1.23)

aaa as DISTRIBUTION(no_comp) of fugacity_constant # parameter b for pure component needed for calculation of fugacity in the vapor phase- (based on Torres thesis-p.250, eq.1.23)

bbb_mix as fugacity_constant # parameter b for mixture needed for calculation of fugacity in the vapor phase- (based on Torres thesis-p.250, eq.1.24)

aaa_mix as fugacity_constant # parameter b for mixture needed for calculation of fugacity in the vapor phase- (based on Torres thesis-p.250, eq.1.23)

Tc as DISTRIBUTION(no_comp) of fugacity_constant # critical temperature of component i [K], needed for calulation of fugacity in the vapor phase- (based on Torres thesis-p.251, Tab.A.1)

Pc as DISTRIBUTION(no_comp) of fugacity_constant # critical pressure of component i [bar], needed for calulation of fugacity in the vapor phase- (based on Torres thesis-p.251, Tab.A.1)

Tr as DISTRIBUTION(no_comp) of fugacity_constant_1 # dimensionless critical temperature of component i [-],Tr=T/Tc ,needed for calulation of fugacity in the vapor phase

Vav as DISTRIBUTION(no_comp) of fugacity_constant_1 # pure component saturated volume - needed for calculation of fugacity in the vapor phase- (based on Torres thesis-p.250, eq.1.36) [ml]

Fg_eq, Fl_eq as molar_flowrate # gas, liquid molar flowrate in the equilibrium (inlet of reactor) [mol/min]

Fg_in,Fl_in as molar_flowrate # gas, liquid molar flowrate in the inlet of set-up [mol/min]

Ug_eq, Ul_eq as volumetric_flowrate # gas, liquid volumetric flowrate in the equilibrium (inlet of reactor) [ml/min]

p_av_MeOH,p_av_MeP as density # density of pure MeOH, MeP reduced by its characteristic volume [-] (Torres thesis, p.258)

p_MeOH,p_MeP as density # density of pure MeOH, MeP [mol/ml] (Torres thesis, p.258,eq.1.37)

dens_mix as density #density of the MeOH:MeP mixture in equilibrium [mol/m l]

**EQUATION**

***#general expression for VLE***

y_eq(1)*phi_v(1)*P_gas_in =g(1)*x_eq(1)*P_vap(1) ;

y_eq(2)*phi_v(2)*P_gas_in =g(2)*x_eq(2)*P_vap(2) ;

y_eq(3)*phi_v(3)*P_gas_in =g(3)*x_eq(3)*He_mix_p(3) ; # Henry's law can be used only for very small conentrations of the component in the colution.

y_eq(4)*phi_v(4)*P_gas_in =g(4)*x_eq(4)*He_mix_p(4) ; # Therefore, it's valid only for CO and C2H4

FOR i:=1 TO no_comp DO

(x_eq(i)*Fl_eq)+(y_eq(i)*Fg_eq)=(Ul_in*Cl_in(i))+(y_in(i)*Fg_in); # mass balance for each component

END

Sigma(x_eq) = 1;

Sigma(y_eq) = 1;

Ug_eq=Fg_eq*R*temp_eq/P_gas_in; # calculation of volumetric flowrate of the gas and the liquid phase in the inlet

dens_mix=x_eq(1)*p_MeOH+x_eq(2)*p_MeP; #calculation of density of the MeOH:MeP mixture in equilibrium - needed for the calculation of Ul in equilibrium

Ul_eq=Fl_eq*dens_mix ; #calculation of liquid volumetric flowrate in equilibrium

**# calculation of inlet molar flowrates in gas and in liquid phase**

Fl_in=Ul_in*Cl_in(1)+Ul_in*Cl_in(2) ; # total lquid molar flowrate in the inlet(mol/min)

Fg_in=(P_gas_in*Ug_in/(R*temp_in)); # total gas molar flowrate in the inlet(mol/min)

**#calculation of phi_v which is the fugacity coefficient of the vapor phase**

Vav(1)=R*Tc(1)*(Z(1)^((1+((1-Tr(1))^(2/7)))))/Pc(1) ;

Vav(2)=R*Tc(2)*(Z(2)^((1+((1-Tr(2))^(2/7)))))/Pc(2) ;

Vav(3)=R*Tc(3)*(Z(3)^((1+((-1+Tr(3))^(2/7)))))/Pc(3) ; #modified as for CO,C2H4 (1-Tr)<0 and a negative number cannot be at a not integer power (2/7)_ I checked even with getting rid of this part (1-Tr=1)

and the results remain the same. So this change does not impact the final results of the VLE.

Vav(4)=R*Tc(4)*(Z(4)^((1+((-1+Tr(4))^(2/7)))))/Pc(4) ; #modified -//-

SQRT(aaa_mix)=SIGMA(y_eq()*(SQRT(aaa()))) ;

bbb_mix=SIGMA(y_eq()*bbb()) ;

Tc(1)=512.64 ; Tc(2)=530.6 ; Tc(3)=132.92 ; Tc(4)=282.34;

Pc(1)=80.97 ; Pc(2)=40.04 ; Pc(3)=34.987 ; Pc(4)=50.4;

```
Z(1)=0.2353 ;  Z(2)=0.2566 ;

Z(3)=0.2896 ;  Z(4)=0.2808;

   FOR i:=1 TO no_comp DO

   log(phi_v(i))=log(Vav(i)/(Vav(i)-
bbb_mix))+(((2*bbb_mix*SQRT(aaa_mix)*SQRT(aaa(i)))+R*temp_eq*aaa_mix*bbb(i))*(log(Va
v(i)/(Vav(i)+bbb_mix)))/(R*temp_eq*(bbb_mix^2)))+(bbb(i)/(Vav(i)-
bbb_mix))+((aaa_mix*bbb(i))/(bbb_mix*(Vav(i)+bbb_mix))) ;

   aaa(i)=(0.42748*(0.08314^2)*(Tc(i)^2.5))/(Pc(i)); #*(temp_eq)^0.5) ;

   bbb(i)=(0.08664*0.08314*Tc(i))/Pc(i) ;

   Tr(i)=temp_eq/Tc(i);

END
```

**# UNIQUAC equation: calculation of g(i) which is the activity coefficient of component i**

```
FOR i:=1 TO no_comp DO

   log(g(i))=(log((phi(i)/x_eq(i))))+(5*q(i)*(log(theta(i)/phi(i))))+lu(i)-
((phi(i)/x_eq(i))*(SIGMA(x_eq()*lu())))+(q(i)*((1-(log(SIGMA(theta()*tau(,i))))-
(SIGMA((theta()*tau(i,))/sum())))) ;

   FOR j:=1 TO no_comp DO

      tau(i,j)=(exp(aa(i,j)+(bb(i,j)/temp_eq)))  ;

   END

END

   FOR k:=1 TO no_comp DO

      sum(k)=SIGMA(theta*tau(,k));

   END
```

**#calculation of components properties needed for the resolution of UNIQUAC equation( for the calculation of activity coefficient,g(i))**

```
   phi()=ro()*x_eq()/ro_total ;

   theta()=q()*x_eq()/q_total ;

   lu()=(5*(ro()-q()))+1-ro()   ;

   ro_total=(SIGMA(ro()*x_eq())) ;

   q_total=(SIGMA(q()*x_eq()))   ;

   ro(1)=1.43111;   ro(2)=3.47858;   ro(3)=1.0679; ro(4)=1.57416;

   q(1)=1.432;      q(2)=3.116;     q(3)=1.112;   q(4)=1.488;

   aa(1,1)=0;       aa(1,2)=0.29199; aa(1,3)=0;    aa(1,4)=0;

   aa(2,1)=0.010522; aa(2,2)=0;      aa(2,3)=0;    aa(2,4)=0;
```

aa(3,1)=0; aa(3,2)=0; aa(3,3)=0; aa(3,4)=0;

aa(4,1)=0; aa(4,2)=0; aa(4,3)=0; aa(4,4)=0;

bb(1,1)=0; bb(1,2)=-408.75; bb(1,3)=0; bb(1,4)=-13023.2;

bb(2,1)=22.382; bb(2,2)=0; bb(2,3)=0; bb(2,4)=0;

bb(3,1)=0; bb(3,2)=0; bb(3,3)=0; bb(3,4)=0;

bb(4,1)=-144.865; bb(4,2)=0; bb(4,3)=0; bb(4,4)=0;

**# calculation of vapor pressures of component i (MeOH, MeP, CO, C2H4) using Antoine equation**

**# constants based on Torres thesis (p.257, Tab.A.6)**

P_vap(1) =10^(-5)*exp(81.768+(-6876/(temp_eq))+(-8.7078*log(temp_eq))+(7.1926E-06*(temp_eq^2))); # P_vap [bar] T [K]

P_vap(2) =10^(-5)*exp(70.717+(-6439.7/(temp_eq))+(-6.9845*log(temp_eq))+(2.0129E-17*(temp_eq^6))) ; # P_vap [bar] T [K]

P_vap(3) =0 ; # we need to set the zero value because P_vap is defined as 4component row but we are not interested in P-vap of CO,C2H4

P_vap(4) =0 ; # same

**#Henry's constant for components i where xi<=0.03 (CO, C2H4) in the mixture MeOH:MeP at elevated pressure**

**# Henry's constant of components i at pure MeOH, MeP at vapor pressure (p.256, eq.1.33, Tab.A.5)**

He_MeOH(1)=0 ; # we need to set the zero value because He_MeOH is defined as 4component row but we are not interested in He of MeOH, MeP

He_MeOH(2)=0 ; # same

He_MeP(1)=0 ; # same

He_MeP(2)=0 ; # same

**#calculation of He of CO in MeOH at T, Pv,j based on Torres thesis (p.256, eq.1.33, Tab.A.5)**

He_MeOH(3)=10^(-5)*EXP(86.9474+(-3113.31/temp_eq)+(-10.0276*(log(temp_eq)))); # He [bar], temp_eq [K]

**#calculation of He of CO in MeP at T, Pv,j based on Torres thesis (p.256, eq.1.33, Tab.A.5)**

He_MeP(3)=10^(-5)*EXP(16.7289+(509.750/temp_eq));

**#calculation of He of C2H4 in MeOH at T, Pv,j based on Torres thesis (p.256, eq.1.33, Tab.A.5)**

He_MeOH(4)=10^(-5)*EXP(20.6312+(-1054.03/temp_eq));

**#calculation of He of C2H4 in MeP at T, Pv,j based on Torres thesis (p.256, eq.1.33, Tab.A.5)**

He_MeP(4)=10^(-5)*EXP(15.4734+(-719.82/temp_eq)+(0.15527*(log(temp_eq)))+(0.005046*(temp_eq)));

**# Henry's constant of components i at pure MeOH, MeP at elevated pressure- correction by the Poynting factor**

He_MeOH_p(1)=0 ; # we need to set the zero value because He_MeOH_p is defined as 4component row but we are not interested in He of MeOH (only for CO,C2H4)

He_MeOH_p(2)=0 ; # same

He_MeP_p(1)=0 ; # we need to set the zero value because He_MeP_p is defined as 4component row but we are not interested in He of MeP (only for CO,C2H4)

He_MeP_p(2)=0 ; # same

**#calculation of He of CO in MeOH at T, elevated P based on Torres thesis (p.257, eq.1.18)**

log(He_MeOH_p(3))=log(He_MeOH(3))+(Vinf_MeOH(3)*(P_gas_in-P_vap(1))/(R*temp_eq)); # we multiply Vinf with 10-2 to convert m3 Pa/kmol to ml bar/mol

**#calculation of He of CO in MeP at T, elevated P based on Torres thesis (p.257, eq.1.18)**

log(He_MeP_p(3))=log(He_MeP(3))+(Vinf_MeP(3)*(P_gas_in-P_vap(2))/(R*temp_eq));

**#calculation of He of C2H4 in MeOH at T, elevated P based on Torres thesis (p.257, eq.1.18)**

log(He_MeOH_p(4))=log(He_MeOH(4))+(Vinf_MeOH(4)*(P_gas_in-P_vap(1))/(R*temp_eq));

**#calculation of He of C2H4 in MeP at T, elevated P based on Torres thesis (p.257, eq.1.18)**

log(He_MeP_p(4))=log(He_MeP(4))+(Vinf_MeP(4)*(P_gas_in-P_vap(2))/(R*temp_eq));

**#calculation of partial molar volume of i at infinite dilution in pure solvent j (Vinf_j(i) - needed for the correction of He at elevated pressure (Torres thesis,p.258)**

Vinf_MeOH(1)=0 ; Vinf_MeOH(2)=0 ; # we need to set the zero value because Vinf_MeOH is defined as 4component row but we are not interested in He of MeOH (only for CO,C2H4)

Vinf_MeP(1)=0 ; Vinf_Mep(2)=0 ; # we need to set the zero value because Vinf_MeP is defined as 4component row but we are not interested in He of MeP (only for CO,C2H4)

**#of dissolved CO in MeOH (Vinf_MeOH(3))**

Vinf_MeOH(3)/(Z(1)*0.008314*temp_eq)=1-c_MeOH(3); #Vinf [m3 Pa/kmol],Z[-], 0.008314 [m3 Pa/kmol K], temp_eq [K]

**#of dissolved CO in MeP (Vinf_MeP(3))**

Vinf_MeP(3)/(Z(2)*0.008314*temp_eq)=1-c_MeP(3);

**#of dissolved C2H4 in MeOH (Vinf_MeOH(4))**

Vinf_MeOH(4)/(Z(1)*0.008314*temp_eq)=1-c_MeOH(4);

**#of dissolved C2H4 in MeP (Vinf_MeP(4))**

```
Vinf_MeP(4)/(Z(2)*0.008314*temp_eq)=1-c_MeP(4);
```

**#calculation of constant c_j(i)-needed for the calculation of partial molar volume V_inf_j(i)(Torres thesis, p.258)**

```
FOR qq:=no_comp-1 TO no_comp DO  # this was done because we are interested only on CO,C2H4 for Henry's constants

    #calculation of c_MeOH(i)

    IF p_av_MeOH<=2.785 THEN

      log((-c_MeOH(qq))*((V_0(1)/V_0(qq))^0.62))=-2.4467+(2.12074*p_av_MeOH);

    ELSE

      log((-c_MeOH(qq))*((V_0(1)/V_0(qq))^0.62))=3.012214-(1.87085*p_av_MeOH)+(0.71955*(p_av_MeOH^2));

    END


  #calculation of c_Mep(i)

    IF p_av_MeP<=2.785 THEN

      log((-c_MeP(qq))*((V_0(2)/V_0(qq))^0.68))=-2.4467+(2.12074*p_av_MeP);

    ELSE

      log((-c_MeP(qq))*((V_0(2)/V_0(qq))^0.68))=3.012214-(1.87085*p_av_MeP)+(0.71955*(p_av_MeP^2));

    END

  END

V_0(1)= 117.916;          # characteristic volume of MeOH [ml/mol] based on Torres thesis, p.258, Tab.A.7 - needed for calculation of c_j(i)

V_0(2)=282;               # characteristic volume of MeP [ml/mol] based on Torres thesis, p.258, Tab.A.7  - needed for calculation of c_j(i)

V_0(3)=93.2441;           # characteristic volume of CO [ml/mol] based on Torres thesis, p.258, Tab.A.7   - needed for calculation of c_j(i)

V_0(4)=128.68;            # characteristic volume of C2H4 [ml/mol] based on Torres thesis, p.258, Tab.A.7 - needed for calculation of c_j(i)

c_MeOH(1)=0 ; c_MeOH(2)=0 ;   # we need to set the zero value because c_MeOH is defined as 4component row but we are not interested in He of MeOH (only for CO,C2H4)

c_MeP(1)=0  ; c_Mep(2)=0  ;   # we need to set the zero value because c_MeP is defined as 4component row but we are not interested in He of MeP (only for CO,C2H4)
```

**#calculation of p_av_MeOH which is the pure MeOH liquid density reduced by its characteristic volume V_0_MeOH - needed for calculation of c_j(i) - [dimensionless] - based on Torres thesis (p.258)**

p_av_MeOH=p_MeOH*V_0(1);

**#calculation of p_av_MeP which is the pure MeP liquid density reduced by its characteristic volume V_0_MeP - needed for calculation of c_j(i) - [dimensionless] -based on Torres thesis (p.258)**

p_av_MeP=p_MeP*V_0(2);

**#calculation of p_MeOH which is the liquid density of pure MeOH - needed for p_av_MeOH caluclation -[mol/ml] -based on Torres thesis (p.258,eq.1.37)**

p_MeOH=0.001*(2.288/(0.2685^(1+((1-(temp_eq/512.64))^0.2453))));

**#calculation of p_MeP which is the liquid density of pure MeOH - needed for p_av_MeP caluclation -[mol/ml] -based on Torres thesis (p.258,eq.1.37)**

p_MeP=0.001*(0.9147/(0.2594^(1+((1-(temp_eq/530.6))^0.2774))));

**# Henry's constant of components i at MeOH, MeP mixtures at elevated pressure(p.256, eq.1.33, Tab.A.5)**

He_mix_p(1)=0; # we need to set the zero value because He_mix_p is defined as 4component row but we are not interested in He of MeOH (only for CO,C2H4)

He_mix_p(2)=0; # we need to set the zero value because He_mix_p is defined as 4component row but we are not interested in He of MeP (only for CO,C2H4)

**#for CO:**

log(He_mix_p(3))=(x_eq(1)*log(He_MeOH_p(3))+x_eq(2)*log(He_MeP_p(3)))/(x_eq(1)+x_eq(2));#based on eq.5.60,p.267, 'Chem. Therm. for Process Simulation',J.Gmehling

**#for C2H4:**

log(He_mix_p(4))=(x_eq(1)*log(He_MeOH_p(4))+x_eq(2)*log(He_MeP_p(4)))/(x_eq(1)+x_eq(2));

## 2. Reactor Model

PARAMETER

no_comp AS Integer # *Number of components in rxn*

dt AS Real # *Tubing inner diameter (cm)*

Length AS Real # *Length of the reactor (cm)*

Ug AS Real # *Gas volumetric flowrate (ml/min)*

Ul AS Real # *Liquid volumetric flowrate (ml/min)*

A AS Real # *Void fraction prefactor; determined from RTD experiments*

kla AS Real # *Mass transfer coefficient (min-1); determined from correlations. Its value shouldn't affect the results significantly as it is a kinetically controlled system*

kr AS REAL # *reaction rate constant (min-1)*

pi AS Real # *constant*

R AS Real # *gas constant (ml bar/mol K)*

T AS Real # *temperature (K)*

P AS Real # *pressure (bar)*

j AS ARRAY(no_comp) OF Real # *prefactor that indicates if a component is a reactant or a product (-)*

K AS ARRAY(no_comp) OF Real # *gas-liquid interface equilibrium constant, related to Henry's constant (for CO, C2H4) and to vapor pressure (for MeOH, MeP) (-)*

DISTRIBUTION_DOMAIN

Axial AS [0:Length] # *Axial domain*

VARIABLE

Cg AS DISTRIBUTION(Axial, no_comp) OF Concentration # *concentration of components (MeOH, MeP, CO, C2H4) in gas phase (mol/ml)*

Cl AS DISTRIBUTION(Axial, no_comp) OF Concentration # *concentration of components (MeOH, MeP, CO, C2H4) in liquid phase (mol/ml)*

Fg AS DISTRIBUTION(Axial, no_comp) OF MolarFlowrate # *molar flowrate of components (MeOH, MeP, CO, C2H4) in the gas phase (mol/min)*

Fl AS DISTRIBUTION(Axial, no_comp) OF MolarFlowrate # *molar flowrate of components (MeOH, MeP, CO, C2H4) in the liquid phase (mol/min)*

mol_dif AS DISTRIBUTION(Axial, no_comp) OF MolarFlowrate # *mole difference of all componenets between the inlet and the outlet of the reactor to check that the balances are correct (mol/min)*

Xrxn AS DISTRIBUTION(Axial, no_comp) OF MolarFlowrate # *Conversion of reactants between the inlet and the outlet (-)*

x AS DISTRIBUTION(Axial, no_comp) OF Fraction # *fraction of component in the liquid phase (-)*

y AS DISTRIBUTION(Axial, no_comp) OF Fraction # *fraction of component in the gas phase (-)*

Fg_total AS DISTRIBUTION(Axial) OF MolarFlowrate # *total molar flowrate in the gas phase (mol/min)*

Fl_total AS DISTRIBUTION(Axial) OF MolarFlowrate # *total molar flowrate in the liquid phase (mol/min)*

rxn AS DISTRIBUTION(Axial) OF Concentration # *reaction rate expression*

e AS NoType # *liquid volume fraction*

jg AS NoType # *gas superficial velocity (cm/min)*

```
jl          AS  NoType          # liquid superficial velocity (cm/min)

Ac          AS  NoType      # interfacial contact area (cm^2)

BOUNDARY

Fl(0,1)=5.1261875E-5;   # Concentration of MeOH in the liquid phase in the inlet of the reactor (point 2).

Fl(0,2)=4.732016E-5;  # Concentration of MeP in the liquid phase in the inlet of the reactor (point 2).

Fl(0,3)=4.7264077E-8;  # Concentration of CO in the liquid phase in the inlet of the reactor (point 2).

Fl(0,4)=6.0849015E-7;     # Concentration of C2H4 in the liquid phase in the inlet of the reactor(point 2).

Fg(0,1)=2.8710325E-5; # Concentration of MeOH in the gas phase in the inlet of the reactor(point 2).

Fg(0,2)=1.1307638E-5;  # Concentration of MeP in the gas phase in the inlet of the reactor(point 2).

Fg(0,3)=8.144223E-6;   # Concentration of CO in the gas phase in the inlet of the reactor(point 2)

Fg(0,4)=6.9556976E-5;  # Concentration of C2H4 in the gas phase in the inlet of the reactor(point 2).

EQUATION

FOR z:=0|+  TO  Length    DO

# Mole balances for all components in the gas and the liquid phase along the reactor based on molar flowrates. Flowrate change is not taken into  account.

FOR q:=1  TO  no_comp    DO

                    (1/Ac)*(PARTIAL(Fl(z,q),Axial))=(j(q)*rxn(z)*e)+(kla*((Fg(z,q)/(Ug*K(q)))-(Fl(z,q)/Ul)))    ;  #  liquid phase

                    (1/Ac)*(PARTIAL(Fg(z,q),Axial))=-(kla*((Fg(z,q)/(Ug*K(q)))-(Fl(z,q)/Ul)))
;                                   #  gas phase

          END

END

FOR z:=0  TO  Length    DO

Fl_total(z)=SIGMA(Fl(z,));

Fg_total(z)=SIGMA(Fg(z,));

rxn(z)=kr*Fl(z,1)/Ul        ;      # reaction rate expression

FOR q:=1  TO  no_comp    DO

                    Cg(z,q)=Fg(z,q)/Ug    ;      # concentration of gas components

                          Cl(z,q)=Fl(z,q)/Ul    ;      # concentration of liquid components

                         mol_dif(z,q)=((Fg(0,q)+Fl(0,q))-(Fg(z,q)+Fl(z,q)))       ;          # mole difference of all componenets between the inlet and the outlet of the reactor to check that the balances are correct
```

```
                    Xrxn(z,q)=mol_dif(z,q)/(Fg(0,q)+Fl(0,q));
x(z,q)=Fl(z,q)/Fl_total(z) ;
y(z,q)=Fg(z,q)/Fg_total(z) ;
END
END
Ac=pi*(dt^2)/4      ;   # interfacial contact area (cm^2)
e=1-(A*(jg/(jg+jl))) ;   # liquid volume fraction
jg=Ug/Ac       ;   # gas superficial velocity (cm/s)
jl=Ul/Ac       ;   # liquid superficial velocity (cm/s)
```

# Appendix F

## Fourier number calculation

The dimensionless Fourier number, Fo, number is given by eq.**(A.2**),

$$Fo = \frac{D \cdot t}{d^2} \tag{A.2}$$

where D($cm^2/s$) is the diffusion coefficient of MeOH in MeP in our case, t(s) is the contact time between the gas and the liquid and d(cm) is the diffusion path length of the liquid which in our case is equal with the film thickness (≈30μm).

The diffusion coefficient of MeOH in MeP was calculated at 20°C using Wilke and Chang correlation eq.(A.3) [204] and was found equal with 2.06 $10^{-5}$ $cm^2/s$.

$$D = 7.4 \cdot 10^{-8} \frac{\left(x \cdot M\right)^{1/2} \cdot T}{n \cdot V^{0.6}} \tag{A.3}$$

where x is the association parameter which in the case of MeOH is equal with 1.9, M(g/ml) is the molecular weight of MeOH, T(K) is the temperature, n(cP) is the viscosity of the solution and V(ml/mol) is the molar volume of MeP at normal boiling point.

Hence, in order to achieve equilibrium at the gas-liquid interphase, no more than a minute is needed. Therefore, it can be concluded that equilibrium is achieved instantly in the reactor's inlet considering a typical total residence time of approximately 40min.

# Appendix G

## Mass Balance Calculations during Blank Experiment

The mass balance of MeOH was developed for the case of a typical blank experiment to demonstrate the accuracy of the methodology followed for the kinetic study of the MeP system. The initial conditions are listed in Table A. 9. In the inlet a 10%CO:$C_2H_4$ gas stream and a 30:70w/w% MeOH: MeP liquid stream (without catalyst in) were introduced.

**Table A. 9** Operating conditions of blank experiment

| T(K) | P(bara) | $\upsilon_g$ (ml/min) | $\upsilon_\ell$ (ml/min) |
|---|---|---|---|
| 373 | 10 | 2 | 0.005 |

Based on the analysis of the gas and the liquid samples, the composition in the gas and the liquid phase were determined in the set-up feed and outlet as shown in Table A. 10. Then, the composition in the inlet and outlet of the reactor (where temperature increases to 100$^o$C) was calculated by means of the experimental data (in the feed and outlet of the set-up at 25$^o$C) and a VLE model.

**Table A. 10** Gas and liquid compositions in the set-up feed and outlet (as measured experimentally) and in the reactor's inlet and outlet (as calculated by means of the VLE model).

| | **Set-up Feed (Experimental Data)** | | **Reactor's Inlet (VLE predictions)** | | **Set-up Outlet (Experimental Data)** | | **Reactor's Outlet (VLE predictions)** | |
|---|---|---|---|---|---|---|---|---|
| | $y_i$ | $x_i$ | $y_i$ | $x_i$ | $y_i$ | $x_i$ | $y_i$ | $x_i$ |
| **MeOH** | 0 | 0.535 | 0.227 | 0.466 | 0.018 | 0.524 | 0.226 | 0.463 |
| **MeP** | 0 | 0.465 | 0.102 | 0.519 | 0.009 | 0.464 | 0.102 | 0.521 |
| **CO** | 0.098 | 0 | 0.069 | 4.95E-04 | 0.102 | 0 | 0.071 | 5.14E-04 |
| **$C_2H_4$** | 0.872 | 0 | 0.603 | 0.015 | 0.850 | 0 | 0.601 | 0.015 |

Then, by using equations (A.4) and (A.5), the molar flowrates of all components in both the gas and the liquid phase were calculated in all points of the set-up and most importantly in the inlet and outlet of the reactor. The results are presented in Table A. 11.

$$F_g = \frac{\upsilon_g P}{RT} \tag{A.4}$$

$$F_\ell = F_{\ell,MeOH} + F_{\ell,MeP} = \upsilon_\ell C_{MeOH} + \upsilon_\ell C_{MeP} \tag{A.5}$$

**Table A. 11** Molar flowrates of all components in the gas and the liquid phase in the set-up feed and outlet and in the reactor's inlet and outlet.

| | **Set-up Feed** | | **Reactor's Inlet** | | **Set-up Outlet** | | **Reactor's Outlet** | |
|---|---|---|---|---|---|---|---|---|
| | **$F_{gi}$** | **$F_{\ell i}$** | **$F_{gi}$** | **$F_{\ell i}$** | **$F_{gi}$** | **$F_{\ell i}$** | **$F_{gi}$** | **$F_{\ell i}$** |
| **MeOH** | 0 | 7.07E-05 | 2.59E-05 | 4.47E-05 | 1.42E-06 | 6.92E-05 | 2.59E-05 | 4.47E-05 |
| **MeP** | 0 | 6.14E-05 | 1.16E-05 | 4.98E-05 | 7.42E-07 | 6.12E-05 | 1.17E-05 | 5.03E-05 |
| **CO** | 7.91E-06 | 0 | 7.86E-06 | 4.75E-08 | 8.22E-06 | 0 | 8.17E-06 | 4.96E-08 |
| **$C_2H_4$** | 7.04E-05 | 0 | 6.90E-05 | 1.41E-06 | 6.86E-05 | 1.72E-06 | 6.89E-05 | 1.42E-06 |

The error between the molar flowrates in the inlet and the outlet of the reactor is calculated and is shown in Table A. 12.

**Table A. 12** Error% on total molar flowrates of all components between the inlet and outlet of the reactor.

| | **Error %** |
|---|---|
| | **$F_{total}$** |
| **MeOH** | 0.13% |
| **MeP** | -0.90% |
| **CO** | -3.88% |
| **$C_2H_4$** | 0.14% |

The % error in molar flowrates between the inlet and outlet of the reactor is very small for all components and can be attributed to experimental error of gc. Error of carbon monoxide is slightly larger because its actual molar flowrates are of an order of magnitude smaller than the other components. Hence, it can be concluded that the analysis methods used are valid and the set-up is suitable for the kinetic study of MeP system with good accuracy.

# Appendix H

## Fabrication of microseparators

Microfabrication of the microseparators used was carried out by a designated member of the group at the London Centre of Nanotechnology. A typical procedure involved spin coating a positive photoresist on a clean silicon wafer creating a 6μm thick layer. The exposed photoresist was then removed using a developer solution. The patterned wafer was then dry etched using deep reactive ion etching to the desired depth.

The etched wafer was bonded by the author. More specifically, a solution of hydrogen peroxide ($H_2O_2$) and sulphuric acid ($H_2SO_4$) (1:1) was prepared where the silicon wafers and the glasses were submerged for 20 min at 120$^{o}$C in order to clean them. For bonding the silicon wafer to the glass, the two were carefully aligned inside the anodic bonder. Following this, they were heated at 400-450$^{o}$C and then gradually the voltage was increased up to 1kV.

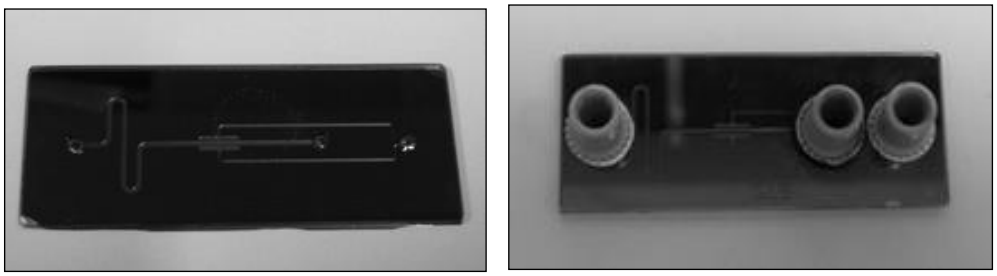

**Figure A. 33** *Photographs of the glass-silicon microseparator before (left) and after (right) the place of the fittings.*

The bottom fittings (Presearch, adhesive ring, PEEK bottom port and gasket) were centred and placed on the surface of the microseparator, they were clamped and they were put in the oven at 165-177$^{o}$C for one hour to develop a complete bond between the port and the substrate. It should be also noted that the unused adhesive rings should be stored in a refrigerated environment (1.7-4.4$^{o}$C) to ensure maximum usable lifetime.

# Appendix I

## Flow Observation

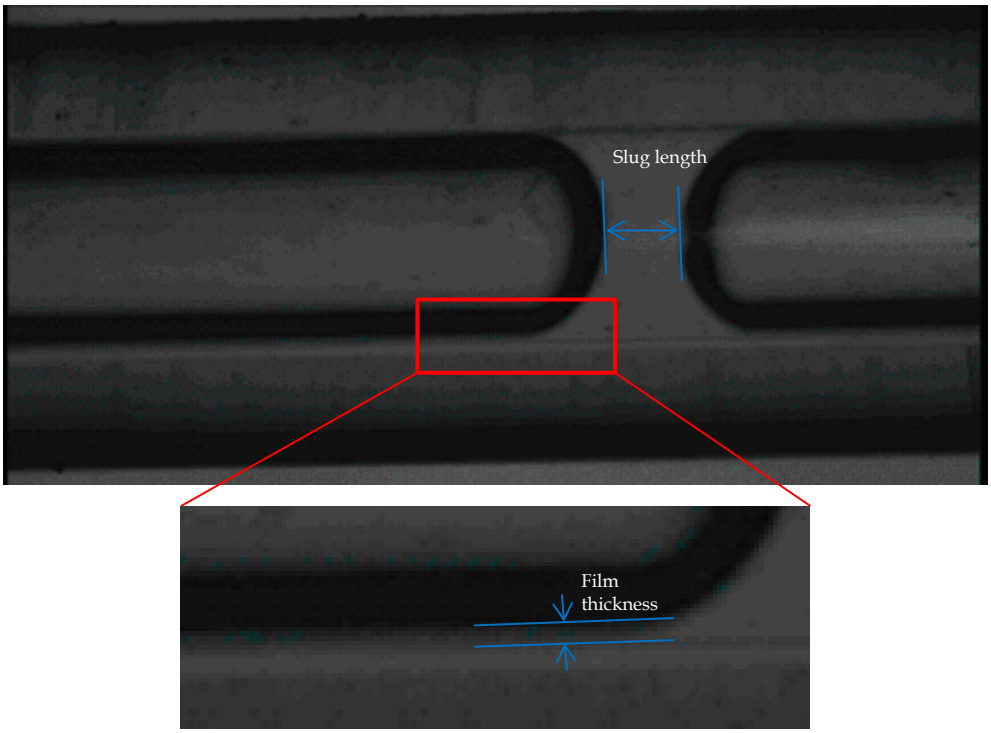


**Figure A. 34** *Typical image of flow observation of gas-liquid flow of the model system into a glass circular capillary with ID=1mm by means of a microscope for gas (2% $CO_2$) and liquid (buffer solution) flowrates 0.3ml/min and 0.03ml/min respectively.*

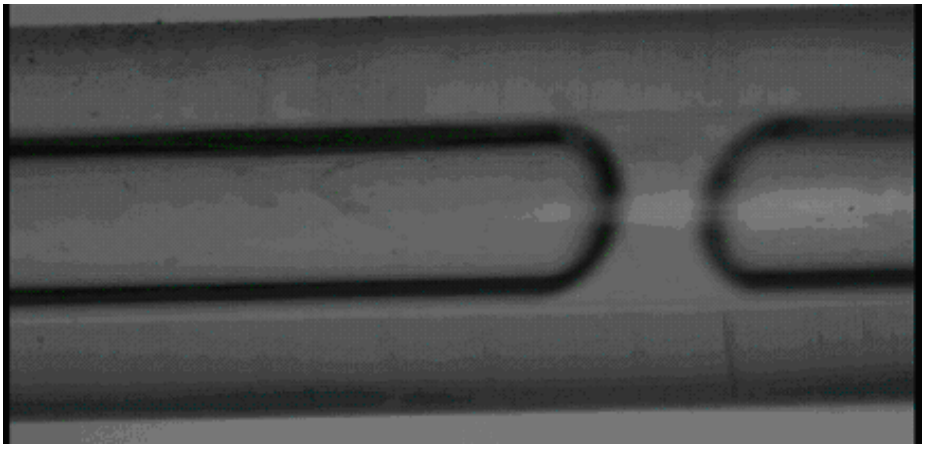

**Figure A. 35** *Typical image of flow observation of gas-liquid flow of the model system into a glass circular capillary with ID=1mm by means of a microscope for gas (2% $CO_2$) and liquid (buffer solution) flowrates 0.5ml/min and 0.03ml/min respectively.*

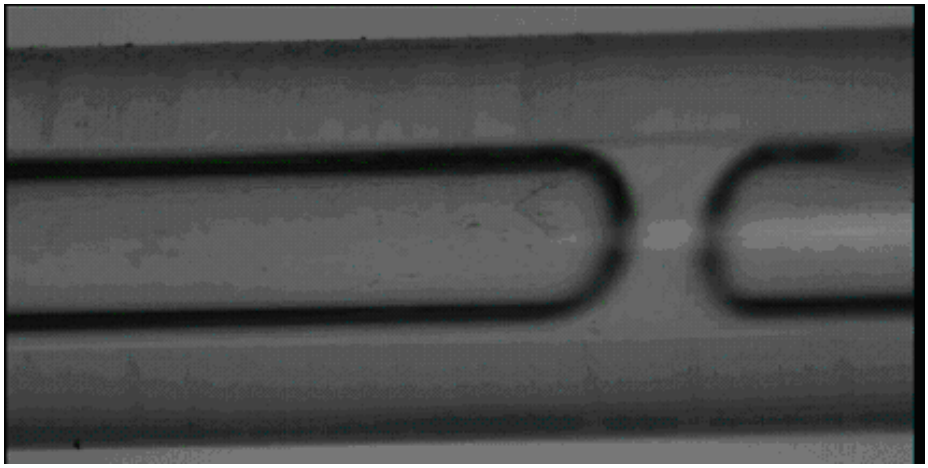

**Figure A. 36** *Typical image of flow observation of gas-liquid flow of the model system into a glass circular capillary with ID=1mm by means of a microscope for gas (2% $CO_2$) and liquid (buffer solution) flowrates 1ml/min and 0.03ml/min respectively.*

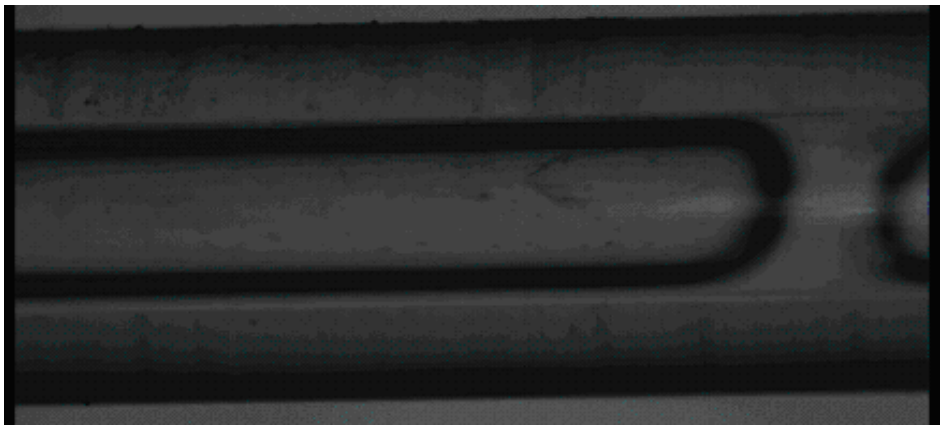

**Figure A. 37** *Typical image of flow observation of gas-liquid flow of the model system into a glass circular tubing with ID=1mm by means of a microscope for gas (2% $CO_2$) and liquid (buffer solution) flowrates 2ml/min and 0.03ml/min respectively.*

# Appendix J

## Supplementary technical data for Chapter 5

1. Standard operating procedure

A standard procedure to start an experiment for the system of the MeP reaction system was developed for safety and reproducibility reasons and consists of the following steps:

- Prepare the catalyst mixture under Argon atmosphere (using a glove box) using degased pure methanol and methyl propionate solutions to adjust the concentration. The prepared liquid mixture that contains the catalyst solution should be always consumed within 2days to avoid catalyst degradation.
- Fill the syringe with the liquid mixture, install it in the syringe pump and collect initial liquid samples for analysis.
- Open He cylinder, set the desired He flowrate value in the He MFC and pressurise the set-up at 12bar by means of a BPR.
- Stop the He flow and test for leaks by monitoring the pressure loss after 10min.After ensuring that there are not any significant leaks, start He again.
- Open gas CO, $C_2H_4$ cylinders (first open the main valve of the cylinder, set the desired outlet pressure and then open the switch-off valve of the gas line).
- Set the desired CO, $C_2H_4$ flowrates value in the MFC's and start the gases.
- Wait until the system is pressurised at 10bara and ensure the gas composition is the desired one with gc analysis of the gas stream
- Set the desired liquid flowrate and start the liquid.
- Switch on the temperature controller.

- After 20min empty the bottom of the separator of any liquid remained from the previous set of experiment.
- Wait 3-4 residence times for the system to reach steady state.
- Take liquid samples every 30min by gradually opening the metering valve in the end of the separator. Liquid samples will be analysed off-line after the end of the experiment.
- Gas analysis is happening online
- Measure gas flowrate leaving the separator by means of a bubble meter installed after the reactor
- Before stopping the experiment, inject methanol tracer to perform RTD experiment and monitor the tracer concentration in the inlet and the outlet of the reactor. When all the tracer has left the set-up all the data needed for the RTD experiment has been collected and we can stop the experiment

To stop the experiment with the MeP system, the next steps need to be followed:

- Switch off the temperature controller
- Stop the liquid
- Switch off the CO, $C_2H_4$ cylinders (first the switch off valve and then the main cylinder valve)
- Depressurise the set-up (from the main gas lines to the BPR) gradually
- Switch off CO, $C_2H_4$ MFC's

Purge the set-up with He for 15min overnight to get rid of any left impurities in the set-up.

2. Safety precautions

Due to the poisonous nature of carbon monoxide, the flammable nature of ethylene and the elevated temperature and pressure conditions, safety precautions were taken before the installation of the new gas cylinders.

The gas lines that connect the gas cylinders with the main set-up were leak tested by pressurising the lines with helium at 12bara and no leaks were found. Moreover, the set-up was enclosed in a ventilated acrylic box and a valve system allowed the flashing with $N_2$ of the lines between the CO cylinder and the set-up. In this way, potential exposure to CO was minimised.

In addition, a pressure relief valve that opens when pressure is larger than 17bar was installed in the CO line of the set-up (Figure 5.1) to prevent any dangerous pressure build up.

The lab was equipped with detectors for carbon monoxide and ethylene that set off alarms when the gas levels exceeded the corresponding established European limits (EH 40 Workplace Exposure Limit LEL for carbon monoxide: 30ppm). An additional carbon monoxide handheld detector was also placed next to the set-up, inside the ventilated acrylic box for a quicker response time.

3. Gas phase analysis

For the gas analysis a polar capillary column (HP-Plot Q, Agilent) and a TCD detector were used. The developed method for the analysis of CO/$C_2H_4$ mixtures is shown in Table A. 13.

**Table A. 13** GC operating conditions for the analysis of the gas effluent from the methoxycarbonylation of ethylene.

| **Column Name** | HP-PLOT Q |
|---|---|
| **Split Flow** | 20:1 |
| **Column Flow** | 2ml/min |
| **Oven Temperature** | 70°C (3min hold)<br>Ramp 50°C/min to 110°C (1min hold)<br>Ramp 20°C/min to 200°C (2min hold) |
| **Carrier Gas** | Helium |
| **Carrier Flowrate** | 5ml/min |
| **Detector** | TCD |
| **Filament Temperature** | 250°C |
| **Make-up Flowrate** | 5ml/min |
| **Reference Flowrate** | 20ml/min |
| **Front Signal Frequency** | 10Hz/0.02min |

A typical chromatograph of the analysis of CO, $C_2H_4$ in the gas phase is shown in Figure A. 38 and the total analysis time was ca. 11min.

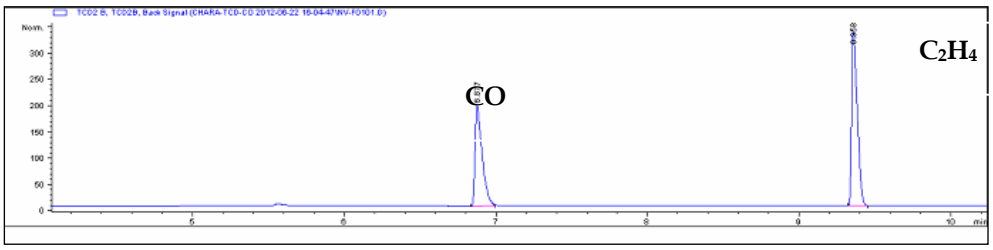


**Figure A. 38** *Typical chromatograph of the gas analysis of a 10%v/v CO:$C_2H_4$ mixture.*

The reproducibility of GC for gas samples was satisfactorily as the relative standard deviation was calculated to be less than 0.5%. The calibrations for

carbon monoxide and ethylene can be found in the Appendix A (Figure A. 10-Figure A. 11).

During experiments partial evaporation of methanol (MeOH) and methyl propionate (MeP) occurred. Being able to quantify the amount of MeOH and MeP in the gas phase directly, under different operating conditions, was essential in order to close the carbon balance of the system and thus validate our analysis method and the accuracy of the experimental results in general.

For the calibration of GC for methanol in the gas phase, a gas stream of $He/N_2$ was bubbled through a flask of 100ml, almost full with MeOH, that was placed inside a cooling bath for controlling the temperature. The gas stream ($He/N_2$/vapour MeOH) was analysed by GC using the method described (Table A. 13). Nitrogen was used as internal standard and based on the change of its peak area before and after passing the flask, the amount of MeOH in the gas phase was calculated. For this purpose, the GC was first calibrated for $N_2$ using $N_2$-He mixtures for a concentration range 5-40% v/v $N_2$-He (Figure A. 12, Appendix A). During the calibration of vapour MeOH, $2ml_{20oC,1bar}$/min of 30%v/v $N_2$:He stream was introduced in the inlet so that the change of $N_2$ peak area would be easily observed. In addition, this experiment was conducted in a range of temperatures (5-20$^{o}$C). In all cases the temperature in the cooling bath was lower than the ambient temperature to avoid any downstream condensation of vapour MeOH.

The fraction of a component i (MeOH, MeP) in the gas phase, $y_i$, can be calculated based on (A.6),

$$y_i = \frac{\gamma_i \cdot x_i \cdot P_i^v(T)}{P^{TOTAL}} \qquad (A.6)$$

where, $\gamma_i$ is the activity coefficient of component i and shows the deviation from the Raoult's law for ideal mixtures, $x_i$ is the fraction of i in the liquid phase. During the calibration pure MeOH was used and therefore $x_{MeOH} = 1$ and $\gamma_{MeOH} = 1$. In all cases, the pressure in the container, $P^{TOTAL}$, was equal to

1.06bara using a pressure sensor (up to 2bar). The vapour pressure of MeOH, $P^{v}_{MeOH}$, was calculated based on Antoine equation,

$$\log\left(P^{v}_{MeOH}(bar)\right) = A - \frac{B}{C + T(^{o}C)} \tag{A.7}$$

where in the case of methanol, A= 5.20277, B= 1580.08 and C= 239.5 for temperature between 263-356K [205].

Based on the above equations the theoretically expected fraction of MeOH in the gas phase in different temperature conditions was calculated (Table A. 14).

**Table A. 14** Theoretical vapour pressure and methanol fraction in the gas phase for a range of temperature conditions, calculated from Antoine's equation (A.7).

| T (K) | $P^{v}_{MeOH}$ (bar) | $y_{MeOH}$ |
|---|---|---|
| 278.15 | 0.054 | 0.052 |
| 283.15 | 0.072 | 0.069 |
| 288.15 | 0.098 | 0.092 |
| 293.15 | 0.13 | 0.12 |

The corresponding experimental results of $y_{MeOH}$ are shown in Figure A. 39, where they are also compared with the theoretically expected values of Table A. 14. It can be seen that there is excellent agreement in all temperatures, fact that indicates the validity of the calibration method. The GC calibration plot for methanol in the gas phase is given in the Appendix A in Figure A. 13.

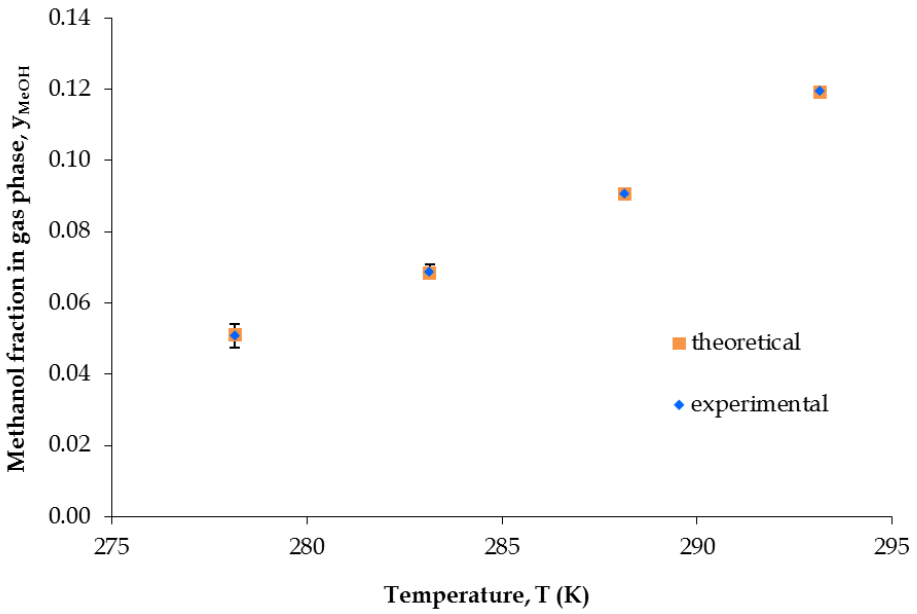


**Figure A. 39** *Experimental and theoretical values of methanol fraction in the gas phase for different temperature conditions.*

Similarly, for GC calibration for MeP in the gas phase the same procedure was followed but in this case a flask of 100ml almost full with MeP was used. The vapour pressure of MeP, $P^{v}_{MeP}$ in bar, was calculated based on (A.9), where in the case of MeP, A= 3.98745, B= 1129.57 and C= 204.24 for temperatures between 267-375K [205]. Based on (A.6) the theoretically expected fraction of MeP in the gas phase in different temperature conditions was calculated (Table A. 15). The experimental results of $y_{MeP}$ and their comparison with the corresponding theoretical values of Table A. 15 are shown in Figure A. 40.

**Table A. 15** Theoretical vapour pressure and methyl propionate fraction in the gas phase for a range of temperature conditions, calculated from Antoine's equation (A.7).

| T (K) | $P^{v}_{MeP}$ (bar) | $y_{MeP}$ |
|---|---|---|
| 278.15 | 0.039 | 0.037 |
| 283.15 | 0.052 | 0.049 |
| 288.15 | 0.0684 | 0.065 |
| 293.15 | 0.0892 | 0.084 |

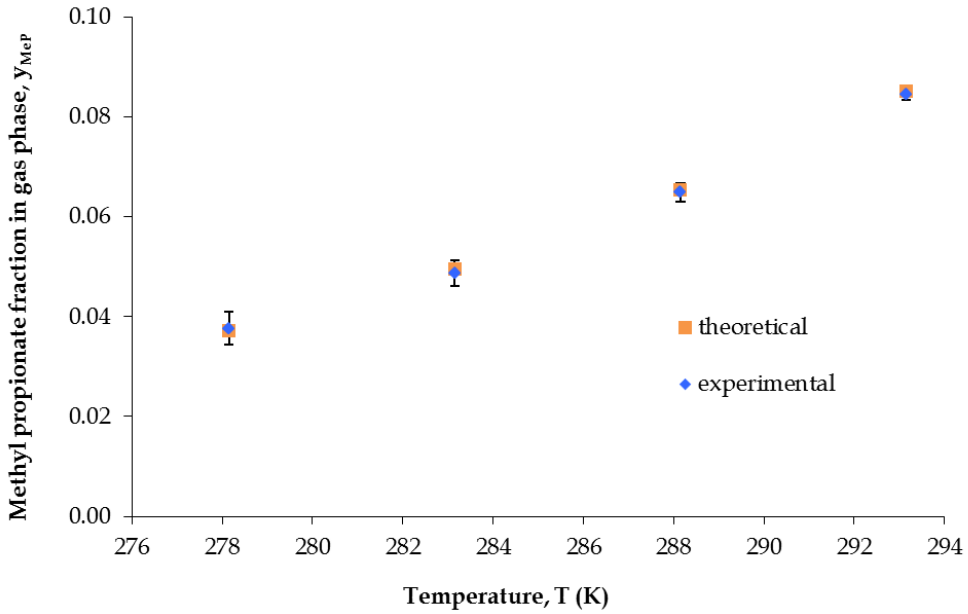


**Figure A. 40** *Experimental and theoretical values of methyl propionate fraction in the gas phase for different temperature conditions.*

It can be seen that again there is good agreement in all cases. The calibration plot for MeP in the gas phase is given in the Appendix in Figure A. 14.

4. Liquid phase analysis

For the liquid analysis a mid-polar capillary column (DB-624, 30m x 320μm x 0.25m, Agilent,) was used. In addition, a 2m long guard column of the same material with the main column was added before the main column to protect it from the acidic nature of the liquid samples. The liquid samples were injected by an auto injector and analysed by means of a FID detector.

The developed GC method for the analysis of MeOH/MeP mixtures is shown in Table A. 16. A typical chromatograph of liquid analysis is shown in Figure A. 41, where it is clear that the peaks are well separated, quite sharp and the total analysis takes no more than 3min. The reproducibility of the analysis was satisfactory as evidenced by analysing the same sample several times. The relative standard deviation for the liquid analysis was less than 2%.

**Table A. 16** GC operating conditions for the liquid analysis of the methoxycarbonylation of ethylene.

| **Column Name** | DB-624 |
|---|---|
| **Split Flow** | 100:1 |
| **Column Flow** | 10ml/min |
| **Oven Temperature** | 190$^{o}$C (3min hold) |
| **Detector** | FID |
| **$H_2$ flowrate** | 30ml/min |
| **Air flowrate** | 400ml/min |
| **Front Signal Frequency** | 50Hz/0.004min |

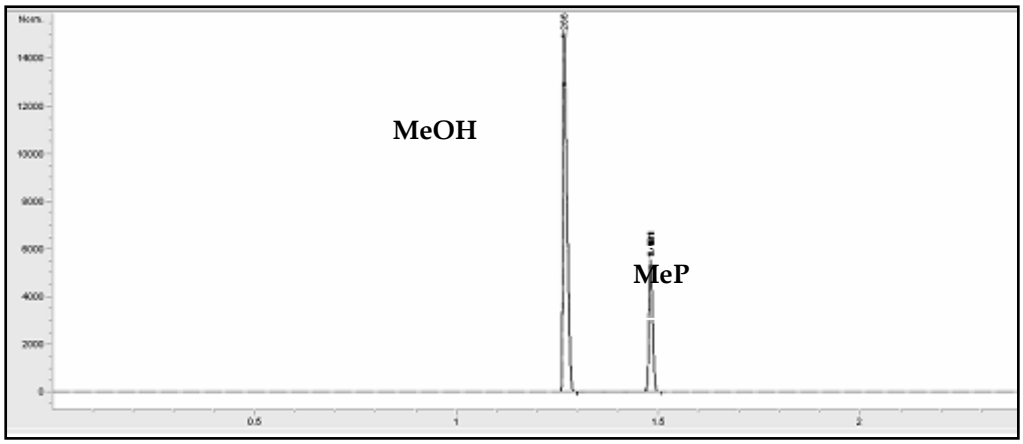


**Figure A. 41** *A typical chromatograph of the liquid analysis of a MeOH:MeP mixture of 80:20%w/w.*

For the GC calibration for methanol and methyl propionate in the liquid mixture, mixtures of them in different compositions were prepared. It should be noted that this binary system deviates from the behaviour of an ideal liquid mixture. Therefore, in order to prepare well-defined MeOH-MeP mixtures, the density and the mass fraction of the mixtures should be expressed as a function of the volume of MeOH added during the mixture preparation. For this purpose, volumetric flasks of 5ml were used and in each of them different volume of MeOH was added. Then, the flask was filled up to 5ml with MeP and the weight of the flask was measured in a balance with accuracy ± 0.0001g. The required MeOH volume added for the preparation of a 5ml MeOH-MeP solution with certain mass fraction and the corresponding density of the mixture are shown in Figure A. 42 and Figure A. 43 respectively.

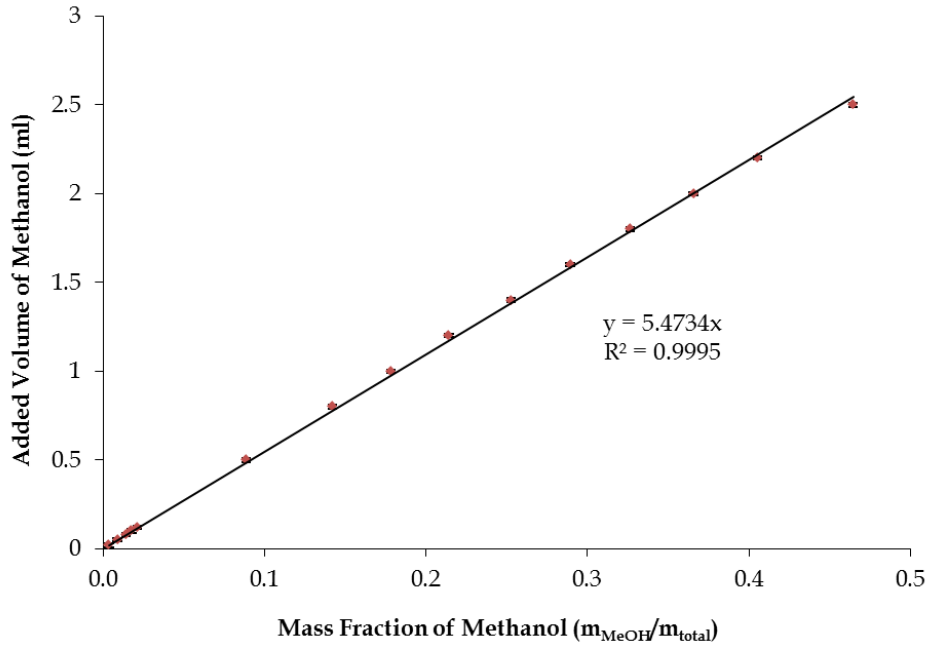


**Figure A. 42** *Required methanol volume for the preparation of a 5ml methanol:methyl propionate mixture with certain mass fraction.*

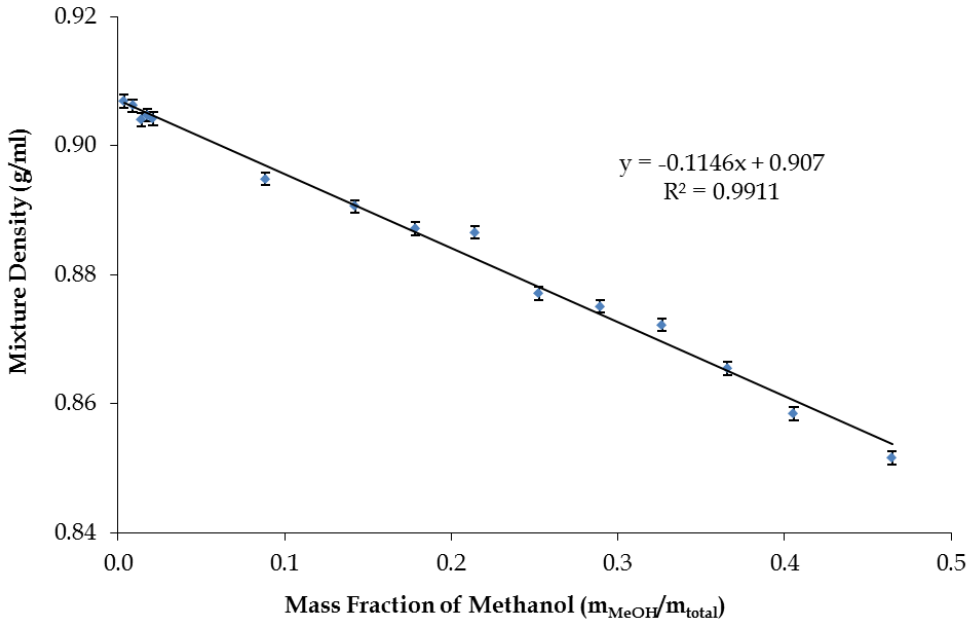


**Figure A. 43** *Density of methanol:methyl propionate mixtures as a function of their mass fraction.*

The GC was calibrated for the analysis of liquid MeOH: MeP mixtures with concentrations that ranged between MeOH:MeP=40:60-10:90%w/w. The mixtures were prepared in a fume cupboard using two pipettes of 1ml. The GC calibration plots for MeOH and MeP are shown in the Appendix A in Figure A. 15 and Figure A. 16 respectively.

5. Catalyst preparation and oxygen effect on catalyst deactivation

Initial experiments showed no reaction occurring, indicating that something was making the catalyst inactive. Over a year was spent investigating the possible sources of this problem. Firstly, the hypothesis that the catalyst is deactivated along the flow set-up, hence some parts of the set-up are responsible for the deactivation, was tested. In order to investigate for surface effects in the reactor, various reactors with different materials were tested such as Stainless Steel, SilcoSteel, Titanium, Hastelloy but no difference on catalyst activity was observed with total absence of reaction. In addition, many other parts of the set-up (e.g pump's syringe, separator, filters, O-rings) were bypassed or replaced to investigate if they are causing catalyst deactivation. No reaction was observed in any case indicating an inactive catalyst. Numerous standard experiments were performed under different operating conditions, rig configurations reactor types and ways of introducing the fluids. However, none of the modifications resulted to a noticeable difference on the reaction rate; no methanol conversion was observed in any case.

After all these tests, there was great confidence that it is not the set-up that deactivates the catalyst. Next hypothesis that was tested was that the catalyst batch used is inactive. For this reason, different catalyst batches of the same and of different concentrations were tried. It was found that using very concentrated catalyst solutions reaction was happening but in significantly less extent than expected. Hence, it was deduced that a portion of the catalyst was deactivated and the only left hypothesis was that this happens during the preparation of the feed mixture where the catalyst is being diluted with methanol and methyl propionate to the desired concentration. To investigate this hypothesis, various standard experiments were conducted using different catalyst concentration in the feed. The operating conditions of a standard experiment were a gas feed of 10%v/v CO:$C_2H_4$

with a flowrate of $0.2ml_{25oC,10bara}/min$ and a liquid composition of 30%wt. MeOH:MeP with a flowrate of $0.005ml/min$ at 100°C and 10bar(absolute).

In Figure A. 44, the reaction rate versus catalyst concentration curve does not pass through the origin as expected, showing that zero reaction rate is observed for a non-zero catalyst concentration. This indicates that ca. $3 \cdot 10^{-4}\, mol/L$ of catalyst was deactivated which corresponds to ca. 34ppm Palladium. This explains why with the standard catalytic solution that contains only 14ppm Palladium we couldn't observe any reaction. A portion of the catalyst was deactivated during the feed preparation. It is worth noting that the actual amount of Palladium species deactivated is very small, however because in our microsystem very small amount of catalyst are required, this amount becomes significant.

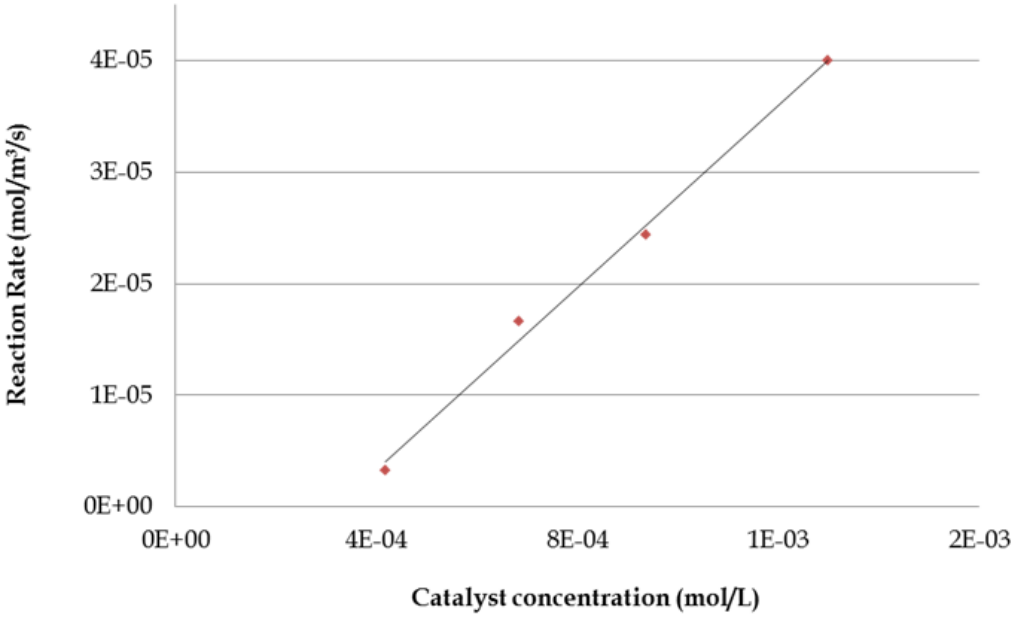


**Figure A. 44** *Observed reaction rate under standard conditions against catalyst concentration in the feed for preparation of the catalytic mixture under air atmosphere.*

It was found that the catalyst deactivation was happening during the preparation of the feed mixture (dilution of cat. mixture with methanol and methyl propionate) under air atmosphere. More specifically, oxygen from the atmosphere dissolved in the liquid mixture, was oxidising and deactivating the catalyst. This was also supported by $^{31}P$ NMR analysis of a

typical feed catalytic mixture (Figure A. 45) where many more peaks (possibly of oxidised species) appear than the two expected of the protonated ligand and the active catalyst at 45ppm and 69ppm respectively.

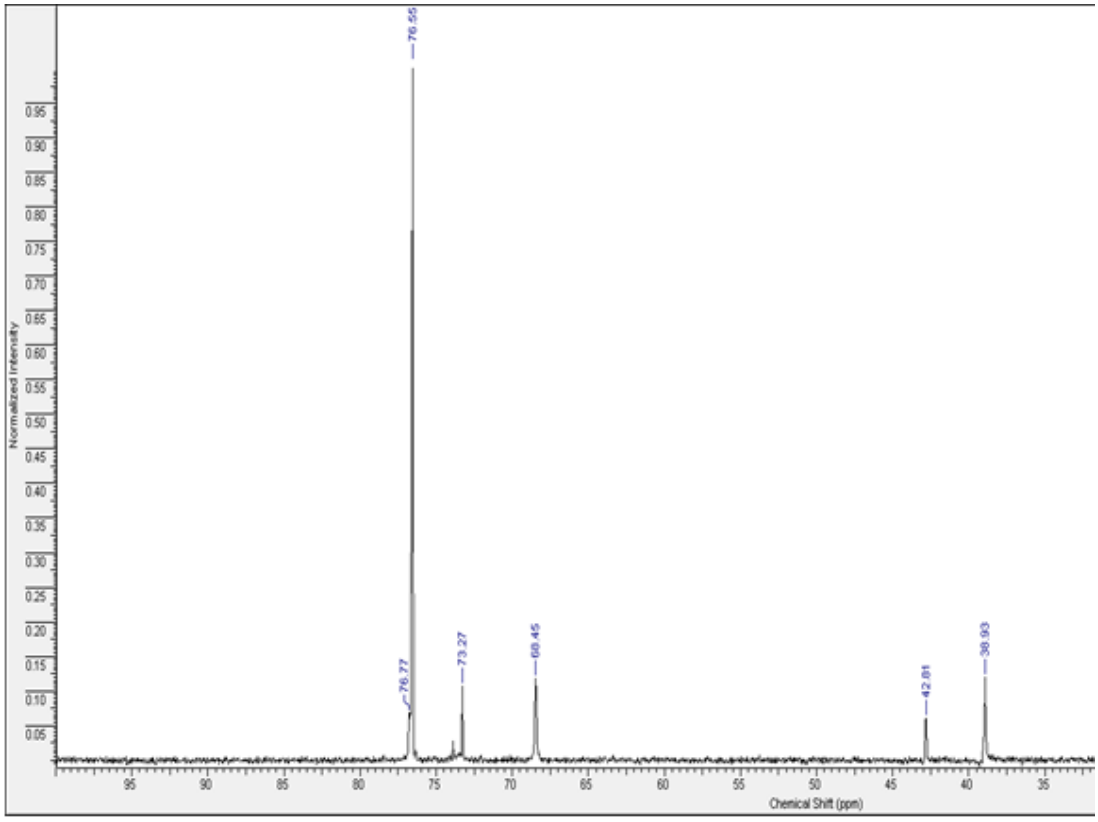


**Figure A. 45** *$^{31}P$ NMR spectrogram of typical feed catalytic mixture.*

Instead, when degasing methanol and methyl propionate with argon and then preparing the feed mixture in a glove box under argon atmosphere, and studying again the effect of catalyst concentration on the reaction rate, the results were very different (Figure A. 46). Now, the effect of catalyst concentration is as expected, with the reaction rate versus catalyst concentration curve passing through the origin, indicating no catalyst deactivation.

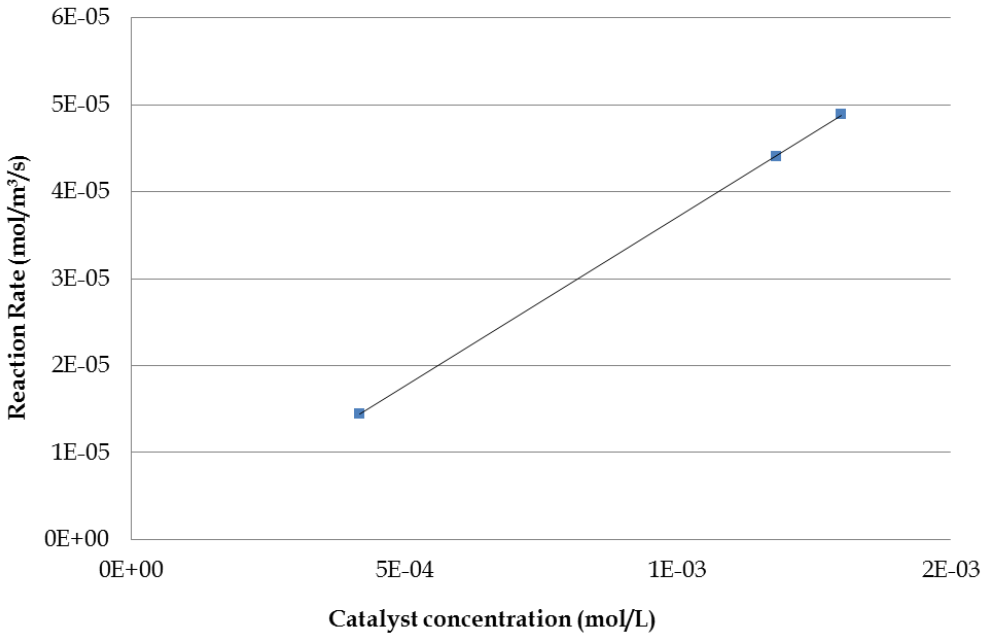


**Figure A. 46** *Observed reaction rate under standard conditions against catalyst concentration in the feed for preparation of the catalytic mixture under argon atmosphere.*

In conclusion, it was found that oxygen of the atmosphere was deactivating the catalyst when preparing the feed mixture under air atmosphere. For this reason, the liquid feed preparation for all the experiments of the kinetic study was done in a glove box under argon atmosphere to prevent any catalyst deactivation. Standard experiments were also regularly performed to validate the stability of the catalyst activity.

6. Reactor pretreatment section

An ethylene pretreatment section was installed upstream of the reactor which consisted of a 2m long Hastelloy tubing with 1.75mm inner diameter. In the pretreatment section the MeOH:MeP liquid solution was mixed with ethylene at 100°C at 10bara. The residence time of the liquid was ca. 30min. In this step, ethylene binds with catalyst, protecting it from contact with a flow rich in carbon monoxide that could poison and possibly deactivate the catalyst. This is suggested based on previous studies in autoclaves reactors by Lucite International.

7. Reactor design

Choosing the material of the reactor is a crucial aspect when designing a reactor. The ideal reactor material is inert and does not interact with any of the reactants, products or the catalyst and remains inert over time. For this reason, the first choice was a fluoropolymer (PFA) capillary, known for its inert nature. The capillary was coiled on a spiral plate (Figure A. 47) which is useful for flow observation.

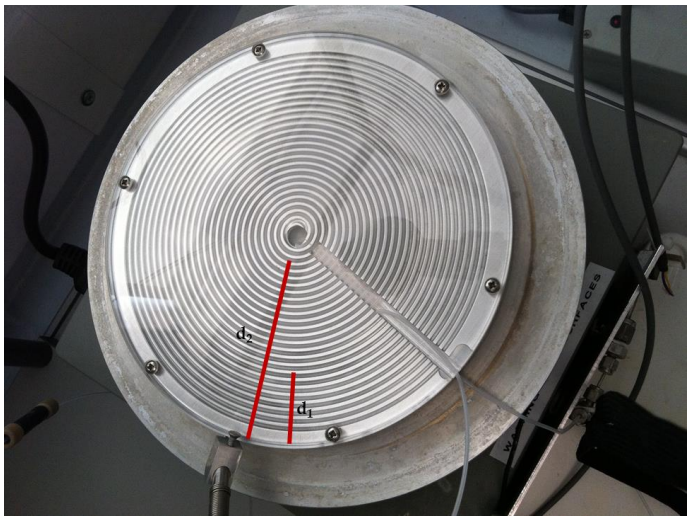


**Figure A. 47** *Spiral plate with PFA capillary reactor.*

To ensure that the reaction inside the PFA reactor on the spiral plate will be at isothermal conditions, the temperature gradient was measured in both

radial direction and along the thickness of the plate for a range of temperatures. In order to measure the temperature gradient in the radial direction, two holes with different depths ($d_1$, $d_2$ with $d_1<d_2$) were drilled on the metallic plate and the temperature was measured by means of two thermocouples. The temperature measurements are shown in Table A. 17. The temperature gradient is less than 0.2°C in all cases which is insignificant.

**Table A. 17** Temperature gradient in the radial direction of the spiral plate for a range of temperatures.

| **Thermocouple 1 ($d_1$)** | **Thermocouple 2 ($d_2$)** |
|---|---|
| **T (°C)** | **T (°C)** |
| 76 | 76.1 |
| 85.4 | 85.6 |
| 94.8 | 94.9 |
| 104.1 | 104.2 |
| 113.3 | 113.5 |

To determine the temperature gradient along the thickness of the plate, the temperature was measured in a few different points for a wide range of temperatures. These points are the bottom of the metallic plate of the reactor, the bottom and the top of the capillary and the bottom and the top of the acrylic plate, installed on top for better insulation (Figure A. 48). The temperature was measured by means of thin thermocouples with thickness equal with 250μm.

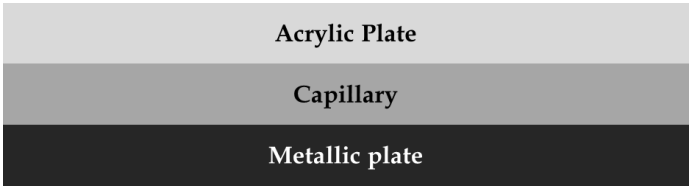


**Figure A. 48** *Layers of spiral plate with capillary reactor.*

In Table A. 18 the temperature measurements are shown. The temperature difference in the bottom and the top of the capillary is always less than 0.5°C. Hence, the reactor can be considered isothermal.

**Table A. 18** Temperature gradient at different points of the spiral reactor.

| T (°C) | | | | |
|---|---|---|---|---|
| **Bottom of metallic plate** | **Bottom of capillary** | **Top of capillary** | **Bottom of acrylic plate** | **Top of acrylic plate** |
| 66 | 65.2 | 64.9 | 53.5 | 44.6 |
| 86.1 | 84.7 | 84.2 | 68.1 | 51.9 |
| 107.2 | 105.4 | 104.7 | 83.5 | 63.4 |
| 128.1 | 125.2 | 124.2 | 100.7 | 80.1 |

Next step was to perform blank experiments (without catalyst in the feed) with this PFA spiral reactor to ensure satisfactory operation. However, blank experiments showed that at high temperature the mole balance of ethylene between the inlet and the outlet of the system did not close. Instead, analysis showed that ethylene concentration significantly decreased in the outlet, but only when the temperature was high. Accuracy of vapour-liquid equilibrium of the system and of the analysis methods were examined, but none of this was the answer. Finally, tubing permeability was found to be the reason for the mole balance discrepancy.

- Permeability experiments

The permeability of the PFA reactor was tested at two temperature conditions (25°C, 100°C) by pressurising the system at 10bara with a gas mixture of CO:$C_2H_4$=1:9v/v and analysing the exiting gas stream in terms of composition and volumetric flowrate (at 25oC, 1bara). The composition of the exiting stream was analysed by GC and its volumetric flowrate was measured by a bubble meter. No liquid was flowing through the system, hence no reaction was taking in this experiment.

In Figure A. 49 the molar flowrate of carbon monoxide and ethylene are shown in the exit of the PFA reactor for two reactor's temperatures.

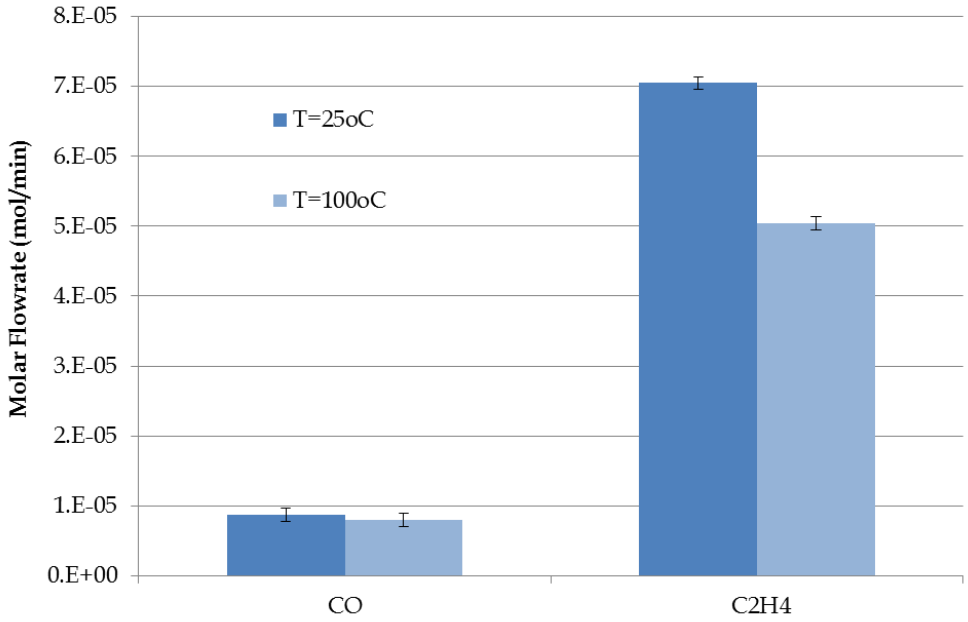


**Figure A. 49** *Molar flowrate of carbon monoxide and ethylene in the outlet (25°C, 1bara) of a PFA tubing using an inlet gas mixture of CO:$C_2H_4$=1:9v/v and reactor's conditions 25°C and 100°C at 10bara.*

At 25°C the molar flowrate of carbon monoxide and ethylene in the outlet of the reactor is equal with that in the inlet. However, when increasing the temperature in the PFA tubing from 25°C to 100°C, ethylene molar flowrate decreases by 29% compared to the inlet. For carbon monoxide the decrease is very small and within the experimental error. Therefore, the tubing is permeable to ethylene at elevated temperature and thus this material cannot be used for the kinetic study of the MeP system.

The same procedure was followed using other fluoropolymer tubings such as ETFE, PEEK and Halar ECTFE but all of them presented the same behaviour as the PFA tubing, permeable to ethylene at elevated temperature. Hence it was concluded that no fluoropolymer tubing is suitable for the kinetic study of the MeP system.

Hastelloy tubing was tested for its permeability following the same procedure as before. In Figure A. 50 the molar flowrate of carbon monoxide and ethylene are shown in the exit of the Hastelloy reactor for two reactor's temperatures.

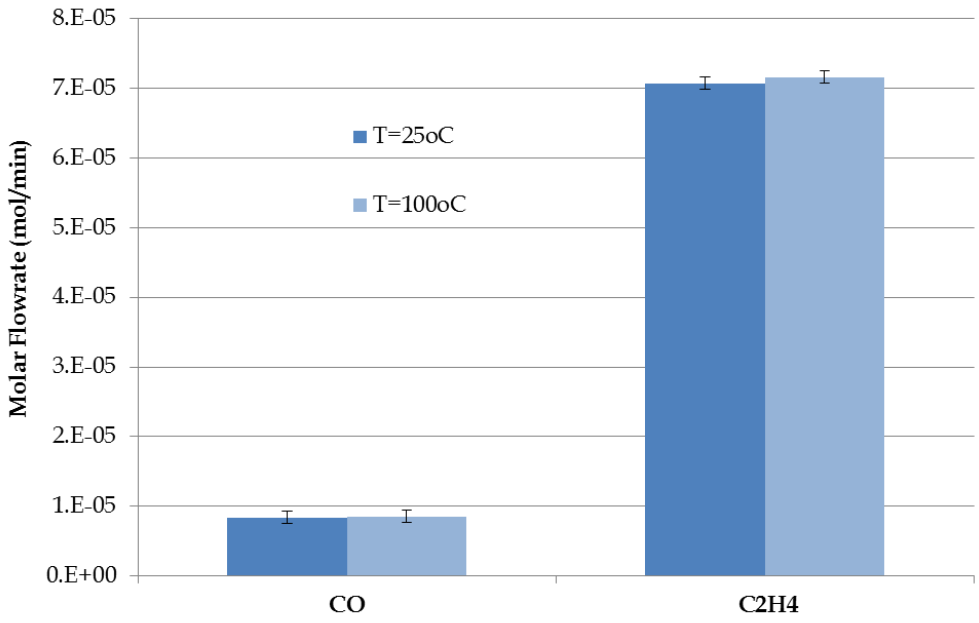


**Figure A. 50** *Molar flowrate of carbon monoxide and ethylene in the outlet (25°C, 1bara) of a Hastelloy tubing using an inlet gas mixture of CO:$C_2H_4$=1:9v/v and reactor's conditions 25°C and 100°C at 10bara.*

The molar flowrate of carbon monoxide and ethylene in the outlet of the Hastelloy reactor found equal to the inlet ones for both temperatures. No significant change was observed in the molar flowrates of carbon monoxide and ethylene at any temperature indicating no permeability of the gases through Hastelloy.

The same procedure was followed using other metal tubings such as Titanium, Stainless Steel and SilcoSteel and none of them found permeable to carbon monoxide or ethylene at elevated temperatures, hence they are all suitable for the kinetic study of the MeP system.

- ❖ Isothermality

Preliminary calculations of the temperature profiles along the capillary reactor were performed in order to investigate if the thermal entry length is significant and if the length to temperature stabilisation is comparable to the total length of the reactor. Single phase flow was considered for ease of the calculations and specifically methanol flowing in PTFE tubing with 1mm inner diameter. PTFE was chosen as it is the least conductive material (hence

the worst case scenario). It has smaller thermal conductivity compared to metal tubing (0.25W/m·K compared to 16W/m·K for stainless steel). Two flowrates were tested, 0.005ml/min and 0.2ml/min which correspond to typical liquid and gas flowrate respectively during this study.

The solution of the energy balance of a single phase flow along a circular pipe considering two resistances, the fluid convection and the tubing conduction, for constant temperature on the walls is given by (A.8) and (A.9) [206],

$$\frac{T_s - T_m(x)}{T_s - T_{m,0}} = exp\left(-\frac{1}{\dot{m} \cdot Cp \cdot R_{tot}}\right) \quad (A.8)$$

$$R_{tot} = \frac{\ln(\frac{OD}{ID})}{2 \cdot \pi \cdot x \cdot k} + \frac{1}{\bar{h} \cdot 2 \cdot \pi \cdot ID \cdot x} \quad (A.9)$$

where $T_s$ and $T_m$ is the walls and the mean temperature (K) respectively, $\dot{m}$ is the mass flowrate of the fluid (kg/s), Cp is the specific heat of the fluid (J/kgK), OD and ID are the outer and the inner diameter of the tubing, x is the distance (cm) in the axial coordinate, $\bar{h}$ is the heat transfer coefficient of the fluid (W/m$^2$K) and k the thermal conductivity of the tubing (W/mK). The heat transfer coefficient of the fluid is calculated based on (A.10),

$$\overline{Nu}_D = \frac{\bar{h} \cdot ID}{k} \quad (A.10)$$

assuming laminar flow in a straight, smooth pipe.

It was found that the centre of the tubing reaches rises from 293K to 373K (typical reaction temperature) in less than 1mm when flowrate is 0.005ml/min and 1.5cm when flowrate is 0.2ml/min, which is insignificant compared to the total reactor length (6m). These results were validated with Comsol simulations (Figure A. 51-Figure A. 52), where a simplified scenario was tested for ease of calculations. Specifically, the temperature profile of a single phase flow (only methanol) was tested along the reactor, a PTFE tubing, rising from 293K in the feed to 373K (typical reaction temperature).

Two simulations were considered for two liquid flowrates at 0.005ml/min and 0.2ml/min typical for the liquid and the gas flowrates.

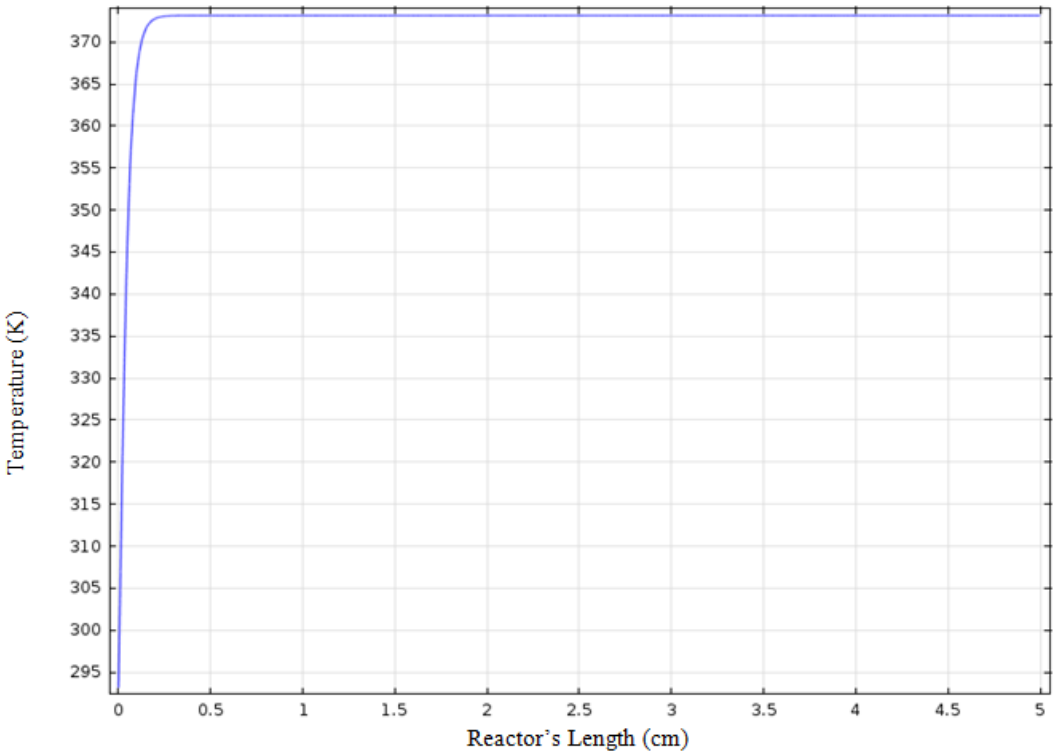


**Figure A. 51** *Temperature profile in axial direction for single phase flow (MeOH only) with 0.005ml/min in a PTFE tubing with 1mm inner diameter at atmospheric pressure and room temperature in the inlet.*

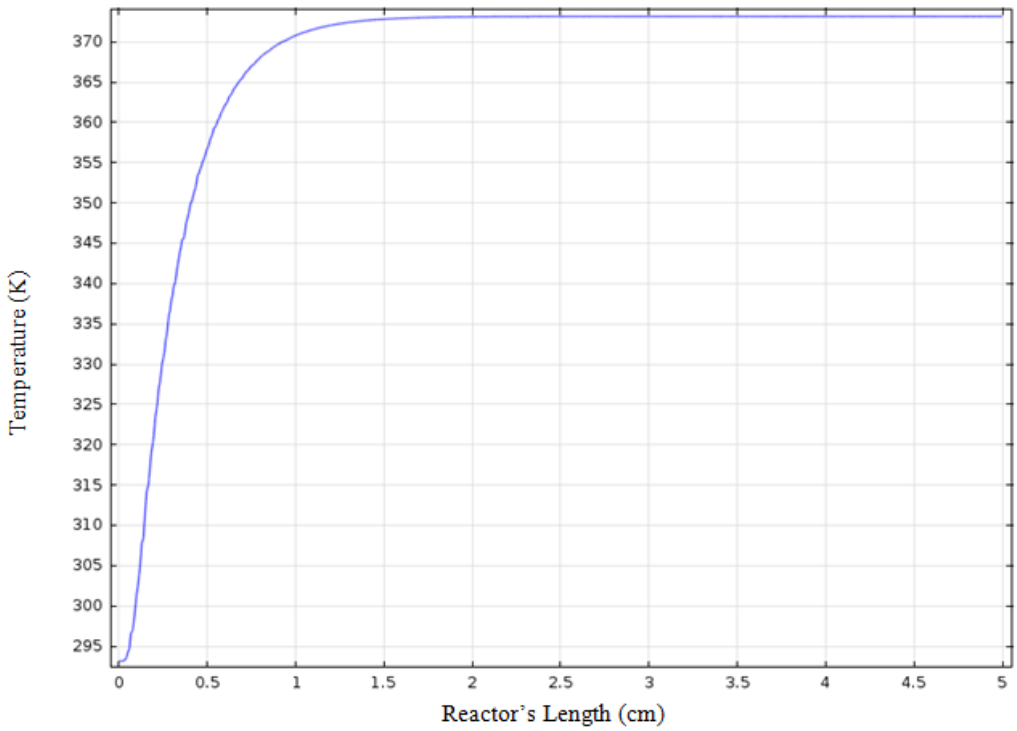


**Figure A. 52** *Temperature profile in axial direction for single phase flow (MeOH only) with 0.2ml/min in a PTFE tubing with 1mm inner diameter at atmospheric pressure and room temperature in the inlet.*

Although the simulation case is a simplified case, it is still representative and indicates that reactor reaches reaction temperature so quickly that entrance effects can be neglected. This is mainly because of the small tubing diameter, the thin tubing walls and the slow flow.

- Blank experiment

A series of blank experiments were performed to ensure that the capillary internal surface is inert and is not interacting with any of the components of the system. The blank experiments were conducted at 100°C, at 10bar with a gas feed mixture of CO:$C_2H_4$ (1:9 v/v, $\upsilon_g$=2$ml_{299K,1bar}$/min) and a liquid feed mixture of 30:70 w/w% MeOH:MeP (with no catalyst, $\upsilon_\ell$=0.01ml/min). In Figure A. 53 the molar flowrates in the inlet and the outlet of the reactor are shown for all components using a Hastelloy reactor with 1mm inner diameter. The molar flowrates were calculated based on GC analysis of the gas and liquid phase in the inlet and outlet of the reactor.

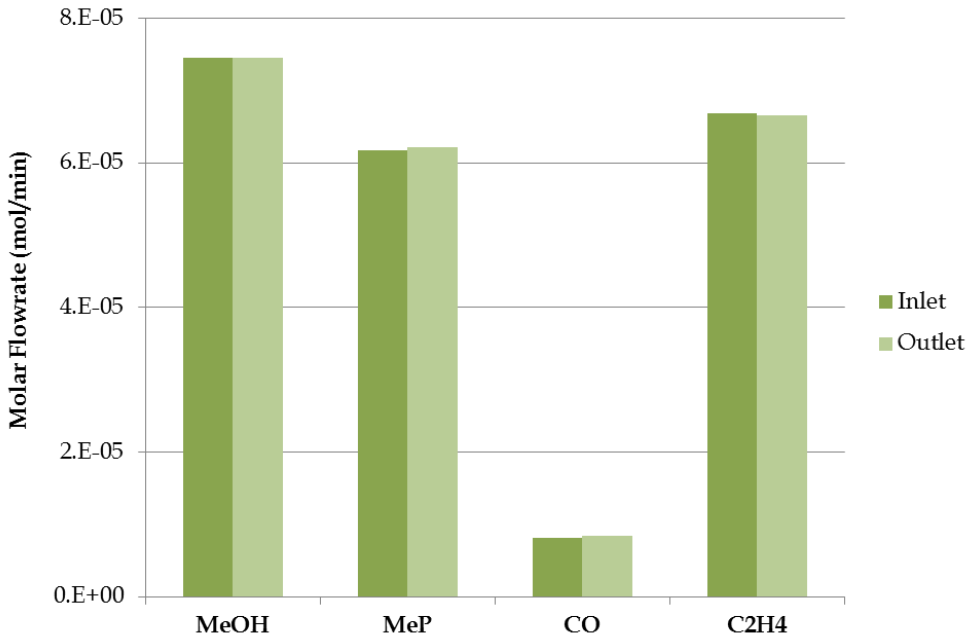


**Figure A. 53** *Molar flowrates of all components in the inlet and the outlet of a Hastelloy capillary reactor during a blank experiment.*

There is no significant change in the molar flowrates of any of the components between the inlet and the outlet indicating that there is no interaction with the reactor's surface and hence the Hastelloy reactor is suitable for our kinetic study. Same inert behaviour was also observed with all other metal tubings used such as Titanium, Stainless and SilcoSteel. However, Hastelloy was the final choice of the reactor material, as it is also used industrially for the same process and has presented excellent stability over time.

- ❖ Standard experiment

A standard experiment was performed in order to check that the carbon balance closes and hence that the analysis methodology is accurate for the kinetic study. Standard experiments were repeated regularly in order to ensure that the activity of the catalyst remained constant. The standard experiment was conducted at 373.15K, at 10bara using a 6m long Hastelloy reactor with 1mm inner diameter. A gas mixture of $CO:C_2H_4$ (1:7 v/v, $\upsilon_g$=1.8ml$_{298K,1bar}$/min) and a liquid mixture of 30:70 w/w% MeOH:MeP ($\upsilon_l$=0.005ml/min) were used in the feed. The results of the standard

experiment are shown in Figure A. 54, where the molar flowrates of all components are shown in the inlet and the outlet of the reactor.

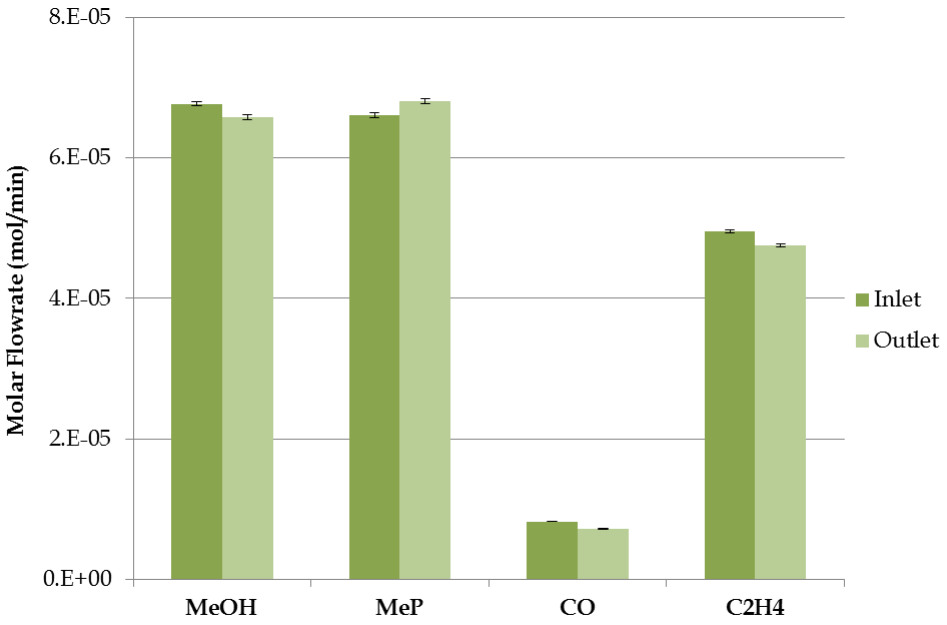


**Figure A. 54** *Molar flowrates of all components in the inlet and outlet of the reactor for a standard experiment in a Hastelloy reactor.*

Based on the results of the standard experiment the mole balances of all components of the system were calculated and are presented in Table A. 19.

**Table A. 19** Mole balance of MeP system for standard experiment.

| mol/min | Inlet | Outlet | Mole Difference | % Mole Difference |
|---|---|---|---|---|
| **MeOH** | 6.77E-05 | 6.58E-05 | -1.90E-06 | 2.8 |
| **MeP** | 6.61E-05 | 6.8E-05 | 1.92E-06 | 2.9 |
| **CO** | 8.27E-06 | 7.19E-06 | -1.08E-06 | 13 |
| **$C_2H_4$** | 4.96E-05 | 4.75E-05 | -2.03E-06 | 4.1 |

Mole differences of all components are very close to each other indicating a good carbon balance. Specifically the carbon balance closed within 3% difference. This validates the accuracy of the analysis methods used and proves that this experimental configuration is well defined and hence very suitable for kinetic studies.

8. Separator design

Following the reactor, the reaction is quenched due to the drop of the temperature and the gas-liquid mixture enters a separator. Two different designs of gas-liquid separators were tested for this purpose. Firstly, a glass microseparator (mikroglas) used for the experiments with the model reaction (Chapter 3.3.1.2) could be used for our kinetic study as the manufacturer specified that it can stand up to 15bara while our study will take place at 10bara. This was also tested experimentally and was found that the microseparator can withstand pressures up to 13bar without any problem. Significant amount of time was spent testing further the microseparator, but it was found that its operational window is very small and it is almost not feasible to use it in our case. This is because the pressure difference required to apply across the microseparator for a successful and stable separation was found to be 0.01-0.02bar. When a higher pressure difference was applied gas was breaking through to the liquid outlet while for a smaller pressure difference liquid was escaping to the gas side. The required pressure difference (0.01-0.02bar) is proportionally very small for a high pressure system like ours where the total pressure is 10bara; it is only 1% of the total pressure. This means that even a very small pressure fluctuation of 1% of the total pressure can affect the stability of the separation.

A custom-made stainless steel (SS) gravity-based separator of 3ml internal volume was tested which was made with stainless steel tube, a tee-junction and a few stainless steel fittings. A schematic of this simple high-pressure separator is shown in Figure A. 55.

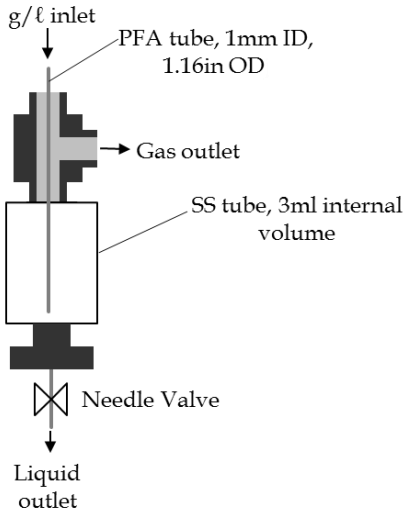


**Figure A. 55** *Stainless steel gas-liquid high-pressure separator based on gravity.*

The separator was tested successfully with a $N_2$/water mixture at 12bar (absolute). In the bottom of the separator a metering valve was added in order to have a smoother liquid sampling without any sudden pressure drop.

9. Tracer effect on RTD experiments

For the step-change of the liquid feed concentration, ideal tracers would be chemical components that are already present in the reaction system such as methanol, methyl propionate or mixtures of them. In this way the system won't be disturbed as it would if a completely different chemical was used for the step change. In addition, due to the fact that the sensors are integrated with the set-up for the kinetic study, the hydrodynamic study of the system can be conducted simultaneously with the kinetic experiments, after every run.

A series of RTD experiments were conducted to investigate the effect of the tracer choice on RTD parameters such as the liquid residence time, the dispersion factor and the void fraction. Ideally, the solvent should not affect these results. Four different tracers were tried (pure MeOH, MeOH:MeP=70:30%wt, MeOH:MeP=50:50%wt, pure MeP) at certain gas ($CO:C_2H_4$=1:9) and liquid (MeOH:MeP=30:70%wt) flowrates (Table A. 20) at

373K, 10bar. It should be noted that the typical liquid concentration in the feed during the kinetic study was 30:70%wt. MeOH:MeP. The Hastelloy reactor used had an internal diameter of 1mm and 6m length.

In Table A. 20 the flowrates in the feed of the set-up and the reactor inlet are shown where different temperature conditions apply. In the feed of the set-up the flowrates were based on the set values of the mass flow controllers (after correction for the temperature and the pressure) and the syringe pump. In the reactor the compositions of the gas and the liquid stream change due to the change in the temperature. For example methanol and methyl propionate evaporate resulting to an increase of the gas flowrate. To take into account this vapour-liquid equilibrium (VLE) effect, a VLE model was utilised that is able to predict the new compositions and flowrates in the reactor (100$^{o}$C) when knowing the corresponding compositions and flowrates in the feed (25$^{o}$C). More information about the VLE model can be found later in Appendix J. The VLE effect is another reason why it is important to study the hydrodynamics of the system under reaction conditions.

**Table A. 20** Gas and liquid flowrates and gas to liquid ratio in the feed of the set-up and under reaction conditions.

| | **Feed of set-up 299K, 10bar** | **Reactor Inlet 373K, 10bar** |
|---|---|---|
| **$\upsilon_g$ (ml/min)** | 0.2 | 0.277 |
| **$\upsilon_\ell$ (ml/min)** | 0.01 | 0.0083 |
| **g/ℓ ratio** | 20 | 33 |

For these flowrates, the observed flow pattern (by means of a microscope) in the feed of the set-up (25$^{o}$C, 10bara) where the tubing was transparent (made of PFA with same inner diameter) was slug-annular flow with elongated bubbles ($L_{bubble}$>30cm) and relatively short liquid slugs ($L_{slug}$<2mm). Under reaction conditions (100$^{o}$C, 10bara) it is expected to have a more annular-like flow pattern due to the increase of the gas flowrate and the decrease of the

liquid flowrate (as liquid evaporates when temperature increases). It was though not feasible to observe the temperature effect experimentally. The reactor was made of Hastelloy which was not transparent.

The analysis of the RTD experiments was based on the assumption that the inlet signal was a perfect step and therefore no deconvolution of the data is needed. This assumption enables a quicker and simpler data analysis and in the same time it was found that affect only slightly our results. Concerning the liquid residence time measurement it was found that this assumption causes small error in our findings of less than 10%. Due to this simplification, the real dispersion factor would be slightly smaller than the one calculated, due to upstream dispersion that was not excluded. Hence in this way we establish the worst case scenario.

The results of the RTD experiments with different tracers are shown inTable A. 21, where $\tau_\ell$ is the experimentally measured liquid residence time, D/uL is the dispersion number that found by comparison of the RTD curves with corresponding curves in the literature [8]. A sample demonstration of the analysis of the RTD signal can be found in Appendix D.

**Table A. 21** Effect of solvent of the step-change on the RTD results.

| **Tracer** | **Mean liquid residence time, $\tau_\ell$ (s)** | **Dispersion number, D/uL** | **Void fraction prefactor A** |
|---|---|---|---|
| **Pure MeOH** | 1829 | 0.006 ± 0.001 | 0.956 |
| **70:30%wt.MeOH:MeP** | 1835 | 0.0065 ± 0.001 | 0.956 |
| **50:50%wt.MeOH:MeP** | 1880 | 0.012 ± 0.001 | 0.955 |
| **Pure MeP** | 1910 | 0.0148 ± 0.001 | 0.949 |

The last column in Table A. 21 corresponds to the numerical prefactor, A, found to satisfy (A.11) and (A.12). It should be reminded here that for the most common hydrodynamic correlations, Armand's model and homogenous model A=0.833 and A=1 respectively.

$$\varepsilon_\ell = 1 - \left[ A\left( \frac{j_g}{j_g + j_\ell} \right) \right] \tag{A.11}$$

$$\tau_\ell = \varepsilon_\ell \frac{L}{j_\ell} \tag{A.12}$$

The residence time is not affected significantly by the choice of the tracer. The dispersion number however increases slightly when the tracer is more concentrated with MeP. This is due to the decreased viscosity of the solution in that case, which results to a thinner liquid film around the bubbles and hence a larger dispersion number [174,184]. However, the dispersion number in all cases is small, hence the flow can be considered to satisfy plug flow criterion (D/uL<0.01).

The tracer does not affect the void fraction prefactor significantly. Prefactor value is between the corresponding value of Armand's and homogenous model (closer to the later one), hence none of these model is predictive in this case. This may be due to the fact that in these studies [70-72,76,78] different gas-liquid systems were studied, hence the liquid film thickness (which affects largely the prefactor A) was different due to the different liquid properties. This fact highlights the necessity of conducting RTD experiments for the determination of the void fraction and not following one of the existing models.

After confirming that the choice of the tracer for the step change is not affecting the hydrodynamic results, pure methanol was chosen for the rest of the RTD experiments.

10. Characterisation of the mass transfer characteristics of the system

Another crucial aspect in a kinetic study of a system is to ensure that there are no mass transfer limitations based on Hatta criterion,

$$Ha = \frac{\sqrt{k_r \cdot D_{A\ell}}}{k_\ell} < 0.3 \quad \text{(A.13)}$$

where $k_r (= s^{-1})$ is the reaction rate constant of the reaction, $D_{Al} (= m^2/s)$ is the reactant A diffusivity into the liquid and $k_l (= m/s)$ the mass transfer coefficient of A in the liquid phase.

There are several hydrodynamic models available in the literature for the calculation of the mass transfer coefficient, $k_\ell\alpha$, in a system (Chapter 2.3.2). Using four of them Hatta number was calculated for the cases A (Table 5-1) and the results are shown in Table A. 22. It was assumed that the reaction rate constant is equal to $7 \cdot 10^{-5} s^{-1}$ (based on previous, preliminary studies on the MeP system), the diffusivity equal to $9 \cdot 10^{-9}$ $m^2 s^{-1}$ (based on the diffusivities of carbon monoxide and ethylene in methanol at elevated temperature, [207,208]) and the film thickness equal to 19μm based on RTD results. The flow characteristics of the system were based on flow observation at 25°C. At reaction temperature (100°C) the bubble length is expected to be even larger and the liquid slug smaller due to evaporation of the liquid phase.

In Table A. 22, it is shown that all models except Yue et al. model give similar results. Yue model results to significantly higher Hatta numbers, probably because of the use of rectangular channels, but still in that case Hatta numbers are below the limit for the kinetic control.

**Table A. 22** Hatta number for case A based on various mass transfer models.

| **Mass transfer model** | $k_\ell\alpha$ **($s^{-1}$)** | $k_\ell$ **(m/s)** | **Hatta number** |
|---|---|---|---|
| Bercic and Pintar **[102]** | 0.053 | 0.0013 | $5.93 \cdot 10^{-4}$ |
| van Baten **[105]** (only film contribution) | 11.46 | 0.0016 | $4.91 \cdot 10^{-4}$ |
| Yue **[99]** | 0.199 | 0.000028 | 0.028 |
| Sun **[209]** | 16.3 | 0.0023 | $3.45 \cdot 10^{-4}$ |

It was concluded that in the range of flowrates we are planning to work, MeP system will operate under kinetic control as Hatta number is well below the kinetic control criterion (Ha<0.3).

## 11. Vapour-liquid equilibrium model

A VLE model developed by Torres [210] for the same gas-liquid system was used and will be described in brief here. In Figure A. 56 the equilibrium block is shown, where knowing the initial compositions in the inlet, it is possible to calculate the compositions of the gas and the liquid phase in a new equilibrium position by means of a vapour-liquid equilibrium model.

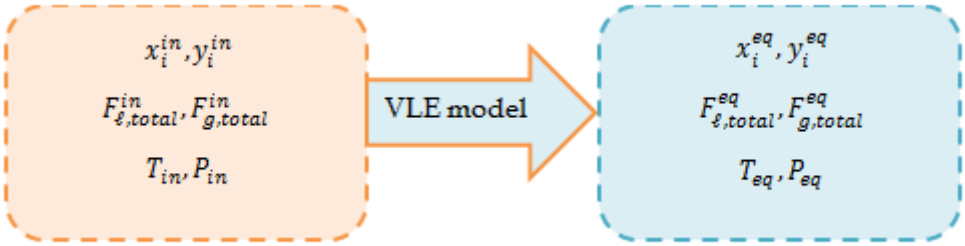


**Figure A. 56** *Study block for vapour-liquid equilibrium model.*

The mole balance in the equilibrium block is shown in (A.14),

$$x_i^{in} \cdot F_{\ell,total}^{in} + y_i^{in} \cdot F_{g,total}^{in} = x_i^{eq} \cdot F_{\ell,total}^{eq} + y_i^{eq} \cdot F_{g,total}^{eq} \quad \text{(A.14)}$$

where, $x_i, y_i$ are the fractions of component i in the liquid and in the gas phase respectively, while $F_{\ell,total}, F_{g,total}$ are the total molar flowrates in the liquid and in the gas phase respectively. The summation of the fractions in the liquid and in the gas phase should be equal to 1.

$$\sum x_i = 1 \quad \text{(A.15)}$$

$$\sum y_i = 1 \quad \text{(A.16)}$$

For the calculation of the composition in the equilibrium block, the equilibrium equations are also needed. For components that are very dilute

in the liquid phase ($x_i$<0.1) such as carbon monoxide and ethylene, Henry's law can be applied,

$$y_i \cdot \phi_i^v \cdot P = \gamma_i \cdot x_i \cdot He_i^{mix,p} \quad \text{(A.17)}$$

where $\phi_i^v$ is the fugacity coefficient of component i in the gas phase, P is the total pressure of the system, $\gamma_i$ is the activity coefficient of component i in the liquid phase (determined by UNIQUAC equation) and $He_i^{mix,p}$ is the Henry's constant for the component i in the liquid mixture after correction for the elevated pressure (Poynting factor). For the rest of the components (methanol, methyl propionate) the following equilibrium equation can be used,

$$y_i \cdot \phi_i^v \cdot P = \gamma_i \cdot x_i \cdot P_i^{vap} \quad \text{(A.18)}$$

where $P_i^{vap}$ is the vapour pressure of component i determined by Antoine equation.

More details for the equations and the constants used for the calculation of $\phi_i^v$, $\gamma_i$, $He_i^{mix,p}$, $P_i^{vap}$ can be found in Torres thesis [210]. The model was written in gPROMS modelling software and the solvers used for the initialisation and for the block solution are BDNLSOL and SPARSE respectively. The model is presented analytically in Appendix E.

There is only one modification made in our case on the equations listed in Torres thesis that should be noted. This is for the calculation of the pure component saturated volume, $\overline{V}$, necessary for calculation of the fugacity constant, $\phi_i^v$. The original equation (Torres thesis, p.250, eq. 1.36) is shown below,

$$\overline{V} = \frac{R \cdot T_c \cdot \left(Z^{RA}\right)^{\left[1+(1-T_r)^{2/7}\right]}}{P_c} \quad \text{(A.19)}$$

where $T_c$, $P_c$ are the critical temperature and pressure of each component respectively, $T_r$ $\left(=T/T_c\right)$ is the dimensionless critical temperature of each

component and $Z^{RA}$ is the Rackett compressibility factor. The problem appears when trying to use (A.19) for carbon monoxide and ethylene. Their critical temperatures (132.92K and 282.34K respectively) are well below the experimentally operating temperature (295-390K) resulting to a negative ($1-T_r$) term. The problem is that mathematically is not permitted to raise a negative number to a non-integer number (2/7) and therefore gPROMS crashes when faces this calculation. An arbitrary modification of (A.19) was made to overcome this problem and is shown in (A.20),

$$\overline{V} = \frac{R \cdot T_c \cdot \left(Z^{RA}\right)^{\left[1+(T_r-1)^{2/7}\right]}}{P_c} \qquad \text{(A.20)}$$

In order to validate that the VLE model was correctly transferred in gPROMS, that the modification made does not affect its accuracy and that the constants used are the correct ones, a validation of the model was performed by comparing its predictions by previous experimental data of Torres [210]. Simulations were performed for an inlet gas stream of $x_{C2H4}$:$x_{CO}$=5:1 and a liquid stream of 30:70 wt.% MeOH:MeP. The temperature considered in the equilibrium block was 363K while the equilibrium pressure were between 3-18bar.

In Figure A. 57-Figure A. 59 the fraction of the components in the gas and the liquid phase are shown respectively against different pressure conditions in the equilibrium block.

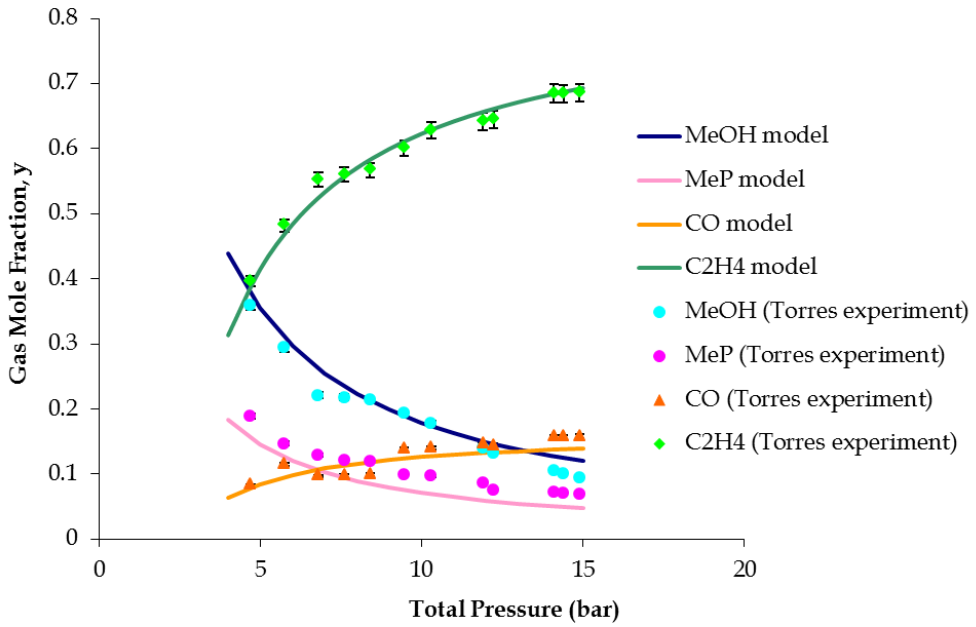


**Figure A. 57** *VLE model predictions for gas fraction of all components against pressure at 363K.*

The VLE model predictions both for the gas and the liquid fractions are in excellent agreement with Torres results, especially for the pressure range we are interested in, between 8-12bar.

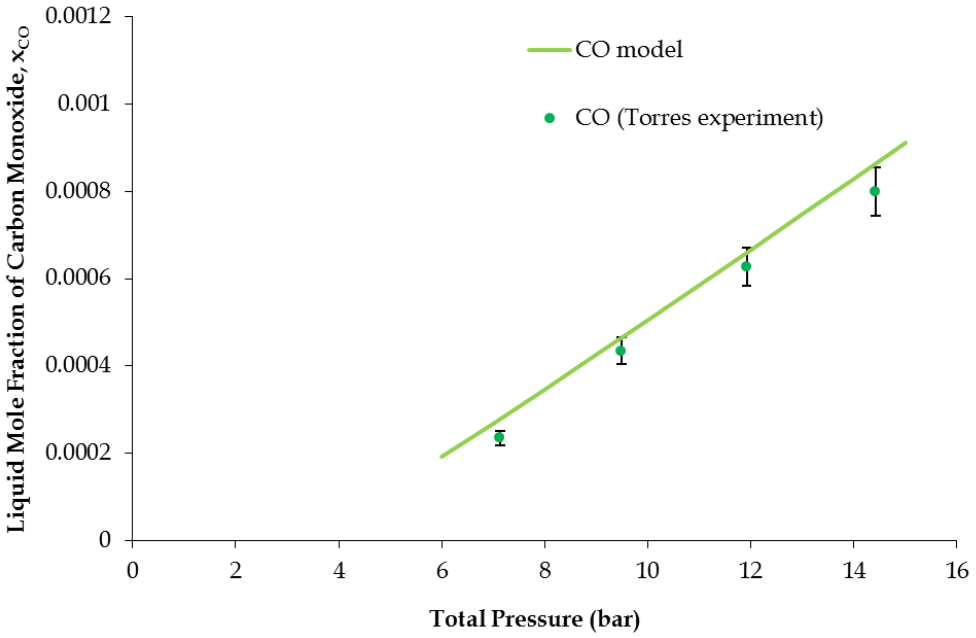


**Figure A. 58** *VLE model predictions for liquid fraction of carbon monoxide against pressure at 363K.*

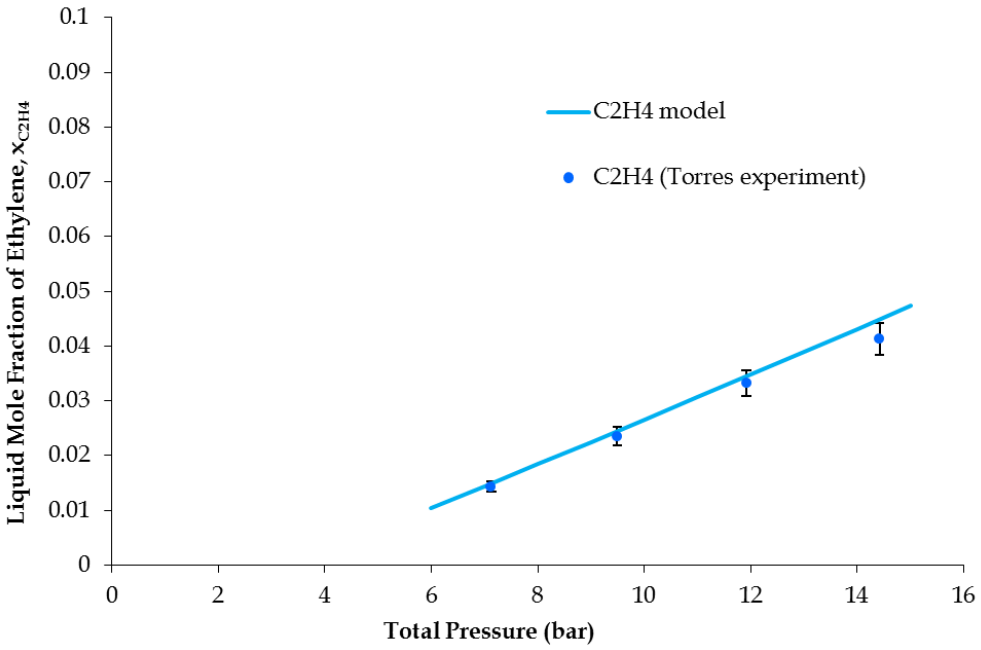


**Figure A. 59** *VLE model predictions for liquid fraction of carbon monoxide against pressure at 363K.*

This model will allow to determine the compositions in the inlet and outlet of the reactor at reaction conditions based on experimentally known compositions in the inlet and outlet of the set-up (T=ambient, P=atmospheric).

12. Conversion data for kinetic experiments of Chapter 5

**Table A. 23** Operating conditions and methanol conversion for kinetics experiments presented in Chapter 5.

| P bara | T K | Inlet $y_{CO}$ | Inlet $y_{C2H4}$ | Inlet $y_{He}$ | %wt. MeOH | Pd mol/m³ | $X_{MeOH}$ % |
|---|---|---|---|---|---|---|---|
| 10 | 100 | 0.126 | 0.5 | 0.45 | 31.8 | 1.30E-03 | 9.07 |
| 10 | 100 | 0.332 | 0.5 | 0.168 | 31.8 | 1.30E-03 | 18.54 |
| 10 | 100 | 0.23 | 0.5 | 0.27 | 31.8 | 1.30E-03 | 14 |
| 10 | 100 | 0.426 | 0.5 | 0.074 | 31.8 | 1.30E-03 | 19.3 |
| 10 | 100 | 0.096 | 0.5 | 0.404 | 31.8 | 1.30E-03 | 7.1 |
| 10 | 100 | 0.1 | 0.9 | 0 | 31.8 | 1.30E-03 | 9.63 |
| 10 | 100 | 0.1 | 0.9 | 0 | 80 | 1.30E-03 | 3.4 |
| 10 | 100 | 0.1 | 0.9 | 0 | 20.9 | 1.30E-03 | 10.89 |
| 10 | 88 | 0.1 | 0.9 | 0 | 30 | 2.82E-04 | 6.82 |
| 10 | 94 | 0.1 | 0.9 | 0 | 30 | 2.82E-04 | 7.6 |
| 10 | 100 | 0.1 | 0.9 | 0 | 30 | 2.82E-04 | 6.4 |
| 10 | 106 | 0.1 | 0.9 | 0 | 30 | 2.82E-04 | 6.8 |
| 10 | 111 | 0.1 | 0.9 | 0 | 30 | 2.82E-04 | 6.2 |
| 10 | 100 | 0.1 | 0.709 | 0.191 | 31.8 | 1.30E-03 | 7.89 |
| 10 | 100 | 0.1 | 0.529 | 0.371 | 31.8 | 1.30E-03 | 7.1 |
| 10 | 100 | 0.1 | 0.465 | 0.435 | 31.8 | 1.30E-03 | 5.33 |
| 10 | 100 | 0.1 | 0.35 | 0.55 | 31.8 | 1.30E-03 | 4.55 |
| 10 | 100 | 0.1 | 0.83 | 0.07 | 31.8 | 1.30E-03 | 8.88 |
| 10 | 100 | 0.1 | 0.4 | 0.5 | 31.8 | 1.30E-03 | 6.71 |
| 10 | 100 | 0.1 | 0.235 | 0.665 | 31.8 | 1.30E-03 | 5.1 |
| 10 | 100 | 0.1 | 0.64 | 0.26 | 31.8 | 1.30E-03 | 7.6 |